MULTISCALE REDUCED ORDER MODELING OF COMPLEX MULTI-BAY STRUCTURES

Marc P. Mignolet

Arizona State University

JULY 2013
Final Report

AIR FORCE RESEARCH LABORATORY
AF OFFICE OF SCIENTIFIC RESEARCH (AFOSR)
ARLINGTON, VIRGINIA 22203
AIR FORCE MATERIEL COMMAND

REPORT DOCUMENTATION PAGE

1. REPORT DATE *(DD-MM-YYYY)*	2. REPORT TYPE	3. DATES COVERED *(From - To)*

4. TITLE AND SUBTITLE	5a. CONTRACT NUMBER
	5b. GRANT NUMBER
	5c. PROGRAM ELEMENT NUMBER

6. AUTHOR(S)	5d. PROJECT NUMBER
	5e. TASK NUMBER
	5f. WORK UNIT NUMBER

7. PERFORMING ORGANIZATION NAME(S) AND ADDRESS(ES)	8. PERFORMING ORGANIZATION REPORT NUMBER

9. SPONSORING/MONITORING AGENCY NAME(S) AND ADDRESS(ES)	10. SPONSOR/MONITOR'S ACRONYM(S)
	11. SPONSOR/MONITOR'S REPORT NUMBER(S)

12. DISTRIBUTION/AVAILABILITY STATEMENT

13. SUPPLEMENTARY NOTES

14. ABSTRACT

15. SUBJECT TERMS

16. SECURITY CLASSIFICATION OF:			17. LIMITATION OF ABSTRACT	18. NUMBER OF PAGES	19a. NAME OF RESPONSIBLE PERSON
a. REPORT	b. ABSTRACT	c. THIS PAGE			
					19b. TELEPHONE NUMBER *(Include area code)*

MULTISCALE REDUCED ORDER MODELING OF COMPLEX MULTI-BAY STRUCTURES

AFOSR Contract FA9550-10-1-0080

FINAL REPORT

The focus of this investigation was on achieving quantum improvements in the reduced order modeling of structures undergoing large deformations with particular focus on those of future hypersonic vehicles. One key feature of the present effort was on spanning a much broader ranges of scales than prior investigations (reviewed in [P.1]) had achieved, i.e. being able to capture the effects of localized geometrical defects (stress "hot spots" at the microscale level) but also to consider macroscale structures which are assemblies of panels themselves considered here as the microscale, see Fig. 1.
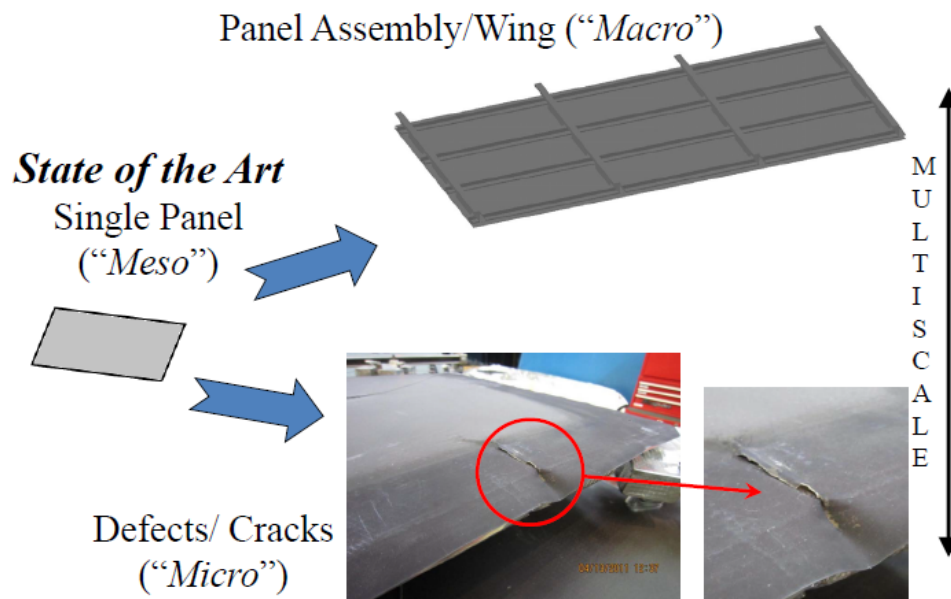

Figure 1. Multiscale structural perspective for hypersonic vehicles.

The above plan was separated into the 4 separate investigations:
1. The micro-meso upscaling process, i.e. how to account for microscale features in nonlinear reduced order models of mesoscale models.
2. The reduced order modeling of mesoscale structures with "difficult" features such as curved structures with snap-through motions and cantilevered ones
3. The extension of the mesoscale strategies for the construction of monolithic (single scale) reduced order models of macroscale structures
4. The meso-macro upscaling process.

The work carried out in these 4 directions under this AFOSR grant is highlighted below, see the journal and conference papers and attachments for full details.

1. MICRO-MESO UPSCALING PROCESS

The two key questions addressed in this part of the investigations were:

(i) can a reduced order model of the *displacement* field of the structure with defect provide an accurate prediction of the *stress* hot spots induced by localized defects?
and

(ii) can a reduced order model of the *defect-free* mesoscale structure be enriched to yield an accurate estimation of the displacement and stress fields of the structure with defect(s)?

The first of the above questions is really on the applicability of the nonlinear reduced order modeling strategy to structures with defects while the second seeks an efficient methodology to account for either uncertain defects or for evolving defects, such as the propagation of a crack (although the plasticity involved at the crack tip cannot be accounted for at present).

This task was addressed on a panel with a notch in [S.1], [C.10], and [T.1] and the answer to both of the above questions is a definite yes. The basis of the reduced order model does indeed exhibit a notch effect which leads to an accurate representation of not only the displacement field but also the stress. Further, two enrichments strategies were successfully formulated and validated that rely on the reduced order model of the defect-free structure to predict the stress field of its counterpart with defect(s).

2. REDUCED ORDER MODELING OF "DIFFICULT" MESO STRUCTURES

The various extensions of the nonlinear reduced order modeling addressed in tasks 1, 3, and 4 will give rise to a broad array of structural geometries and boundary conditions to be considered which will stretch the current capabilities and validations of the methodology. It was accordingly decided to focus some of the present efforts on resolving some of the long standing difficulties encountered in the reduced order modeling of shallow curved structures and cantilevered ones. This component of the investigation was addressed in [C.3], [C.7], [C.9], and [T.2] and has led to great progress in handling these difficult geometries and boundary conditions. In particular:

(i) it was demonstrated that these difficulties are in fact rooted in differences (the definition of elasticity) in the formulation of the finite element technique and in the reduced order modeling definition. This important finding casts a new light on how the identification of the reduced order model ought to be carried out in these "difficult" conditions.

(ii) based on the finding of (i), a novel identification technique was devised to capture the snap-through boundary and response of shallow curved structures that uses pre- and post-snap through configurations. This approach was successfully validated on a curved beam and a thin cylindrical shell.

(iii) the reduced order modeling of cantilevered structures was also improved significantly leading to a successful implementation onto as complex models as the wing of the Predator UAV.

3. MONOLITHIC REDUCED ORDER MODELING OF MACRO STRUCTURES

Discussing the strength and weaknesses of meso-macro upscaling procedures (see section 4 below) is best carried out in comparison with a monolithic, i.e. single scale, model of the same structure. To this end, a complex 9-bay panel was considered and its

nonlinear reduced order model investigated. This process was not only successful, see [S.2], [C.1], [C.5], and [T.1], but also led to significant improvements in the formulation: both a deepening of the dual mode basis and the formulation of a much more expedient identification technique of the coefficients. These findings not only extend the domain of applications of monolithic reduced order models but of also of their multi-scale counterparts.

4. MESO-MACRO UPSCALING PROCESS

The last component of the investigation focused on the upscaling, and more globally the transfer of information, between meso and macro scales using nonlinear reduced order models. This issue was first addressed in a component mode synthesis-type approach in which reduced order models of meso components are constructed and assembled to form the macro structure in a bottom-up strategy. This effort is detailed in Chapter 4.5 of [T.1] where it is demonstrated that this approach will in general not result in a smaller or simpler reduced order model.

This finding is in fact not unexpected given the optimality of the basis used in constructing the reduced order model. Thus, a simplification of the modeling in an upscaling process will require an approximation of the displacement field as discussed in other multi-scale mechanics problems. To achieve this approximation, a top-down approach was suggested in [T.1] in which a "coarse" monolithic reduced order model of the entire structure (as performed in section 3) is enriched on one or a few meso scale components (those of particular interest) to provide an accurate representation of their response. Note that the coarseness of the overall macro model will invariably induce epistemic uncertainty on the prediction of the meso components. Thus, a successful top-down meso-macro multiscaling *must* be accomplished in an uncertain setting.

The construction of *uncertain* nonlinear reduced order model was then emphasized to complete the top-down multiscaling strategy. This effort has been very successful as demonstrated in [P.2], [P.3], [C.2], [C.4], [C.6], [C.8], and [C.11]. The assembly of these various pieces and its implementation on the 9-bay structure discussed in the bottom-up strategy and in section 3 is currently being finalized.

PUBLISHED JOURNAL PAPERS UNDER THIS FUNDING

[P.1] Mignolet, M.P., Przekop, A., Rizzi, S.A, and Spottswood, S.M., "A Review of Indirect/Non-Intrusive Reduced Order Modeling of Nonlinear Geometric Structures," Invited Paper, *Journal of Sound and Vibration*, Vol. 332, No. 10, pp. 2437-2460, 2013.

[P.2] Murthy, R., Wang, X.Q., Perez, R., Mignolet, M.P., and Richter, L.A. "Uncertainty-Based Experimental Validation of Nonlinear Reduced Order Models," *Journal of Sound and Vibration*, Vol. 331, pp. 1097-1114, 2012.

[P.3] Capiez-Lernout, E., Soize, C., and Mignolet, M.P., "Computational Stochastic Statics of an Uncertain Curved Structure with Geometrical Nonlinearity in Three-Dimensional Elasticity," *Computational Mechanics*, Vol. 49, No. 1, pp. 87-97, 2012.

SUBMITTED JOURNAL PAPERS UNDER THIS FUNDING

[S.1] Perez, R.A., Wang, X.Q., and Mignolet, M.P., "Nonlinear Geometric Response of Panels with Localized Geometric Defects by Reduced Order Models – A Notched Panel," Submitted to *Journal of Sound and Vibration*. – See Appendix A.

[S.2] Perez, R.A., Wang, X.Q., and Mignolet, M.P., "Reduced Order Model for the Geometric Nonlinear Response of Complex Structures," Submitted to *Journal of Computational and Nonlinear Dynamics*. – See Appendix B.

CONFERENCE PAPERS UNDER THIS FUNDING

[C.1] Perez, R.A., Wang, X.Q., Matney, A.K., and Mignolet, M.P., "Reduced Order Modeling for the Static and Dynamic Geometric Nonlinear Responses Of a Complex Multi-Bay Structure," Proceedings of the 11th International Conference on Recent Advances in Structural Dynamics," Pisa, Italy, Jul. 1-3, 2013.

[C.2] Capiez-Lernout, E., Soize, C. and Mignolet, M.P., "Nonlinear Stochastic Dynamical Post-Buckling Analysis Of Uncertain Cylindrical Shells," Proceedings of the 11th International Conference on Recent Advances in Structural Dynamics, Pisa, Italy, Jul. 1-3, 2013.

[C.3] Wang, X.Q., Perez, R., and Mignolet, M.P., "Nonlinear Reduced Order Modeling of Complex Wing Models," Proceedings of the 54th Structures, Structural Dynamics and Materials Conference, Apr. 8-11, 2013, Boston, Massachusetts, AIAA Paper AIAA-2013-1520.

[C.4] Capiez-Lernout, E., Soize, C., and Mignolet, M.P., "Uncertainty Quantification for Post-Buckling Analysis of Cylindrical Shells with Experimental Comparisons," Proceedings of the Congress on Computational Methods in Applied Sciences and Engineering (ECCOMAS 2012), Sep. 10-14, 2012, Vienna, Austria.

[C.5] Perez, R., Wang, X.Q., and Mignolet, M.P., "Reduced Order Model for the Geometric Nonlinear Response of Complex Structures," Proceedings of the 24th ASME Mechanical Vibration and Noise Conference, Aug. 12-15, 2012, Chicago, Illinois, ASME Paper DETC2012/MECH-71141.

[C.6] Capiez-Lernout, E., Soize, C., and Mignolet, M.P., "Uncertainty Quantification in Computational Nonlinear Elasticity, " Proceedings of the ASME 2012 11th Biennal Conference on Engineering Systems Design And Analysis (ESDA 2012), Jul. 2-4, 2012, Nantes, France, Paper ESDA2012-82246.

[C.7] Matney, A., Perez, R.A, Spottswood, S.M., Wang, X.Q., and Mignolet, M.P., "Nonlinear Structural Reduced Order Modeling Methods for Hypersonic Structures," Proceedings of the 53rd Structures, Structural Dynamics and Materials Conference, Apr. 23-26, 2012, Honolulu, Hawaii, AIAA Paper AIAA-2012-1972.

[C.8] Capiez-Lernout, E., Soize, C., and Mignolet, M.P., "Effect of Structural Uncertainties on the Nonlinear Elastic Behavior of a Curved Beam. Stochastic Computational Modeling and Comparison with Simulated Experiments," Proceedings of the 8th International Conference on Structural Dynamics (EURODYN 2011), Jul. 4-6, 2011, Leuven, Belgium.

[C.9] Chang, Y.-W., Wang, X.Q., Capiez-Lernout, E., Mignolet, M.P., and Soize, C., "Reduced Order Modeling for the Nonlinear Geometric Response of Some Curved Structures," Proceedings of the 2011 International Forum of Aeroelasticity and Structural Dynamics, Jun. 26-30, 2011, Paris, France, IFASD-2011-185.

[C.10] Perez, R., Wang, X.Q., and Mignolet, M.P., "Reduced Order Modeling for the Nonlinear Geometric Response of Cracked Panels," Proceedings of the 52nd Structures, Structural Dynamics and Materials Conference, Apr. 4-7 2011, Denver, Colorado, AIAA 2011-2018.

[C.11] Murthy, R., Wang, X.Q., Perez, R., and Mignolet, M.P., "Uncertainty-Based Experimental Validation of Nonlinear Reduced Order Models," Proceedings of the 10th International Conference on Recent Advances in Structural Dynamics, RASD-10, Southampton, United Kingdom, Jul 12-14, 2010, Paper sd2010-029.

THESES UNDER THIS FUNDING

[T.1] Perez, R.A., "Multiscale Reduced Order Models for the Geometrically Nonlinear Response of Complex Structures," Ph.D., December 2012.

[T.2] Chang, Y.W.," Reduced Order Modeling for the Nonlinear Geometric Response of a Curved Beam," M.S., August 2011.

ATTACHMENT A

Perez, R.A., Wang, X.Q., and Mignolet, M.P., "Reduced Order Model for the Geometric Nonlinear Response of Complex Structures," Submitted to *Journal of Computational and Nonlinear Dynamics*, Manuscript CND-13-1181.

REDUCED ORDER MODEL FOR THE GEOMETRIC NONLINEAR RESPONSE OF COMPLEX STRUCTURES

Ricardo Perez, X.Q. Wang, and Marc P. Mignolet

SEMTE, Faculties of Mechanical and Aerospace Engineering
Arizona State University
Tempe, Arizona 85287-6106, USA

Tel.: (480) 965-3292,Fax: (480) 727-9321
raperez1@asu.edu. xwang138@asu.edu, marc.mignolet@asu.edu

ABSTRACT

This paper focuses on the development of nonlinear reduced order modeling techniques for the prediction of the response of complex structures exhibiting "large" deformations, i.e. a geometrically nonlinear behavior, and modeled within a commercial finite element code. The present investigation builds on a general methodology successfully validated in recent years on simpler beam and plate structures by:

(i) developing a novel identification strategy of the reduced order model parameters that enables the consideration of the large number of modes (> 50 say) that would be needed for complex structures, and

(ii) extending an automatic strategy for the selection of the basis functions used to represent accurately the displacement field.

The above novel developments are successfully validated on the nonlinear static response of a 9-bay panel structure modeled with 96,000 degrees of freedom within Nastran.

Keywords: reduced order modeling, nonlinear geometric response, finite elements

INTRODUCTION

Significant efforts have centered in the last decade or so on the construction of reduced order models (ROMs) of structures undergoing "large" deformations, i.e. exhibiting geometric nonlinearity, from finite element models generated using *commercial* codes (e.g. Nastran, Abaqus, DYNA3D), see [1] for a recent review.

The use of commercial finite element codes enables the straightforward consideration of complex models, allows a broad ensemble of possible element types and capabilities, but also permits a direct transition to the industrial setting where these codes are routinely used. The counterpart of these advantages is the unavailability of certain information and the uncertainty on the formulation implemented in the finite element modeling and response computation.

Notwithstanding the above difficulties, the ROM capabilities have progressed from applications to flat structures (see [2-9]), to moderately large motions of curved structures (see [10-14]), and a first assessment on a notched panel [15]. Further, the coupling of these nonlinear structural reduced order models with aerodynamics, either full or reduced order model has also been successfully demonstrated in [16-18]. A similar coupling but of the structural dynamics and thermal aspects, the two in reduced order model format, has also been proposed and validated in [19-21]. Finally, the introduction of uncertainty in the reduced order model has finally been formulated and implemented [22,23].

The reduced order models developed in the above investigations are parametric, i.e. the form of the equations governing the generalized coordinates is fixed, linear in mass and damping operators with a stiffness operator exhibiting linear, quadratic, and cubic terms in all combinations of generalized coordinates as derived from finite deformation elasticity in the

reference configuration (see review below). Then, the key challenges in the construction of such a reduced order model are:

(i) the estimation of these parameters of the model from a set of finite element results. Current methods for this identification are based on computed static responses for specified loads [3,6], or in reverse, necessary loads to achieve a particular displacement (see [8,24]). This strategy becomes computationally expensive as the size of the model increases as it is proportional to the third power of the number of modes retained.

(ii) the selection of the basis to represent well and "economically" (with a small basis) the displacements.

These challenges have been well addressed for the simple structures reviewed above and with a small number of modes, typically less than 20. However, for more complex structural models, i.e. those which exhibit more complex physical behavior and thus necessitate a larger number of modes for an accurate representation of their response, e.g. the 9-bay panel of [25], a revisit of the identification approach and basis selection strategy were found necessary [25]. This revisit is the focus of the present investigation and both a new identification approach and a deepened validation of the dual mode basis selection strategy of [8] will be presented.

The application of these novel approaches is demonstrated for the construction of a reduced order model of the 9-bay panel modeled within Nastran with 96,000 degrees of freedom. An excellent agreement between the nonlinear static responses obtained by Nastran and by the obtained 85-mode nonlinear reduced order model is achieved.

REDUCED ORDER MODEL FORM AND GOVERNING EQUATIONS

The reduced order models considered in this investigation are based on a representation of the nonlinear geometric response of the structure in the form

$$\underline{u}(t) = \sum_{n=1}^{M} q_n(t)\, \underline{\psi}^{(n)} \tag{1}$$

where $\underline{u}(t)$ denotes the vector of displacements of the finite element degrees of freedom. Further, $\underline{\psi}^{(n)}$ are specified, constant basis functions and $q_n(t)$ are the time dependent generalized coordinates.

The derivation of the governing equations for these coordinates is achieved here from the equations of finite deformation elasticity in the undeformed configuration Ω_0. Specifically, the equations of motion for an infinitesimal element are (summation is implied over repeated indices)

$$\frac{\partial}{\partial X_k}\left(F_{ij}\, S_{jk}\right) + \rho_0\, b_i^0 = \rho_0\, \ddot{u}_i \tag{2}$$

where $\underline{\underline{S}}$ is the second Piola-Kirchhoff stress tensor (double underline is used here for matrices), ρ_0 denotes the density in the reference configuration, and $\underline{b}^0$ is the vector of body forces, all of which are assumed to depend on the position $\underline{X} \in \Omega_0$, [26,27]. In Eq. (2), $\underline{\underline{F}}$ denotes the deformation gradient tensor of components

$$F_{ij} = \frac{\partial x_i}{\partial X_j} = \delta_{ij} + \frac{\partial u_i}{\partial X_j} \tag{3}$$

where δ_{ij} is the Kronecker delta and $\underline{u} = \underline{x} - \underline{X}$ is the displacement vector, $\underline{x}$ being the position vector in the deformed configuration. The material is assumed here to be linear elastic in that $\underline{\underline{S}}$ and $\underline{\underline{E}}$ (the Green strain tensor) satisfy

$$S_{ij} = C_{ijkl} \, E_{kl} \tag{4}$$

where $\underline{\underline{C}}$ is a fourth order elasticity tensor, function in general of the undeformed coordinates $\underline{X}$.

In parallel to its discrete counterpart in Eq. (1), the displacement field u_i in the continuous structure is sought in the modal-like representation

$$u_i(\underline{X},t) = \sum_{n=1}^{M} q_n(t) \, U_i^{(n)}(\underline{X}) \qquad i = 1,2,3 \tag{5}$$

where $U_i^{(n)}(\underline{X})$ are specified, constant basis functions satisfying the boundary conditions also in the undeformed configuration.

A set of nonlinear ordinary differential equations governing the evolution of the generalized coordinates $q_n(t)$ can then be obtained by introducing Eq. (5) in Eqs (2)-(4) and imposing (Galerkin approach) the error to be orthogonal to the basis. This process leads [8] to the requisite reduced order model equations

$$M_{ij}\ddot{q}_j + D_{ij}\dot{q}_j + K_{ij}^{(1)} \, q_j + K_{ijl}^{(2)} q_j q_l + K_{ijlp}^{(3)} q_j q_l q_p = F_i \quad . \tag{6}$$

Note in Eq. (6) that a linear damping term $D_{ij}\dot{q}_j$ has been added to collectively represent various dissipation mechanisms. Further, M_{ij} denotes the elements of the mass matrix, $K_{ij}^{(1)}$,

$K_{ijl}^{(2)}$, $K_{ijlp}^{(3)}$ are the linear, quadratic, and cubic stiffness coefficients and F_i are the modal forces.

The knowledge of the displacements provides a complete solution of the problem and other quantities can then be evaluated. For example, any component of the second Piola-Kirchhoff stress tensor at any point can be expressed as

$$S_{ij} = \overline{S}_{ij} + \hat{S}_{ij}^{(m)} q_m + \widetilde{S}_{ij}^{(m,n)} q_m\, q_n \tag{7}$$

where the coefficients $\overline{S}_{ij}$, $\hat{S}_{ij}^{(m)}$, and $\widetilde{S}_{ij}^{(m,n)}$ depend only on the point $\underline{X}$ considered.

ROM PARAMETERS IDENTIFICATION

The estimation of the parameters of Eq. (6) is an important step of the reduced order model construction. First, the mass components M_{ij} and modal forces F_i can be identified as in linear modal models, i.e.

$$M_{ij} = \underline{\psi}^{(i)T} M_{FE} \underline{\psi}^{(j)} \qquad F_i = \underline{\psi}^{(i)T} \underline{F}(t) \tag{8a, 8b}$$

where M_{FE} is the finite element mass matrix and $\underline{F}(t)$ is the excitation vector on the structure.

Next is the determination of the stiffness coefficients $K_{ij}^{(1)}$, $K_{ijl}^{(2)}$, and $K_{ijlp}^{(3)}$. In this regard, note first that the linear coefficients $K_{ij}^{(1)}$ could be determined as in linear modal models, i.e.

$$K_{ij}^{(1)} = \underline{\psi}^{(i)T} K_{FE}^{(1)} \underline{\psi}^{(j)} \tag{9}$$

where $K_{FE}^{(1)}$ is the finite element linear stiffness matrix.

Another approach must however be adopted for $K_{ijl}^{(2)}$ and $K_{ijlp}^{(3)}$ as nonlinear stiffness matrices are typically not available from a commercial finite element code. Formal expressions, as

6

integrals over the undeformed domain of the structure, for the linear, quadratic, and cubic stiffness coefficients were obtained [8] in the process of deriving Eq. (6). They have been used to estimate the coefficients (see [23]) through a discretization of the domain consistent with the finite element model. Non-intrusive (or indirect) methods (see [1] for review) have also been developed to identify these coefficients based on computed static responses and it is this latter strategy which is considered here.

In this regard, a reduction in this computational effort is obtained by noting the symmetrical role of j and l in the quadratic terms and j, l, and p in the cubic ones, which indicates that the summations over those indices can be restricted to $p \geq l \geq j$ leading to approximately $M^4 / 6$ coefficients to be identified.

Two approaches have been proposed to identify the above quadratic and cubic stiffness parameters (and potentially the linear ones as well) from a series of static finite element solutions. The first one relies on prescribing a series of load cases and projecting the induced responses on the basis functions $\underline{\psi}^{(n)}$ to obtain the corresponding generalized coordinates values $q_j^{(p)}$, p being the index of the load cases (see [3,6]). Then, introducing these values into Eq. (6) for each load case yields

$$K_{ij}^{(1)} q_j^{(p)} + K_{ijl}^{(2)} q_j^{(p)} q_l^{(p)} + K_{ijlr}^{(3)} q_j^{(p)} q_l^{(p)} q_r^{(p)} = F_i^{(p)}, \quad i = 1, ..., M \qquad (9)$$

where M denotes the number of basis functions (or modes) in the reduced order model. Proceeding similarly for P load cases yields a set of linear algebraic equations for the coefficients $K_{ijl}^{(2)}$ and $K_{ijlp}^{(3)}$, and possibly the linear stiffness coefficients $K_{ij}^{(1)}$ as well, which can be solved in a least squares format to complete the identification of the stiffness parameters.

An alternate strategy has also been proposed (e.g. see [24] and the modification of [8]) in which the *displacements* are prescribed and the required force distributions are obtained from the finite element code. The corresponding modal forces are then evaluated from Eq. (8b) and a set of equations of the form of Eq. (9) is again obtained. Appropriately selecting the displacement fields to be imposed can lead to a particularly convenient identification of the stiffness coefficients. Specifically, the imposition of displacements proportional to the basis function $\underline{\psi}^{(n)}$ only, i.e.

$$\underline{u} = q_n \, \underline{\psi}^{(n)} \qquad \underline{\hat{u}} = \hat{q}_n \, \underline{\psi}^{(n)} \qquad \underline{\tilde{u}} = \tilde{q}_n \, \underline{\psi}^{(n)} \tag{10}$$

leads to the 3 sets of equations

$$K_{in}^{(1)} \, q_n + K_{inn}^{(2)} q_n^2 + K_{innn}^{(3)} \, q_n^3 = F_i \quad \text{(no sum on } n\text{)}$$

$$K_{in}^{(1)} \, \hat{q}_n + K_{inn}^{(2)} \hat{q}_n^2 + K_{innn}^{(3)} \, \hat{q}_n^3 = \hat{F}_i \quad \text{(no sum on } n\text{)} \tag{11}$$

$$K_{in}^{(1)} \, \tilde{q}_n + K_{inn}^{(2)} \tilde{q}_n^2 + K_{innn}^{(3)} \, \tilde{q}_n^3 = \tilde{F}_i \quad \text{(no sum on } n\text{)}$$

in which no sum over the index n is to be understood and for $i = 1, ..., M$. In fact, these 3 sets of equations permit the direct evaluation of the coefficients $K_{in}^{(1)}$, $K_{inn}^{(2)}$, and $K_{innn}^{(3)}$ for all i. Repeating this effort for $n = 1, ..., M$ thus yields a first set of stiffness coefficients.

Proceeding similarly but with combinations of two basis functions, i.e.

$$\underline{u} = q_n \, \underline{\psi}^{(n)} + q_m \, \underline{\psi}^{(m)} \quad m \geq n \tag{12}$$

and relying on the availability of the coefficients $K_{in}^{(1)}$, $K_{inn}^{(2)}$, $K_{innn}^{(3)}$ and $K_{im}^{(1)}$, $K_{imm}^{(2)}$, $K_{immm}^{(3)}$ determined above, leads to equations involving the three coefficients $K_{inm}^{(2)}$, $K_{innm}^{(3)}$, and $K_{inmm}^{(3)}$.

Thus, imposing three sets of displacements of the form of Eq. (12) provides the equations needed to also identify $K_{inm}^{(2)}$, $K_{innm}^{(3)}$, and $K_{inmm}^{(3)}$.

Finally, imposing displacement fields as linear combinations of three modes, i.e.

$$\underline{u} = q_n \, \underline{\psi}^{(n)} + q_m \, \underline{\psi}^{(m)} + q_r \, \underline{\psi}^{(r)} \quad r \geq m \geq n \tag{13}$$

permits the identification of the last coefficients, i.e. $K_{inmr}^{(3)}$.

Proceeding either with load cases, i.e. Eq. (9), or with imposed displacement solutions, Eqs. (10)-(13), M coefficients (1 for each value of i) can be evaluated for each load/displacement solution. Accordingly, there will be approximately $M^3/6$ such solutions to be determined, each one of which requires a full finite element nonlinear analysis. For an $M = 60$ basis function reduced order model, there will thus be 36,000 solutions which represents a very significant upfront computational effort.

An alternate approach is proposed here, which relies on the availability of the final *tangent stiffness matrix* for each load/imposed displacement case. The advantage of this approach is that an $M \times M$ matrix is obtained for each solution and thus a reduction of the computational effort to $O(M^2)$ is expected. The specific details of this novel algorithm are developed below.

The *iu* component of the reduced order tangent stiffness matrix is derived from the cubic stiffness operator of Eq. (6) as

$$\begin{aligned}
K_{iu}^{(T)} &= \frac{\partial}{\partial q_u} \left[K_{ij}^{(1)} q_j + K_{ijl}^{(2)} q_j q_l + K_{ijlp}^{(3)} q_j q_l q_p \right] \\
&= K_{iu}^{(1)} + \left[K_{iju}^{(2)} + K_{iuj}^{(2)} \right] q_j + \left[K_{ijlu}^{(3)} + K_{ijul}^{(3)} + K_{iujl}^{(3)} \right] q_j q_l
\end{aligned} \tag{14}$$

It is proposed here to determine the stiffness coefficients $K_{ij}^{(1)}$, $K_{ijl}^{(2)}$, and $K_{ijlp}^{(3)}$ by imposing the matching, for a series of deformed configurations, of the reduced order tangent stiffness matrix with the projection on the basis of its finite element counterpart $\hat{K}^{(T)}$. That is,

$$K^{(T)}(\underline{q}^{(p)}) = \Psi^T \hat{K}^{(T)}(\underline{u}^{(p)})\Psi \quad \text{where} \quad \underline{u}^{(p)} = \Psi \underline{q}^{(p)} \tag{15}$$

for a series of $p = 1, ..., P$ deformed configurations. In the above equations, the subscript ^{T} denotes the operation of matrix transposition and Ψ is the modal matrix

$$\Psi = \left[\underline{\psi}^{(1)} \; \underline{\psi}^{(2)} \cdots \underline{\psi}^{(M)} \right]. \tag{16}$$

The deformed configurations $\underline{u}^{(p)} = \Psi \underline{q}^{(p)}$ selected here are those of the imposed displacement scheme, Eqs. (10)-(12). Consider first the situation in which the imposed displacement is along a single basis function, i.e. $\underline{u} = q_j \underline{\psi}^{(j)}$. The corresponding ROM tangent stiffness matrix can then be written as (no sum on j)

$$K_{iu}^{(T)} = K_{iu}^{(1)} + \left[K_{iju}^{(2)} + K_{iuj}^{(2)} \right] q_j + \left[K_{ijju}^{(3)} + K_{ijuj}^{(3)} + K_{iujj}^{(3)} \right] q_j^2 \tag{17}$$

Since the elements $K_{ijl}^{(2)}$ and $K_{ijlp}^{(3)}$ were assumed to be zero unless $p \ge l \ge j$, the above equation is equivalent to

$$K_{iu}^{(T)} = \left[\Psi^T \hat{K}^{(T)} \Psi \right]_{iu} = K_{iu}^{(1)} + K_{iju}^{(2)} q_j + K_{ijju}^{(3)} q_j^2 \qquad j < u \tag{18}$$

$$K_{iu}^{(T)} = \left[\Psi^T \hat{K}^{(T)} \Psi \right]_{iu} = K_{iu}^{(1)} + 2 K_{iuu}^{(2)} q_u + 3 K_{iuuu}^{(3)} q_u^2 \quad j = u \tag{19}$$

$$K_{iu}^{(T)} = \left[\Psi^T \hat{K}^{(T)} \Psi \right]_{iu} = K_{iu}^{(1)} + K_{iuj}^{(2)} q_j + K_{iujj}^{(3)} q_j^2 \qquad j > u \tag{20}$$

from which the coefficients $K_{ijl}^{(2)}$, $K_{ijjl}^{(3)}$, and $K_{ijll}^{(3)}$ can be estimated if it is assumed that the linear stiffness coefficients are obtained from Eq. (9).

To complete the identification of the reduced order model, it remains to evaluate the coefficients $K_{ijlu}^{(3)}$ for $j \neq l$, $j \neq u$, and $u \neq l$. They can be evaluated from the knowledge of $K_{iu}^{(T)}$ corresponding to a displacement field which involves both basis functions j and l, i.e. of the form of Eq. (12). Then, $K_{iu}^{(T)}$ is given by Eq. (14) in which no summation on j and l applies. Specifically, for $u > l > j$, one has

$$K_{iu}^{(T)} = \left[\Psi^T \hat{K}^{(T)} \Psi \right]_{iu} = K_{iu}^{(1)} + \left[K_{iju}^{(2)} q_j + K_{ilu}^{(2)} q_l \right] + \left[K_{ijlu}^{(3)} q_j q_l + K_{ijju}^{(3)} q_j^2 + K_{illu}^{(3)} q_l^2 \right] \quad (21)$$

in which all terms are known except $K_{ijlu}^{(3)}$.

Note in the above procedure that no combination of three modes, as in Eq. (13), is necessary and thus, as suggested at the beginning of this section, the number of deformed configurations to consider is only of order $O\left(M^2 \right)$, it is indeed $2M + M(M-1)/2$. To corroborate this analysis, shown in Table 1 are the number of static solutions required for the new, tangent stiffness-based identification scheme and the imposed displacement force-based method. These results clearly show the reduction in computational effort necessary which converges to $M/3$ for large M.

However, the CPU time required in the construction of the tangent stiffness matrix and its transformation to the modal tangent stiffness matrix ought to be taken into account to perform a fair comparison. For the 9-bay panel considered in the ensuing sections and with 96,000 degrees of freedom, the CPU time required to produce a static solution with tangent stiffness matrix was found to be approximately 1.5 times the time to obtain the same solution without computing the tangent stiffness matrix. The combination of these factors suggests that the net reduction in

computational time implied by the tangent stiffness algorithm is a factor of the order of *M*/4 to *M*/5 for large *M*.

A limited set of comparisons were performed, on the 9-bay panel described below and on a flat clamped-clamped beam, to assess whether the stiffness coefficients identified by the imposed displacement methods based on the forces and the tangent stiffness matrix were noticeably different and/or they led to reduced order model with different predictive capabilities. While some, typically small, differences in the coefficients were found, the two methods led to reduced order model predictions that were very close to each other suggesting that the methods provide an equal accuracy in estimating the stiffness coefficients.

ROM BASIS SELECTION

The selection of the basis functions $\underline{\psi}^{(n)}$ represents a key challenge of the reduced order modeling strategy: if the structural response is not well represented within this basis, the corresponding prediction of the reduced order model will in general be poor. The modes/basis functions needed for a nonlinear problem are certainly expected to include those used for the corresponding linear problem, but others are also anticipated to model the difference in physical behavior induced by the nonlinearity. This situation is particularly clear in shell-like structures subjected to transverse loadings in which the linear response is predominantly transverse while the tangential/in-plane displacement field plays a fundamental role (the "membrane-stretching" effect, see [1,3,6] for discussion) in large motions.

This issue was addressed in [8] through the inclusion in the basis of an additional set of basis functions referred to as dual modes aimed at capturing the membrane stretching effects. The key idea in this approach is to first subject the structure to a series of "representative" static loadings,

and determine the corresponding *nonlinear* displacement fields. Then, extract from them additional basis functions, the "dual modes", to append to the linear basis, i.e. the modes that would be used in the linear case. It was argued in [8] that the representative static loadings should be selected to excite primarily the linear basis modes and, in fact, in the absence of geometric nonlinearity (i.e. for a linear analysis) should only excite these modes. i.e. the applied load vectors $\underline{F}_{FE}^{(m)}$ on the structural finite element model should be such that the corresponding linear static responses are of the form

$$\underline{u}^{(m)} = \sum_i \alpha_i^{(m)} \underline{\psi}^{(i)} \tag{22}$$

which occurs when

$$\underline{F}_{FE}^{(m)} = \sum_i \alpha_i^{(m)} K_{FE}^{(1)} \underline{\psi}^{(i)} \tag{23}$$

where $\alpha_i^{(m)}$ are coefficients to be chosen with m denoting the load case number. A detailed discussion of the linear combinations to be used is presented in [8] but, in all validations carried out, it has been sufficient to consider the cases

$$\underline{F}_{FE}^{(m)} = \alpha_i^{(m)} K_{FE}^{(1)} \underline{\psi}^{(i)} \quad i = \text{dominant mode} \tag{24}$$

and

$$\underline{F}_{FE}^{(m)} = \frac{\alpha_i^{(m)}}{2} K_{FE}^{(1)} \left[\underline{\psi}^{(i)} + \underline{\psi}^{(j)} \right] \quad i = \text{dominant mode}, j \neq i \tag{25}$$

where a "dominant" mode is loosely defined as one expected to provide a large component of the panel response to the physical loading. The ensemble of loading cases considered is formed by selecting several values of $\alpha_i^{(m)}$ for each dominant mode in Eq. (24) and also for each mode $j \neq i$ in Eq. (25). Note further that both positive and negative values of $\alpha_i^{(m)}$ are suggested and

that their magnitudes should be such that the corresponding displacement fields $\underline{u}^{(m)}$ range from near linear cases to some exhibiting a strong nonlinearity.

The next step of the basis construction is the extraction of the nonlinear effects in the obtained displacement fields, which is achieved by removing from the displacements fields their projections on the linear basis. Finally, a proper orthogonal decomposition (POD) analysis of each set of "nonlinear responses" is then sequentially carried out to extract the dominant features of these responses which are then selected as dual modes, see [8] for full details.

Validating the appropriateness of these dual modes can be done in particular by demonstrating notable improvements in the projection of snap-shots of the full response on a basis that includes them vs. one that does not, see ensuing section for details. A more visual approach would be to demonstrate that the deflections induced by the loadings of Eq. (24) and (25) are similar to those obtained with the physical loading of interest for a broad range of overall magnitude. This effort could be done by plotting the corresponding displacement fields and comparing them. A more expedient strategy would be to visualize these displacement fields in the *N*-dimensional space, where *N* is the number of degrees of freedom of the structure, and to show that the displacements induced by the physical loading and by the ones of Eq. (24) and (25) closely occupy the same part of the space. Since *N* is typically much larger than 3, this space cannot be represented graphically but 2- and 3-dimensional sections of it can be very informative.

To exemplify this situation, consider the clamped-clamped aluminum beam of [19] subjected to both static and dynamic uniform loads. In the absence of symmetry breaking, the transverse displacements are symmetric while the inplane ones are antisymmetric. Three representative descriptors of the displacement field are thus the transverse displacements of the beam middle and of another point, taken here as the 1/4 point, and the inplane displacement of that same off-

center point. The magnitude of these displacements is plotted vs. each other in Fig. 1 for a series of loadings. First are a uniform static load of varying magnitude, loads of the form of Eq. (24) using the first symmetric mode (1-1 Dual) and the second symmetric mode (2-2 Dual), and finally loads in the form of Eq. (25) with combinations between the first symmetric mode and the two following ones (1-2 Dual and 1-3 Dual). Also included in Fig. 1 are snap shots of the dynamic stationary response to a uniformly distributed load varying randomly in time as a white noise bandlimited process in the frequency range [0,1042Hz] simulating an acoustic loading of overall sound pressure level (*OASPL*) of 143dB.

It is clearly seen from Fig. 1 that the displacements induced by the loadings of Eq. (24) for the 1-1 Dual and Eq. (25) closely occupy the same space as both static and dynamic physical loads and thus they can efficiently be used in the construction of the basis for the representation of the full nonlinear response. Note as well that the displacements induced by the loading of Eq. (24) for the 2-2 Dual does not occupy the same space as the other ones and thus is not a good candidate for the basis, i.e. its inclusion in the basis would not be detrimental but would not be very beneficial either. This observation was indeed expected as mode 2 is not a dominant mode, i.e. it does not or rarely does (in the dynamic case) represent the largest component of the response. This finding confirms the selection strategy of the modes, dominant or not, in Eq. (24) and (25). The appropriateness of the above duals extends well beyond the uniform loads, static or dynamic, discussed above; they are appropriate for the class of loading conditions in which the response is dominated by mode 1 (the mode selected as dominant). To confirm this expectation, the displacements induced by triangular loads (zero at the clamp supports and maximum at the beam middle) are also plotted in Fig. 1 and they also closely occupy the same space.

The above dual mode construction has been very successfully applied to various beams and plates structural models, e.g. see [8,9,14-21], to capture the nonlinear interaction, both static and dynamic, between transverse and "in-plane" motions.

VALIDATION MODEL DESCRIPTION

The 9-bay fuselage sidewall panel of [25] modeled within Nastran was considered for the validation of the (i) basis selection strategy and (ii) novel stiffness coefficients identification. The 9-bay panel is a section of the sidewall fuselage panel studied in [28], see Fig. 2 for a picture of the actual hardware taken from [28]. The finite element model of the 9-bay panel, shown in Fig. 3, has 96,000 degrees of freedom. The dimensions of the skin panel are 58.11in by 25.06in, and it is subdivided into nine bays by a riveted frame and longeron substructure. Each bay measures 18.75in by 7.5in between rivet lines. The thickness of the skin panel and frame substructure is of 0.05in and 0.04in for the longeron substructure. The finite element model consists of 4-node plate elements. Further, beam elements were used to model the rivets that join the skin panel to the frame and longeron substructures. The material properties are shown in Table 2. The edges of the skin panel are simply supported.

REDUCED ORDER MODEL OF THE 9-BAY PANEL

One of the complexities of the 9-bay panel considered here is in its high modal density, the structure has 89 linear modes in the [0,500]Hz frequency band. This presents a challenge in the construction of a compact basis; therefore, it becomes very important to identify the most important modes that are needed to represent the response of the structure.

To support this selection process, a small database of nonlinear static and dynamic responses was constructed. It includes the static responses to 10 different uniform pressures applied to the skin panel and of magnitudes ranging from 0.015 psi to 0.6 psi. The corresponding peak transverse deflections varied from 0.1 skin panel thicknesses to 2.5 thicknesses. Further, also considered was a short time history of the dynamic response of the panel to an acoustic excitation modeled as a uniform pressure applied only on the skin panel and varying in time as a white noise in the frequency range [0,500]Hz. The overall sound pressure level (*OASPL*) was 144dB and a series of 200 "snapshots" were obtained from the stationary part of the MSC/Nastran SOL 400 nonlinear dynamic response.

The appropriateness of a basis to model the response can be assessed by the representation error

$$\varepsilon_{rep} = \frac{\left\| \underline{u} - \underline{u}_{proj} \right\|}{\left\| \underline{u} \right\|} \tag{27}$$

where $\underline{u}$ is the static displacement field computed by the finite element code and $\underline{u}_{proj}$ is its projection on the selected basis. The representation error ε_{rep} was plotted as a function of the number of retained linear modes and the modes at which noticeable drops in this error occurred were recorded. This process led to the identification of a set of 49 linear modes, with natural frequencies ranging from 68Hz to 541Hz. The mean of the representation error of the dominant transverse displacement (T3 or z component) was equal to 0.43% for the skin panel and 0.5% for the frame-longeron substructure. Further, the mean representation errors for the in-plane component along the length of the skin panel (T1 or x component) were equal to 56% for the skin panel and 1.1% for the frame-longeron substructure. The mean representation errors for the component along the width (T2 or y component), which is the dominant "in-plane" component

17

for the skin panel, were equal to 71% for the skin panel and 5.1% for the frame-longeron substructure. The large errors of the in-plane components of the skin panel are fully expected and result from the membrane stretching that occurs when the behavior of the panel is in the nonlinear regime, and which the linear basis cannot capture.

The 14 linear modes with the largest modal components, i.e. modes 1, 5, 6, 7, 9, 10, 13, 15, 16, 25, 26, 28, 46 and 50, were used to construct the dual modes. Since the modal component of mode 1 is much larger than the other ones, it was considered as the only dominant mode in Eqs. (24)-(25). The POD-based dual mode construction procedure highlighted above (see [8] for full details) was performed for the data obtained for mode 1 alone and each of the 13 combinations of mode 1 and another of the 13 largest responding modes. In each of these 14 situations, 10 different loading factors $\alpha_i^{(m)}$ were used, half positive and half negative, and leading to peak deflections ranging from 1 to approximately 2.4 skin panel thicknesses. The remainders of these 140 deflections, after projection on the 49 linear modes identified above, were analyzed by POD. A key aspect of this approach is to select the POD modes that contain new information originating from the geometric nonlinearity. In this light, there are two main substructures of interest, the skin panel and the frames. For the skin panel, it is of interest to select the POD eigenvectors with largest eigenvalues and having a dominant in-plane component (T1 and T2). On the other hand, it can be seen from Fig. 3(a) that the frames are analogous to a cantilevered structure. Therefore, it is of interest to select the POD eigenvectors with largest eigenvalues and having dominant T3 components, which is in the tangential or axial direction of the frames. Thirty-six duals modes were identified this way leading to a 85-mode model.

Another perspective on the adequacy of the dual modes is provided by the 3-dimensional section of the *N*-dimensional space of displacements shown in Fig. 4 which focuses on the

transverse displacements at the middle points of the center panel and of the corner and side panels (panels 1 and two, see Fig. 3b) and the T2 displacement at these latter points. Clearly, the duals shown closely occupy the same space as the physical uniform loading, as seen in connection with the beam model, see Fig. 1.

9-BAY PANEL STATIC VALIDATION

Having completed the reduced order model construction, it was desired to assess its predictive capability in comparison with Nastran. To this end, a loading of 0.6 psi, leading to a 2.5 thicknesses maximum skin panel deflection, was considered and shown in Figs. 5-12 are contour plots of the different displacement components. Note the excellent matching, both qualitatively and quantitatively, between reduced order model and NX/Nastran results. The norm errors of the former in comparison to the latter, for the skin panel degrees-of-freedom, were 1.1% for the transverse (T3) component, 3.5% for the in-plane T2 component, 45% for the other, much smaller, in-plane component T1, and 5% for the in-plane magnitude (see also Table 3). Clearly, the matching of the dominant components, T3 and T2, is very good. On the other hand, the relative error of the T1 component is still rather large but it is clear from Figs. 7-12 that this component is much smaller than its T2 counterpart (as stated above).

The prediction errors for the frame substructure were equal to 1.3% for T3, 13% for T1, 8% for T2, and 12% for the magnitude of the in-plane displacements.

A peak displacement of 2.5 thicknesses is usually considered to be well within the nonlinear range for a clamped-clamped panel. To confirm this assessment, a linear Nastran analysis was carried out for the same loading condition and shown in Fig. 13 are the resulting T3, T2, and T1 components of the skin panel displacements. Note the dramatic difference in the T2

displacements between linear and nonlinear analyses (Figs 7 and 13b). Fewer differences in the shape of the T3 components are observed, but the peak magnitude is notably reduced in the nonlinear case, 2.5 thicknesses as compared to 5 thicknesses in the linear case, as expected.

9-BAY PANEL NONLINEAR DYNAMIC VALIDATION

The 9-bay panel was subjected to a uniform pressure on its top surface varying randomly in time as a white noise band-limited process in the frequency range [0,500]Hz to simulate an acoustic loading. The acoustic excitation consisted of an overall sound pressure level (*OASPL*) of 144dB. Further, to permit a close comparison between the full finite element and ROM results, a simple Rayleigh damping model was adopted, i.e. for which the damping matrix is $D = \alpha M + \beta K$ with α=7.55/s and β=5.6E-6s. This selection led to damping ratios between 0.65% and 1% for all transverse modes in the excitation band. The excitation level considered led to a peak transverse displacement of approximately 2.5 skin panel thicknesses, clearly within the geometric nonlinear regime.

The computational effort required to obtain a long time history of the nonlinear dynamic response of the 96,000 degree-of-freedom 9-bay panel was found to be very large. For instance, the analysis of 100,000 time steps required approximately 700GB of scratch space and the analysis lasted 6 days using 4 cores. Therefore, four time histories of 100,000 time steps were analyzed in MSC/Nastran SOL 400, the power spectral densities computed, and their mean used for validation of the 85-mode ROM. The ROM results were obtained using a Newmark-β scheme with the resulting nonlinear algebraic equations solved using a fixed point algorithm. The time step of these computations was selected as 8.33e-5 s.

Shown in Figs. 15 and 16 are plots of the power spectral density of the transverse (T3) and in-plane (T1 and T2) responses of the middle point of bays 1 and 2 (see Fig. 3(b) for panel numbering). The T2 component is very small at the middle point of bay 5; therefore, only the power spectral density of the T3 and T1 components are shown in Fig. 17. Finally, the power spectral density of the transverse and in-plane components, at point A of the frame, is shown in Fig. 18. Clearly, the matching of the T2 and T3 components of the Nastran response is very good at all points. Further, the matching of the dominant T1 component at point A is excellent as well. In addition, the matching of the dominant peaks of the T1 component of the skin panel is very good.

While it might be appealing to focus solely on the skin panel for the construction of the duals, a careful observation of the response of the T1 and T3 components at point A discourages the pursuit of this option. Not only is the energy of both components large, but as seen in Fig. 18(b), there are two dominant modes in the response of the T1 component. These modes are 1 and 7; mode 1 is a global mode, however, the response of mode 7 is mostly localized to the frame where point A is contained. The large T1 response of the frames is expected to lead to a tangential displacement (T3 direction), which can be modeled with the appropriate dual.

Besides computational efficiency, another strong advantage of reduced order models is their ease in coupling with other discipline codes, especially other reduced order models, at the contrary of full order models. In the present context, coupling with the aerodynamics is of primary importance because of the loading and potential heating it induces on the structure, with the potential of instability (e.g. flutter, buckling) they create. The consideration of heat convection to the structure requires the modeling of its temperature distribution and the associated coupling with the structural deformations. These latter efforts can also be achieved

21

within a reduced order modeling framework as demonstrated for example in [1,19-21] but will not be addressed here further leaving the loading as the sole effect of aerodynamics on the structure.

To demonstrate the coupling, the aerodynamic was represented through a third order piston theory with the flow assumed along the x direction, see Fig. 3, on the top of the panel (i.e. the side opposite to the longerons).

According to the third order piston theory, the aerodynamic pressure acting on the panel can be expressed as

$$p = p_\infty + \frac{2q_\infty}{M_\infty}\left[\left(\frac{1}{U_\infty}\frac{\partial u_3}{\partial t} + \frac{\partial u_3}{\partial x}\right) + \frac{\gamma+1}{4}M_\infty\left(\frac{1}{U_\infty}\frac{\partial u_3}{\partial t} + \frac{\partial u_3}{\partial x}\right)^2 + \frac{\gamma+1}{12}M_\infty^2\left(\frac{1}{U_\infty}\frac{\partial u_3}{\partial t} + \frac{\partial u_3}{\partial x}\right)^3\right]$$

(28)

where u_3 is the transverse displacement of the top surface of the panel given by Eq. (5). In Eq. (28), p_∞, q_∞, U_∞, M_∞ are the upstream conditions of the static pressure, dynamic pressure, speed, and Mach number, respectively. Further, $\gamma = 1.4$ for air.

When coupled with the structural reduced order model, this aerodynamic pressure is projected onto the structural basis to obtain the modal forces F_i in Eq. (6), then the governing equation becomes

$$M_{ij}\ddot{q}_j + (D_{ij} - A_{D,ij})\dot{q}_j + (K_{ij}^{(1)} - A_{K,ij})q_j + K_{ijl}^{(2)}q_jq_l + K_{ijlp}^{(3)}q_jq_lq_p - F_{NL,i} = F_{\infty,i}. \quad (29)$$

In this equation, $F_{\infty,i}$ is the modal force corresponding to the free stream pressure p_∞, A_K and A_D are the linear aerodynamic stiffness and damping matrices arising from the second term in Eq. (28), and $F_{NL,i}$ is the modal force corresponding to the last two terms in Eq. (28) which are nonlinear in the structural displacements.

22

The linear aerodynamic matrices A_K and A_D were obtained as follows. Consider first the former matrix which is induced by the linear displacement-dependent term in Eq. (28), i.e..

$$p_{Lx} = \frac{2q_\infty}{M_\infty}\left(\frac{\partial u_3}{\partial x}\right) \tag{30}$$

The resulting modal force $F_{Lx,i}$ is then expressed as

$$F_{Lx,i} = A_{K,ij}\, q_j \tag{31}$$

which leads to the identification of A_K. That is, determine first $q_j\,\underline{\psi}^{(j)}$ for each j and take its u_3 component, then compute p_{Lx} from Eq. (30) given the altitude and Mach number. Finally, project that pressure load onto the basis to obtain $F_{Lx,i}$. When $q_j = 1$, $F_{Lx,i}$ is exactly the needed term $A_{K,ij}$. The matrix A_D was obtained in a similar way from $p_{Lt} = \frac{2q_\infty}{M_\infty U_\infty}\left(\frac{\partial u_3}{\partial t}\right)$.

The above aero-structure coupling strategy was validated using the flat plate panel example of [29]. A nonlinear reduced order model of this panel was generated and the coupling with the aerodynamics implemented as discussed above. Then, the amplitudes of post-flutter LCO obtained from Eq. (29) for various flow speeds were compared with those given in Fig. 5 of [29]. A close agreement was obtained validating the above approach.

For the 9-bay panel, the altitude and Mach number were assumed to be 40,000ft and 1.6 which is below flutter speed. In the computations, the linear aerodynamic matrices were put on the left hand side of the equation, and directly added to the linear structural counterparts as shown in Eq. (29). The nonlinear aerodynamic force was included in the time marching in the following way: at each time step, the physical (finite element) nonlinear aerodynamic force was computed from

Eq. (28), then projected onto the structural basis to obtain $F_{NL,i}$. Within each time step, it was then handled as the quadratic and cubic stiffness terms

Shown in Figs 15-18 are the corresponding spectra of the displacements induced on the aeroelastic system by the acoustic excitation. Comparing the responses with and without aerodynamics, it is seen that the latter induces here a reduction of the response which is consistent with the flow being below flutter speed. The computations can similarly be carried out above flutter speed as well. In such cases, the structural basis must also include all of the linear modes required for an accurate prediction of the linear flutter speed and mode, in addition to those dictated by the acoustic loading.

SUMMARY

This paper focused on the development and validation of nonlinear reduced order modeling techniques for the prediction of the response of complex structures exhibiting a geometrically nonlinear behavior, and modeled within a commercial finite element code.

A novel identification strategy of the reduced order model parameters was first derived which is based on the use of the tangent stiffness matrix and necessitates a computational effort only proportional to M^2, where M is the number of basis functions, as opposed to M^3 in the current formulations. This novel algorithm leads to large computational savings especially for complex structures for which the number of basis functions is large and the computation of a nonlinear static solution expensive.

A 9-bay panel structure modeled with 96,000 degrees of freedom within Nastran was considered for the validation of this algorithm and of the "dual" mode concept proposed and demonstrated previously on simple structural models. The construction of the reduced order

model of the 9-bay panel was described systematically leading to a 85-mode model. Comparisons with full finite element results demonstrated that this model provides very accurate predictions of both static and dynamic responses of the panel in significantly nonlinear situations, e.g. 2.5 thicknesses peak displacements.

Finally, the coupling of the structural reduced order model with aerodynamics was demonstrated in a simple case in which the latter was modeled using third order piston theory.

ACKNOWLEDGMENTS

REFERENCES

[1] Mignolet, M.P., Przekop, A., Rizzi, S.A., and Spottswood, S.M., "A Review of Indirect/Non-Intrusive Reduced Order Modeling of Nonlinear Geometric Structures," *Journal of Sound and Vibration*, Vol. 332, No. 10, pp. 2437-2460, 2013.

[2] McEwan, M.I., Wright, J.R., Cooper, J.E., and Leung, A.Y.T., "A combined Modal/Finite Element Analysis Technique for the Dynamic Response of a Nonlinear Beam to Harmonic Excitation," *Journal of Sound and Vibration*, Vol. 243, pp. 601-624, 2001.

[3] Hollkamp, J.J., Gordon, R.W., and Spottswood, S.M., "Nonlinear Modal Models for Sonic Fatigue Response Prediction: A Comparison of Methods," Journal of Sound and Vibration, Vol. 284, pp. 1145-1163, 2005.

[4] Mignolet, M.P., Radu, A.G., and Gao, X., "Validation of Reduced Order Modeling for the Prediction of the Response and Fatigue Life of Panels Subjected to Thermo-Acoustic Effects,"

Proceedings of the 8th International Conference on Recent Advances in Structural Dynamics, Southampton, United Kingdom, Jul. 14-16, 2003.

[5] Radu, A., Yang, B., Kim, K., and Mignolet, M.P., "Prediction of the Dynamic Response and Fatigue Life of Panels Subjected to Thermo-Acoustic Loading," *Proceedings of the 45th Structures, Structural Dynamics, and Materials Conference*, Palm Springs, California, Apr. 19-22, 2004. Paper AIAA-2004-1557.

[6] Hollkamp, J.J., and Gordon, R.W., 2008, "Reduced-Order Models for Nonlinear Response Prediction: Implicit Condensation and Expansion," *Journal of Sound and Vibration*, Vol. 318, pp. 1139–1153.

[7] Przekop, A., and Rizzi, S.A., "A Reduced Order Method for Predicting High Cycle Fatigue of Nonlinear Structures," *Computers and Structures*, Vol. 84, No. 24-25, pp. 1606-1618, 2006.

[8] Kim, K., Radu, A.G., Wang, X.Q., and Mignolet, M.P., "Nonlinear Reduced Order Modeling of Isotropic and Functionally Graded Plates," *International Journal of Non-Linear Mechanics*, Vol. 49, pp. 100-110, 2013.

[9] Kim, K., Khanna, V., Wang, X.Q., and Mignolet, M.P., "Nonlinear Reduced Order Modeling of Flat Cantilevered Structures," *Proceedings of the 50th Structures, Structural Dynamics, and Materials Conference*, Palm Springs, California, May 4-7, 2009. AIAA Paper AIAA-2009-2492.

[10] Przekop A., and Rizzi S.A., "Nonlinear Reduced Order Random Response Analysis of Structures with Shallow Curvature," AIAA Journal Vol. 44 (8), pp. 1767-1778, 2006.

[11] Gordon R.W., and Hollkamp, J.J., "Reduced-Order Modeling of the Random Response of Curved Beams using Implicit Condensation," AIAA-2006-1926, 2006.

[12] Spottswood, S.M., Hollkamp, J.J., and Eason, T.G., "On the Use of Reduced-Order Models for a Shallow Curved Beam Under Combined Loading," *Proceedings of the 49th Structures,*

Structural Dynamics, and Materials Conference, Schaumburg, Illinois, Apr. 7-10, 2008. AIAA Paper AIAA-2008-1873.

[13] Przekop, A., and Rizzi, S.A., "Dynamic Snap-Through of Thin-Walled Structures by a Reduced-Order Method," *AIAA Journal*, Vol. 45, No. 10, pp. 2510–2519, 2007.

[14] Spottswood, S.M., Eason, T.G., Wang, X.Q., and Mignolet, M.P., "Nonlinear Reduced Order Modeling of Curved Beams: A Comparison of Methods," *Proceedings of the 50th Structures, Structural Dynamics, and Materials Conference*, Palm Springs, California, May 4-7, 2009. AIAA Paper AIAA-2009-2433.

[15] Perez, R., Wang, X.Q., and Mignolet, M.P., "Reduced Order Modeling for the Nonlinear Geometric Response of Cracked Panels," *Proceedings of the 52th Structures, Structural Dynamics, and Materials Conference*, Denver, Colorado, April 4-7, 2011. AIAA Paper AIAA-2011-2018.

[16] Kim, K., Kim, Y.C., Mignolet, M.P., Liu, D.D., Chen, P.C., Lee, D.H., "Random Aeroelastic Response Due to Strong Hypersonic Unsteady-Wave/Shock Interaction with Acoustic Loads," *Proceedings of the 48th Structures, Structural Dynamics, and Materials Conference*, Honolulu, Hawaii, Apr. 23-26, 2007. AIAA Paper AIAA-2007-2014.

[17] Liu, D.D., Chen, P.C., Zhang, Z., Wang, Z., Yang, S., Lee, D.H., Mignolet, M.P., Kim, K., Liu, F., Lindsley, N., and Beran, P., "Continuous Dynamic Simulation of Nonlinear Aerodynamic/Nonlinear Structure Interaction (NANSI) for Morphing Wing Aeroelasticity," *Proceedings of the 50th Structures, Structural Dynamics, and Materials Conference*, Palm Springs, California, May 4-7, 2009. AIAA Paper AIAA-2009-2572.

[18] Liu, D.D., Wang, Z., Yang, S., Cai, C., Wang, X.Q., and Mignolet, M.P., "Nonlinear Aeroelastic Methodology for A Membrane-on-Ballute Model with Hypersonic Bow Shock,"

Proceedings of the 50th Structures, Structural Dynamics, and Materials Conference, Palm Springs, California, May 4-7, 2009. AIAA Paper AIAA-2009-2363.

[19] Perez, R., Wang, X.Q., and Mignolet, M.P., "Nonlinear Reduced Order Models for Thermoelastodynamic Response of Isotropic and FGM Panels," *AIAA Journal*, Vol. 49, pp. 630-641, 2011.

[20] Perez, R., Wang, X.Q., and Mignolet, M.P., "Steady and Unsteady Nonlinear Thermoelastodynamic Response of Panels by Reduced Order Models," *Proceedings of the 51th Structures, Structural Dynamics, and Materials Conference*, Orlando, Florida, April 12-15, 2010. AIAA Paper AIAA-2010-2724.

[21] Matney, Perez, R., and Mignolet, M.P., "Nonlinear Unsteady Thermoelastodynamic Response of a Panel Subjected to an Oscillating Flux by Reduced Order Models," *Proceedings of the 52th Structures, Structural Dynamics, and Materials Conference*, Denver, Colorado, April 4-7, 2011. AIAA Paper AIAA-2011-2016.

[22] Mignolet, M.P., and Soize, C., "Stochastic Reduced Order Models for Uncertain Geometrically Nonlinear Dynamical Systems," *Computer Methods in Applied Mechanics and Engineering*, Vol. 197, 2008, pp. 3951-3963.

[23] Capiez-Lernout, E., Soize, C., and Mignolet, M.P., "Computational Stochastic Statics of an Uncertain Curved Structure with Geometrical Nonlinearity in Three-Dimensional Elasticity," *Computational Mechanics*, Vol. 49, No. 1, pp. 87-97, 2012.

[24] Muravyov, A.A., and Rizzi, S.A., "Determination of Nonlinear Stiffness with Application to Random Vibration of Geometrically Nonlinear Structures," Computers and Structures, Vol. 81, pp. 1513-1523, 2003

[25] Przekop, A., Rizzi, S.A., and Groen, D.S., "Nonlinear Acoustic Response of an Aircraft Fuselage Sidewall Structure by a Reduced-Order Analysis," *Proceedings of the 9th International Conference on Recent Advances in Structural Dynamics*, Southampton, United Kingdom, Jul. 17-19, 2006.

[26] Fung, Y.C., and Tong, T., *Classical and Computational Solid Mechanics*, World Scientific, River Edge, New Jersey, 2001.

[27] Bonet, J., and Wood, R.D., *Nonlinear Continuum Mechanics for Finite Element Analysis*, Cambridge University Press, Cambridge, 1997.

[28] Buehrle, R.D., Fleming, G.A., Pappa, R.S., and Grosveld, F.W., "Finite Element Model Development For Aircraft Fuselage Structures," *Proceedings of the 18th Modal Analysis Conference*, San Antonio, Texas, Feb., 2000.

[29] Gray, C.E., Mei, C., and Shore, C.P., "Finite Element Method for Large-Amplitude Two-Dimensional Panel Flutter at Hypersonic Speeds," *AIAA Journal*, Vol. 29 (1), pp. 290-298, 1991.

Table 1. Number of static solutions needed for ROM identification

Number of Modes	Imposed Displ. Tangent Stiffness ID Method	Imposed Displ. Force ID Method
15	135	815
25	350	3,275
75	2,950	76,075

Table 2. 9-bay panel material properties

Young's Modulus	10.5×10^6 psi
Poisson's Ratio	0.33
Density	$2.614 \times 10^{-4} \text{lb}_f\text{-s}^2/\text{in}^4$

Table 3. Summary of Representation And Prediction Errors

	Skin Panel		Frame-Longeron Substructure	
	Rep. Err.	Pred. Err.	Rep. Err.	Pred. Err.
T3	0.28%	1.1%	0.42%	1.3%
In-Plane Mag	9.30%	5%	1.67%	12%
T2	9.11%	3.5%	2.98%	8%
T1	39.12%	45%	1.67%	13%
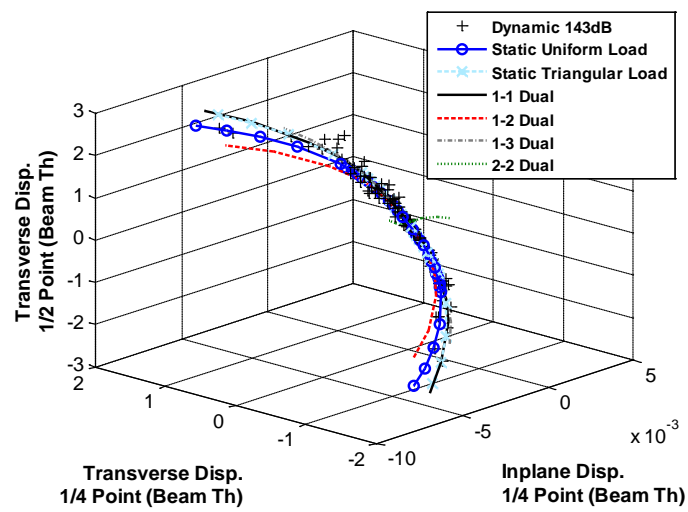
Figure 1. Displacements from Nastran at two points of a clamped-clamped beam under various loadings, transverse displacement at middle point vs. Transverse and inplane displacements at quarter point.

Figure 2. Sidewall fuselage panel taken from [26]. 9-bay panel is a section of this structure.
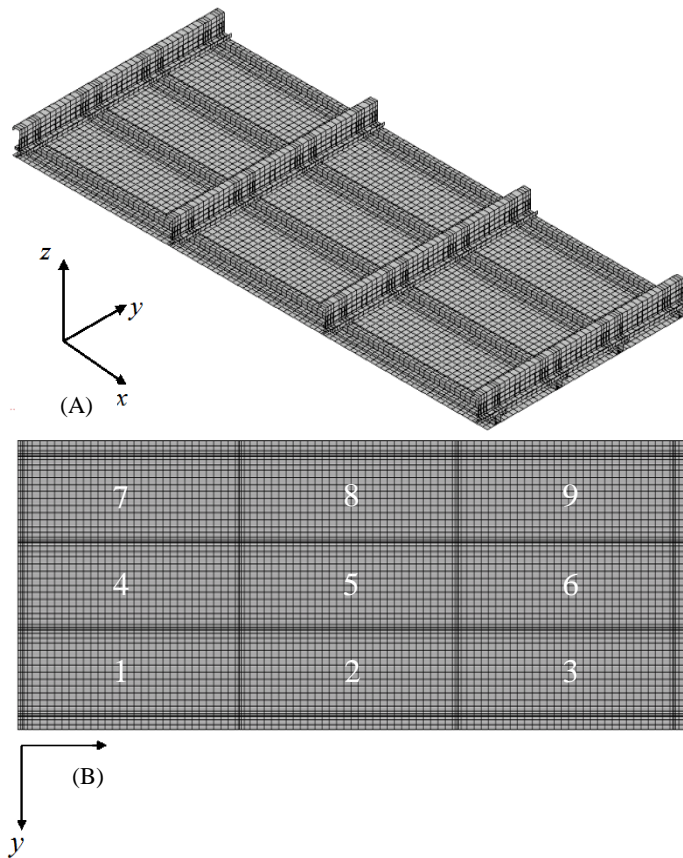
Figure 3. Finite element model of the 9-bay fuselage sidewall panel, (a) isometric view, (b) top view.
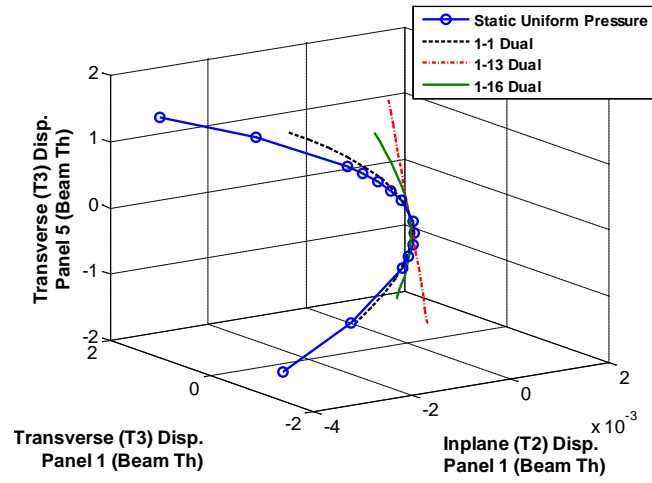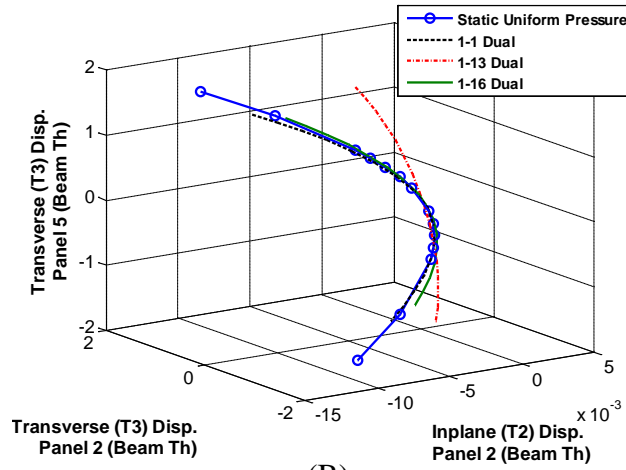
Figure 4. Displacements from Nastran at two points of the 9-bay panel under various loadings, transverse displacement at the middle point of the center panel and transverse and inplane (T2) displacement at the middle point of: a) panel 1 and b) panel 2.
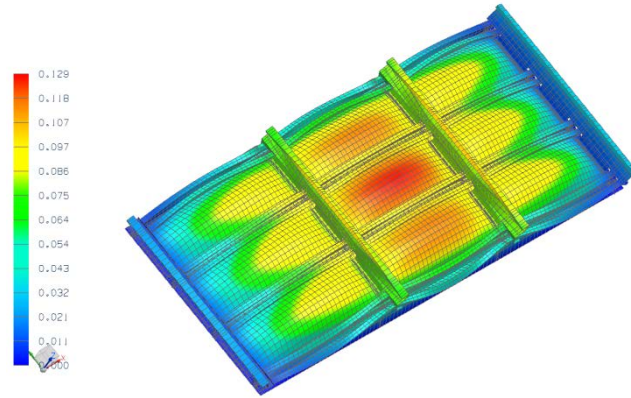
Figure 5. Translation magnitude induced by a uniform pressure of 0.6 psi, NX/Nastran.
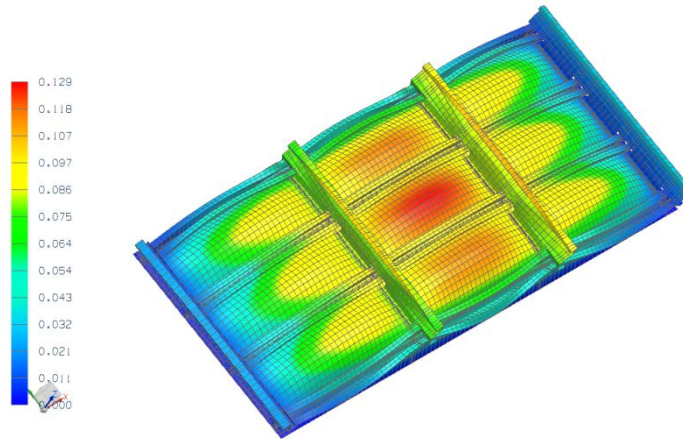
Figure 6. Translation magnitude induced by a uniform pressure of 0.6 psi, 85-mode ROM.
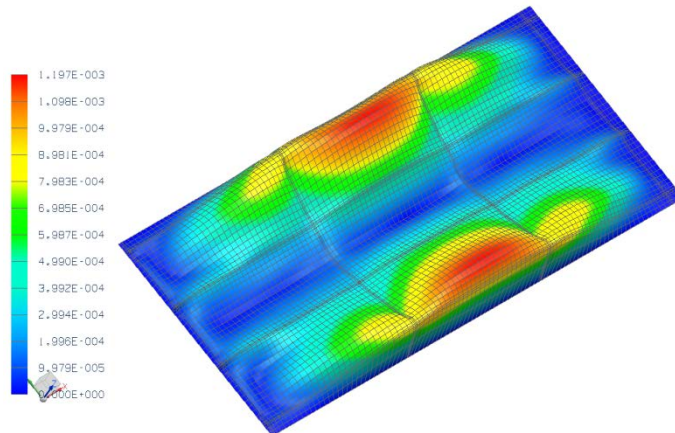
Figure 7. Magnitude of the in-plane displacement induced by a uniform pressure of 0.6 psi, skin panel only, NX/Nastran.
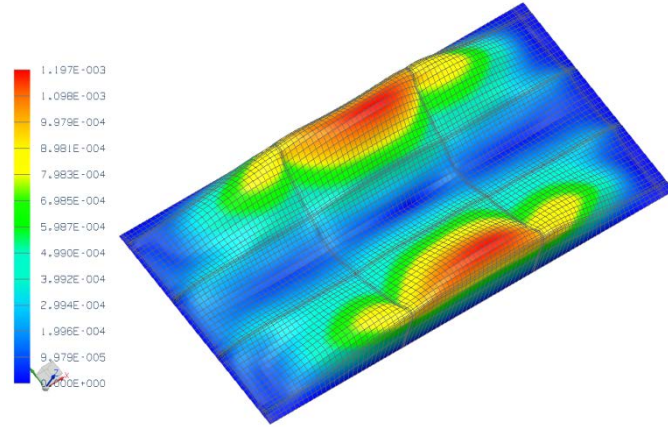
Figure 8. Magnitude of the in-plane displacement induced by a uniform pressure of 0.6 psi, skin panel only, 85-mode ROM.
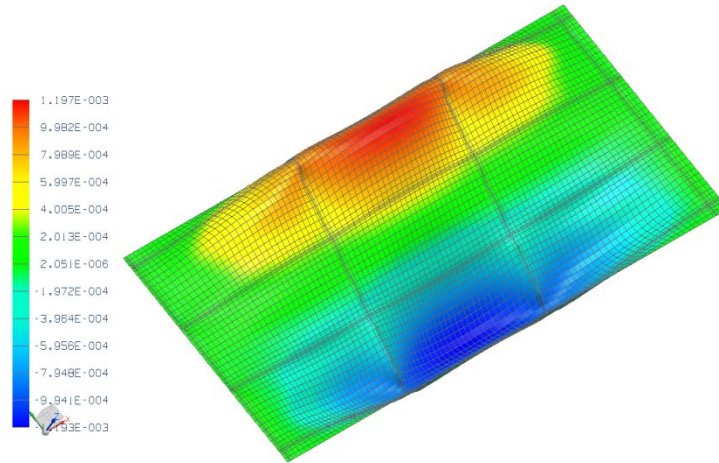
Figure 9. In-plane displacement along T2 induced by a uniform pressure of 0.6 psi, skin panel only, NX/Nastran.
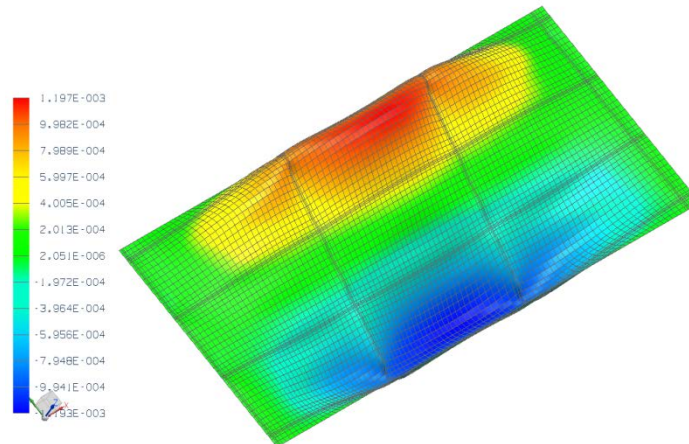
Figure 10. In-plane displacement along T2 induced by a uniform pressure of 0.6 psi, skin panel only, 85-mode ROM.
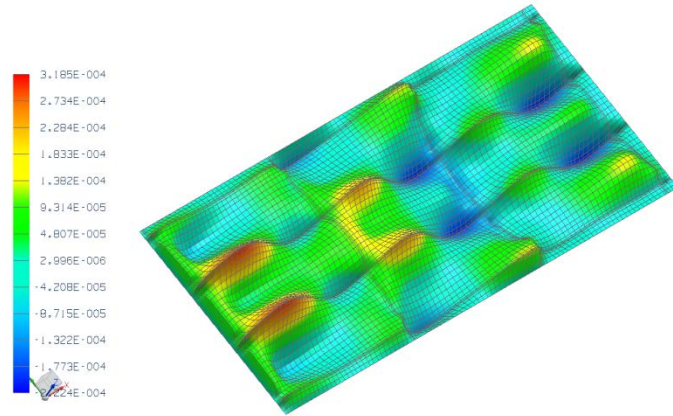
Figure 11. In-plane displacement along T1 induced by a uniform pressure of 0.6 psi, skin panel only, NX/Nastran.
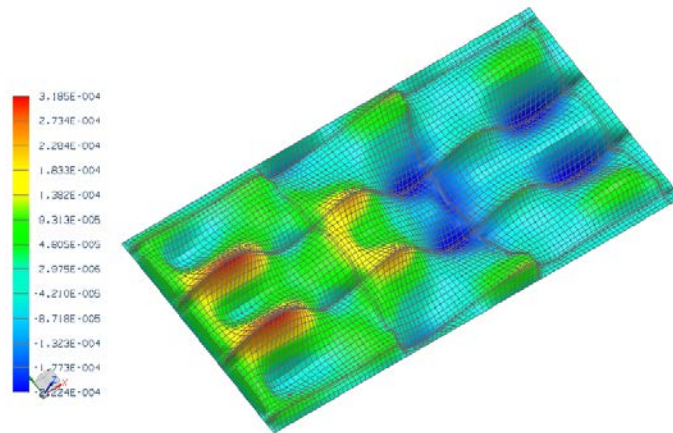
Figure 12. In-plane displacement along T1 induced by a uniform pressure of 0.6 psi, skin panel only, 85-mode ROM.
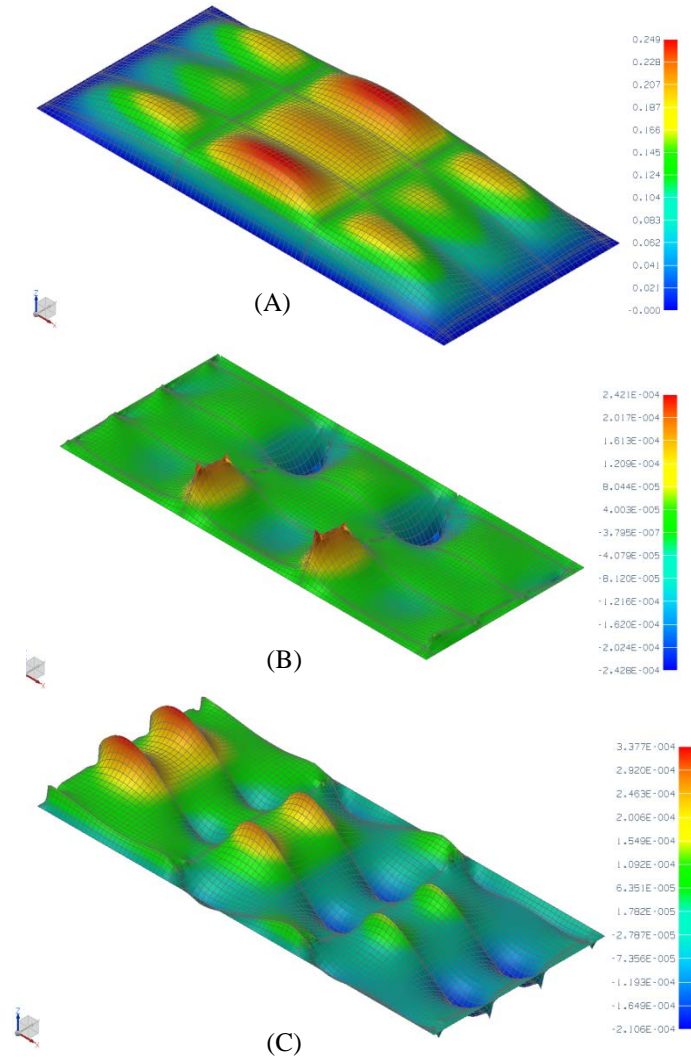
Figure 13. Nastran linear response induced by a uniform pressure of 0.6 psi, (a) transverse component (T3), (b) in-plane component along T2, and (c) in-plane component along T1.
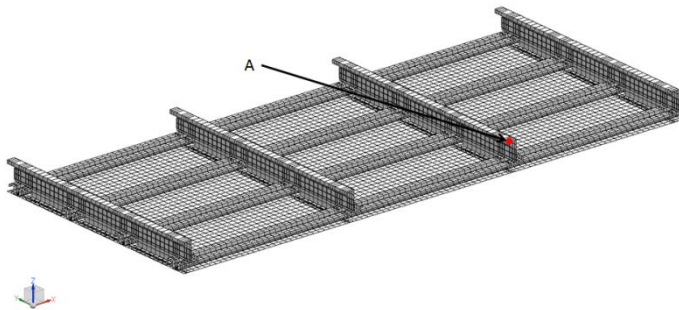
Figure 14. Location of selected frame node for output of results.
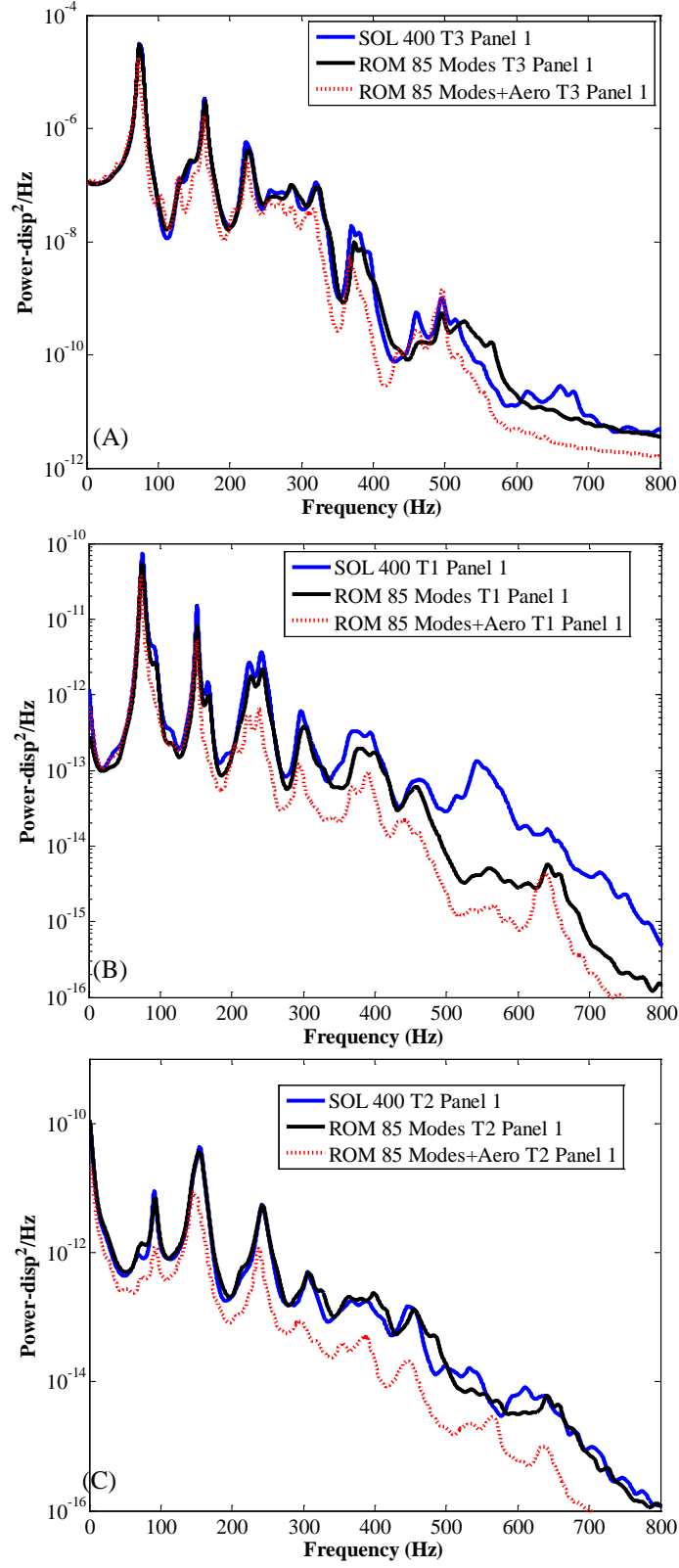
Figure 15. Power spectral density of the transverse (T3) and in-plane (T1 and T2) deflections at the middle point of bay 1. Reduced order model and finite element ("SOL 400"), *SPL* =144dB.
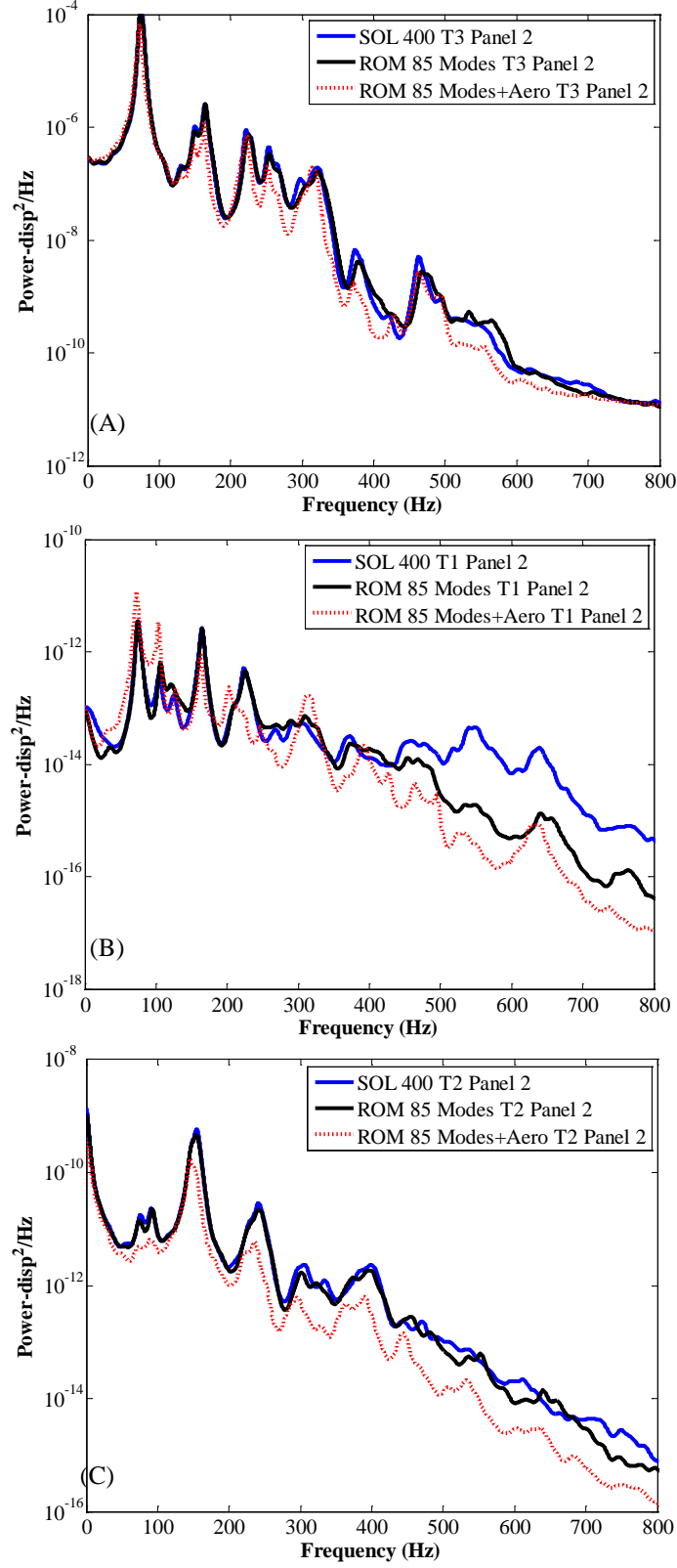
Figure 16. Power spectral density of the transverse (T3) and in-plane (T1 and T2) deflections at the middle point of bay 2. Reduced order model and finite element ("SOL 400"), *SPL* =144dB.
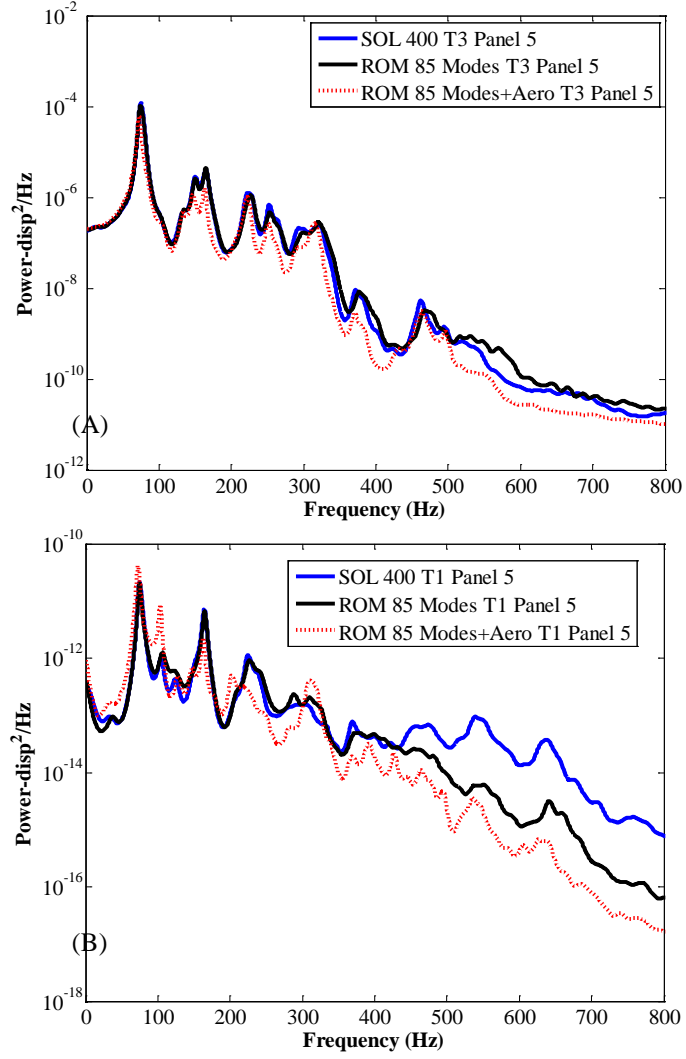
Figure 17. Power spectral density of the transverse (T3) and in-plane (T1) deflections at the middle point of bay 5. Reduced order model and finite element ("SOL 400"), *SPL* =144dB.
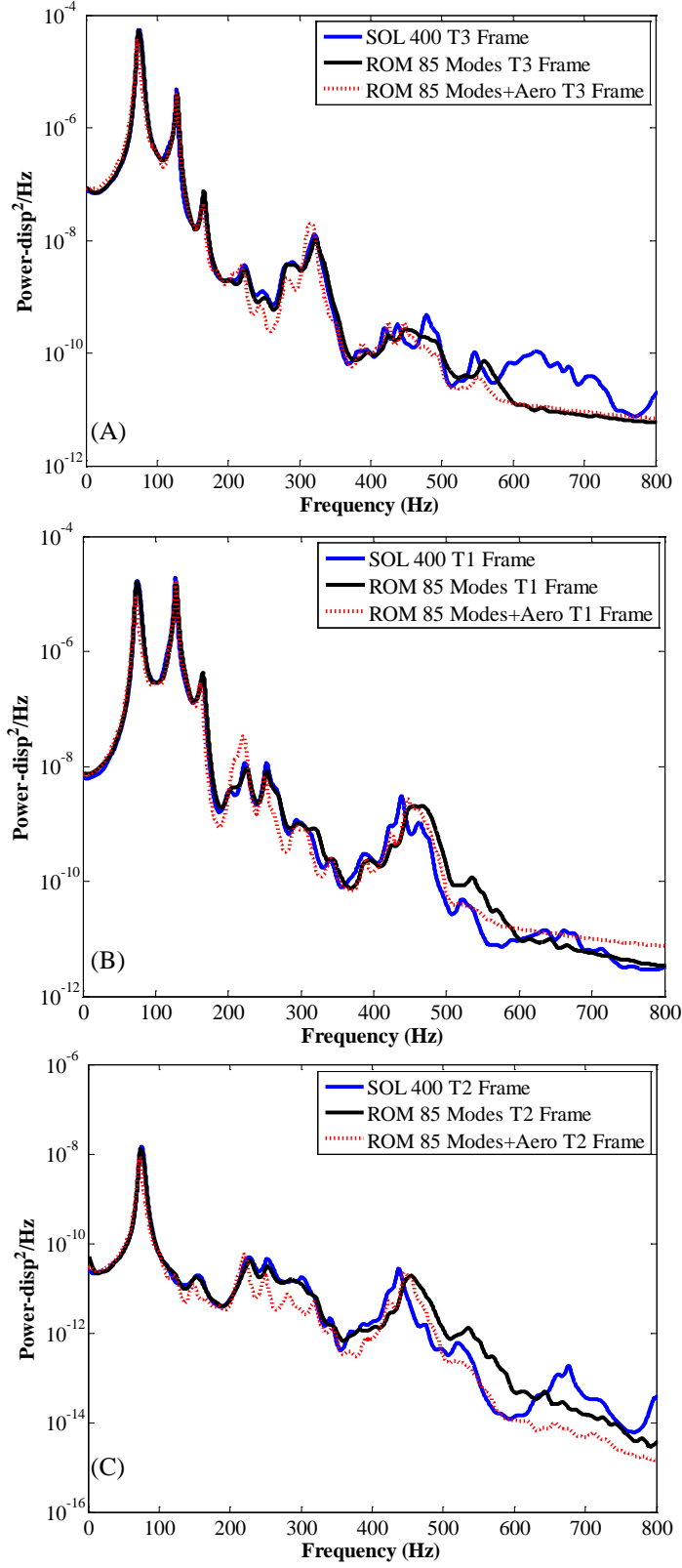
Figure 18. Power spectral density of the transverse (T3) and in-plane (T1) deflections at point A of the frame. Reduced order model and finite element ("SOL 400"), *SPL* =144dB.

ATTACHMENT B

Perez, R.A., Wang, X.Q., and Mignolet, M.P., "Nonlinear Geometric Response of Panels with Localized Geometric Defects by Reduced Order Models – A Notched Panel," Submitted to *Journal of Sound and Vibration*, Manuscript JSV-S-13-01345.

Title: Nonlinear Geometric Response of Panels with Localized Geometric Defects by Reduced Order Models - A Notched Panel

Corresponding Author: Marc P. Mignolet,

Corresponding Author's Institution: Arizona State University

First Author: Ricardo A Perez, Ph.D.

Order of Authors: Ricardo A Perez, Ph.D.; X.Q. Wang, Ph.D.; Marc P. Mignolet

Abstract: The focus of this investigation is on a first assessment of the predictive capabilities of nonlinear geometric reduced order models for the prediction of the large displacement and stress fields of panels with localized geometric defects, the case of a notch serving to exemplify the analysis. It was first demonstrated that the reduced order models of the notched panel does indeed provide a close match of the displacement and stress fields obtained from full finite element analyses for moderately large static and dynamic responses (peak displacement of 2 and 4 thicknesses). As might be expected, the reduced order model of the virgin panel would also yield a close approximation of the displacement field but not of the stress one. A detailed comparison of the two reduced order models has shown that the difference resides in the basis functions employed for the notched panel, more specifically those modeling primarily the in-plane displacements (the "dual" modes), which notably reflect the presence of the notch. These observations have then led to two "enrichment" techniques seeking to superpose the notch effects on the virgin panel stress field so that a reduced order model of the latter can be used. A very good prediction of the full finite element stresses, for both static and dynamic analyses, was indeed achieved with both enrichments.

NONLINEAR GEOMETRIC RESPONSE OF PANELS WITH LOCALIZED GEOMETRIC DEFECTS BY REDUCED ORDER MODELS – A NOTCHED PANEL

Ricardo Perez[*], X. Q. Wang[†], and Marc P. Mignolet[‡]
Arizona State University, Tempe, AZ 85287-6106, USA

[*]Currently Postdoctoral Research Engineer, Universal Technology Corporation
[†]Associate Research Scientist, SEMTE, Faculties of Mechanical and Aerospace Engineering
[‡] Professor, SEMTE, Faculties of Mechanical and Aerospace Engineering

ABSTRACT

The focus of this investigation is on a first assessment of the predictive capabilities of nonlinear geometric reduced order models for the prediction of the large displacement and stress fields of panels with localized geometric defects, the case of a notch serving to exemplify the analysis. It was first demonstrated that the reduced order models of the notched panel does indeed provide a close match of the displacement *and stress* fields obtained from full finite element analyses for moderately large static and dynamic responses (peak displacement of 2 and 4 thicknesses). As might be expected, the reduced order model of the *virgin* panel would also yield a close approximation of the displacement field but not of the stress one. A detailed comparison of the two reduced order models has shown that the difference resides in the basis functions employed for the notched panel, more specifically those modeling primarily the in-plane displacements (the "dual" modes), which notably reflect the presence of the notch. These observations have then led to two "enrichment" techniques seeking to superpose the notch effects on the virgin panel stress field so that a reduced order model of the latter can be used. A very good prediction of the full finite element stresses, for both static and dynamic analyses, was indeed achieved with both enrichments.

1. INTRODUCTION

Interest in the prediction of the dynamic response of thin panels undergoing "large" deformations (i.e., exhibiting geometric nonlinearity) has motivated a noteworthy interest in the construction of reduced order models (ROMs) from finite element models generated using commercial codes (e.g. Nastran, Abaqus), see [1] for a recent review. This non-intrusive formulation allows for the relatively straightforward consideration of complex structural problems using tools that are routinely used in the industrial setting. The counterpart of these advantages is the unavailability of certain information and the uncertainty on the formulation implemented in the finite element modeling and response computation.

Notwithstanding the above difficulties, the ROM capabilities have progressed from applications to flat structures (see [2-9]), to moderately large motions of curved structures (see [10-14]). Further, the coupling of these nonlinear structural reduced order models with aerodynamics, either full or reduced order model has also been successfully demonstrated in [15-17]. A similar coupling but of the structural dynamics and thermal aspects, the two in reduced order model format, has also been proposed and validated in [18-20]. In addition, validation studies with experiments have been carried out for different types of panels [3, 23-24]. The introduction of uncertainty in the reduced order model has finally been formulated and implemented [25,26].

The reduced order models developed in the above investigations are parametric, i.e. the form of the equations governing the generalized coordinates is fixed, linear in mass and damping operators with a stiffness operator exhibiting linear, quadratic, and cubic terms in all combinations of generalized coordinates as derived from finite deformation elasticity in the reference configuration (see review below).

Panels represent a basic building block of wings and aircraft fuselage; however, smaller scales are also present. These scales may result from the structural design (e.g. fasteners) or may arise from damage (e.g. cracks, debonds) and are expected to have a localized effect in the stress field. In this light, the focus of the present investigation is on a first assessment of the predictive capabilities of reduced order models for panels that have a localized geometric defect, such as a notch which will be considered here. Two particular questions to be addressed here are:

(1) how well do reduced order models capture the stress distribution in the notch near-field, and

(2) how could the reduced order modeling process of the defect-free (or virgin) panel be employed?

For completeness, the derivation of the reduced order modeling strategy is first briefly reviewed.

2. REDUCED ORDER MODELING

2.1. Reduced Order Model Form and Governing Equations

The reduced order models considered here are based on a representation of the nonlinear geometric response in terms of a set of basis functions

$$\underline{u}(t) = \sum_{n=1}^{M} q_n(t) \, \underline{\psi}^{(n)} \tag{1}$$

where $\underline{u}(t)$ represents the vector of displacements of the finite element degrees of freedom, $\underline{\psi}^{(n)}$ are specified, constant basis functions, and $q_n(t)$ are the time dependent generalized coordinates.

The reduced order modeling (ROM) procedure described here is achieved in the undeformed configuration Ω_0 for which the field equations are (summation is implied over repeated indices)

$$\frac{\partial}{\partial X_k}\left(F_{ij} \, S_{jk}\right) + \rho_0 \, b_i^0 = \rho_0 \, \ddot{u}_i \tag{2}$$

where $\underline{\underline{S}}$ is the second Piola-Kirchhoff stress tensor (double underlines are used here for matrices), ρ_0 is the density with respect to the reference configuration, and $\underline{b}^0$ is the vector of body forces, all of which are assumed to depend on the position $\underline{X} \in \Omega_0$, [27,28]. Further, in Eq. (2), $\underline{\underline{F}}$ denotes the deformation gradient tensor of components

$$F_{ij} = \frac{\partial x_i}{\partial X_j} = \delta_{ij} + \frac{\partial u_i}{\partial X_j} \tag{3}$$

where δ_{ij} is the Kronecker delta and $\underline{u} = \underline{x} - \underline{X}$ is the displacement vector, $\underline{x}$ being the position vector in the deformed configuration. An important aspect of the present formulation is that the material is assumed to be linear elastic in that $\underline{\underline{S}}$ and $\underline{\underline{E}}$ (the Green strain tensor) satisfy

$$S_{ij} = C_{ijkl} E_{kl} \tag{4}$$

where $\underline{\underline{C}}$ is a fourth order elasticity tensor, function in general of the undeformed coordinates $\underline{X}$

To proceed, assume next the displacement field u_i in the continuous structure in the form

$$u_i(\underline{X}, t) = \sum_{n=1}^{M} q_n(t) U_i^{(n)}(\underline{X}) \qquad i = 1,2,3 \tag{5}$$

where $U_i^{(n)}(\underline{X})$ are specified, constant basis functions satisfying the boundary conditions also in the undeformed configuration. Equation (5) is the continuous space equivalent of the discrete, finite element model, representation of Eq. (1),

By introducing Eq. (5) in Eqs. (2)-(4) and imposing the condition that the error be orthogonal to the basis (Galerkin approach), a set of nonlinear ordinary differential equations for the generalized coordinates $q_n(t)$ can be obtained. This leads [8] to the reduced order model equations

$$M_{ij}\ddot{q}_j + D_{ij}\dot{q}_j + K_{ij}^{(1)} q_j + K_{ijl}^{(2)}q_j q_l + K_{ijlp}^{(3)}q_j q_l q_p = F_i \quad . \tag{6}$$

where a linear damping term $D_{ij}\dot{q}_j$ has been added to collectively represent various dissipation

mechanisms. Further, M_{ij} denotes the elements of the mass matrix, $K_{ij}^{(1)}$, $K_{ijl}^{(2)}$, $K_{ijlp}^{(3)}$ are the

linear, quadratic, and cubic stiffness coefficients and F_i are the modal forces. Integral

expressions for all coefficients of Eq. (6) are given in [8]. They can be used for their estimation

(see [26]) but an indirect evaluation of many of these coefficients from the finite element model

is also possible (see [1,8,22]).

From the displacements, a complete solution of the problem and other quantities can then be

evaluated. For example, any component of the second Piola-Kirchhoff stress tensor at any point

can be expressed as

$$S_{ij} = \overline{S}_{ij} + \hat{S}_{ij}^{(m)} q_m + \widetilde{S}_{ij}^{(m,n)} q_m q_n \tag{7}$$

where the coefficients $\overline{S}_{ij}$, $\hat{S}_{ij}^{(m)}$, and $\widetilde{S}_{ij}^{(m,n)}$ depend only on the point $\underline{X}$ considered.

2.2. Basis Selection

One of the key aspects of the reduced order modeling strategy is the selection of the basis

functions $\underline{\psi}^{(n)}$. A poor representation of the structural response within this basis is expected to

lead to a poor prediction of the response by the reduced order model. The basis is expected to

include the modes used for the corresponding linear problem, but this basis needs to be enriched

to model the difference in physical behavior induced by the geometric nonlinearity. Shell-like

structures subjected to transverse loading present a clear example of this situation, where the

linear response is predominantly transverse while the tangential/in-plane displacement field plays

a fundamental role (the "membrane-stretching" effect, see [1,3,6] for discussion) in large motions.

This issue was addressed in [8] through the inclusion in the basis of an additional set of basis functions, referred to as dual modes, aimed at capturing the membrane stretching effects. They are extracted from the *nonlinear* displacement fields of the structure to a series of "representative" static loadings. As argued in [8], these representative static loadings should be selected to excite primarily the modes from the linear basis. In fact, for a linear analysis the loading should only excite these modes, i.e., the applied load vectors $\underline{F}_{FE}^{(m)}$ on the structural finite element model should be such that the corresponding linear static responses are of the form

$$\underline{u}^{(m)} = \sum_i \alpha_i^{(m)} \underline{\psi}^{(i)} \tag{8}$$

which occurs when

$$\underline{F}_{FE}^{(m)} = \sum_i \alpha_i^{(m)} K_{FE}^{(1)} \underline{\psi}^{(i)} \tag{9}$$

where $\alpha_i^{(m)}$ are coefficients to be chosen with m denoting the load case number. A detailed discussion of the linear combinations to be used is presented in [8] but, in all validations carried out, it has been sufficient to consider the cases

$$\underline{F}_{FE}^{(m)} = \alpha_i^{(m)} K_{FE}^{(1)} \underline{\psi}^{(i)} \qquad i = \text{dominant mode} \tag{10}$$

and

$$\underline{F}_{FE}^{(m)} = \frac{\alpha_i^{(m)}}{2} K_{FE}^{(1)} \left[\underline{\psi}^{(i)} + \underline{\psi}^{(j)} \right] \quad i = \text{dominant mode}, \ j \neq i \tag{11}$$

where a "dominant" mode is loosely defined as one expected to provide a large component of the panel response to the physical loading. The ensemble of loading cases considered is formed by

selecting several values of $\alpha_i^{(m)}$ for each dominant mode in Eq. (10) and also for each mode $j \neq i$ in Eq. (11). Further, note that both positive and negative values of $\alpha_i^{(m)}$ are suggested and that their magnitudes should be such that the corresponding displacement fields $\underline{u}^{(m)}$ range from near linear cases to some exhibiting a strong nonlinearity.

The next step consists in the extraction of the nonlinear effects in the obtained displacement fields, which is achieved by removing from the displacements fields their projections on the linear basis. Finally, a proper orthogonal decomposition (POD) analysis of each set of "nonlinear responses" is then sequentially carried out to extract the dominant features of these responses which are then selected as dual modes, see [8] for full details on this approach.

3. MODELS FOR VALIDATION: NOTCHED AND VIRGIN PANEL MODELS

A beam-like panel with the properties given in Table 1 was considered here with and without notch. The panel was assumed to have clamped-clamped boundary conditions and to be subjected to a uniform pressure of varying magnitude.

The notched beam exhibited a rounded notch of length equal to one-fourth of the beam thickness placed at 30% of the length of the beam and along its entire width as shown in Figs. 1 and 2. Clearly, plane stress conditions cannot be assumed to exist on the *x-z* plane since it is not a thin membrane. On the other hand, plane strain conditions do not exist since this is not a long body problem. Therefore, the structure was discretized throughout its entire domain with 8-node brick elements (CHEXA in NX/Nastran), and 14 such elements were used along the width of the beam. Along the length, the notched beam was divided in different parts, as shown in Fig. 1, to capture the local effects of the notch without excessive meshing away from that zone. Away from the notch (parts (a) and (c) in Fig 1), 4 elements were used through the thickness of the

beam and a uniform division along the length was performed with 20 elements for part (a) and 47 elements for part (c). The finer meshing around the notch (part (b) in Fig 1) is shown in Fig. 2(a). Note further from this figure that the notch is rounded to avoid any plasticity in its vicinity, which is not considered in this first effort. The purpose of this work being on the validation of the reduced order modeling strategy in comparison with the corresponding finite element predictions, a very fine mesh was not necessary and was not used to accelerate the computations.

A virgin beam model was also considered and, for ease of comparison, its meshing was selected to be identical to the one of the notched beam but with the notch filled with CHEXA elements, see Fig. 2(b), and with the same material properties, see Table 1.

4. REDUCED ORDER BASIS: NOTCHED AND VIRGIN PANELS

It was first of interest to compare the basis functions of the reduced order models, i.e., the transverse and duals modes, of the virgin and notched beams to assess the effects, local and/or global, of the notch.

The transverse linear modes were first investigated and were obtained, for the two beams, from a normal modes solution in NX/Nastran (SOL 103). The natural frequencies of the first 4 symmetric modes of the two beams are shown in Table 2. As expected, given the small size of the notch, its effect on the first few natural frequencies is very small.

The transverse and in-plane (along the length of the beam) components of the first mode shape along one of the top edges of the beams ($y=0$, $z=h$) are shown in Figs. 3-4. The first observation to be drawn is that the notch does not affect noticeably the transverse displacements, but appears to induce a sharp peak in its in-plane counterpart. However, this peak is an artifact of the geometry, i.e., the notched beam data presented includes the displacement at the nodes along

the flat edge of the beam but also those along the faces of the notch. Since these points are much closer to the neutral axis of the beam, their in-plane displacements are expected to be smaller as seen in Fig. 5. Plotting the same nodal displacements for the virgin beam, see Figs. 6-7, confirms this explanation of the peak.

The linear modes of the structure only represent one part of the basis, modeling primarily the transverse displacements, while the dual modes (see [8,9,14]) capture the nonlinearly induced in-plane motions. In this light, it was also desired to assess the effects of the notch on these dual modes. Thus, the 4 dual modes corresponding to the 4 linear modes were created using Eqs (10)-(11) with mode 1 dominant, for both notched and virgin beams. The POD-based dual mode construction procedure highlighted above (see [8] for full details) was performed for the data obtained for mode 1 alone and each of the 3 combinations of mode 1 and another of the 3 largest responding modes. In each of these 4 situations, 10 different loading factors $\alpha_i^{(m)}$ were used, half positive and half negative, and leading to peak deflections ranging from 1 to approximately 4.4 skin panel thicknesses. The remainders of these 40 deflections, after projection on the 4 linear modes identified above, were analyzed by POD.

Shown in Figs. 8-9 are the transverse and in-plane components of the first (dominant) dual. Note that the notch is most present in the transverse component of the dual mode, see Fig. 8, which is quite different for the notched and virgin beams. In particular, note for the former the presence of a large, broad (as measured by the width of the notch) peak at the location of the notch. On the contrary, the in-plane components of this dual mode are almost unaffected by the notch, see Fig. 9. The most noticeable difference in the in-plane displacement is a jump occurring at the location of the notch, as seen in Fig. 10. Similar observations were drawn for the other 3 dual modes.

Using the 4 linear and 4 dual modes analyzed above, reduced order models were built for both notched and virgin beams with the coefficients estimated from the stiffness evaluation procedure of [22] as modified in [4,5,8].

5. STATIC VALIDATION: DISPLACEMENT AND STRESS FIELDS

To assess the adequacy of the reduced order models obtained and assess the effects of the notch, the beams were loaded with uniform pressure acting on the bottom surface. Two different pressures were chosen, 2.6kPa and 17kPa, which led to peak transverse displacements of approximately 2 and 4 beam thicknesses, well within the nonlinear range. The static responses were computed with the reduced order model as well as by a nonlinear NX/Nastran analysis (SOL 106). Shown in Figs. 11-14 is a comparison of the predicted transverse and in-plane displacements at the beam's upper and lower edges. Clearly, the matching is excellent for both transverse and in-plane displacements, even in the direct vicinity of the notch (see Fig. 15). In Figs. 15-16, the response of the virgin beam was plotted at the same node locations as the response of the notched beam. Interestingly, the reduced order model of the virgin beam does an excellent job in capturing the in-plane displacement field in the notch region.

Figures 17-20 show the static response of the beam to pressures equal to -2.6kPa and -17kPa, applied on the bottom surface of the beam, and leading to peak transverse displacements of -2 and -4 beam thicknesses. Clearly, the matching is excellent for both cases, and once more the reduced order model of the virgin beam does an excellent job in capturing the in-plane displacement field in the notch region.

Shown in Table 3 is a summary of the prediction errors for the three displacement components. The prediction errors were computed from the norm of the difference between

NX/Nastran and the ROM prediction divided by the norm of the NX/Nastran results. Results are shown for the ROMs of the notched and virgin beam. Clearly, the linear modes chosen to represent the transverse displacements, along with the modeling of the in-plane displacements by the duals, result in a very good matching of the transverse component with respect to NX/Nastran.

The previous results have demonstrated that the reduced order model of the notched beam is able to capture accurately the displacement field of this beam, thereby extending published validation cases, see [1] for review. Furthermore, it has been observed, not too unexpectedly, that the displacement fields of the notched and virgin beams are indeed very close to each other, suggesting that the latter could be used for the prediction of the response of the former.

Before any such connection can be established, however, it is necessary to assess the capability of the notched beam reduced order model to capture the stress distribution of this beam. To this end, shown in Figs 23-26 are the dominant stresses S_{xx} along the top edge of the beam (y=0, z=h), as computed by the reduced order model of the notched beam, see Eq. (7), and by NX/Nastran nonlinear for all loading cases analyzed above. Clearly, the agreement is very good to excellent, even in the notch near field, as seen from the results in Tables 3-4. It is thus concluded from these validation cases that the nonlinear geometric reduced order modeling technique developed is also applicable to notched panels for the prediction of both their displacement and stress fields.

6. DYNAMIC DISPLACEMENT AND STRESS FIELDS

Lastly, a dynamic transverse loading was added and the response computed in NX/Nastran SOL 601. The beam was subjected to a uniform pressure on its bottom surface varying randomly

in time as a white noise band-limited process in the frequency range [0,1042Hz] to simulate an acoustic loading. The acoustic excitation consisted of an overall sound pressure level (*OASPL*) of 147dB. Furthermore, to permit a close comparison between the NX/Nastran and ROM results, a simple Rayleigh damping model was adopted, i.e. for which the damping matrix is $D = \alpha M + \beta K$ with α=12.838/s and β=2.061E-6s. This selection led to damping ratios between 0.5% and 1.3% for all four transverse modes in the excitation band. The time histories computed from the reduced order model were obtained with a Newmark-β solver with the resulting nonlinear algebraic equations solved using a fixed-point algorithm. A time step of 4E-5s was used for these computations.

The power spectra of the transverse displacement at the middle of the beam and of the in-plane displacement at the beam quarter point, both at the upper edge (i.e., y=0, z=h) are shown in Figs. 27-29. Clearly, based on the matching of the power spectral density of the NX/Nastran results, the ROM of the notched beam and of the virgin beam match very well the dynamics of the beam. Interestingly, the matching of the power spectrum of the in-plane displacement along the T1 direction at the notch tip is very good as well, even for the ROM of the virgin beam.

The power spectral density of the dominant S_{xx} element stresses, at different locations along the beam are shown in Figs. 30-32. Away from the notch, the power spectrum of both ROMs match NX/Nastran. Figure 32 shows clearly the amplification of the stress field at the notch. The power spectrum corresponding to the ROM of the notched beam matches its NX/Nastran counterpart very well.

7. STRESS FIELD LOCAL ENRICHMENT

7.1. Motivation

The findings from the previous section provide a framework to carry out dynamic simulations of the notched beam at a much reduced computational cost than a full finite element

analysis. Yet, the reduced order model, in both its basis and its coefficients, depends on the crack geometry. This property is unfortunate in certain applications in which this geometry may be variable, e.g. when considering the notch as an uncertain defect or when envisioning the use of the reduced order model for crack propagation. For such analyses, it would be highly desirable to rely on a reference geometry, most simply the virgin beam, and enrich the solution by an extra component accounting for the existence and geometry of the crack as opposed to building a new reduced order model for every new notch geometry.

The loading considered in the present validation cases, and representative of the applied loads on panels, leads primarily to bending and stretching (from the nonlinear effects) and thus a mode I deformation is dominant. Accordingly, it is proposed here to add to the virgin beam stress distribution, induced by the pressure loading, a term that accounts for the presence of the crack. Following a stress intensity factor perspective, it is suggested that this term, referred to as an enrichment, be computed as the increment of stress induced by the crack, for a loading corresponding to the in-plane stress distribution of the virgin beam in the vicinity of the crack. Further, this enrichment term will be computed in a linear static analysis. Effectively, this approach replaces the stress distribution of the virgin beam in the vicinity of the crack by a stress distribution of the cracked beam that smoothly connects to the virgin far-field behavior.

Two separate versions of this strategy were considered and assessed on the notched beam from previous sections. In the first one, the loading applied to the notched beam is uniform through the thickness with magnitude equal to the stress estimated from the virgin reduced order model on the top of the beam at 2 thicknesses away from the notch. Note that the stress distribution on the notched beam was computed from the finite element model. However, only one such computation is necessary, i.e., for a unit in-plane load, and then is scaled according to

the stress predicted on the virgin beam. This enrichment is equivalent to having a constant stress intensity factor, equal to $S_{xx}^{(max)}/S_{xx}^{(nominal)}$, where $S_{xx}^{(nominal)}$ is equal to the virgin beam stress.

The large deformations considered here lead to a coupling between bending and membrane stretching that modifies the configuration of the stresses for different loading levels. Therefore, the stress intensity factor is also expected to change as the loading level is modified. In this light, the second stress enrichment considered was computed by applying a pressure varying through the thickness and equal to the S_{xx} stress distribution at a location 2 beam thicknesses from the center of the notch. This pressure distribution was applied in a linear static analysis to one of the ends of the beam, while keeping the other end fixed. As with the previous enrichment, this analysis was performed on both notched and virgin beams. Then, the resulting stress from the notched beam was subtracted by the stress field from the virgin beam to obtain the localized stress at the location of the notch. The disadvantage of this method is that a linear static analysis has to be performed every time the loading changes.

7.2. Validation of Stress Enrichment: Static Loading

Shown in Table 4 are the peak stresses at the notch, as computed by the reduced order model of the virgin beam with the two enrichments that were previously described. Clearly, the agreement is very good for the largest stresses (Case 1 and Case 2). Note that the stresses of the NX/Nastran analysis for the virgin beam were enriched as well to assess the accuracy of the enrichment procedure independently of the reduced order model. The enriched NX/Nastran stress results agree very well with the corresponding predictions on the notched beam.

7.3. Validation of Stress Enrichment: Dynamic Loading

For completeness it was desired to assess the effect of the enrichments in a dynamic analysis. The dynamic loading described in section 6 was used. The power spectral density of the S_{xx} element stresses, at different locations along the beam are shown in Figs. 33-36. Interestingly, both enrichments lead to almost identical stress results. As seen in Fig. 33, the addition of the two enrichment schemes to the ROM of the virgin beam, resulted in a good matching of NX/Nastran near the notch. This clearly is very pleasing, especially after looking at the results shown in Fig. 32.

8. SUMMARY

The focus of this investigation was on a first assessment of the predictive capabilities of nonlinear reduced order models for panels with a localized defect, i.e. a stress "hot spot". An aluminum clamped-clamped beam with a notch placed at 30% of its length and of depth equal to a quarter of the thickness was considered as an example. As expected, the notch was found to have a negligible effect on the first few natural frequencies of the beam, but also on the corresponding mode shapes. In addition, only small notch-related effects could also be detected on the in-plane component of the dual modes, which are basis functions constructed to capture the nonlinear transverse in-plane coupling occurring in large deformations. However, a large, rather broad peak was observed in the smaller transverse component of the dual modes of the notched beam which is absent on the corresponding plot for the virgin beam.

The displacement field induced by a uniform pressure on the beam large enough to induce nonlinearity, i.e. peak transverse displacements of the order of 2 and 4 thicknesses, was also found to be very weakly dependent on the notch. Further, this displacement field was shown to be well predicted by the reduced order models of both cracked and virgin beams.

In regards to the prediction of the stress field, it was found that the notch beam reduced order model was indeed able to capture accurately the stress distribution induced by the pressure loading. Excellent prediction of the displacements and stresses was also achieved under dynamic loading conditions.

Nevertheless, it was questioned whether a prediction based on the virgin beam reduced order model could also be used if appropriately "enriched" with the notched beam stress field in a superposition-like manner. Two enrichment options were assessed that rely on this stress field as obtained, in a *linear* finite element static analysis, from a notched beam subjected to the stress state induced on the virgin beam near the notch location. This methodology led to good to excellent predictions of the stress field near the notch for both static and dynamic excitations.

REFERENCES

[1] Mignolet, M.P., Przekop, A., Rizzi, S.A., and Spottswood, S.M., "A Review of Indirect/Non-Intrusive Reduced Order Modeling of Nonlinear Geometric Structures," *Journal of Sound and Vibration*, Vol. 332, No. 10, pp. 2437-2460, 2013.

[2] McEwan, M.I., Wright, J.R., Cooper, J.E., and Leung, A.Y.T., "A combined Modal/Finite Element Analysis Technique for the Dynamic Response of a Nonlinear Beam to Harmonic Excitation," *Journal of Sound and Vibration*, Vol. 243, pp. 601-624, 2001.

[3] Hollkamp, J.J., Gordon, R.W., and Spottswood, S.M., "Nonlinear Modal Models for Sonic Fatigue Response Prediction: A Comparison of Methods," *Journal of Sound and Vibration*, Vol. 284, pp. 1145-1163, 2005.

[4] Mignolet, M.P., Radu, A.G., and Gao, X., "Validation of Reduced Order Modeling for the Prediction of the Response and Fatigue Life of Panels Subjected to Thermo-Acoustic Effects," *Proceedings of the 8th International Conference on Recent Advances in Structural Dynamics*, Southampton, United Kingdom, Jul. 14-16, 2003.

[5] Radu, A., Yang, B., Kim, K., and Mignolet, M.P., "Prediction of the Dynamic Response and Fatigue Life of Panels Subjected to Thermo-Acoustic Loading," *Proceedings of the 45th Structures, Structural Dynamics, and Materials Conference*, Palm Springs, California, Apr. 19-22, 2004. Paper AIAA-2004-1557.

[6] Hollkamp, J.J., and Gordon, R.W., 2008, "Reduced-Order Models for Nonlinear Response Prediction: Implicit Condensation and Expansion," *Journal of Sound and Vibration*, Vol. 318, pp. 1139–1153.

[7] Przekop, A., and Rizzi, S.A., "A Reduced Order Method for Predicting High Cycle Fatigue of Nonlinear Structures," *Computers and Structures*, Vol. 84, No. 24-25, pp. 1606-1618, 2006.

[8] Kim, K., Radu, A.G., Wang, X.Q., and Mignolet, M.P., "Nonlinear Reduced Order Modeling of Isotropic and Functionally Graded Plates," *International Journal of Nonlinear Mechanics*, Vol. 49, pp. 100-110, 2013.

[9] Kim, K., Khanna, V., Wang, X.Q., and Mignolet, M.P., "Nonlinear Reduced Order Modeling of Flat Cantilevered Structures," *Proceedings of the 50th Structures, Structural Dynamics, and Materials Conference*, Palm Springs, California, May 4-7, 2009. AIAA Paper AIAA-2009-2492.

[10] Przekop A., and Rizzi S.A., "Nonlinear Reduced Order Random Response Analysis of Structures with Shallow Curvature," AIAA Journal Vol. 44 (8), pp. 1767-1778, 2006.

[11] Gordon R.W., and Hollkamp, J.J., "Reduced-Order Modeling of the Random Response of Curved Beams using Implicit Condensation," AIAA-2006-1926, 2006.

[12] Spottswood, S.M., Hollkamp, J.J., and Eason, T.G., "On the Use of Reduced-Order Models for a Shallow Curved Beam Under Combined Loading," *Proceedings of the 49th Structures, Structural Dynamics, and Materials Conference*, Schaumburg, Illinois, Apr. 7-10, 2008. AIAA Paper AIAA-2008-1873.

[13] Przekop, A., and Rizzi, S.A., "Dynamic Snap-Through of Thin-Walled Structures by a Reduced-Order Method," *AIAA Journal*, Vol. 45, No. 10, pp. 2510–2519, 2007.

[14] Spottswood, S.M., Eason, T.G., Wang, X.Q., and Mignolet, M.P., "Nonlinear Reduced Order Modeling of Curved Beams: A Comparison of Methods," *Proceedings of the 50th Structures, Structural Dynamics, and Materials Conference*, Palm Springs, California, May 4-7, 2009. AIAA Paper AIAA-2009-2433.

[15] Kim, K., Kim, Y.C., Mignolet, M.P., Liu, D.D., Chen, P.C., Lee, D.H., "Random Aeroelastic Response Due to Strong Hypersonic Unsteady-Wave/Shock Interaction with Acoustic Loads," *Proceedings of the 48th Structures, Structural Dynamics, and Materials Conference*, Honolulu, Hawaii, Apr. 23-26, 2007. AIAA Paper AIAA-2007-2014.

[16] Liu, D.D., Chen, P.C., Zhang, Z., Wang, Z., Yang, S., Lee, D.H., Mignolet, M.P., Kim, K., Liu, F., Lindsley, N., and Beran, P., "Continuous Dynamic Simulation of Nonlinear Aerodynamic/Nonlinear Structure Interaction (NANSI) for Morphing Wing Aeroelasticity," *Proceedings of the 50th Structures, Structural Dynamics, and Materials Conference*, Palm Springs, California, May 4-7, 2009. AIAA Paper AIAA-2009-2572.

[17] Liu, D.D., Wang, Z., Yang, S., Cai, C., Wang, X.Q., and Mignolet, M.P., "Nonlinear Aeroelastic Methodology for A Membrane-on-Ballute Model with Hypersonic Bow Shock," *Proceedings of the 50th Structures, Structural Dynamics, and Materials Conference*, Palm Springs, California, May 4-7, 2009. AIAA Paper AIAA-2009-2363.

[18] Perez, R., Wang, X.Q., and Mignolet, M.P., "Nonlinear Reduced Order Models for Thermoelastodynamic Response of Isotropic and FGM Panels," *AIAA Journal*, Vol. 49, pp. 630-641, 2011.

[19] Perez, R., Wang, X.Q., and Mignolet, M.P., "Steady and Unsteady Nonlinear Thermoelastodynamic Response of Panels by Reduced Order Models," *Proceedings of the 51th Structures, Structural Dynamics, and Materials Conference*, Orlando, Florida, April 12-15, 2010. AIAA Paper AIAA-2010-2724.

[20] Matney, Perez, R., and Mignolet, M.P., "Nonlinear Unsteady Thermoelastodynamic Response of a Panel Subjected to an Oscillating Flux by Reduced Order Models," *Proceedings of the 52th Structures, Structural Dynamics, and Materials Conference*, Denver, Colorado, April 4-7, 2011. AIAA Paper AIAA-2011-2016.

[21] Matney, A., Perez, R., Spottswood, S.M., Wang, X.Q., and Mignolet, M.P., "Nonlinear Structural Reduced Order Modeling Methods for Hypersonic Structures", *Proceedings of the 53rd Structures, Structural Dynamics, and Materials Conference*, Honolulu, Hawaii, April 23-26, 2012. AIAA Paper AIAA-2012-1972.

[22] Muravyov, A.A., and Rizzi, S.A., "Determination of Nonlinear Stiffness with Application to Random Vibration of Geometrically Nonlinear Structures," Computers and Structures, Vol. 81, pp. 1513-1523, 2003

[23] Hollkamp, J.J., Gordon R.W., and Beberniss, T.J., "Revisiting the Nonlinear Response of a Plate to Acoustic Loading," *Proceedings of the 49th Structures, Structural Dynamics, and Materials Conference*, Schaumburg, Illinois, April 7-10, 2008. AIAA-2008-2233.

[24] Murthy, R., Wang, X.Q., Perez, R., Mignolet, M.P., and Richter, L.A. "Uncertainty-Based Experimental Validation of Nonlinear Reduced Order Models", Journal of Sound and Vibration Vol. 331 (5), pp. 1097-1114, 2012.

[25] Mignolet, M.P., and Soize, C., "Stochastic Reduced Order Models for Uncertain Geometrically Nonlinear Dynamical Systems," Computer Methods in Applied Mechanics and Engineering, Vol. 197, 2008, pp. 3951-3963.

[26] Capiez-Lernout, E., Soize, C., and Mignolet, M.P., "Computational Stochastic Statics of an Uncertain Curved Structure with Geometrical Nonlinearity in Three-Dimensional Elasticity," Computational Mechanics, Vol. 49, No. 1, pp. 87-97, 2012.

[27] Fung, Y.C., and Tong, T., *Classical and Computational Solid Mechanics*, World Scientific, River Edge, New Jersey, 2001.

[28] Bonet, J., and Wood, R.D., *Nonlinear Continuum Mechanics for Finite Element Analysis*, Cambridge University Press, Cambridge, 1997.

Table 1. Clamped-Clamped Beam Properties

Beam Length	0.2286 m
Cross-section Width	0.0127 m
Cross-section Thickness	7.88 10-4 m
Density	2700 kg/m3
Young's Modulus	73,000 MPa
Shear Modulus	27,730 MPa

Table 2. Natural frequencies along with relative error between notched and virgin beams.

Mode No.	Virgin Beam (Hz)	Notched Beam (Hz)	Relative Difference (%)
1	81.561	81.551	0.010
3	442.075	441.900	0.040
6	1098.527	1097.261	0.110
10	2061.725	2061.693	0.001

Table 3. Summary of prediction errors, notched beam and virgin beam ROMs.

Peak T3 Disp (Beam Thicknesses)	Prediction Error Transverse (T3) Component (%)		Prediction Error Transverse (T1) Component (%)		Prediction Error Transverse (T2) Component (%)	
	Notched Beam	Virgin Beam	Notched Beam	Virgin Beam	Notched Beam	Virgin Beam
2	0.2	0.4	1	1.4	2.4	3.4
4	0.5	0.9	3.9	3.7	5.9	7.4
-2	0.3	0.3	1.4	1.4	3.4	3
-4	1	0.6	3.8	3.9	7.4	7.1

Table 4. Peak in-plane element stresses in the notch region for the four loading cases studied: 2.6kPa (Case 1), 17kPa (Case 2), -2.6kPa (Case 3), -17kPa (Case 4). Relative errors are with respect to the Nastran results of the notched beam.

Computation	Case 1		Case 2		Case 3		Case 4	
	MPa	Erel (%)	MPa	Erel (%)	MPa	Erel (%)	MPa	Erel (%)
Nastran Notched Beam	32.3		105.7		6.4		55.4	
Nastran Virgin Beam + Enrichment #1	32.2	0.3	107	1.2	7.2	12.5	58.2	5
Nastran Virgin Beam + Enrichment #2	32.3	0	107.2	1.4	7.1	11	58	4.6
ROM Notched Beam	32.7	1.2	105.8	0.1	7.3	14	65.2	17
ROM Virgin + Enrichment #1	32.7	1.2	105.6	0.1	9.3	45	67.7	22
ROM Virgin + Enrichment #2	32.8	1.5	105.9	0.2	9.2	44	67.7	22

Figure 1. Notched beam model: Part (b) shows the zone near the notch with a finer mesh than parts (a) and (c) which are away from the notch.

(a)   (b)
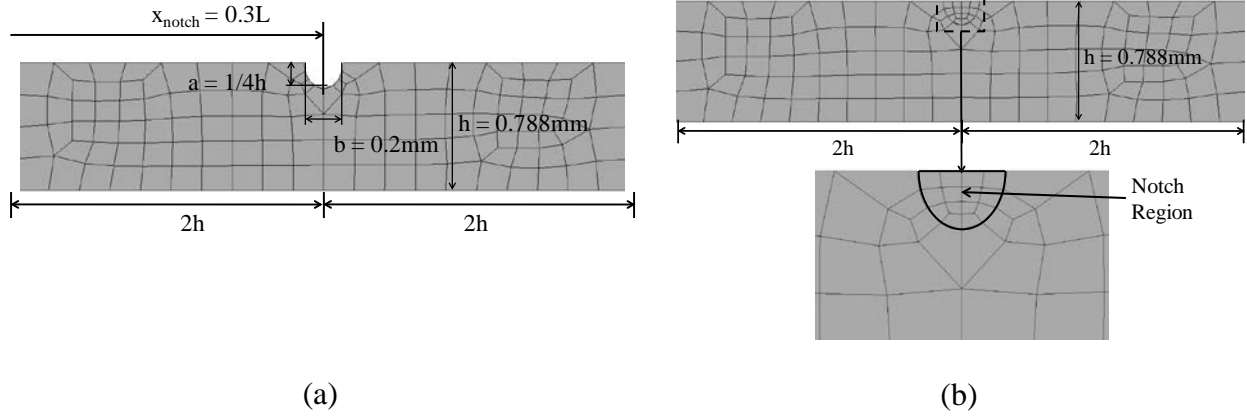
Figure 2. Geometry and finite element mesh near the notch region: (a) notched beam and (b) virgin beam. Where L=0.2286m and h=7.88x10-4m.
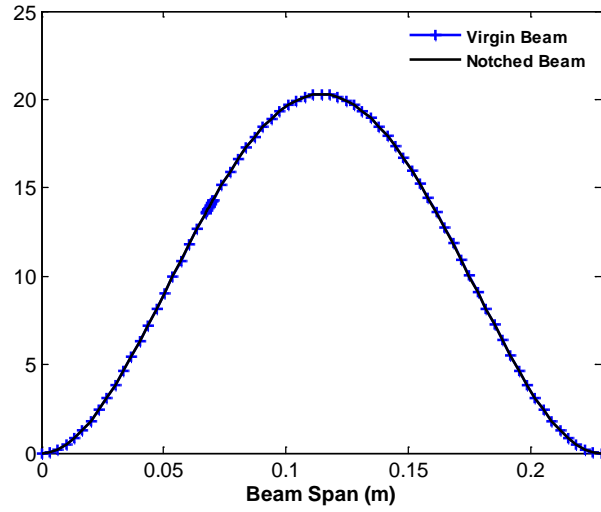
Figure 3. Transverse component of the first linear mode along one of the top edges of the beam.
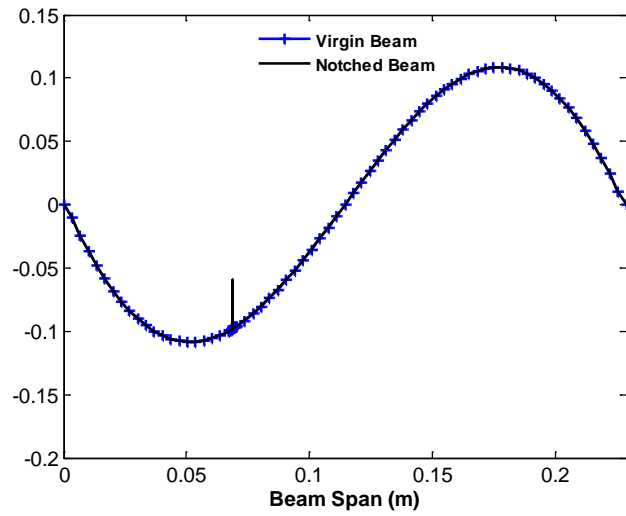
Figure 4. In-plane component of the first linear mode along one of the top edges of the beam.
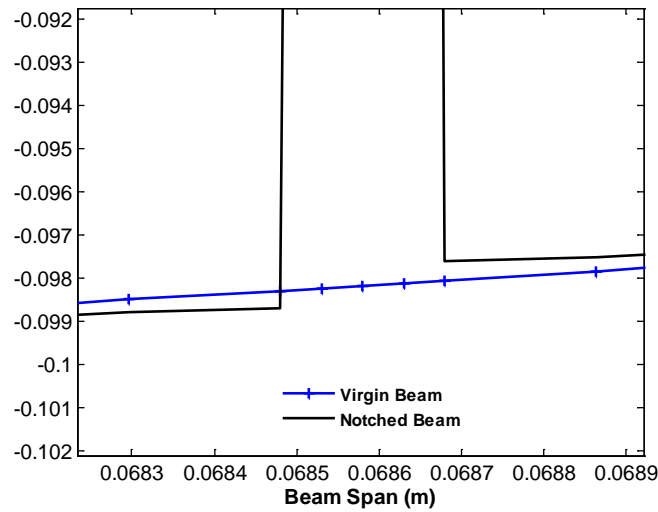
Figure 5. Zoomed-in view of the in-plane displacements near the location of the notch.
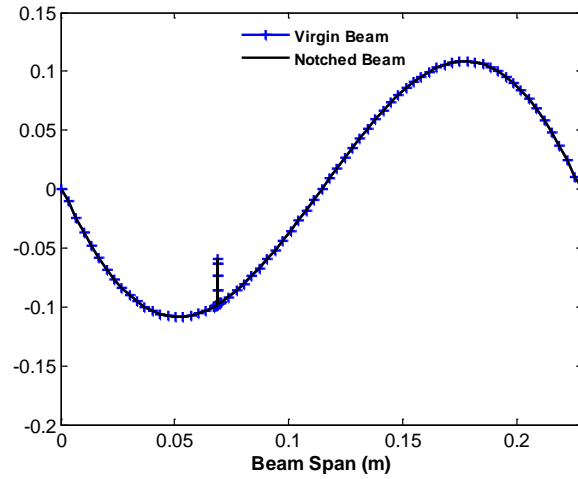
Figure 6. In-plane component of the first linear mode, curves correspond to displacements at the same nodes.
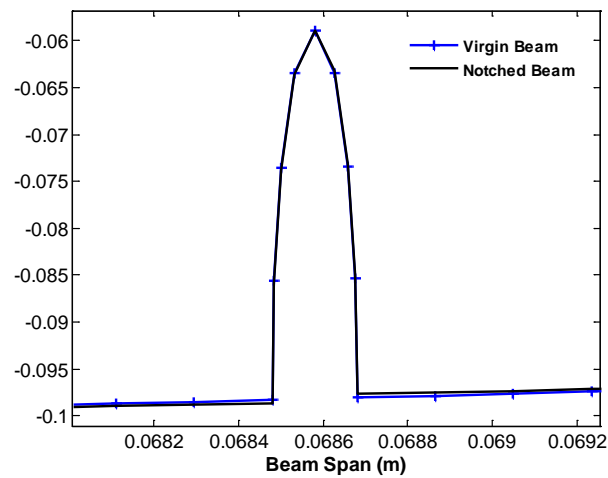
Figure 7. Zoomed-in view of the in-plane component, curves correspond to displacements at the same nodes.
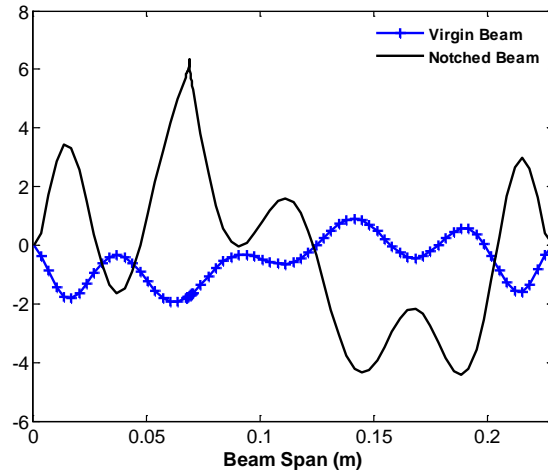
Figure 8. Transverse component of the first dual mode along one of the top edges of the beam.
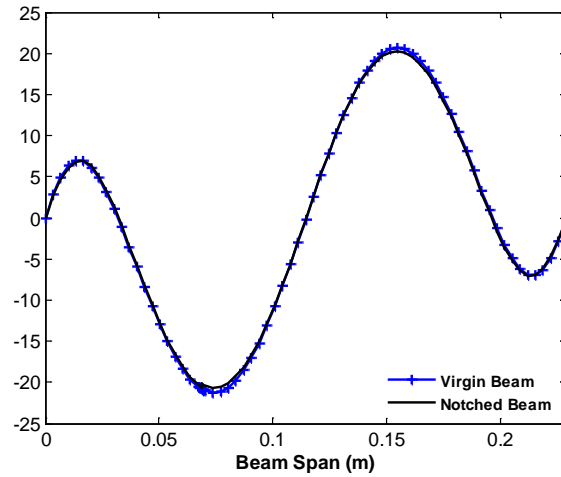
Figure 9. In-plane component of the first dual mode along one of the top edges of the beam.
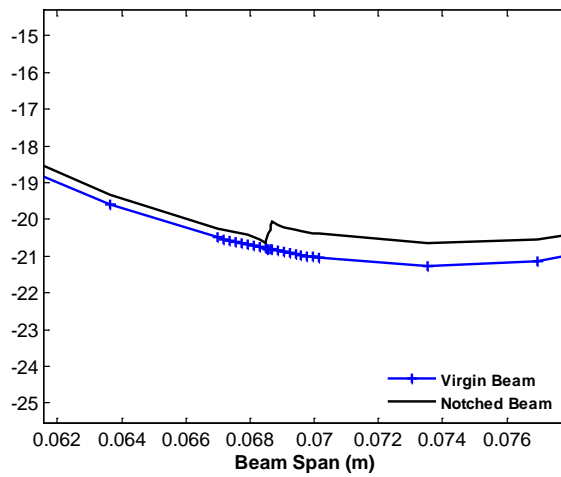
Figure 10. Zoomed-in view of the in-plane displacements near the location of the notch.
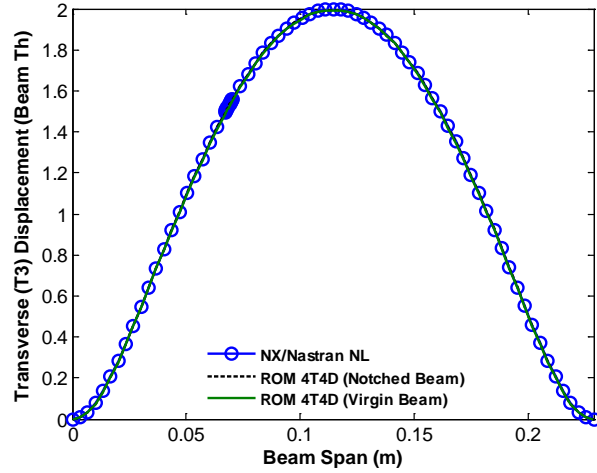
Figure 11. Transverse displacements at the top ($y=0$, $z=h$) edge of the beam induced by a uniform pressure of 2.6kPa on its bottom surface. Reduced order models ("ROM 4T4D"), nonlinear static FEA ("NX/Nastran NL").
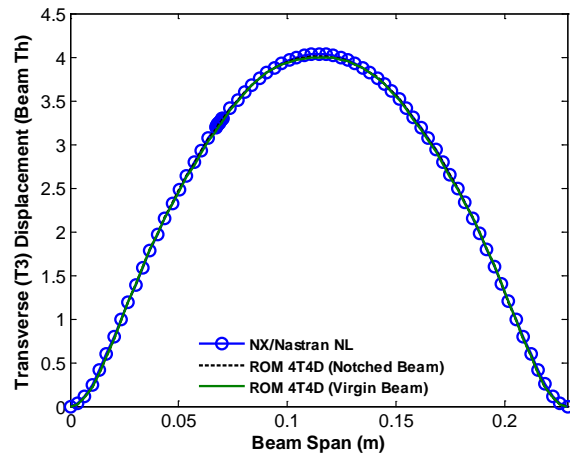
Figure 12. Transverse displacements at the top ($y=0$, $z=h$) edge of the beam induced by a uniform pressure of 17kPa on its bottom surface. Reduced order models ("ROM 4T4D"), nonlinear static FEA ("NX/Nastran NL").
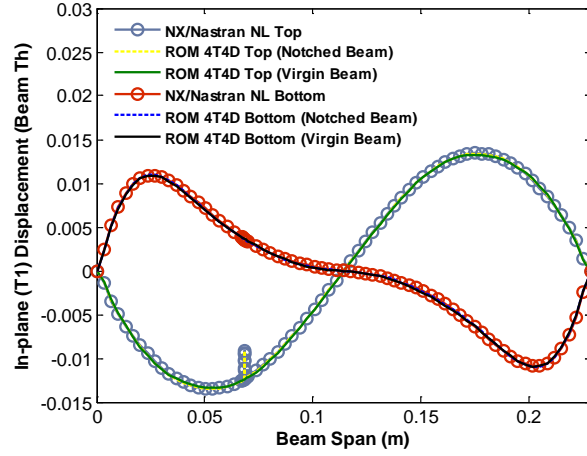
Figure 13. In-plane disp. at the top ($y=0$, $z=h$) and bottom ($y=0$, $z=0$) edges of the beam induced by a uniform pressure of 2.6kPa on its bottom surface. Reduced order models ("ROM 4T4D"), nonlinear static FEA ("NX/Nastran NL").
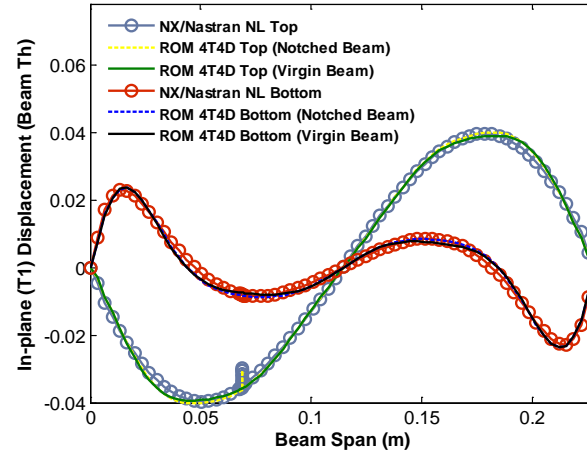
Figure 14. In-plane disp. at the top ($y=0$, $z=h$) and bottom ($y=0$, $z=0$) edges of the beam induced by a uniform pressure of 17kPa on its bottom surface. Reduced order models ("ROM 4T4D"), nonlinear static FEA ("NX/Nastran NL").
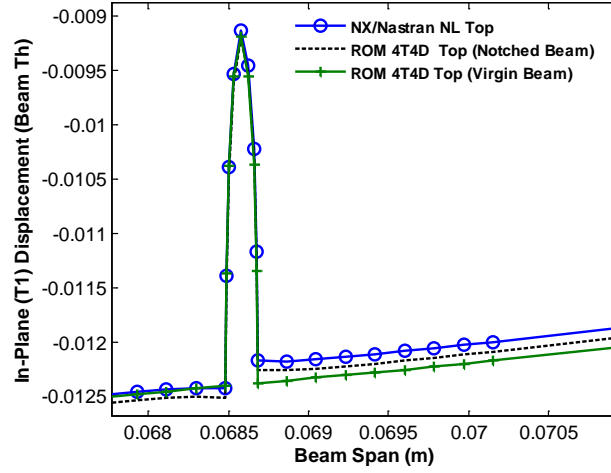
Figure 15. Close-up view of the in-plane disp. (T1) at the beam top edge ($y=0$, $z=h$) due to a uniform pressure of 2.6kPa. Reduced order models ("ROM 4T4D"), nonlinear static FEA ("NX/Nastran NL").
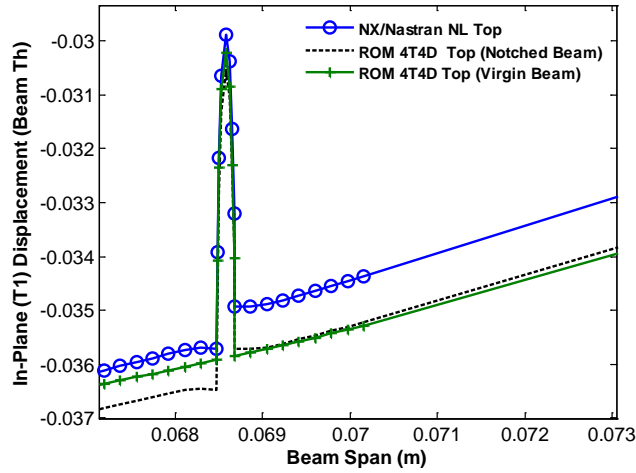
Figure 16. Close-up view of the in-plane disp. (T1) at the beam top edge ($y=0$, $z=h$) due to a uniform pressure of 17kPa. Reduced order models ("ROM 4T4D"), nonlinear static FEA ("NX/Nastran NL").
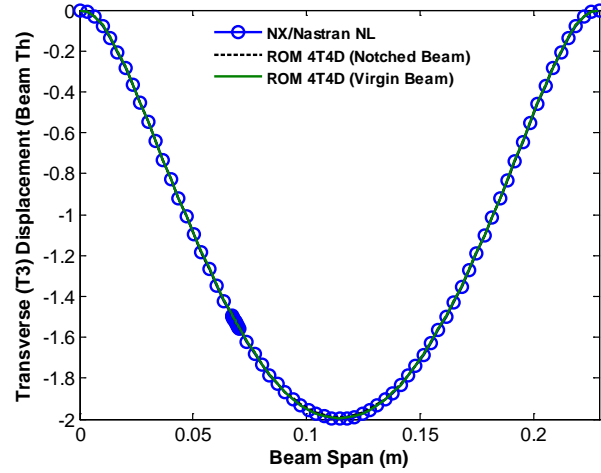
Figure 17. Transverse disp. at the top ($y=0$, $z=h$) edge of the beam induced by a uniform pressure of -2.6kPa on its bottom surface. Reduced order models ("ROM 4T4D"), nonlinear static FEA ("NX/Nastran NL").
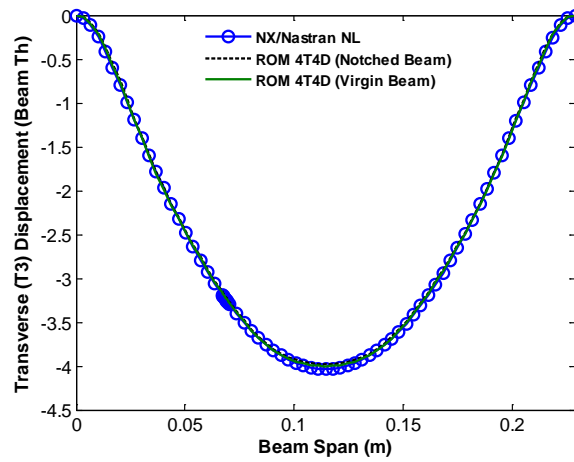
Figure 18. Transverse disp. at the top ($y=0$, $z=h$) edge of the beam induced by a uniform pressure of -17kPa on its bottom surface. Reduced order models ("ROM 4T4D"), nonlinear static FEA ("NX/Nastran NL").
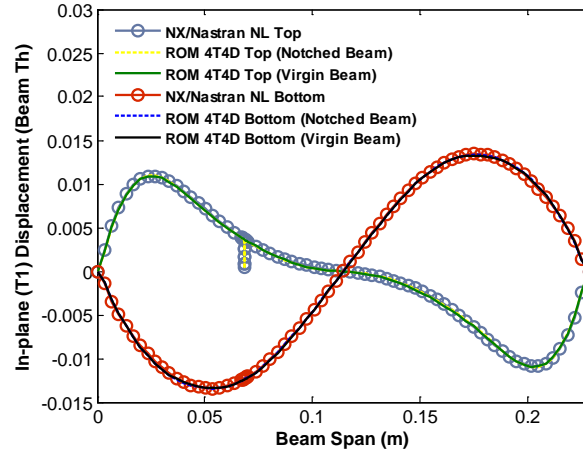
Figure 19. In-plane disp. at the top (*y=0, z=h*) and bottom (*y=0, z=0*) edges of the beam induced by a uniform pressure of -2.6kPa on its bottom surface. Reduced order models ("ROM 4T4D"), nonlinear static FEA ("NX/Nastran NL").
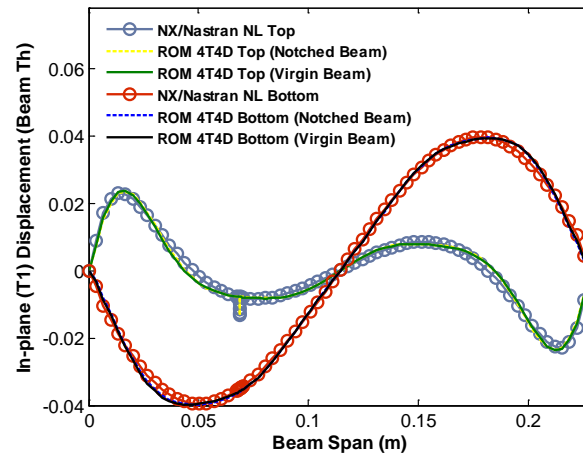
Figure 20. In-plane disp. at the top (*y=0, z=h*) and bottom (*y=0, z=0*) edges of the beam induced by a uniform pressure of -17kPa on its bottom surface. Reduced order models ("ROM 4T4D"), nonlinear static FEA ("NX/Nastran NL").
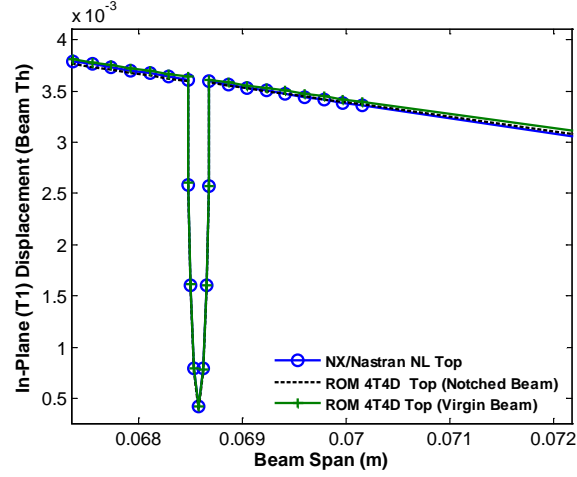
Figure 21. Close-up view of the in-plane disp. (T1) at the beam top edge (*y=0, z=h*) due to a uniform pressure of (a) -2.6kPa and (b) -17kPa. Reduced order models ("ROM 4T4D"), nonlinear static FEA ("NX/Nastran NL").
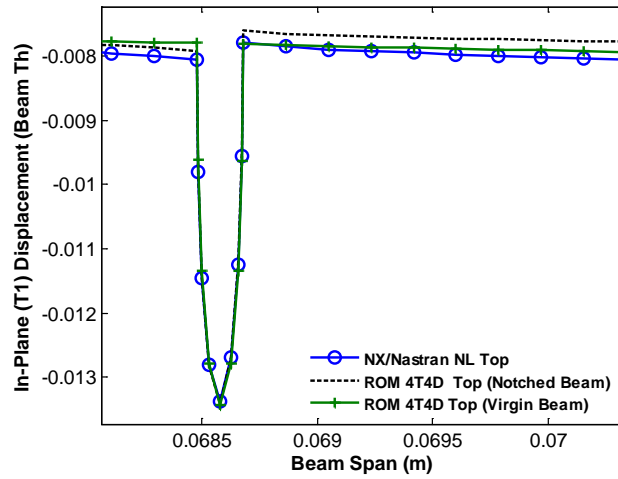
Figure 22. Close-up view of the in-plane disp. (T1) at the beam top edge (*y=0, z=h*) due to a uniform pressure of (a) -2.6kPa and (b) -17kPa. Reduced order models ("ROM 4T4D"), nonlinear static FEA ("NX/Nastran NL").
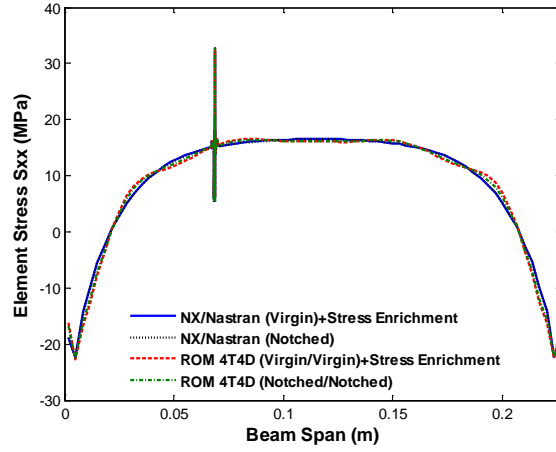
Figure 23. Element stress S_{xx} near the beam edge at $y=0$, $z=h$, induced by a uniform pressure of 2.6kPa. Reduced order model with stress enrichment ("ROM 4T4D+Stress Enrichment)", nonlinear static FEA ("NX/Nastran").
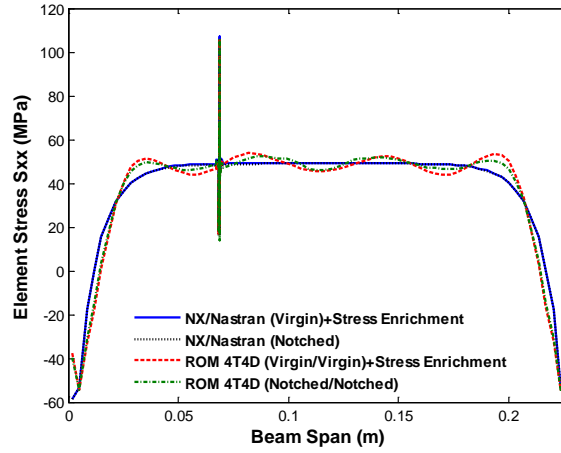
Figure 24. Element stress S_{xx} near the beam edge at $y=0$, $z=h$, induced by a uniform pressure of 17kPa. Reduced order model with stress enrichment ("ROM 4T4D+Stress Enrichment)", nonlinear static FEA ("NX/Nastran").
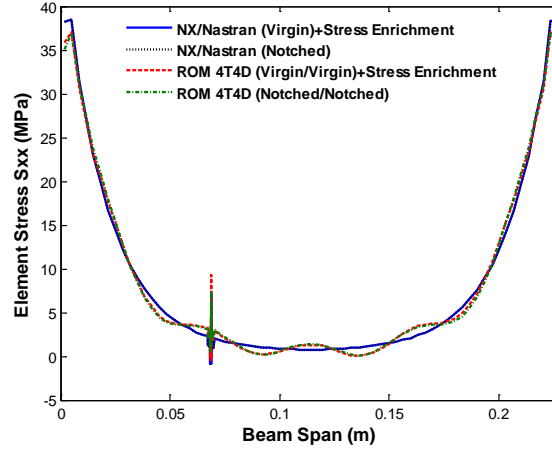
Figure 25. Element stress S_{xx} near the beam edge at $y=0$, $z=h$, induced by a uniform pressure of -2.6kPa. Reduced order model with stress enrichment ("ROM 4T4D+Stress Enrichment)", nonlinear static FEA ("NX/Nastran").
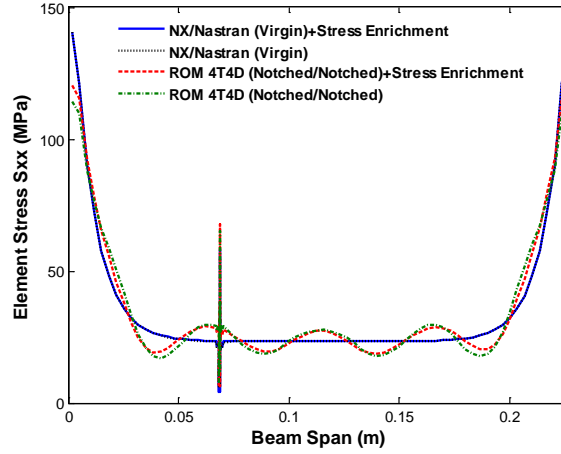
Figure 26. Element stress S_{xx} near the beam edge at $y=0$, $z=h$, induced by a uniform pressure of -17kPa. Reduced order model with stress enrichment ("ROM 4T4D+Stress Enrichment)", nonlinear static FEA ("NX/Nastran").
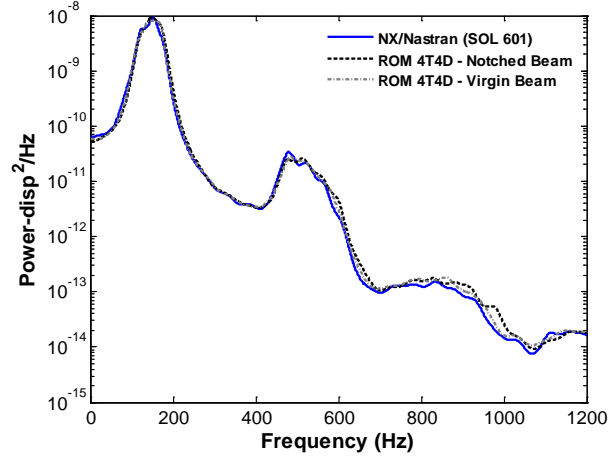
Figure 27. Power spectral density of the transverse displacement at the beam middle point, $x=1/2L$, $y=0$, $z=h$ ($OASPL = 147$dB). Reduced order model ("ROM(4T4D)") and FEA ("NX/Nastran").
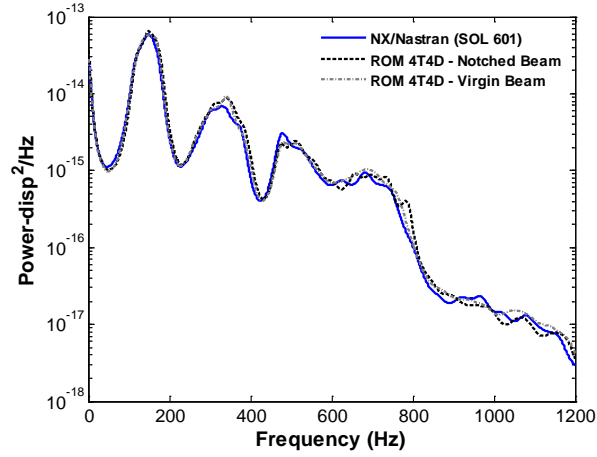
Figure 28. Power spectral density of the in-plane displacement at the notch tip ($OASPL = 147$dB). Reduced order model ("ROM(4T4D)") and FEA ("NX/Nastran").
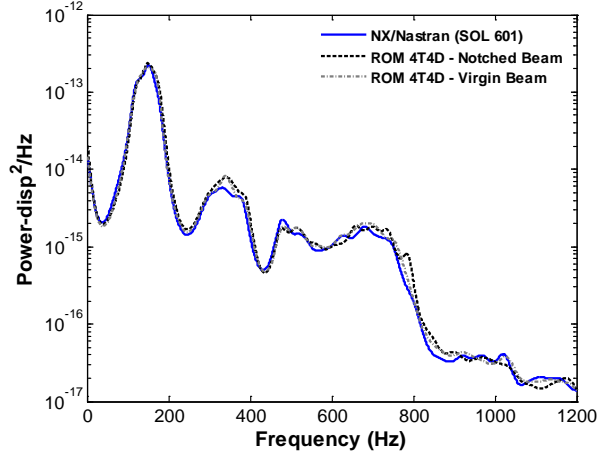
Figure 29. Power spectral density of the in-plane displacement at the beam quarter point, $x=1/4L$, $y=0$, $z=h$ ($OASPL = 147$dB). Reduced order model ("ROM(4T4D)") and FEA ("NX/Nastran").
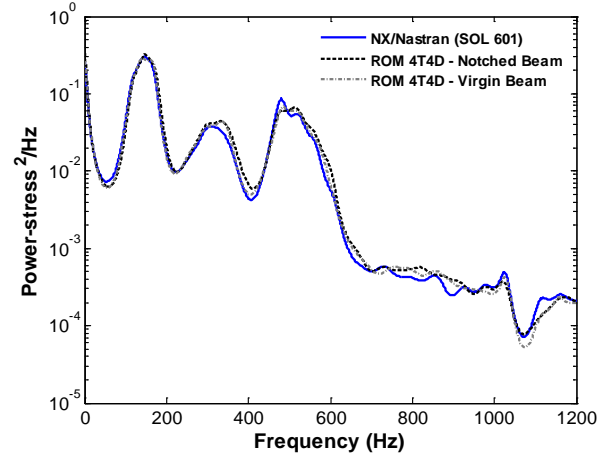
Figure 30. Power spectral density of the S_{xx} element stress near the middle of the beam at $y=0$, $z=h$ ($OASPL = 147$dB). Reduced order model ("ROM(4T4D)") and FEA ("NX/Nastran").
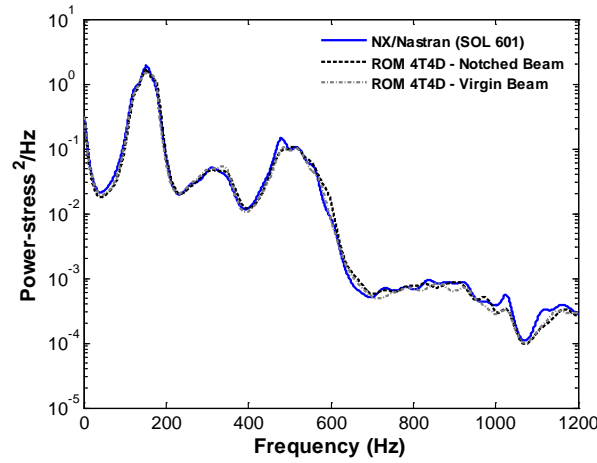
Figure 31. Power spectral density of the S_{xx} element stress near the support of the beam at $y=0$, $z=h$ ($OASPL = 147$dB). Reduced order model ("ROM(4T4D)") and FEA ("NX/Nastran").
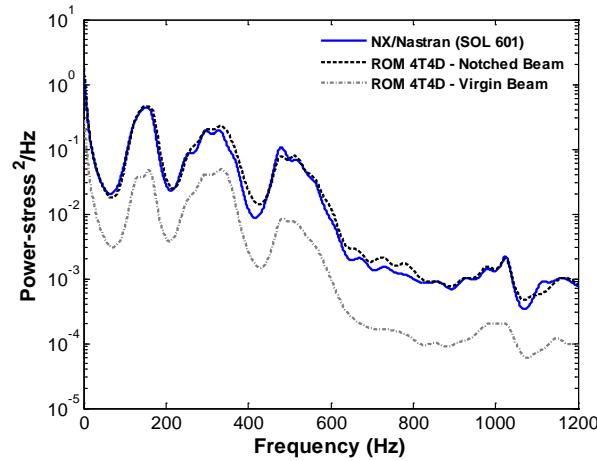
Figure 32. Power spectral density of the S_{xx} element stress near the notch at $y=0$, $z=h$ ($OASPL = 147$dB). Reduced order model ("ROM(4T4D)") and FEA ("NX/Nastran").
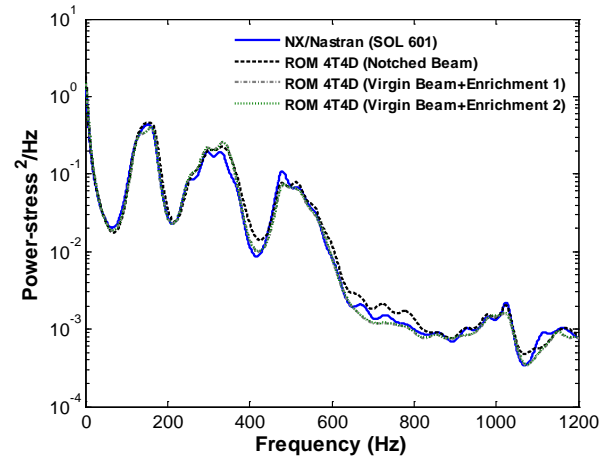
Figure 33. Power spectral density of the S_{xx} element stress near the notch tip at $y=0$, $z=h$ (*OASPL* = 147dB). Reduced order model ("ROM(4T4D)") and FEA ("NX/Nastran").
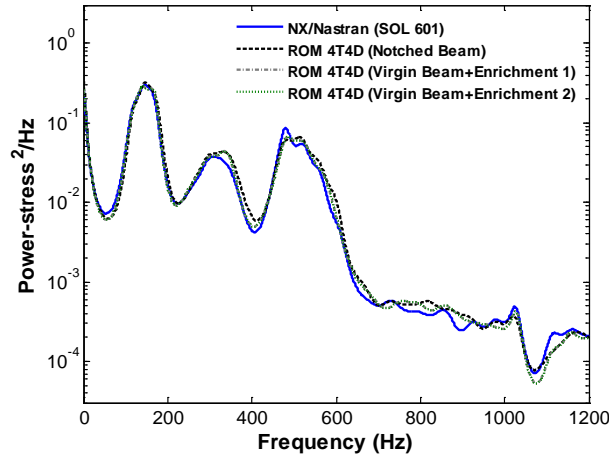
Figure 34. Power spectral density of the S_{xx} element stress near the middle of the beam at $y=0$, $z=h$ (*OASPL* = 147dB). Reduced order model ("ROM(4T4D)") and FEA ("NX/Nastran").
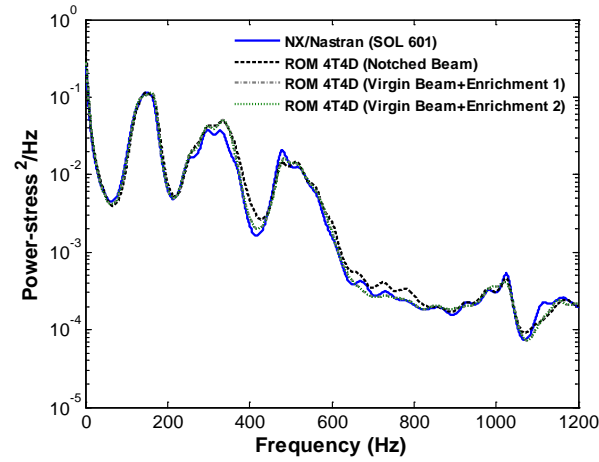
Figure 35. Power spectral density of the S_{xx} element stress at 2 beam thicknesses from the notch tip and $y=0$, $z=h$ (*OASPL* = 147dB). Reduced order model ("ROM(4T4D)") and FEA ("NX/Nastran").
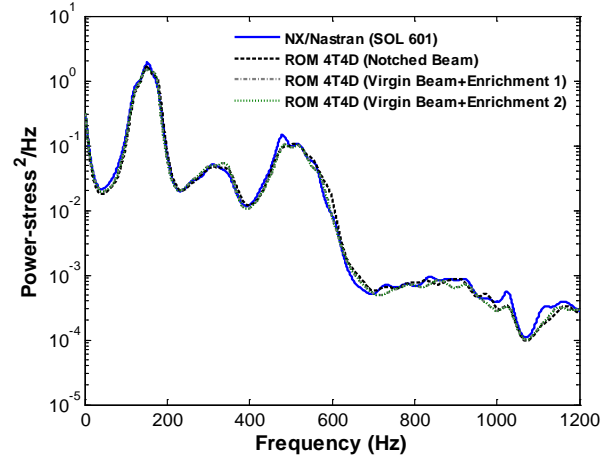
Figure 36. Power spectral density of the S_{xx} element stress near the support of the beam at $y=0$, $z=h$ (OASPL = 147dB). Reduced order model ("ROM(4T4D)") and FEA ("NX/Nastran").

ATTACHMENT C

Perez, R.A. "Multiscale Reduced Order Models for the Geometrically Nonlinear Response of Complex Structures," Ph.D., December 2012.

Multiscale Reduced Order Models for

the Geometrically Nonlinear Response of Complex Structures

by

Ricardo Angel Perez

A Dissertation Presented in Partial Fulfillment
of the Requirements for the Degree
Doctor of Philosophy

Approved November 2012 by the
Graduate Supervisory Committee:

Marc Mignolet, Chair
Jay Oswald
Stephen Spottswood
Pedro Peralta
Hanqing Jiang

ARIZONA STATE UNIVERSITY

December 2012

ABSTRACT

The focus of this investigation includes three aspects. First, the development of nonlinear reduced order modeling techniques for the prediction of the response of complex structures exhibiting "large" deformations, i.e. a geometrically nonlinear behavior, and modeled within a commercial finite element code. The present investigation builds on a general methodology, successfully validated in recent years on simpler panel structures, by developing a novel identification strategy of the reduced order model parameters, that enables the consideration of the large number of modes needed for complex structures, and by extending an automatic strategy for the selection of the basis functions used to represent accurately the displacement field. These novel developments are successfully validated on the nonlinear static and dynamic responses of a 9-bay panel structure modeled within Nastran. In addition, a multi-scale approach based on Component Mode Synthesis methods is explored.

Second, an assessment of the predictive capabilities of nonlinear reduced order models for the prediction of the large displacement and stress fields of panels that have a geometric discontinuity; a flat panel with a notch was used for this assessment. It is demonstrated that the reduced order models of both virgin and notched panels provide a close match of the displacement field obtained from full finite element analyses of the notched panel for moderately large static and dynamic responses. In regards to stresses, it is found that the notched panel reduced order model leads to a close prediction of the stress distribution obtained on the notched panel as computed by the finite element model. Two enrichment techniques, based on superposition of the notch effects on the virgin panel stress field, are proposed to permit a close prediction of the stress distribution of the notched panel from the reduced order model of the virgin one. A very

i

good prediction of the full finite element results is achieved with both enrichments for static and dynamic responses.

Finally, computational challenges associated with the solution of the reduced order model equations are discussed. Two alternatives to reduce the computational time for the solution of these problems are explored.

A mi familia, gracias por brindarme su apoyo y amor.

To Whittney, thank you for your constant love, patience, and support.

And whatever you do, whether in word or deed, do it all in the name of the Lord Jesus, giving thanks to God the Father through him (Colossians 3:17).

ACKNOWLEDGMENTS

TABLE OF CONTENTS

LIST OF TABLES

LIST OF FIGURES

xiv

xix

CHAPTER 1

OVERVIEW

1.1 Motivation

The development of affordable and reusable hypersonic vehicles has been a goal of the USAF and NASA for several years. These hypersonic aircraft operate in very complex environments, with loads that arise from the aerodynamics, acoustics, and thermal effects. These loads in turn, arise from the engine exhaust, turbulence, aerodynamic heating, among other sources (see [1] for a detailed description of these conditions). Furthermore, these loads are large enough, alone or in combination, to induce geometrically nonlinear behavior of the structure and/or its substructures. The nonlinearity results in a stiffening of the structure, due to coupling between bending and membrane stretching which occurs as out-of-plane loading is applied. Therefore, the geometric nonlinearity is in general beneficial; unfortunately it leads to difficulties in the prediction of the response. In addition, the dynamic excitation is also likely to create fatigue (sonic fatigue) and eventually cracks in the panels. The appearance of such cracks will trigger the key question: when will the panels have to be replaced to maintain safe flight conditions? Therefore, there are three computational challenges in the prediction of the response of hypersonic aircraft:

- High loading which results in geometric nonlinear effects.

- Coupling between aerodynamics, thermal problem, and structure implies three separate analyses that must share information.

- Prediction of fatigue life and damage as well as health monitoring for specific mission profiles.

Clearly, accurate and efficient computational tools are needed to address questions during the design stages, but also during the lifespan of the aircraft to be able to

1

deal with maintenance issues in an efficient way. Such predictions are clearly within the range of standard, commercial finite element software (e.g. Nastran and Abaqus), but even with current computing power they imply a computationally heavy task. The computational expense will be even more for panels that have cracks, because of the fine meshing required near the cracks to accurately capture the stress field. Furthermore, the random nature of the acoustic loading and uncertainties in the loads and in the model, would transform the problem into a random vibration one, which might require the consideration of multiple time histories in a Monte Carlo setting.

1.2. Linear Reduced Order Models - Modal Models

For a system with N degrees-of-freedom a set of N coupled equations has to be solved in order to obtain the response of the system. The solution becomes more complex as N becomes large. In such cases, a method known as *modal analysis* [2] allows to obtain the dynamic response with a much smaller number of degrees-of-freedom.

Consider the following discrete N-degree-of-freedom linear dynamic system

$$\underline{\underline{M}}\,\underline{\ddot{u}} + \underline{\underline{D}}\,\underline{\dot{u}} + \underline{\underline{K}}\,\underline{u} = \underline{F} \tag{1.1}$$

where M, D, and K are the mass, damping, and stiffness matrices of the system; they are $N \times N$ matrices. The homogeneous solution of the undamped system (D equal to the zero matrix) results in N eigenvalues and N eigenvectors (mode shapes). Assuming the structure is classically damped, the undamped and damped mode shapes coincide [3]. The mode shapes, due to their property of orthogonality, are linearly independent, so they form a basis of the N-dimensional space. This means that the solution of Eq. (1.1) can be expressed as follows

$$\underline{u}(t) = \sum_{n=1}^{N} q_n(t)\,\underline{\psi}^{(n)} \tag{1.2}$$

where the $q_n(t)$ are called the generalized coordinates and $\underline{\psi}^{(n)}$ are the mode shapes.

Since the mass and stiffness matrices of the system are symmetric, and assuming the modes are mass normalized, the following properties follow:

$$\left(\underline{\psi}^{(n)}\right)^T \underline{\underline{M}} \underline{\psi}^{(n)} = 1$$

$$\left(\underline{\psi}^{(n)}\right)^T \underline{\underline{K}} \underline{\psi}^{(n)} = \omega_n^2$$

(1.3)

where, ω_n is the nth natural frequency from the undamped system. Therefore, substitution of Eq. (1.2) into Eq. (1.1), pre-multiplying by the transpose of the mode shapes, and using Eqs. (1.3) yields a set of uncoupled differential equations

$$\ddot{q}_i + 2\varsigma\omega_i\dot{q}_i + \omega_i^2 \, q_i = F_i \quad \text{for } i = 1,..., N$$

(1.4)

where, ς is the damping ratio of the system. Furthermore, the solution can be approximated by truncating Eq. (1.2) to M modes, where $M << N$.

1.3. Nonlinear Reduced Order Models

Linear modal models are easy to build from commercial finite element codes. The advantage in using commercial codes is in the availability of a variety of materials, boundary conditions, loadings, and types of analyses (e.g., linear static, nonlinear static, etc.).

The extension of linear modal models to the study of structures undergoing "large" deformations (i.e., exhibiting geometric nonlinearity) has received significant attention during the last decade or so. The formulation of these nonlinear reduced order models (ROMs) is based on the use of finite element models generated using *commercial* codes (e.g. Nastran, Abaqus, DYNA3D), see [4] for a recent review. This not only facilitates the analysis of realistic structural models and complex boundary conditions,

3

but it also permits a direct transition to the industrial setting where they are routinely used.

The ROM capabilities have progressed significantly during the last decade or so. Starting with applications to flat structures, the ROM methodology has been used to predict the response of simple clamped-clamped beams (see [5-8]), flat cantilevered beams (see [9]), and panels (see [10-12]) under both dynamic and static loadings. Also, the analysis of moderately large deflections of curved structures has been performed (see [13-17]). The coupling of these nonlinear structural reduced order models with aerodynamics, either full or reduced order model, has also been successfully demonstrated in [18-20]. The coupling of the structural dynamics and thermal aspects, the two in reduced order model format, has been proposed and validated for uniform steady-state thermal loadings of beams and panels [21], non-uniform transient temperature fields of a 3-D panel [22], the structural dynamic analysis of a beam subjected to a moving heat flux [23], and the analysis of a 3-D hypersonic panel [24].

These developments have dealt with mono-bay structures, i.e., beams and plates with various boundary conditions, material properties, and loads. However, structures are seldom free of imperfections, and cracks, debonds, fasteners, shock impingement points, etc. can have a significant effect in the stress field. Furthermore, aircraft are formed from assemblies of elastic substructures and components (e.g., panels, spars, ribs, etc.). Therefore, the interaction of these components under high loading conditions can be significant. In this light, an important challenge in the development of the ROM capabilities is to be able to go from mono-bay structures ("meso" scale) down to the "micro" scale and up to the "macro" scale. Shown in Fig. 1.1 is a schematic that illustrates these three different scales.
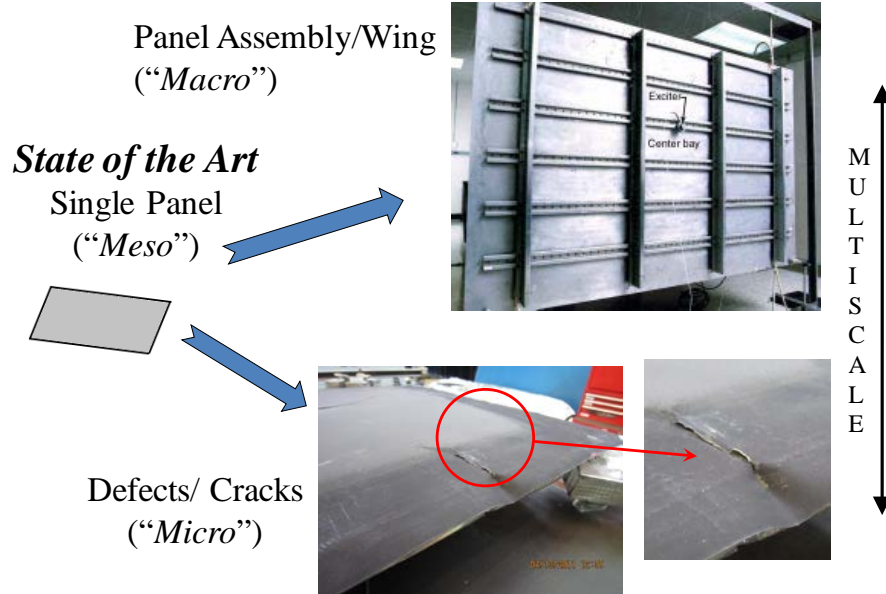
Figure 1.1. Schematic showing examples of the micro, meso, and macro scales.

The final challenge will be to incorporate the multi-scale character of the structure with the multidisciplinary nature that arises from the variety of loadings described in section 1.1. Shown in Fig. 1.2 is a schematic of these challenges, where all the couplings are represented by arrows. The present work will focus on the structural problem with acoustic loading.
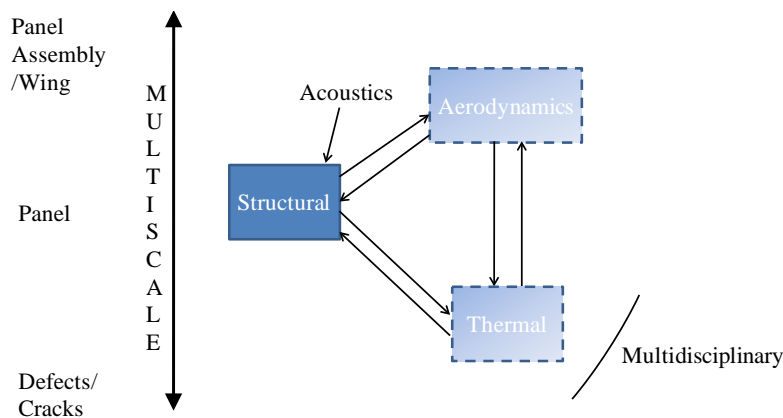
Figure 1.2. Schematic showing the multi-scale and multidisciplinary aspects of the computational challenges in the prediction of the response of hypersonic aircraft

The objective of the present work is to expand the ROM capabilities to the macro and micro-scales. There are two key aspects in the construction of a ROM: the

5

identification of the ROM parameters and the selection of a basis to represent the motions. The challenges associated with these two aspects have been seen to increase as more complex structural models are studied, since larger ROMs are required to capture the dominant aspects of the response. This in turn, implies an increase in the computational effort in the identification of the ROM parameters. In this light, a novel approach that requires a reduced computational effort for the identification of the ROM parameters will be introduced. The other challenge is related to the selection of a basis, so a new type of basis enrichment will be presented. Both propositions make use of the tangent stiffness matrix of the structure computed at certain displacement configurations. Furthermore, they will facilitate the construction of ROMs for complex models such as those within the macro-scale category. A validation on a complex structure will proceed.

The second objective is to assess the ROM capabilities for problems in the micro-scale. The main question to be addressed is: Can a displacement-based ROM capture a localized stress distribution? The following phenomenological issues will be addressed:

1) Is the displacement field affected by the local defect?
2) Does the defect need to be accounted for in the displacement?
3) Can a local enrichment of the stress be developed?

1.4. Outline

In Chapter 2 a background of nonlinear reduced order modeling is presented. The formulation of the ROM equations, along with the general methodology for the identification of the ROM parameters, and a discussion on the selection of the basis to represent the displacements is reviewed.

In Chapter 3, the formulation of the new identification procedure for the ROM parameters is discussed. In addition, the new type of basis enrichment is presented. The advantages of the new identification procedure are discussed.

In Chapter 4, the results of the validation of the methodologies developed in Chapter 3 on a complex model will be presented. The validation consists of static and dynamic excitations. In addition, a multi-scale approach based on Component Mode Synthesis tools is explored on a 9-bay panel.

The assessment of the ROM capabilities for problem in the micro-scale is done in Chapter 5. Both static and dynamic validation results are presented.

Two algorithmic improvements aimed at reducing the computational time of the solution of the ROM equations of motion are presented in Chapter 6. A summary is presented in Chapter 7.

CHAPTER 2

BACKGROUND ON REDUCED ORDER MODEL FORMULATION

2.1. Introduction

A reduced order model (ROM) is defined here as a modal-like representation of the displacement field u_i

$$u_i(\underline{X},t) = \sum_{n=1}^{M} q_n(t)\, U_i^{(n)}(\underline{X}) \qquad (2.1)$$

In these equations, the functions $U_i^{(m)}$ are specified functions of the position vector $\underline{X}$ in the undeformed configuration, chosen to satisfy the necessary boundary conditions. Furthermore, $q_n(t)$ is a time dependent generalized coordinate of the structural problem, which is required to satisfy the governing equations. The following sections will deal with the derivation of the governing equations for the structural problem. Then, the reduced order models will be derived following a Galerkin approach. Finally, an identification procedure for the parameters of the model as well as the selection of the functions $U_i^{(m)}$ will be reviewed, both based on a commercial finite element code.

2.2. Geometric Nonlinear Formulation

In structural dynamic problems related to beams, plates, and shells the von Karman strain definition is often used. However, it is of interest here to study a more general situation. Thus, an arbitrary linearly elastic (i.e., with a linear relation between Green strain and second Piola-Kirchhoff stress tensors) body undergoing large deformations will be considered. The elastodynamic problem will be derived in the undeformed configuration for convenience in the derivation of the reduced order model. In the deformed configuration, the panel is continuously changing; therefore, the basis

functions for the reduced order model would similarly vary in order to satisfy the geometric boundary conditions, thus the reason for choosing the undeformed configuration.

The position vector of a point of the structure will be denoted by $\underline{X}$ in the reference configuration and $\underline{x}$ in the deformed one. Then, the displacement vector is $\underline{u} = \underline{x} - \underline{X}$ and the deformation gradient tensor $\underline{F}$ is then defined by its components as

$$F_{ij} = \frac{\partial x_i}{\partial X_j} = \delta_{ij} + \frac{\partial u_i}{\partial X_j} \tag{2.2}$$

where δ_{ij} denotes the Kronecker delta. Associated with the displacement field $\underline{u}$ are deformations that are characterized by the Green strain tensor $\underline{E}$ of components

$$E_{ij} = \frac{1}{2}\left(F_{ki}\, F_{kj} - \delta_{ij}\right) \tag{2.3}$$

In the above equation and in the following ones summation is implied on all repeated indices, unless stated otherwise. The equation of motion of the structure is then given by (e.g. see [26])

$$\frac{\partial}{\partial X_k}\left(F_{ij}\, S_{jk}\right) + \rho_0\, b_i^0 = \rho_0\, \ddot{u}_i \quad \text{for } \underline{X} \in \Omega_0 \tag{2.4}$$

where $\underline{S}$ denotes the second Piola-Kirchhoff stress tensor, ρ_0 is the density in the reference configuration, and $\underline{b}^0$ is the vector of body forces, all of which are assumed to depend on the coordinates X_i and are expressed in the reference configuration, where the structure occupies the domain Ω_0. The boundary $\partial\Omega_0$ of the domain, which the structure occupies in the reference configuration, is composed of two parts, $\partial\Omega_0^t$ where tractions are prescribed and $\partial\Omega_0^u$ on which displacements are given. Therefore, the boundary conditions are

$$F_{ij}S_{jk}n_k^0 = t_i^0 \quad \text{for } \underline{X} \in \partial\Omega_0^t \tag{2.5}$$

9

and

$$\underline{u} = \underline{0} \qquad \text{for } \underline{X} \in \partial\Omega_0^u \qquad\qquad (2.6)$$

where the displacement boundary condition assumes the corresponding sides to be fixed, which is usually the case in structural dynamic problems.

In Eqs. (2.4) and (2.5) the vectors $\underline{b}^0$ and $\underline{t}^0$ are obtained by transforming the body forces and tractions in the deformed configuration back to the reference configuration. This transformation is achieved by the following relations

$$\underline{b}^0 = J\underline{b} \quad \text{and} \quad \underline{t}^0 = \left(\frac{da}{dA}\right)\underline{t} \qquad\qquad (2.7)$$

where J is the Jacobian of the transformation $\underline{x} = \underline{x}(\underline{X})$, i.e. $J = det(\underline{F})$. Also, the area ratio can be obtained from Nanson's formula (see [26])

$$\frac{da}{dA}\underline{n} = J\underline{\underline{F}}^{-T}\underline{N} \qquad\qquad (2.8)$$

where $\underline{N}$ is the unit normal vector to the boundary $\partial\Omega_0$ at point $\underline{X}$ and $\underline{n}$ is its counterpart in the deformed configuration.

2.3. Constitutive Relations

To complete the formulation of the problem, it is necessary to define the material constitutive relations, which stem from the Helmholtz free energy (per unit mass) H defined as

$$H = E - T S \qquad\qquad (2.9)$$

where E denotes the elastic energy and S denotes the specific entropy. Then, since the second Piola-Kirchhoff stress tensor and the Green strain rate are work conjugates, using conservation of energy along with Eq. (2.9) one has

$$\rho_0\left(\frac{\partial H}{\partial E_{ij}}\right)_T = S_{ij} \qquad\qquad (2.10)$$

10

$$\left(\frac{\partial H}{\partial T} \right)_{E_{ij}} = -S. \tag{2.11}$$

In the present investigation, the Duhamel-Neumann form of the Helmholtz free energy (see [27]) will by assumed, i.e.,

$$\rho_0 \, H = \frac{1}{2} C_{ijkl} \, E_{ij} \, E_{kl} - C_{ijkl} \, \alpha_{kl} \, (T - T_0) \, E_{ij} + f(T, T_0) \tag{2.12}$$

where $\underline{C}$ denotes the fourth order elasticity tensor and $\underline{\alpha}$ is the second order tensor of thermal expansion. Furthermore, T_0 is the reference temperature, and

$$f(T, T_0) = -\rho_0 \, C_v \, T_0 \left[\frac{T}{T_0} \ln \left(\frac{T}{T_0} \right) - \frac{T}{T_0} + 1 \right] \tag{2.13}$$

in which C_v is the specific heat per unit mass measured in the state of constant strain (see [27]).

Introducing Eqs. (2.12) and (2.13) in Eqs. (2.10) and (2.11) leads to the stress-strain relation

$$S_{ij} = \rho_0 \left(\frac{\partial H}{\partial E_{ij}} \right)_T = C_{ijkl} \left[E_{kl} - \alpha_{kl} \, (T - T_0) \right] \tag{2.14}$$

In the sequel, it will be assumed that the structure is not subjected to thermal effects, thus Eq. (2.14) reduces to

$$S_{ij} = C_{ijkl} E_{kl} . \tag{2.15}$$

Finally, the fourth order elasticity tensor $\underline{C}$ satisfies the symmetry conditions

$$C_{ijkl} = C_{jikl} = C_{ijlk} = C_{klij} \tag{2.16}$$

and the positive definiteness property

$$A_{ij} C_{ijkl} A_{kl} \geq 0 \tag{2.17}$$

for any second order tensor $\underline{A}$.

2.4. Structural Reduced Order Model

The previous sections have provided the governing equations of the continuous problem of determining the stress and displacement fields everywhere in the structure considered.

Substitution of Eq. (2.1) in the equation of motion, Eq. (2.4), introduces an error in the solution

$$\xi_i(\underline{X},t) = \sum_{n=1}^{M} \left[\rho_0 \ddot{q}_n(t) U_i^{(n)}(\underline{X}) - \rho_0 b_i^0 - \frac{\partial}{\partial X_k}\left(F_{ij}S_{jk}\right) \right] \neq 0 \qquad (2.18)$$

where S_{jk} is given by Eq. (2.15). It is desired to minimize the error ξ_i. To this end, following a Galerkin approach the error is forced to be orthogonal to the basis functions $U_i^{(m)}(\underline{X})$ so that

$$\int_{\Omega_0} U_i^{(m)}(\underline{X})\xi_i(\underline{X},t)d\underline{X} \qquad \text{for } m=1,...,M. \qquad (2.19)$$

Substitution of Eq. (2.18) into Eq. (2.19) yields the weak form of the equation of motion

$$\sum_{n=1}^{M} \left\{ \int_{\Omega_0} U_i^{(m)}(\underline{X}) \left[\rho_0 \ddot{q}_n(t) U_i^{(n)}(\underline{X}) - \rho_0 b_i^0 - \frac{\partial}{\partial X_k}\left(F_{ij}S_{jk}\right) \right] d\underline{X} \right\}$$

$$= 0 \qquad \text{for } m=1,...,M. \qquad (2.20)$$

The last integral in the previous expression can be expressed as

$$\int_{\Omega_0} U_i^{(m)} \frac{\partial}{\partial X_k}\left(U_i^{(m)}F_{ij}S_{jk}\right) d\underline{X}$$

$$= \int_{\Omega_0} \frac{\partial}{\partial X_k}\left(U_i^{(m)}F_{ij}S_{jk}\right) d\underline{X} - \int_{\Omega_0} \frac{\partial U_i^{(m)}}{\partial X_k} F_{ij}S_{jk} d\underline{X} \qquad (2.21)$$

It follows that, by using the Divergence theorem, the previous expression can be simplified into the following

$$\int_{\Omega_0} \frac{\partial}{\partial X_k} \left(F_{ij} S_{jk} \right) d\underline{X}$$
$$= \int_{\partial \Omega_0^t} U_i^{(m)} t_i^0 d\underline{X} - \int_{\Omega_0} \frac{\partial U_i^{(m)}}{\partial X_k} F_{ij} S_{jk} d\underline{X}. \tag{2.22}$$

It is left to expand the term $F_{ij}S_{jk}$ from Eq. (2.22). Using Eqs. (2.2), (2.3), and (2.15)

$$F_{ij}S_{jk} = \frac{\partial x_i}{\partial X_j} C_{jklp} \left[\frac{1}{2} \left(\frac{\partial x_s}{\partial X_l} \frac{\partial x_s}{\partial X_p} - \delta_{lp} \right) \right]. \tag{2.23}$$

Using the fact that $\underline{u} = \underline{x} - \underline{X}$ Eq. (2.23) can be expressed as

$$F_{ij}S_{jk} = \left(\delta_{ij} + \frac{\partial u_i}{\partial X_j} \right) C_{jklp} \left[\frac{\partial u_l}{\partial X_p} + \frac{1}{2} \frac{\partial u_s}{\partial X_l} \frac{\partial u_s}{\partial X_p} \right]. \tag{2.24}$$

Substitution of Eq. (2.1) yields

$$F_{ij}S_{jk}$$
$$= \left(\delta_{ij} + q_n \frac{\partial U_i^{(n)}}{\partial X_j} \right) C_{jklp} \left(q_r \frac{\partial U_l^{(r)}}{\partial X_p} + \frac{1}{2} q_r q_w \frac{\partial U_s^{(r)}}{\partial X_l} \frac{\partial U_s^{(w)}}{\partial X_p} \right), \tag{2.25}$$

where summation is implied by repeated indices.

Subsequently, substitution of Eqs. (2.22) and (2.25) into Eq. (2.20) and after some algebraic manipulations, the formulation of the reduced order model is obtained as

$$M_{ij} \ddot{q}_j + D_{ij} \dot{q}_j + K_{ij}^{(1)} q_j + K_{ijl}^{(2)} q_j q_l + K_{ijlp}^{(3)} q_j q_l q_p = F_i \quad \text{for } i=1,...,M \tag{2.26}$$

where

$$M_{mn} = \int_{\Omega_0} \rho_0 U_i^{(m)} U_i^{(n)} d\underline{X} \tag{2.27}$$

$$K_{mn}^{(1)} = \int_{\Omega_0} \frac{\partial U_i^{(m)}}{\partial X_k} C_{iklp} \frac{\partial U_l^{(n)}}{\partial X_p} d\underline{X} \tag{2.28}$$

$$K_{mnp}^{(2)} = \frac{1}{2} \left[\hat{K}_{mnp}^{(2)} + \hat{K}_{pmn}^{(2)} + \hat{K}_{npm}^{(2)} \right] \tag{2.29}$$

13

$$\hat{K}_{mnp}^{(2)} = \int_{\Omega_0} \frac{\partial U_i^{(m)}}{\partial X_j} C_{ijkl} \frac{\partial U_r^{(n)}}{\partial X_k} \frac{\partial U_r^{(p)}}{\partial X_l} d\underline{X} \qquad (2.30)$$

$$K_{msnp}^{(3)} = \frac{1}{2} \int_{\Omega_0} \frac{\partial U_i^{(m)}}{\partial X_j} \frac{\partial U_i^{(s)}}{\partial X_k} C_{jklw} \frac{\partial U_r^{(n)}}{\partial X_l} \frac{\partial U_r^{(p)}}{\partial X_w} d\underline{X} \qquad (2.31)$$

and,

finally,

$$F_m = \int_{\Omega_0} \rho_0 U_i^{(m)} b_i^0 d\underline{X} + \int_{\partial\Omega_0^t} U_i^{(m)} t_i^0 ds \qquad (2.32)$$

The knowledge of the displacements provides a complete solution of the problem and other quantities can then be evaluated. For example, any component of the second Piola-Kirchhoff stress tensor at any point can be expressed as

$$S_{ij} = \overline{S}_{ij} + \hat{S}_{ij}^{(m)} q_m + \tilde{S}_{ij}^{(m,n)} q_m q_n \qquad (2.33)$$

where the coefficients $\overline{S}_{ij}$, $\hat{S}_{ij}^{(m)}$, and $\tilde{S}_{ij}^{(m,n)}$ depend only on the point $\underline{X}$ considered.

2.5. Identification of ROM Parameters

Formal expressions, as integrals over the undeformed domain of the structure, for the stiffness coefficients $K_{ij}^{(1)}$, $K_{ijl}^{(2)}$, $K_{ijlp}^{(3)}$ were obtained above in the process of deriving Eq. (2.26). Their use would however require a discretization of the domain consistent with the finite element model. To bypass this effort, non-intrusive (or indirect) methods (see [4] for review) have been developed to identify these coefficients based on computed static responses.

The estimation of the mass components M_{ij} and modal forces F_i is achieved as in linear modal models, i.e.

14

$$M_{ij} = \underline{\psi}^{(i)T} M_{FE} \underline{\psi}^{(j)} \tag{2.34}$$

$$F_i = \underline{\psi}^{(i)T} \underline{F}(t) \tag{2.35}$$

where M_{FE} is the finite element mass matrix and $\underline{F}(t)$ is the excitation vector on the structure.

Next is the determination of the stiffness coefficients $K_{ij}^{(1)}$, $K_{ijl}^{(2)}$, and $K_{ijlp}^{(3)}$. In this regard, note first that the linear coefficients $K_{ij}^{(1)}$ could be determined as in linear modal models, i.e.

$$K_{ij}^{(1)} = \underline{\psi}^{(i)T} K_{FE}^{(1)} \underline{\psi}^{(j)} \tag{2.36}$$

where $K_{FE}^{(1)}$ is the finite element linear stiffness matrix.

Another approach must however be adopted for $K_{ijl}^{(2)}$ and $K_{ijlp}^{(3)}$ as nonlinear stiffness matrices are typically not available from a commercial finite element code. A reduction in this computational effort is obtained by noting the symmetrical role of the indices j and l in the quadratic terms and j, l, and p in the cubic ones, which indicates that the summations over those indices can be restricted to $p \geq l \geq j$ leading to approximately $M^4/6$ coefficients to be identified.

Two approaches have been proposed to identify the above quadratic and cubic stiffness parameters (and potentially the linear ones as well) from a series of static finite element solutions. The first one relies on prescribing a series of load cases and projecting the induced responses on the basis functions $\underline{\psi}^{(n)}$ to obtain the corresponding generalized coordinates values $q_j^{(p)}$, p being the index of the load cases (see [6-7]). Then, introducing these values into Eq. (2.26) for each load case yields

15

$$K_{ij}^{(1)} q_j^{(p)} + K_{ijl}^{(2)} q_j^{(p)} q_l^{(p)} + K_{ijlr}^{(3)} q_j^{(p)} q_l^{(p)} q_r^{(p)} = F_i^{(p)} \qquad (2.37)$$
$$, i = 1, ..., M$$

where M denotes the number of basis functions (or modes) in the reduced order model. Proceeding similarly for P load cases yields a set of linear algebraic equations for the coefficients $K_{ijl}^{(2)}$ and $K_{ijlp}^{(3)}$, and possibly the linear stiffness coefficients $K_{ij}^{(1)}$ as well, which can be solved in a least squares format to complete the identification of the stiffness parameters.

An alternate strategy has also been proposed (e.g. see [28] and the modification of [12]) in which the *displacements* are prescribed and the required force distributions are obtained from the finite element code. The corresponding modal forces are then evaluated from Eq. (2.35) and a set of equations of the form of Eq. (2.37) is again obtained. Appropriately selecting the displacement fields to be imposed can lead to a particularly convenient identification of the stiffness coefficients. Specifically, the imposition of displacements proportional to the basis function $\underline{\psi}^{(n)}$ only, i.e.

$$\underline{u} = q_n \, \underline{\psi}^{(n)} \qquad \underline{\hat{u}} = \hat{q}_n \, \underline{\psi}^{(n)} \qquad \underline{\tilde{u}} = \tilde{q}_n \, \underline{\psi}^{(n)} \qquad (2.38)$$

leads to the 3 sets of equations

$$K_{in}^{(1)} q_n + K_{inn}^{(2)} q_n^2 + K_{innn}^{(3)} q_n^3 = F_i \quad \text{(no sum on } n\text{)}$$

$$K_{in}^{(1)} \hat{q}_n + K_{inn}^{(2)} \hat{q}_n^2 + K_{innn}^{(3)} \hat{q}_n^3 = \hat{F}_i \quad \text{(no sum on } n\text{)} \qquad (2.39)$$

$$K_{in}^{(1)} \tilde{q}_n + K_{inn}^{(2)} \tilde{q}_n^2 + K_{innn}^{(3)} \tilde{q}_n^3 = \tilde{F}_i \quad \text{(no sum on } n\text{)}$$

in which no sum over the index n is to be understood and for $i = 1, ..., M$. In fact, these 3 sets of equations permit the direct evaluation of the coefficients $K_{in}^{(1)}$, $K_{inn}^{(2)}$, and $K_{innn}^{(3)}$

16

for all i. Repeating this effort for $n = 1, ..., M$ thus yields a first set of stiffness coefficients.

Proceeding similarly but with combinations of two basis functions, i.e.

$$\underline{u} = q_n \, \underline{\psi}^{(n)} + q_m \, \underline{\psi}^{(m)} \quad m \geq n \tag{2.40}$$

and relying on the availability of the coefficients $K_{in}^{(1)}$, $K_{inn}^{(2)}, K_{innn}^{(3)}$ and $K_{im}^{(1)}$, $K_{imm}^{(2)}$, $K_{immm}^{(3)}$ determined above, leads to equations involving the three coefficients $K_{inm}^{(2)}$, $K_{innm}^{(3)}$, and $K_{inmm}^{(3)}$. Thus, imposing three sets of displacements of the form of Eq. (2.40) provides the equations needed to also identify $K_{inm}^{(2)}$, $K_{innm}^{(3)}$, and $K_{inmm}^{(3)}$.

Finally, imposing displacement fields as linear combination of three modes, i.e.

$$\underline{u} = q_n \, \underline{\psi}^{(n)} + q_m \, \underline{\psi}^{(m)} + q_r \, \underline{\psi}^{(r)} \quad r \geq m \geq n \tag{2.41}$$

permits the identification of the last coefficients, i.e. $K_{inmr}^{(3)}$.

Proceeding either with load cases, i.e. Eq. (2.37), or with imposed displacement solutions, Eq. (2.38) and Eqs. (2.40)-(2.41), M coefficients (1 for each value of i) can be evaluated for each load/displacement solution. Accordingly, there will be approximately $M^3/6$ such solutions to be determined, each one of which requires a full finite element nonlinear analysis. For an $M = 60$ basis function reduced order model, there will thus be 36,000 solutions which represents a very significant upfront computational effort.

Note, that the modal forces F_i will in general be affected by the "pull back" operations of Eq (2.7). However, this issue was not addressed here because the displacements of the panels considered in this investigation did not exceed a few thicknesses.

Finally, it remains to discuss the selection of the q values for the imposed displacement fields from Eq. (2.38) and Eqs. (2.40)-(2.41). The first difficulty in the selection of an appropriate q value lies in the numerical precision of the computations. This can be clearly appreciated with an example. Assuming a static displacement proportional to the first mode only, Eq. (2.26) becomes equal to

$$K_{11}^{(1)} q_1 + K_{111}^{(2)} q_1^2 + K_{1111}^{(3)} q_1^3 = F_1 \tag{2.42}$$

In order to solve for the $K_{1111}^{(3)}$ coefficient, division by q_1^3 would be required. If q_1 is a very "small" number, then there is the risk of amplifying any "noise" that might be present in F_1 and/or any of the coefficients $K_{11}^{(1)}$ and $K_{111}^{(2)}$. When the formulation of the finite element code used to create the ROM matches the formulation presented above, i.e. it is based on the reference configuration, then any value for the q coefficients (that is large enough to avoid numerical errors) would be good enough to identify the stiffness coefficients. However, this is not always the case; for example, the geometric nonlinear computations in Nastran are carried out with respect to the deformed configuration. So, if "large" q values are used, then the Lagrangian formulation used to derive the ROM becomes too different from the formulation used by Nastran, and the resulting stiffness coefficients do not represent well the problem. Therefore, there exists a range of values that yield fitting stiffness coefficients. For problems such as simple beams and panels this range has been found to be such that the resulting peak transverse displacement is larger than half beam or panel thicknesses but below one thickness.

2.6. ROM Basis Selection

The selection of the basis functions $\underline{\psi}^{(n)}$ represents a key challenge of the reduced order modeling strategy: if the structural response is not well represented within this basis, the corresponding prediction of the reduced order model will in general be

poor. The modes/basis functions needed for a nonlinear problem are certainly expected to include those used for the corresponding linear problem, but others are also anticipated to model the difference in physical behavior induced by the nonlinearity. This situation is particularly clear in shell-like structures subjected to transverse loadings in which the linear response is predominantly transverse while the tangential/in-plane displacement field plays a fundamental role (the "membrane-stretching" effect, see [4,6-7] for discussion) in large motions.

This issue was addressed in [12] through the inclusion in the basis of an additional set of basis functions referred to as *dual modes*, aimed at capturing the membrane stretching effects. The key idea in this approach is to first subject the structure to a series of "representative" static loadings, and determine the corresponding *nonlinear* displacement fields. Then, extract from them additional basis functions, the "dual modes", to append to the linear basis, i.e. the modes that would be used in the linear case. It was argued in [12] that the representative static loadings should be selected to excite primarily the linear basis modes and, in fact, in the absence of geometric nonlinearity (i.e. for a linear analysis) should only excite these modes. i.e. the applied load vectors $\underline{F}_{FE}^{(m)}$ on the structural finite element model should be such that the corresponding linear static responses are of the form

$$\underline{u}^{(m)} = \sum_i \alpha_i^{(m)} \underline{\psi}^{(i)} \tag{2.43}$$

which occurs when

$$\underline{F}_{FE}^{(m)} = \sum_i \alpha_i^{(m)} K_{FE}^{(1)} \underline{\psi}^{(i)} \tag{2.44}$$

where $\alpha_i^{(m)}$ are coefficients to be chosen with m denoting the load case number. A detailed discussion of the linear combinations to be used is presented in [12] but, in all validations carried out, it has been sufficient to consider the cases

$$\underline{F}_{FE}^{(m)} = \alpha_i^{(m)} K_{FE}^{(1)} \underline{\psi}^{(i)} \quad i = \text{dominant mode} \tag{2.45}$$

and

$$\underline{F}_{FE}^{(m)} = \frac{\alpha_i^{(m)}}{2} K_{FE}^{(1)} \left[\underline{\psi}^{(i)} + \underline{\psi}^{(j)} \right] \quad i = \text{dominant mode}, \ j \neq i \tag{2.46}$$

where a "dominant" mode is loosely defined as one expected to provide a large component of the panel response to the physical loading. The ensemble of loading cases considered is formed by selecting several values of $\alpha_i^{(m)}$ for each dominant mode in Eq. (2.45) and also for each mode $j \neq i$ in Eq. (2.46). Note further that both positive and negative values of $\alpha_i^{(m)}$ are suggested and that their magnitudes should be such that the corresponding displacement fields $\underline{u}^{(m)}$ range from near linear cases to some exhibiting a strong nonlinearity. Finally, a proper orthogonal decomposition (POD) analysis of each set of "nonlinear responses" is then sequentially carried out to extract the dominant features of these responses which are then selected as dual modes, see [12] for full details.

Validating the appropriateness of these dual modes can be done in particular by demonstrating notable improvements in the projection of snap-shots of the full response on a basis that includes them vs. one that does not, see ensuing section for details. A more visual approach would be to demonstrate that the deflections induced by the loadings of Eqs. (2.45) and (2.46) are similar to those obtained with the physical loading of interest for a broad range of overall magnitude. This effort could be done by plotting the corresponding displacement fields and comparing them. A more expedient strategy

20

would be to visualize these displacement fields in the N-dimensional space, where N is the number of degrees of freedom of the structure, and to show that the displacements induced by the physical loading and by the ones of Eqs. (2.45) and (2.46) closely occupy the same part of the space. Since N is typically much larger than 3, this space cannot be represented graphically but 2- and 3-dimensional sections of it can be very informative.

To exemplify this situation, consider the clamped-clamped aluminum beam of [21] subjected to both static and dynamic uniform loads. In the absence of symmetry breaking, the transverse displacements are symmetric while the in-plane ones are anti-symmetric. Three representative descriptors of the displacement field are thus the transverse displacements of the beam middle and of another point, taken here as the 1/4 point, and the in-plane displacement of that same off-center point. The magnitude of these displacements is plotted vs. each other in Fig. 2.1 for a series of loadings. First are a uniform static load of varying magnitude, loads of the form of Eq. (2.45) using the first symmetric mode (1-1 Dual) and the second symmetric mode (2-2 Dual), and finally loads in the form of Eq. (2.46) with combinations between the first symmetric mode and the two following ones (1-2 Dual and 1-3 Dual). Also included in Fig. 2.1 are snap shots of the dynamic stationary response to a uniformly distributed load varying randomly in time as a white noise bandlimited process in the frequency range [0,1042Hz] simulating an acoustic loading of overall sound pressure level (*OASPL*) of 143dB.

It is clearly seen from Fig. 2.1 that the displacements induced by the loadings of Eq. (2.45) for the 1-1 Dual and Eq. (2.46) closely occupy the same space as both static and dynamic physical loads and thus they can efficiently be used in the construction of the basis for the representation of the full nonlinear response. Note as well that the displacements induced by the loading of Eq. (2.45) for the 2-2 Dual does not occupy the same space as the other ones and thus is not a good candidate for the basis, i.e. its

21

inclusion in the basis would not be detrimental but would not be very beneficial either. This observation was indeed expected as mode 2 is not a dominant mode, i.e. it does not or rarely does (in the dynamic case) represent the largest component of the response. This finding confirms the selection strategy of the modes, dominant or not, in Eqs. (2.45) and (2.46). The appropriateness of the above duals extends well beyond the uniform loads, static or dynamic, discussed above; they are appropriate for the class of loading conditions in which the response is dominated by mode 1 (the mode selected as dominant). To confirm this expectation, the displacements induced by triangular loads (zero at the clamp supports and maximum at the beam middle) are also plotted in Fig. 2.1 and they also closely occupy the same space.
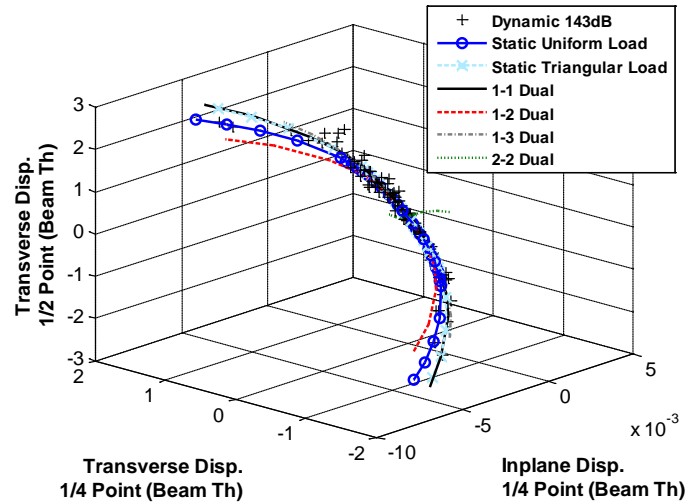

Figure 2.1. Displacements from NX/Nastran at two points of a clamped-clamped beam under various loadings. Transverse displacement at middle point vs. transverse and in-plane displacements at quarter point

22

CHAPTER 3

NEW IDENTIFICATION AND BASIS ENRICHMENT METHODOLOGIES

3.1. Introduction

The use of commercial finite element codes enables the straightforward consideration of complex models, allows a broad ensemble of possible elements and capabilities, but also permits a direct transition to the industrial setting where these codes are routinely used. The counterpart of these advantages is the unavailability of certain information and the uncertainty on the formulation implemented in the finite element modeling and response computation. As seen in Chapter 2, the developed reduced order models are parametric, i.e. the form of the equations governing the generalized coordinates is fixed, linear in mass and damping operators with a stiffness operator exhibiting linear, quadratic, and cubic terms in all combinations of generalized coordinates as derived from finite deformation elasticity in the reference configuration. One of the key challenges involved in the ROM is accordingly the estimation of the parameters of the model from a set of finite element results. As seen in the previous chapter, current methods for this identification are based on computed static responses for specified loads [6-7], or in reverse, necessary loads to achieve a particular displacement (see [12,28]). This strategy becomes computationally expensive as the size of the model increases as it is proportional to the third power of the number of modes retained. Therefore, a new strategy for the identification of these coefficients, which makes use of the tangent stiffness matrix of the structure, will be presented and validated in this chapter. It is proportional to the square of the number of modes and thus provides a significant reduction in the computational cost associated with the model building.

A second challenge involved in complex structural model is the selection of the basis to represent well and "economically" (with a small basis) the displacements. In this

regard, it will be shown that the modes obtained from the tangent stiffness matrix, computed at certain displacement configurations, form an excellent enrichment to capture the geometric nonlinearities in addition to the modes of the linear structure and the *dual modes*.

3.2. Identification Methodology for Complex Models

An alternate identification approach is proposed here, which relies on the availability of the final *tangent stiffness matrix* for each load or imposed displacement case. The advantage of this approach is that an $M \times M$ matrix is obtained for each solution and thus a reduction of the computational effort to $O(M^2)$ is expected. The specific details of this novel algorithm are developed below.

The *iu* component of the reduced order tangent stiffness matrix is derived from the cubic stiffness operator of Eq. (2.26) as

$$K_{iu}^{(T)} = \frac{\partial}{\partial q_u} \left[K_{ij}^{(1)} q_j + K_{ijl}^{(2)} q_j q_l + K_{ijlp}^{(3)} q_j q_l q_p \right] \tag{3.1}$$
$$= K_{iu}^{(1)} + \left[K_{iju}^{(2)} + K_{iuj}^{(2)} \right] q_j + \left[K_{ijlu}^{(3)} + K_{ijul}^{(3)} + K_{iujl}^{(3)} \right] q_j q_l$$

It is proposed here to determine the stiffness coefficients $K_{ij}^{(1)}$, $K_{ijl}^{(2)}$, and $K_{ijlp}^{(3)}$ by imposing the matching, for a series of deformed configurations, of the reduced order tangent stiffness matrix with the projection on the basis of its finite element counterpart $\hat{K}^{(T)}$. That is,

$$K^{(T)}(\underline{q}^{(p)}) = \Psi^T \hat{K}^{(T)}(\underline{u}^{(p)}) \Psi \quad \text{where} \quad \underline{u}^{(p)} = \Psi \underline{q}^{(p)} \tag{3.2}$$

for a series of $p = 1, ..., P$ deformed configurations. In the above equations, the subscript ^{T} denotes the operation of matrix transposition and Ψ is the modal matrix

$$\Psi = \left[\underline{\psi}^{(1)} \, \underline{\psi}^{(2)} \dots \underline{\psi}^{(M)} \right] \tag{3.3}$$

The deformed configurations $\underline{u}^{(p)} = \Psi \underline{q}^{(p)}$ selected here are those of the imposed displacement scheme, Eq. (2.38) and Eqs. (2.40)-(2.41). Consider first the situation in which the imposed displacement is along a single basis function, i.e. $\underline{u} = q_j \, \underline{\psi}^{(j)}$. The corresponding ROM tangent stiffness matrix can then be written as (no sum on j)

$$K_{iu}^{(T)} = K_{iu}^{(1)} + \left[K_{iju}^{(2)} + K_{iuj}^{(2)} \right] q_j + \left[K_{ijju}^{(3)} + K_{ijuj}^{(3)} + K_{iujj}^{(3)} \right] q_j^2 \tag{3.4}$$

Since the elements $K_{ijl}^{(2)}$ and $K_{ijlp}^{(3)}$ were assumed to be zero unless $p \geq l \geq j$, the above equation is equivalent to

$$K_{iu}^{(T)} = \left[\Psi^T \hat{K}^{(T)} \Psi \right]_{iu} = K_{iu}^{(1)} + K_{iju}^{(2)} q_j + K_{ijju}^{(3)} q_j^2 \qquad j < u$$

$$K_{iu}^{(T)} = \left[\Psi^T \hat{K}^{(T)} \Psi \right]_{iu} = K_{iu}^{(1)} + 2 K_{iuu}^{(2)} q_u + 3 K_{iuuu}^{(3)} \, q_u^2 \quad j = u \tag{3.5}$$

$$K_{iu}^{(T)} = \left[\Psi^T \hat{K}^{(T)} \Psi \right]_{iu} = K_{iu}^{(1)} + K_{iuj}^{(2)} q_j + K_{iujj}^{(3)} q_j^2 \qquad j > u$$

from which the coefficients $K_{ijl}^{(2)}$, $K_{ijjl}^{(3)}$, and $K_{ijll}^{(3)}$ can be estimated if it is assumed that the linear stiffness coefficients are obtained from Eq. (2.36).

To complete the identification of the reduced order model, it remains to evaluate the coefficients $K_{ijlu}^{(3)}$ for $j{\neq}l$, $j{\neq}u$, and $u{\neq}l$. They can be evaluated from the knowledge of $K_{iu}^{(T)}$ corresponding to a displacement field which involves both basis functions j and l, i.e. of the form of Eq. (2.40). Then, $K_{iu}^{(T)}$ is given by Eq. (4.1) for which no summation on j and l applies. Specifically, for $u > l > j$, one has

$$K_{iu}^{(T)} = \left[\Psi^T \hat{K}^{(T)} \Psi \right]_{iu}$$
$$= K_{iu}^{(1)} + \left[K_{iju}^{(2)} q_j + K_{ilu}^{(2)} q_l \right] + \left[K_{ijlu}^{(3)} q_j q_l + K_{ijju}^{(3)} q_j^2 + K_{illu}^{(3)} q_l^2 \right] \qquad (3.6)$$

in which all terms are known except $K_{ijlu}^{(3)}$.

Note in the above procedure, that no combination of three modes, as in Eq. (2.41), is necessary and thus, as suggested at the beginning of this section, the number of deformed configurations to consider is only of order $O(M^2)$, it is indeed $2M + M(M-1)/2$. To corroborate this analysis, shown in Table 4.1 are the number of static solutions required for the new, tangent stiffness-based identification scheme and the imposed displacement force-based method. These results clearly show the reduction in computational effort necessary which converges to $M/3$ for large M.

However, the CPU time required in the construction of the tangent stiffness matrix and its transformation to the modal tangent stiffness matrix ought to be taken into account to perform a fair comparison. For the 9-bay panel considered in the ensuing sections and with 96,156 degrees of freedom, the CPU time required to produce a static solution with tangent stiffness matrix was found to be approximately 1.5 times the time to obtain the same solution without computing the tangent stiffness matrix. The combination of these factors suggests that the net reduction in computational time implied by the tangent stiffness algorithm is a factor of the order of $M/4$ to $M/5$ for large M.

Table 3.1. Number of Static Solutions Needed for ROM Identification

Number of Modes	Imposed Displ. Tangent Stiffness ID Method	Imposed Displ. Force ID Method
15	135	815
25	350	3,275
75	2,950	76,075

A limited set of comparisons were performed, on the 9-bay panel described below and on a flat clamped-clamped beam, to assess whether the stiffness coefficients

identified by the imposed displacement methods based on the forces and the tangent stiffness matrix were noticeably different, and/or they led to reduced order model with different predictive capabilities. While some, typically small, differences in the coefficients were found, the two methods led to reduced order model predictions that were very close to each other suggesting that the methods provide an equal accuracy in estimating the stiffness coefficients.

Finally, another advantage of this method lies in the numerical accuracy issue discussed at the end of Chapter 2.4. Indeed, since no combination of three modes is needed the largest power in the identification is quadratic. Therefore, smaller values of q can be used without bringing a problem of accuracy such as the one described in that chapter.

3.3. ROM Basis for Complex Models

The dual mode construction from the previous chapter has been very successfully applied to various beam and plate structural models, e.g. see [9, 12, 17-25], to capture the nonlinear interaction, both static and dynamic, between transverse and "in-plane" motions. Its application to the 9-bay panel of [29] did provide a basis that represented much better the nonlinear response, especially in the in-plane (tangential) direction, than the one based on the linear modes but yet not well enough to obtain an accurate reduced order model prediction of the full order Nastran results. This observation suggested that the load cases of Eq. (2.45) and (2.46) do provide a very valuable platform to identify the nonlinear effects, but it also demonstrated that other, smaller components, are also present.

A potential solution to capture these components of the response would be to expand the summation in Eq. (2.46) to include more than 2 modes. Such an effort would however likely bring many static solutions to be determined and analyzed. If such modes

were indeed included, it would be expected that the coefficients $\alpha_i^{(m)}$ multiplying them would be small, reflecting the small discrepancies observed. Then, the changes in the displacement fields $\underline{u}^{(m)}$ would probably also be small and thus may be captured in a perturbation-like format. Central to such an analysis would be the finite element tangent stiffness matrix $\hat{K}^{(T)}(\underline{u}^{(m)})$ evaluated at the displacements $\underline{u}^{(m)}$ induced by the loadings of Eqs. (2.45) and (2.46).

The above discussion suggests that this tangent stiffness matrix does also contain valuable basis information. To extract it, it was proposed to first proceed with a generalized eigenvector analysis of each matrix $\hat{K}^{(T)}(\underline{u}^{(m)})$ yielding the vectors $\underline{\phi}_j^{(m)}$ such that

$$\hat{K}^{(T)}(\underline{u}^{(m)})\,\underline{\phi}_j^{(m)} = \lambda_j^{(m)} M_{FE} \underline{\phi}_j^{(m)}. \tag{3.7}$$

Next, the eigenvectors $\underline{\phi}_j^{(m)}$ that are most significantly excited by the loading were retained and projected on the basis consisting of the linear and dual modes. Finally, a POD analysis of the ensemble of eigenvector projections was carried out to extract the new information in the eigenvectors $\underline{\phi}_j^{(m)}$. The basis functions thus retained to complement the linear and dual modes are referred to in the sequel as "tangent dual modes".

A somewhat similar argument to the one developed above has recently been proposed [30] for enriching the linear modes by eigenvectors of the second derivative of the tangent stiffness matrix evaluated at the undeformed configuration.

28

CHAPTER 4

VALIDATION ON A MIDDLE COMPLEXITY MODEL

4.1. Model Description

The 9-bay panel of [29] modeled within Nastran was considered for the validation of the novel (i) stiffness coefficients identification and (ii) basis selection strategy. This panel is a section of the sidewall fuselage panel studied in [31], see Fig. 4.1. The finite element model of the 9-bay panel, shown in Fig. 4.2, has a total of 96,156 degrees of freedom. The dimensions of the skin panel are 58.11in by 25.06in, and it is subdivided into nine bays by a riveted frame and longeron substructure. Each bay measures 18.75in by 7.5in between rivet lines. The thickness of the skin panel and frame substructure is of 0.05in and of 0.04in for the longeron substructure. The finite element model consists of 4-node plate elements. Furthermore, beam elements were used to model the rivets that join the skin panel to the frame and longeron substructures. The material properties are shown in Table 4.1.The edges of the skin panel are simply supported.
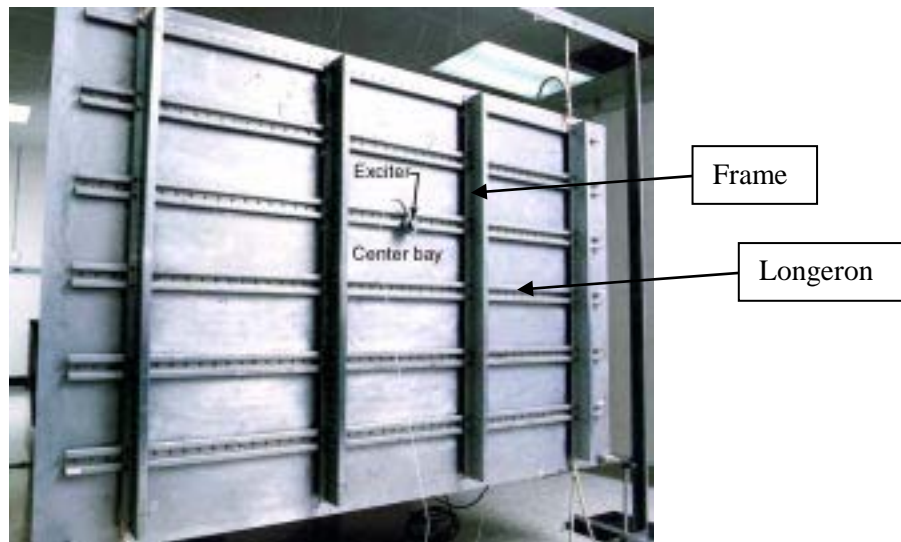
Figure 4.1. Sidewall fuselage panel taken from [31]. 9-bay panel is a section of this structure.

Table 4.1. 9-Bay Panel Material Properties

Young's Modulus	$10.5\times10^6 psi$
Poisson's Ratio	0.33
Density	$2.614\times10^{-4} lb_f\text{-}s^2/in^4$
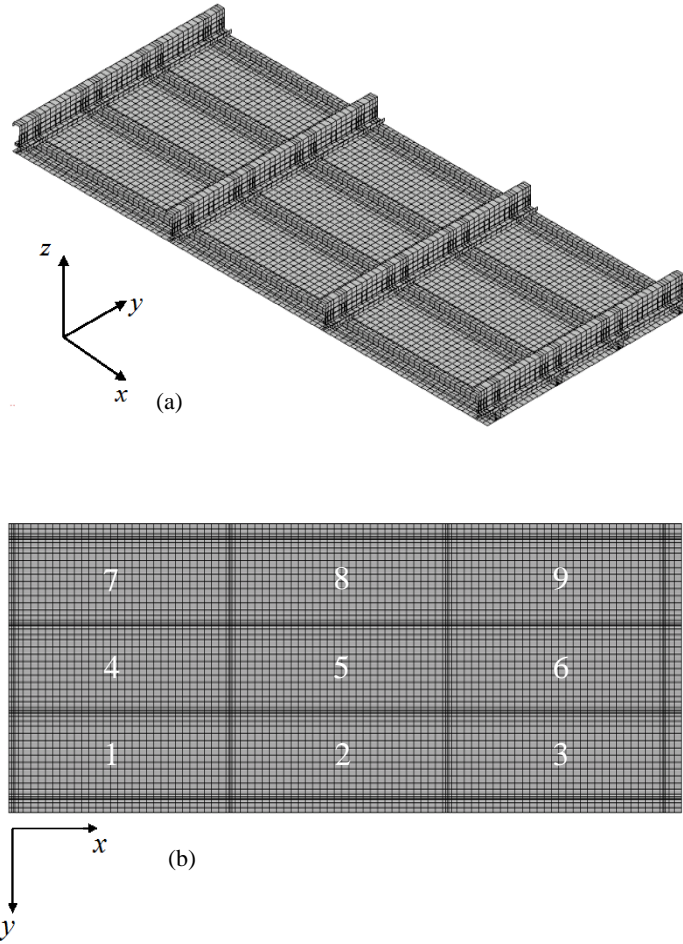
Figure 4.2. Finite element model of the 9-bay fuselage sidewall panel, (a) isometric view, (b) top view.

4.2. Reduced Order Model Basis Selection of the 9-Bay Panel

A series of 10 uniform pressures were applied to the skin panel, and the corresponding NX/Nastran nonlinear static responses (SOL 106) were obtained to provide a sample of "snapshots" for the reduced order model construction. The

magnitudes of the pressures ranged from 0.015psi to 0.6 psi, which led to peak transverse deflections (direction normal to the skin panel) from 0.1 skin panel thicknesses to 2.5 thicknesses. A reduced order basis formed from 51 linear modes, 13 dual modes, and 18 tangent dual modes was built to represent the displacements.

The appropriateness of a basis to model the response can be assessed by the representation error

$$\varepsilon_{rep} = \frac{\left\| \underline{u} - \underline{u}_{proj} \right\|}{\left\| \underline{u} \right\|} \qquad (4.1)$$

where $\underline{u}$ is the static displacement field computed by the finite element code and $\underline{u}_{proj}$ is its projection on the selected basis. The representation error ε_{rep} was plotted as a function of the number of retained linear modes and the modes at which noticeable drops in this error occurred were recorded. This process led to the identification of a set of 51 linear modes, with natural frequencies ranging from 68Hz to 900Hz. The resulting transverse displacement (T3 or z component) representation errors, for the 2.5 thickness level case, were equal to 0.44% for the skin panel and 0.6% for the frame-longeron substructure. Furthermore, the representation errors for the in-plane component along the length of the skin panel (T1 or x component) were equal to 61% for the skin panel and 2% for the frame-longeron substructure. The errors for the component along the width (T2 or y component), which is the dominant "in-plane" component, were equal to 104% for the skin panel and 10% for the frame-longeron substructure, see Table 4.2 for the skin panel values.

The large errors for the in-plane components are fully expected and result from the membrane stretching that occurs when the behavior of the panel is in the nonlinear regime, and which the linear basis cannot capture. A comparison of these representation errors for the skin panel and the frame-longeron substructure suggests that the

31

nonlinearity is dominant in the skin panel with the frame-longeron substructure behaving approximately linearly.

The 10 linear modes with the largest modal components, i.e. modes 1, 5, 7, 9, 13, 15, 16, 25, 28 and 46, were used to construct the dual modes. Since the modal component of mode 1 is much larger than the other ones (by a factor of at least 10) for all static responses analyzed, it was considered as the only dominant mode in Eqs. (2.45) and (2.46). The POD-based dual mode construction procedure highlighted in Chapter 2 (see [12] for full details) was performed for the data obtained for mode 1 alone and each of the 9 combinations of mode 1 and another of the 10 largest responding modes. In each of these 10 situations, 12 different loading factors $\alpha_i^{(m)}$ were used, half positive and half negative, and leading to peak deflections ranging from 0.12 to approximately 0.6 skin panel thicknesses. The remainders of these 120 deflections, after projection on the 51 linear modes identified above, were analyzed by POD. The POD eigenvectors with largest eigenvalues and leading to a reduction of the representation error of the T2 component (i.e., the dominant in-plane component) were selected as dual modes. Thirteen dual modes were identified in this manner. The representation error of the resulting 64-mode model (51 linear modes and 13 dual modes), shown in Table 4.2, indicates a very sharp drop in the T2 direction confirming the appropriateness of the dual modes. Another perspective on the adequacy of the dual modes is provided by the 3-dimensional section of the *N*-dimensional space of displacements shown in Fig. 4.3, which focuses on the transverse displacements at the middle points of the center bay and of the corner and side bays (bays 1 and 2, see Fig. 4.2b) and the T2 displacement at these latter points obtained from a nonlinear static analysis. Clearly, the duals shown closely occupy the same space as the physical uniform loading, as seen in connection with the beam model, see Fig. 2.1.

Unlike the uniform pressure loading, the loadings used to obtain the 1-1 and 1-16 duals have dominant components on bays 2, 5, and 8. For this reason, the "1-1 Dual" and the "1-16 Dual" curves are much closer to the "Static Uniform Pressure" curve in bay 2 than in bay 1. On the other hand, the 1-13 dual loading has a dominant component on bay 5 and its T2 component is dominant near the long edges of the skin panel.
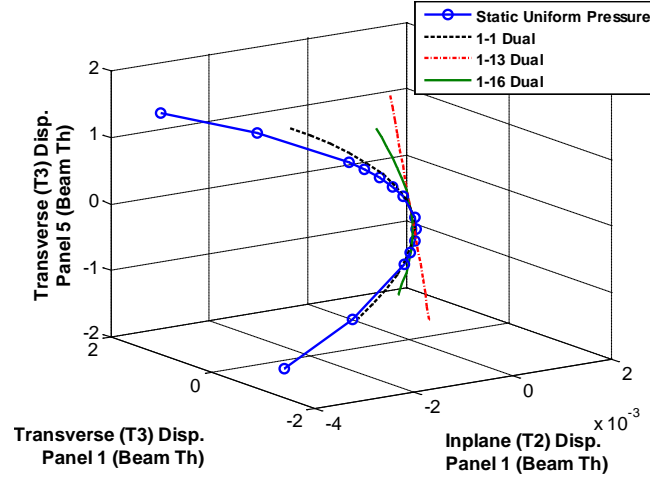
(a)
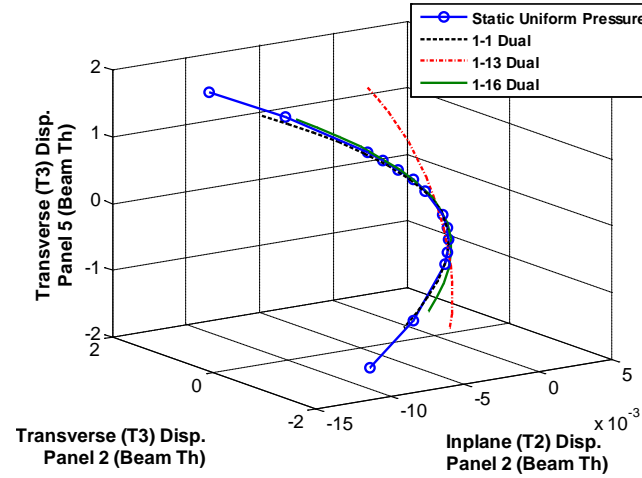
(b)

Figure 4.3. Displacements from NX/Nastran at two points of the 9-bay panel under various loadings, transverse displacements at the middle point of the center bay and transverse and in-plane (T2) displacement at the middle point of: a) bay 1 and b) bay 2.

The basis was then enriched with the tangent duals, obtained from a POD analysis of the eigenvectors of the tangent stiffness matrix computed at peak

displacement levels ranging from 0.003 to 0.015 skin panel thicknesses. It was found that more valuable information, for the representation of the displacement field, could be extracted from the tangent stiffness modes if they were obtained at smaller loading levels than the levels used to compute the dual modes. A possible explanation may be related to the way the nonlinear stiffening affects the various substructures. Indeed, the nonlinear stiffening is more significant in the skin panel than in the frame substructure, since the latter is cantilevered (see Fig. 4.2). Therefore, for large loading factors the motion of the frame in the tangent stiffness modes becomes dominant. However, the objective of the tangent duals is to improve the representation of the in-plane component of the skin panel.

Loadings proportional to combinations of the first mode and modes 5, 13, 15, and 16 were used and only the first mode, i.e. the one with largest "modal force", of each matrix was computed. This process led to 18 tangent dual modes being selected as contributing most to the T2 representation. The final in-plane representation errors for the 82-mode basis at the 2.5 thickness loading level are shown in Table 4.2 and indicate a further drop in the T2 direction as compared to the 64-mode model including only linear and dual modes.

4.3. Static Validation on the 9-Bay Panel

4.3.1. Uniform Loading

Having completed the reduced order model construction, it was desired to assess its predictive capability in comparison with NX/Nastran. To this end, a loading of 0.6 psi, leading to a 2.5 thicknesses maximum skin panel deflection, was considered and shown in Figs. 4.4-4.11 are contour plots of the different displacement components. Note the excellent matching, both qualitatively and quantitatively, between reduced order model and NX/Nastran results. The norm errors of the former in comparison to the latter were

34

1.2% for the transverse (T3) component, 3.3% for the in-plane T2 component, 36% for the other, smaller, in-plane component T1, and 4.3% for the in-plane magnitude (see also Table 4.2). Clearly, the matching of the dominant components, T3 and T2, is very good. On the other hand, the relative error of the T1 component is still rather large but it is clear from Figs. 4.6-4.11 that this component is much smaller than its T2 counterpart (as stated above). The summary of representation and prediction errors for the skin panel presented in Table 4.2 highlights the benefits of each set of basis functions: linear modes, dual modes, and tangent dual modes. Note as well that the final prediction error is only slightly larger than its prediction counterpart suggesting that the model has indeed reached a converged solution near the optimum projection point of the Nastran displacements on the basis.

The prediction errors for the frame substructure were equal to 1.3% for T3, 21% for T1, 2% for T2, and 19% for the magnitude of the in-plane displacements.

Table 4.2. Summary of Representation and Prediction Errors - Skin Panel.

	51-Mode Rep. Error	64-Mode Rep. Error	82-Mode Rep. Error	82-Mode Prediction Error
T3	0.44%	0.35%	0.3%	1.2%
In-Plane Mag.	90%	6.8%	3.4%	4.3%
T2	104%	6.4%	1.8%	3.3%
T1	61%	31%	31%	36%
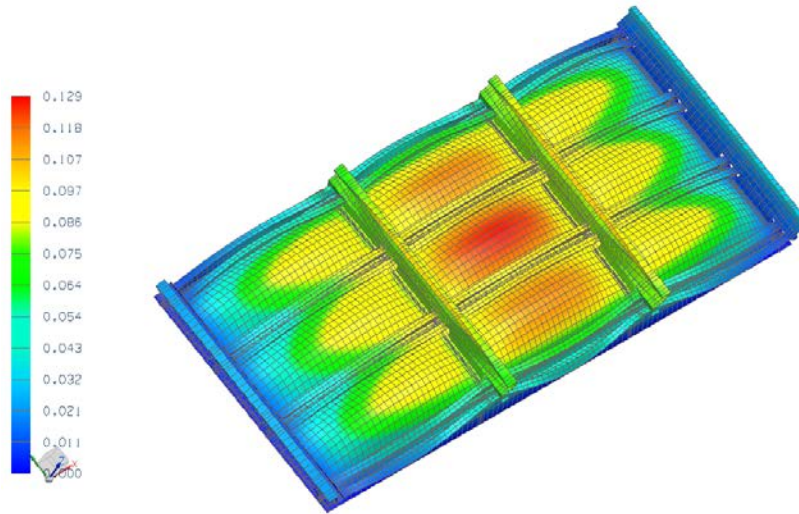
Figure 4.4. Translational displacement magnitude induced by a uniform pressure of 0.6 psi, NX/Nastran.
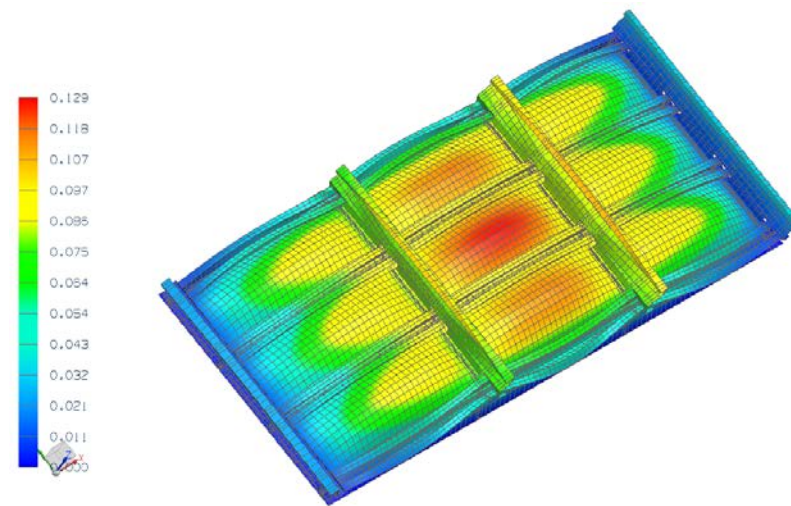
Figure 4.5. Translational displacement magnitude induced by a uniform pressure of 0.6 psi, 82-mode ROM.
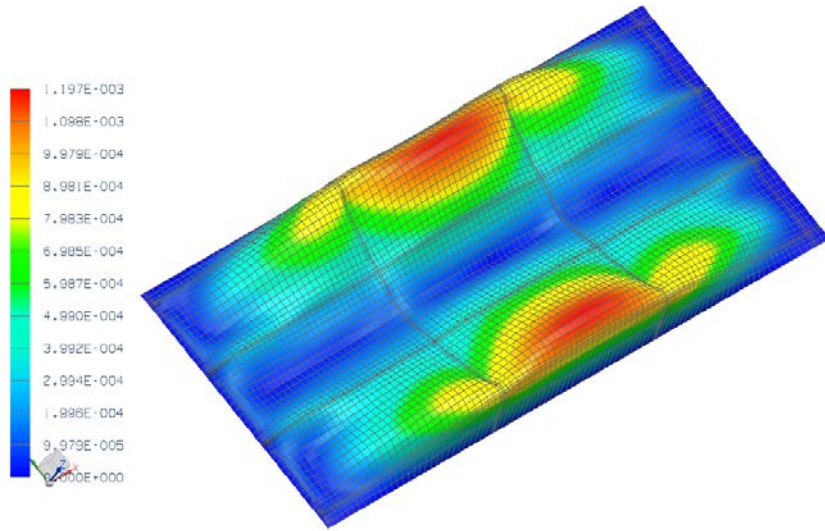
Figure 4.6. Magnitude of the in-plane displacement induced by a uniform pressure of 0.6 psi, skin panel only, NX/Nastran.
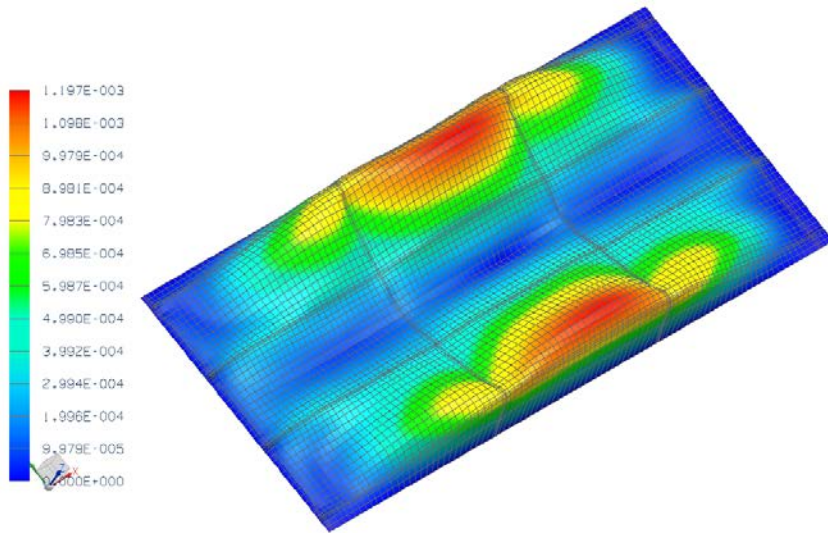
Figure 4.7. Magnitude of the in-plane displacement induced by a uniform pressure of 0.6 psi, skin panel only, 82-mode ROM.
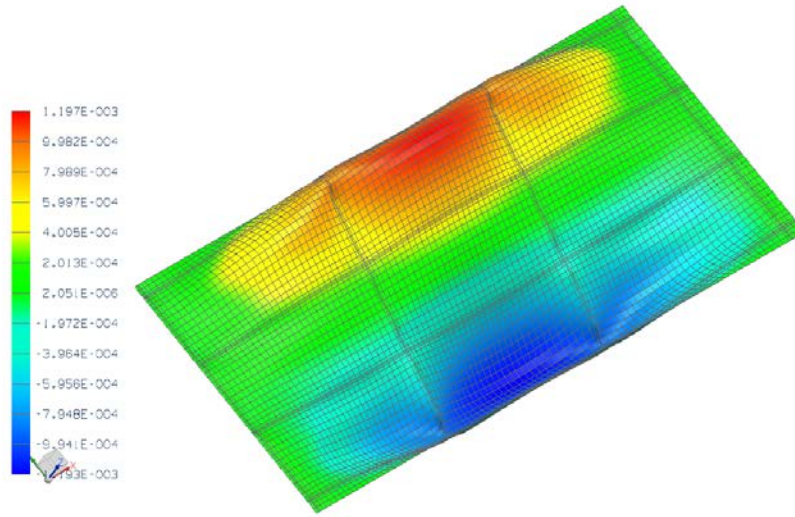
Figure 4.8. In-plane displacement along T2 induced by a uniform pressure of 0.6 psi, skin panel only, NX/Nastran.
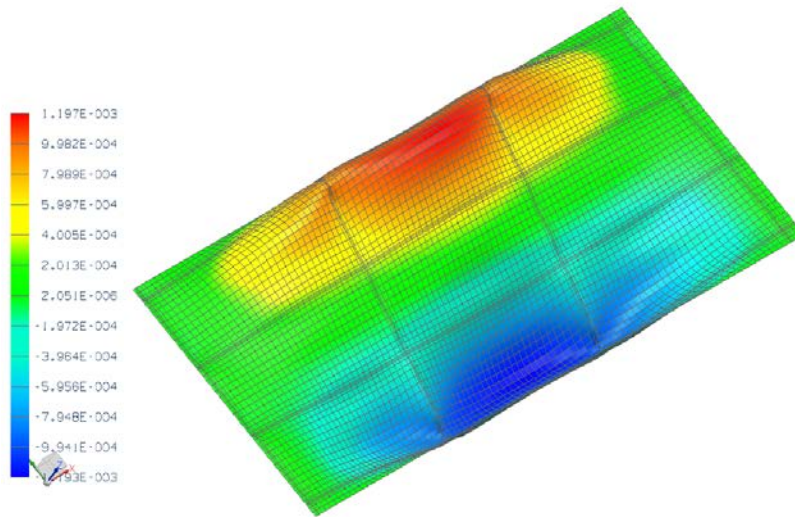
Figure 4.9. In-plane displacement along T2 induced by a uniform pressure of 0.6 psi, skin panel only, 82-mode ROM.
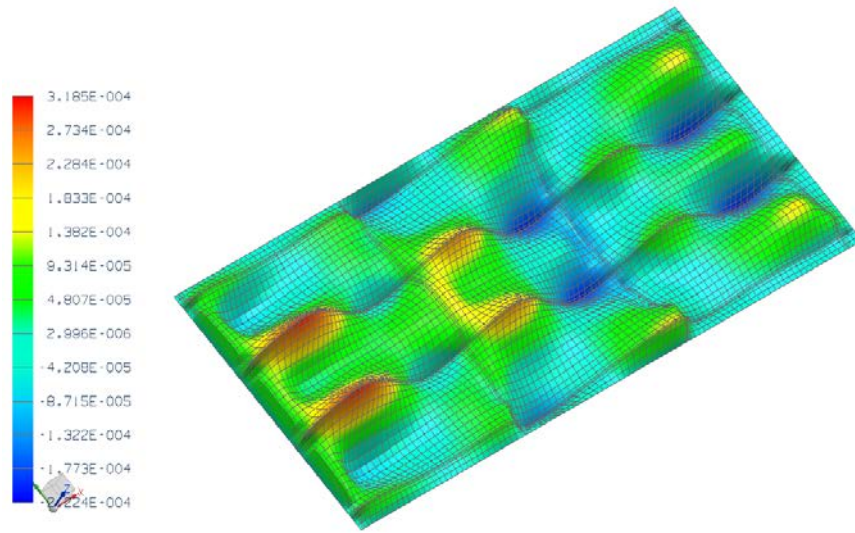
Figure 4.10. In-plane displacement along T1 induced by a uniform pressure of 0.6 psi, skin panel only, NX/Nastran.
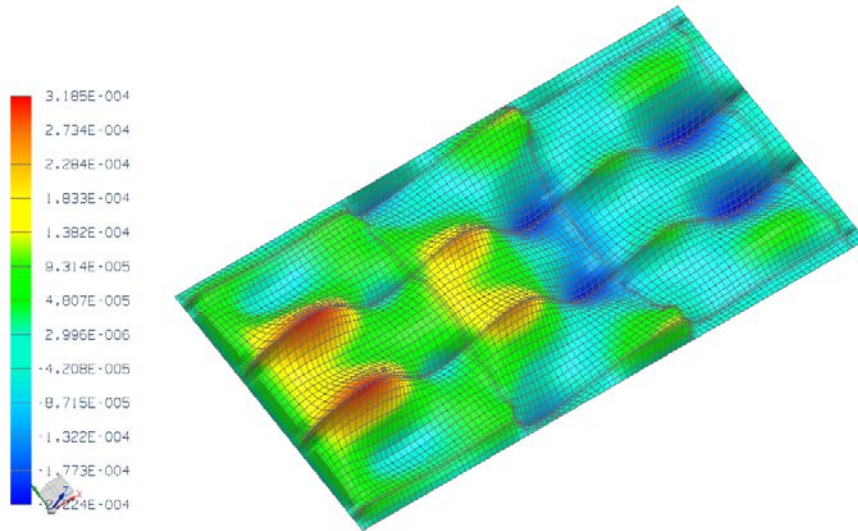
Figure 4.11. In-plane displacement along T1 induced by a uniform pressure of 0.6 psi, skin panel only, 82-mode ROM.

A peak displacement of 2.5 thicknesses is usually considered to be well within the nonlinear range for a clamped-clamped panel. To confirm this assessment, a linear NX/Nastran analysis was carried out for the same loading condition and shown in Figs. 4.12-4.15 are the resulting T3, T2, and T1 components of the skin panel displacements. Note the dramatic difference in the T2 displacements between linear and nonlinear

39

analyses (Figs. 4.8 and 4.14). Fewer differences in the shape of the T3 components are observed, but the peak magnitude is notably reduced in the nonlinear case, 2.5 thicknesses as compared to 5 thicknesses in the linear case, as expected.
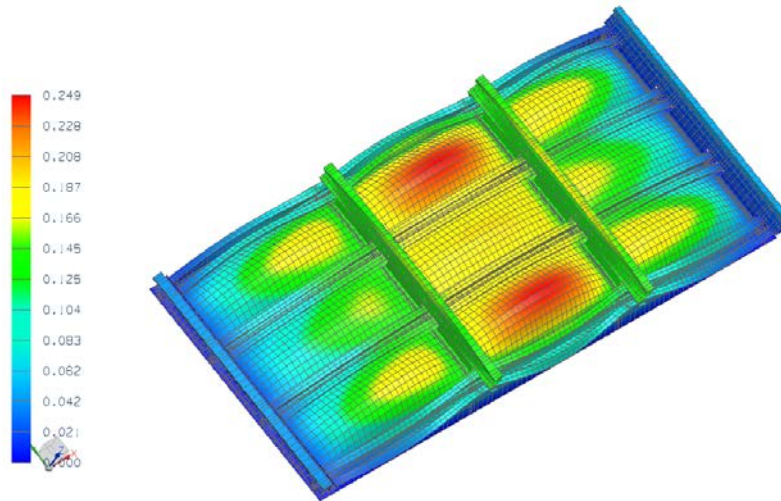
Figure 4.12. NX/Nastran linear response induced by a uniform pressure of 0.6 psi, translational displacement magnitude.
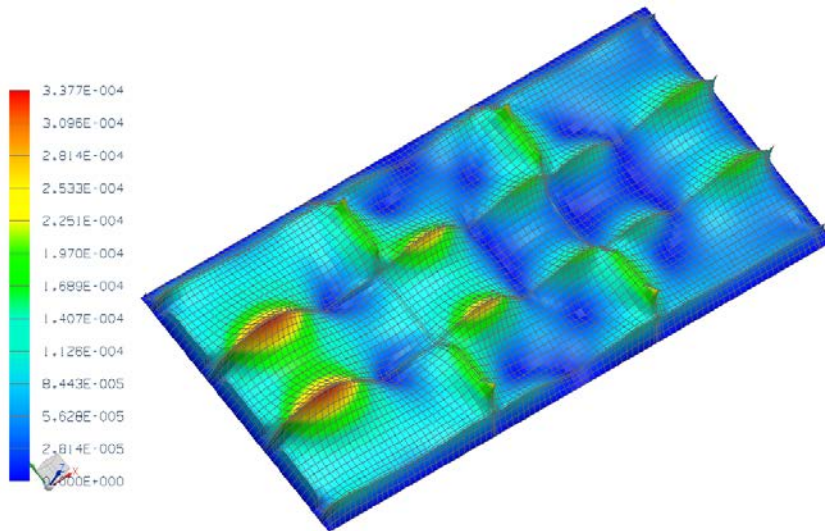
Figure 4.13. NX/Nastran linear response induced by a uniform pressure of 0.6 psi, in-plane component magnitude.
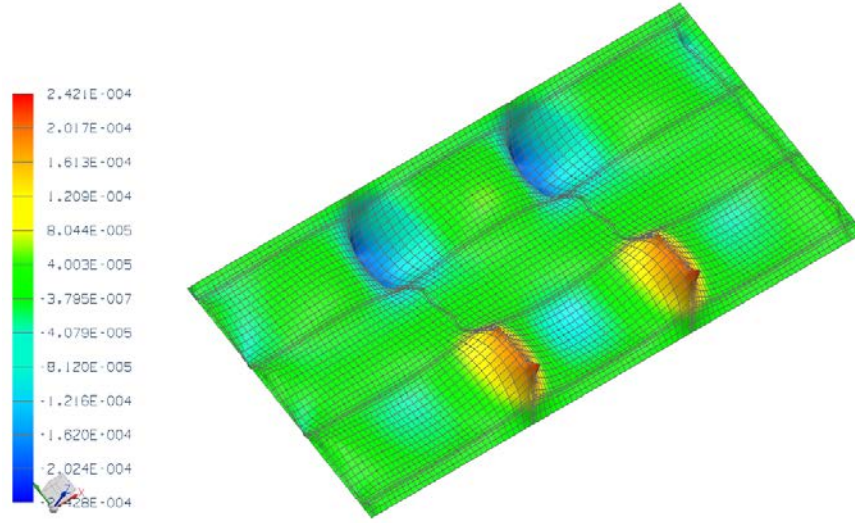
Figure 4.14. NX/Nastran linear response induced by a uniform pressure of 0.6 psi, in-plane component along T2.
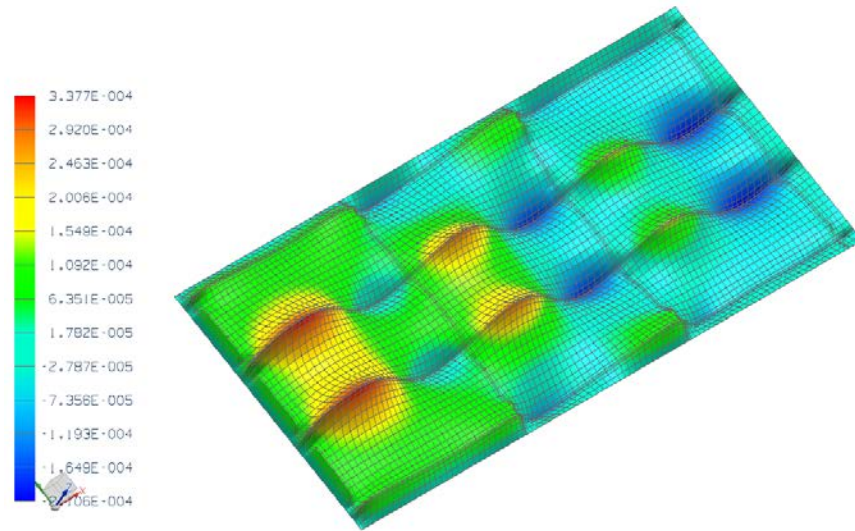
Figure 4.15. NX/Nastran linear response induced by a uniform pressure of 0.6 psi, in-plane component along T1.

4.3.2. Non-Uniform Loading

The modes of the 82-mode ROM were selected to reduce the representation errors from a series of uniform loading cases. In this light, it was desired to assess this model in a non-uniform loading case. To this end, the nonlinear static response due to a non-uniform pressure on the skin panel, varying as a function of x and uniform with

41

respect to *y*, was computed. Shown in Fig. 4.16 is the spatial variation of the loading with respect to *x*. This loading led to a peak transverse displacement of 2.5 skin panel thicknesses.
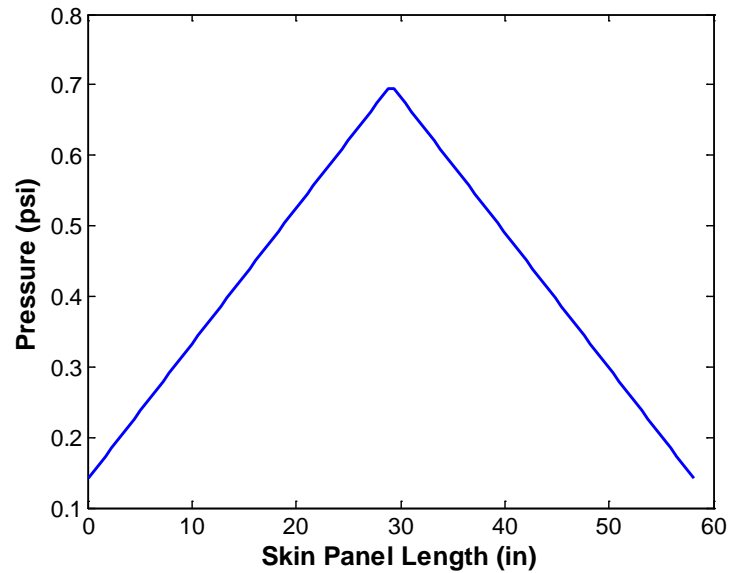
Figure 4.16. Non-uniform pressure variation along the skin panel.

Shown in Table 4.3 are the prediction errors for the skin panel transverse and in-plane degrees-of-freedom, the matching with NX/Nastran is excellent. The prediction errors for the frame substructure were equal to 1% for T3, 17% for T1, 2.6% for T2, and 15% for the magnitude of the in-plane displacements. Shown in Figs. 4.17-4.24 are contour plots of the different displacement components.

Table 4.3. Summary of Prediction Errors - Skin Panel.

	82-Mode Prediction Error
T3	0.9%
In-Plane Mag.	2.5%
T2	2.5%
T1	7%

42
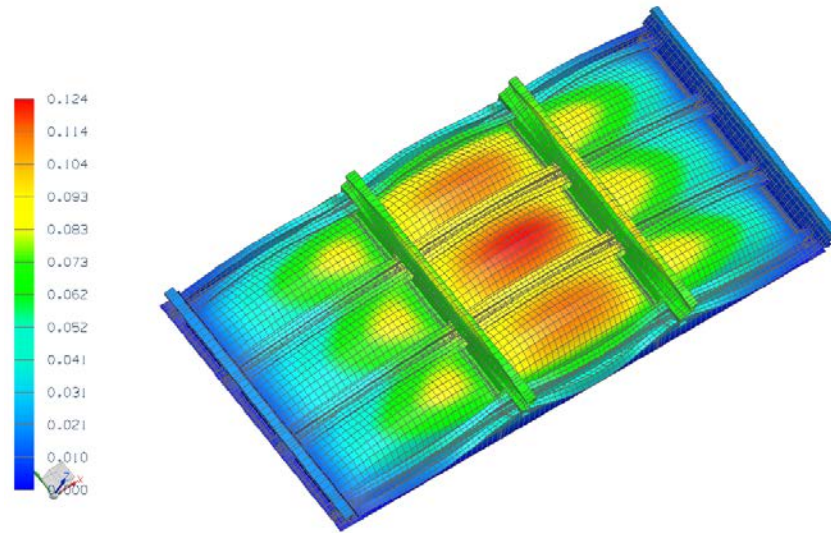
Figure 4.17. Translational displacement magnitude induced by a non-uniform, NX/Nastran.
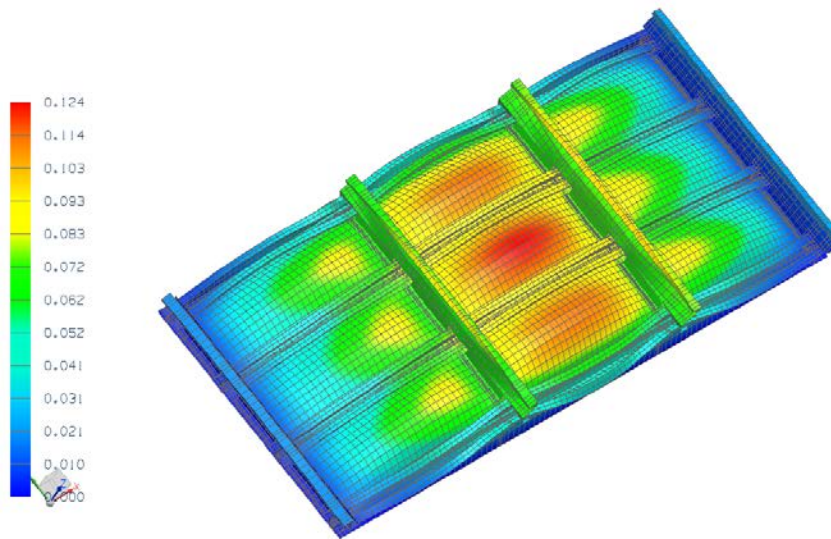
Figure 4.18. Translational displacement magnitude induced by a non-uniform, 82-mode ROM.
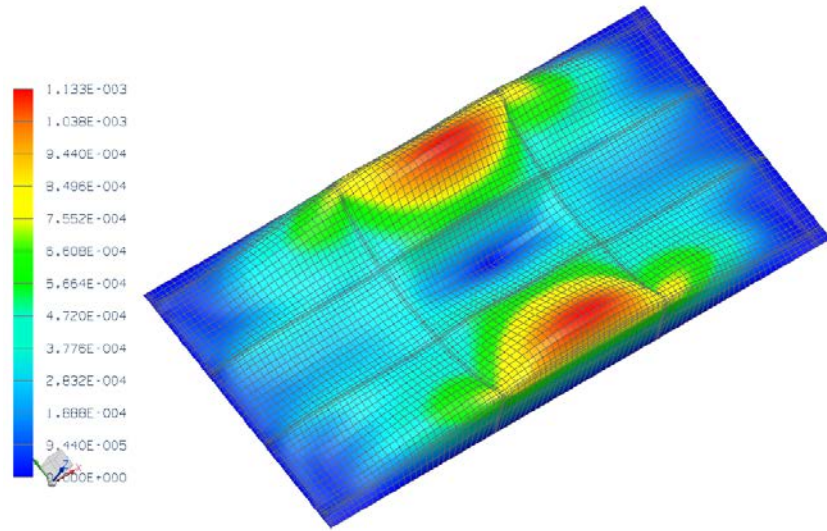
Figure 4.19. Magnitude of the in-plane displacement induced by a non-uniform, skin panel only, NX/Nastran.
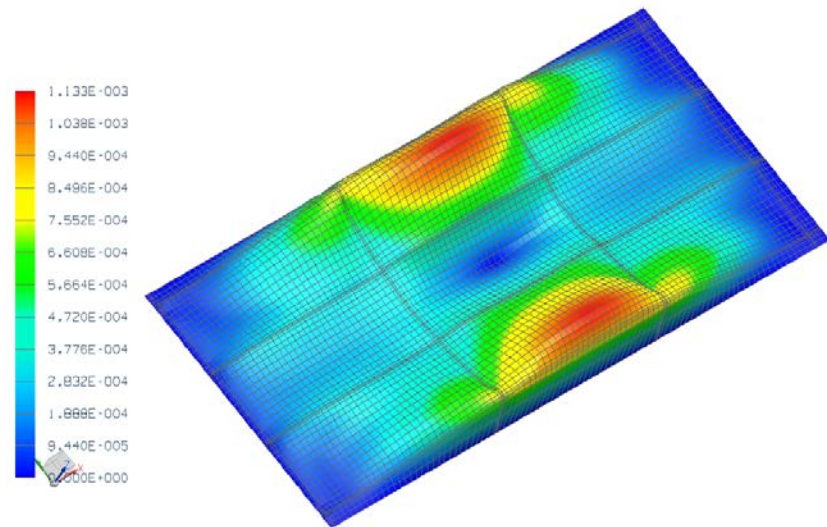
Figure 4.20. Magnitude of the in-plane displacement induced by a non-uniform, skin panel only, 82-mode ROM.
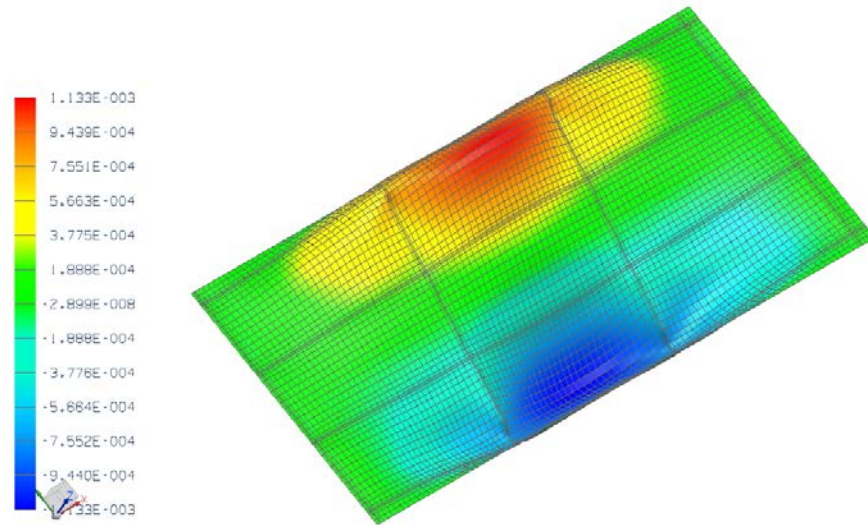
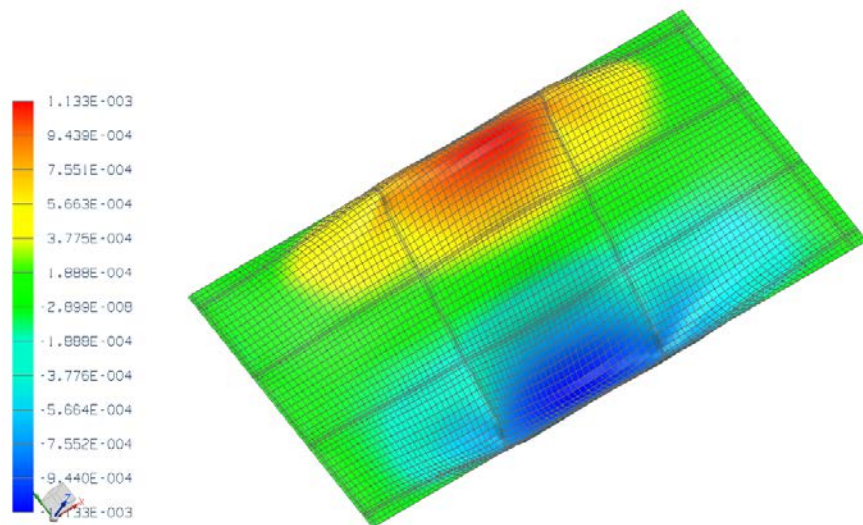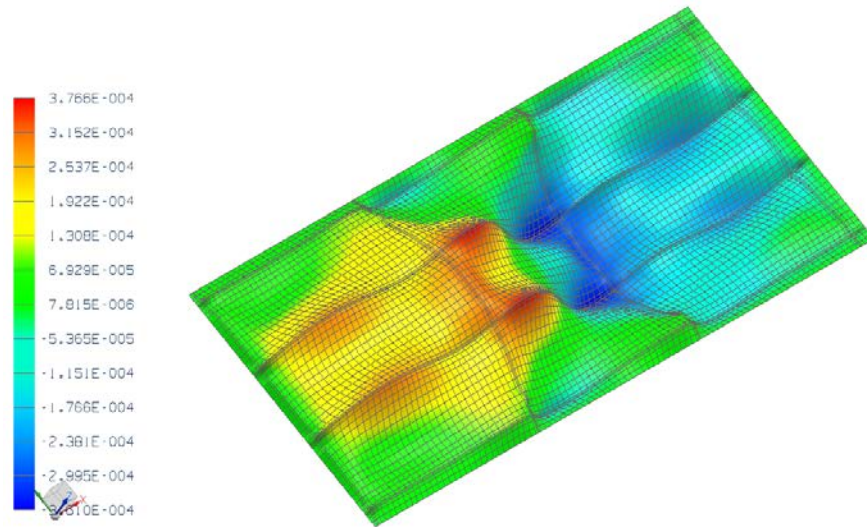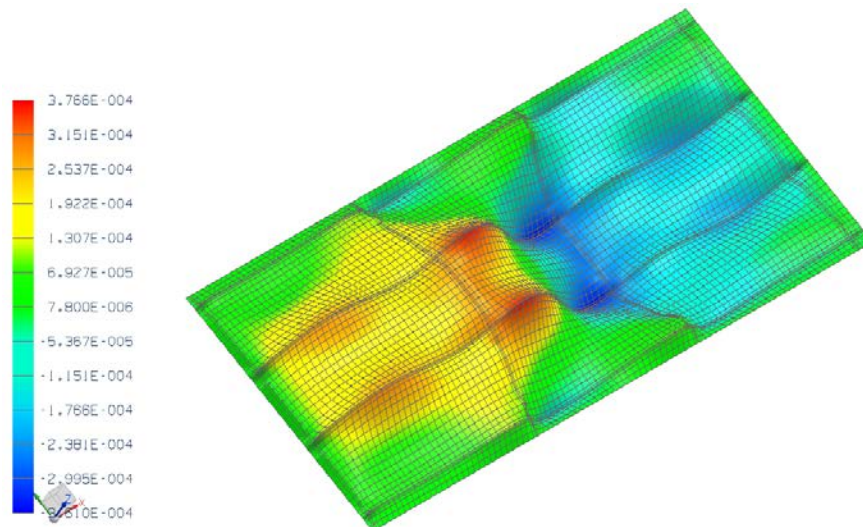Figure 4.21. In-plane displacement along T2 induced by a non-uniform, skin panel only, NX/Nastran.

Figure 4.22. In-plane displacement along T2 induced by a non-uniform, skin panel only, 82-mode ROM.

Figure 4.23. In-plane displacement along T1 induced by a non-uniform, skin panel only, NX/Nastran.

Figure 4.24. In-plane displacement along T1 induced by a non-uniform, skin panel only, 82-mode ROM.

4.4. Dynamic Validation on the 9-Bay Panel of Conventional ROM

The 9-bay panel was subjected to a uniform pressure on its top surface varying randomly in time as a white noise band-limited process in the frequency range [0,500]Hz to simulate an acoustic loading. The acoustic excitation consisted of overall sound pressure levels (*OASPL*) of 136dB and 146dB. Furthermore, to permit a close comparison between the full finite element and ROM results, a simple Rayleigh damping model was adopted, i.e. for which the damping matrix is $D = \alpha M + \beta K$ with α=7.55/s and β=5.6E-6s. This selection led to damping ratios between 0.65% and 1% for all transverse modes in the excitation band.

4.4.1 Linear Dynamic Results

The computational effort required to compute the full dynamic response of the 96,156 degree-of-freedom 9-bay panel was found to be too high with NX/Nastran SOL 109 (full transient analysis). For instance, the amount of scratch space needed to compute the response of a relatively short time history of 50,000 time steps was approximately equal to 320GB. The specifics of why so much scratch space is needed are not known to the author; however, a newer solver in NX/Nastran, SOL 601, was found to be more computationally expedient and it can be used to solve linear and nonlinear problems. This new solver is an integration of the ADINA solver into NX/Nastran, and consequently the elements use a different formulation than the conventional NX and MSC Nastran solution sequences, like SOL 109, and some differences in the natural frequencies were found. Since it was not possible to obtain a time history of the response large enough with SOL 109, a modal transient analysis was performed with the first 89 modes which have natural frequencies within the frequency band of excitation. A comparison between SOL 601 (in its linear mode) and the modal analysis, for an acoustic excitation of 106dB, is shown in Figs. 4.25-4.28 at selected points. These points correspond to the middle points of bays 1,

2 and 5, and point A (see Fig. 4.29) in the frame substructure. The middle point of bay 5 is where the maximum global T3 displacement occurs; the middle point of bay 2 is near the peak of the T2 component; near the middle point of bay 1 the nonlinear effects on the T1 component can be observed; and point A in the frame is important because it is where the T1 and T3 components are dominant in the frame-longeron substructure.

The large modal density in the frequency range considered in this analysis can be clearly seen by the large number of peaks in the power spectral density plots. The family of modes between 334Hz to 434Hz has very small modal amplitudes in the transverse direction at the middle points of bays 2 and 5, which explains the sharp drop in energy in that frequency band. Finally, the sharp drop in the energy at 500Hz is because the acoustic excitation has no energy to induce resonance of the modes with natural frequencies higher than 500Hz.
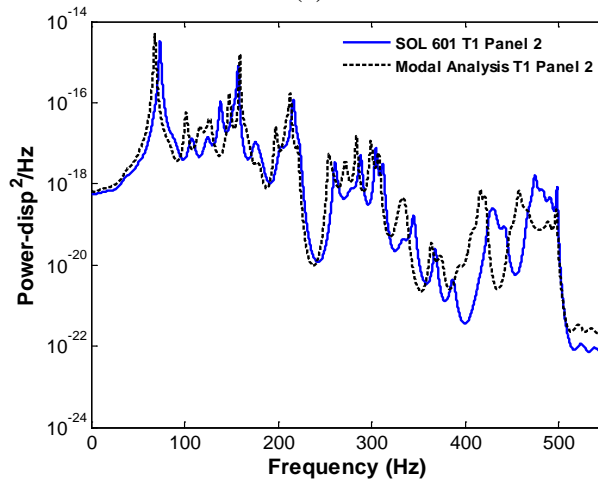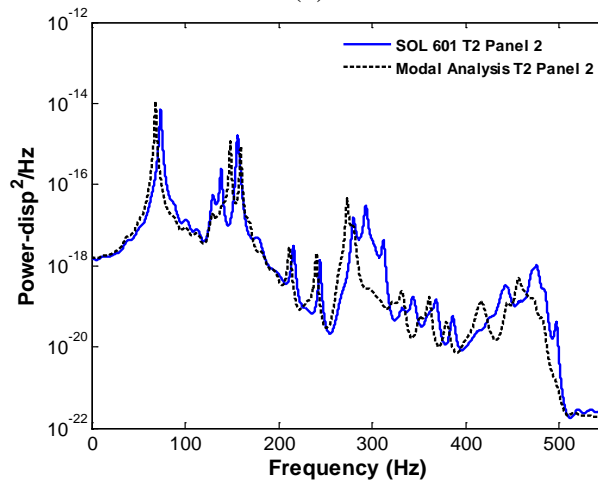
(a)

(b)
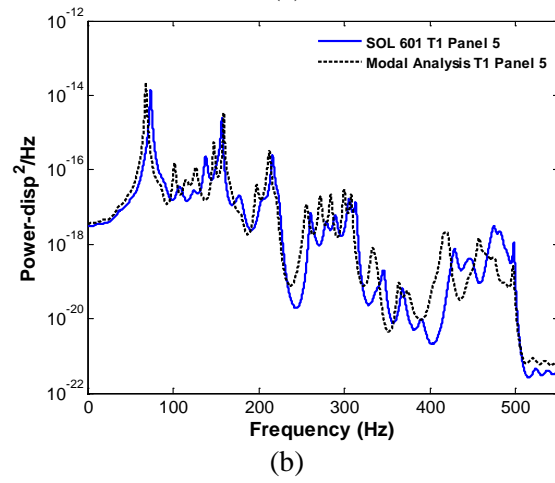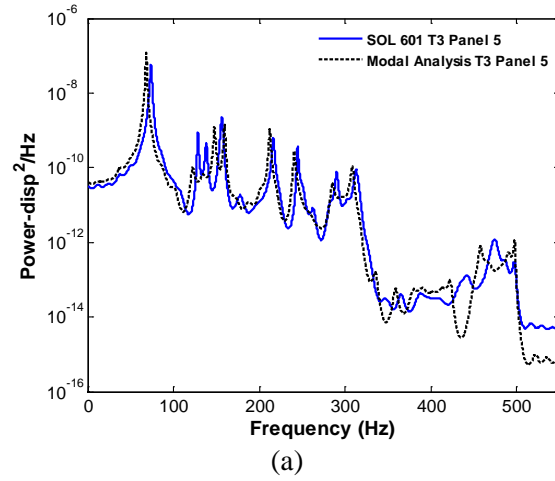
Figure 4.25. Power spectral density of the transverse (T3) and in-plane (T1) deflections at the middle point of bay 5. Full transient finite element analysis ("SOL 601") and transient modal analysis, *SPL* =106dB.
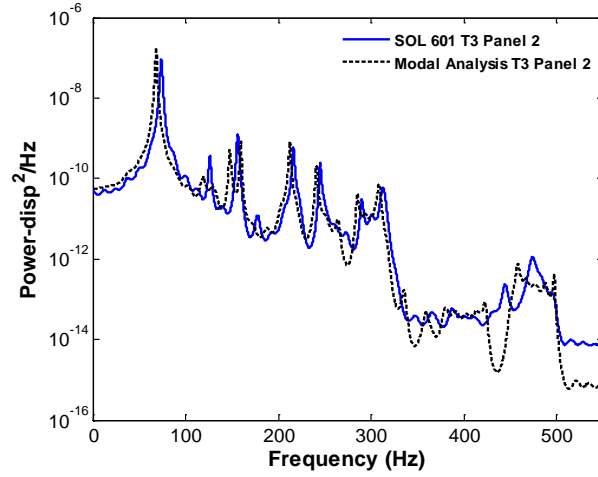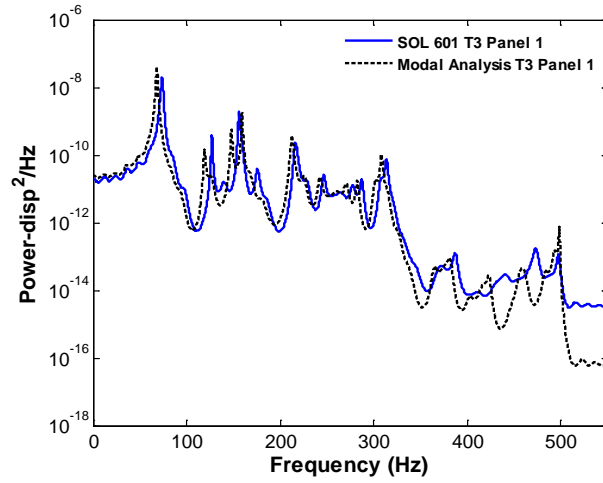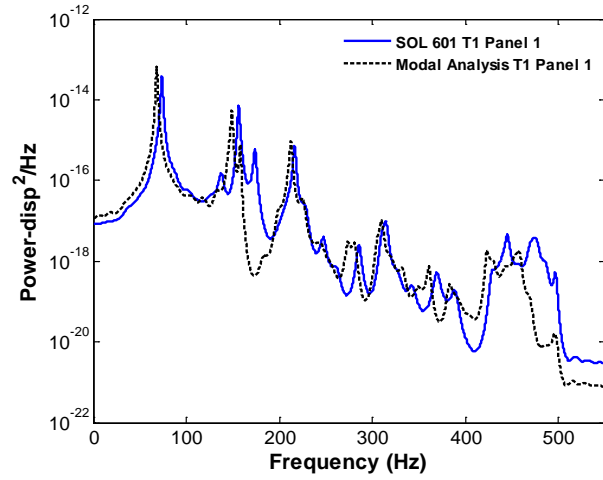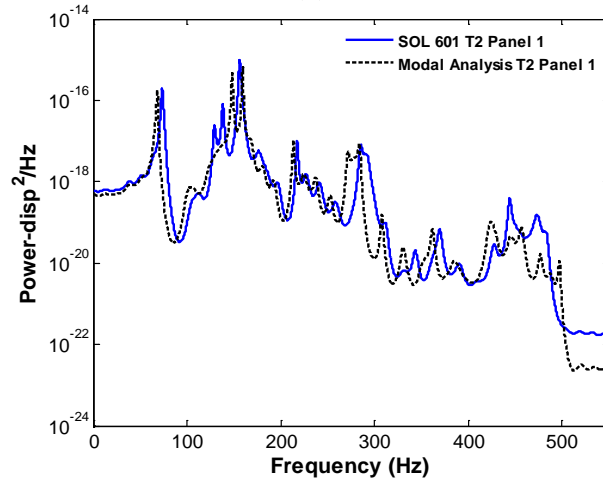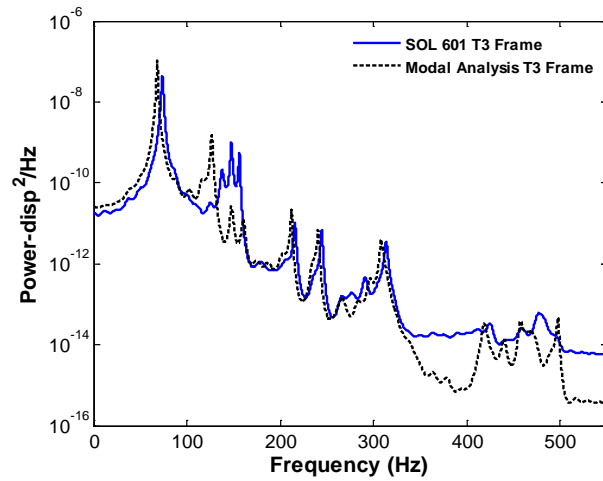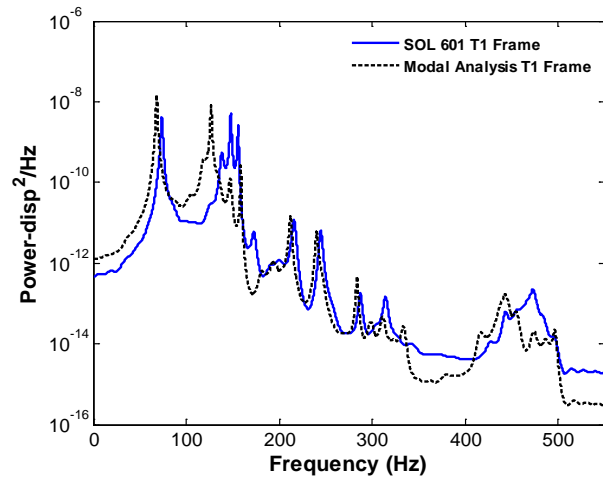
(a)

(b)

(c)

Figure 4.26. Power spectral density of the transverse (T3) and in-plane (T1 and T2) deflections at the middle point of bay 2. Full transient finite element analysis ("SOL 601") and transient modal analysis, *SPL* =106dB.

50

(a)

(b)

(c)

Figure 4.27. Power spectral density of the transverse (T3) and in-plane (T1 and T2) deflections at the middle point of bay 1. Full transient finite element analysis ("SOL 601") and transient modal analysis, *SPL* =106dB.

(a)

(b)

Figure 4.28. Power spectral density of the transverse (T3) and in-plane (T1 and T2) deflections at point A of the frame. Full transient finite element analysis ("SOL 601") and transient modal analysis, *SPL* =106dB.
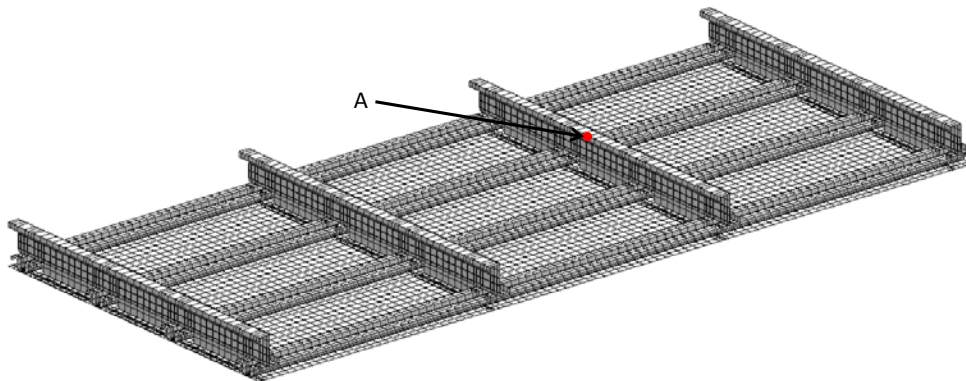

Figure 4.29. Location of selected frame node for output of results.

4.4.2. Nonlinear Dynamic Validation Results

Two excitation levels were used for the dynamic validation; the first one with a sound pressure level of 136dB, which led to a peak transverse displacement of approximately 1 skin panel thickness; and the second one with a sound pressure level of 146dB, which led to a peak transverse displacement of approximately 2.5 skin panel thicknesses. These two levels ranged from lowly to highly nonlinear.

The computational effort required to obtain the nonlinear dynamic response of the 96,156 degree-of-freedom 9-bay panel was found to be very large. Two different solvers were considered: MSC/Nastran SOL 400 and NX/Nastran SOL 601. The advantage of using SOL 400 is that it shares the same element formulation as SOL 106, which was used to identify the nonlinear stiffness coefficients of the reduced order model. Unfortunately, a very large amount of disk space was required to store the scratch data generated during the run (e.g., 700GB for 100,000 time steps), a successful SOL 400 simulation of a long time history was not possible given our current computational resources. Therefore, NX/Nastran SOL 601 was chosen. The wall time used for the solution of 250,000 time steps was approximately equal to 8 days using 6 processors.

A series of 200 "snapshots" were obtained from the stationary part of the NX/Nastran SOL601 dynamic simulation for the 136dB and 144dB excitation levels. The representation errors were computed and the mean representation error was used as a measure of the appropriateness of the basis. Shown in Table 4.3 are the mean representation errors, for both excitation levels, corresponding to the 82-mode basis identified in a previous section. Clearly, the errors are large, especially for the 144dB level. Therefore, the basis identification procedure described for the static validation was used with the "snapshots" of the dynamic problem. A reduced order basis was identified

from 48 linear modes and 21 dual modes. The mean representation errors for this basis are also shown in Table 4.4.

The first 9 dominant linear modes were 1, 13, 16, 25, 15, 7, 5, 28, and 46; where the modes were sorted from most to least dominant. The modal component of mode 1 was found to be larger than the other ones for most of the dynamic "snapshots" analyzed; therefore, it was considered as the only dominant mode in Eqs. (2.45) and (2.46). The 21 dual modes of the 69-mode basis were obtained from the 5 most dominant modes. The POD-based dual mode construction procedure highlighted above was performed for the data obtained for mode 1 alone and each of the n combinations of mode 1 and another of the n largest responding modes, where n is equal to 4. For each of these n situations, 12 different loading factors $\alpha_i^{(m)}$ were used, half positive and half negative, and leading to peak deflections ranging from 0.6 to approximately 1.3 skin panel thicknesses. The residuals of these $12 \times n$ deflections, after projection on the 48 linear modes identified above, were analyzed by POD. The POD eigenvectors with largest eigenvalues and leading to a reduction of the representation error of the T2 component (i.e., the dominant in-plane component) were selected as dual modes. Shown in Table 4.4 are the mean representation errors for the 69-mode model. Clearly, the representation of the response corresponding to both excitation levels is better than for the 82-mode model.

Table 4.4. Summary of Mean Representation Errors - Skin Panel

|	69-Mode (136dB)	82-Mode (136dB)	69-Mode (144dB)	82-Mode (144dB)
T3	0.2%	0.2%	0.5%	0.7%
In-Plane Mag.	3.3%	16.8%	14.6%	37.3%
T2	3.7%	23.4%	19.7%	55.7%
T1	6.6%	26.2%	22.6%	61.1%

Next, it was desired to assess the predictive capabilities of the reduced order models in comparison with the dynamic solution of SOL601 in NX/Nastran. Shown in Figs. 4.30 and 4.31 are plots of the power spectral density of the transverse (T3) and in-plane (T1 and T2) responses of the middle point of bays 1 and 2 (see Fig. 4.2(b) for panel numbering). The T2 component is very small at the middle point of bay 5 and point A (see Fig. 4.29) of the frame; therefore, only the power spectral density of the T3 and T1 components are shown in Figs. 4.32 and 4.33. Clearly, the matching of the T3 component is very good. Furthermore, the dominant aspects of the in-plane response (i.e., the first peaks for which the energy of the response is larger) are also captured well. Most of the peaks of the power spectral plots are sharp, which indicates that the level of nonlinearity is not too large for this excitation level.

The power spectral densities of the transverse (T3) and in-plane (T1 and T2) responses of the middle points of bays 1 and 2 are shown in Figs. 4.34 and 4.35. The results for the T3 and T1 components of the middle point of bay 5 and point A of the frame are shown in Figs. 4.36 and 4.37. The matching of the first peak of the T3 component (dominant component) is excellent for all cases. Furthermore, the energy level of the rest of the peaks was well captured by the 69-mode model, except for the frame, where it can be seen that the ROM response is stiffer than the SOL 601 results. The matching of the T2 component at bays 1 and 2 is excellent for all frequencies. The correlation of the first peak of the T1 component is very good for all cases.
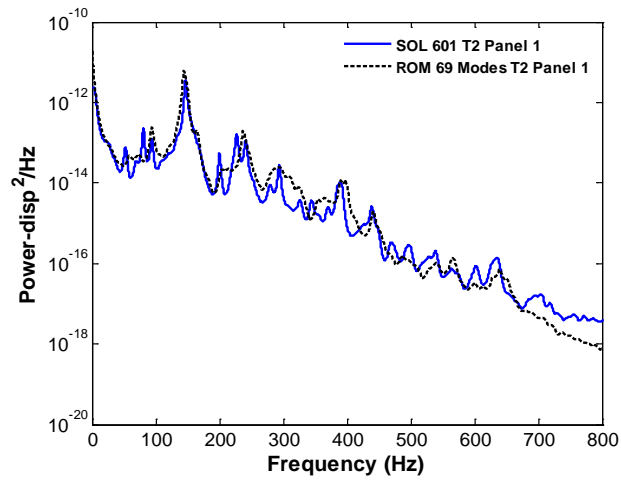
The wall time used for the solution of 250,000 time steps was approximately equal to 10 days using only 1 processor (please see Chapter 6 for a discussion on algorithmic improvements that permit the reduction of the computational time).
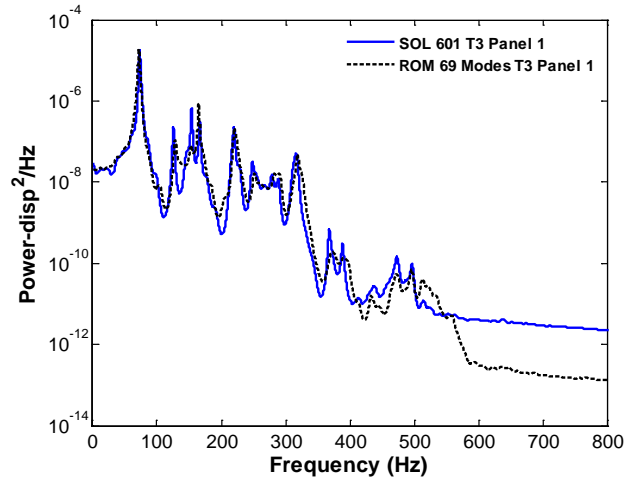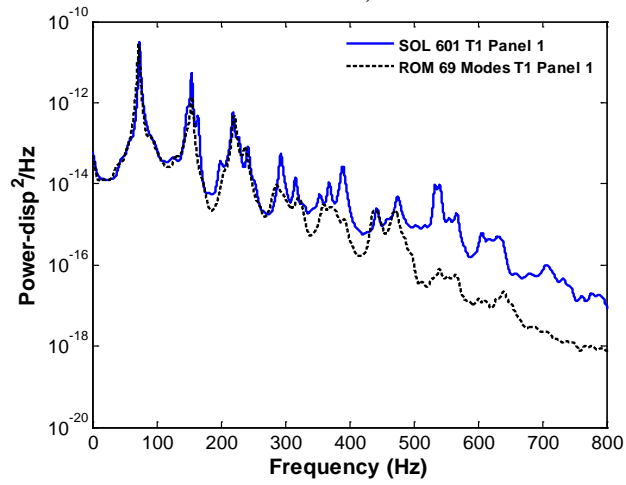
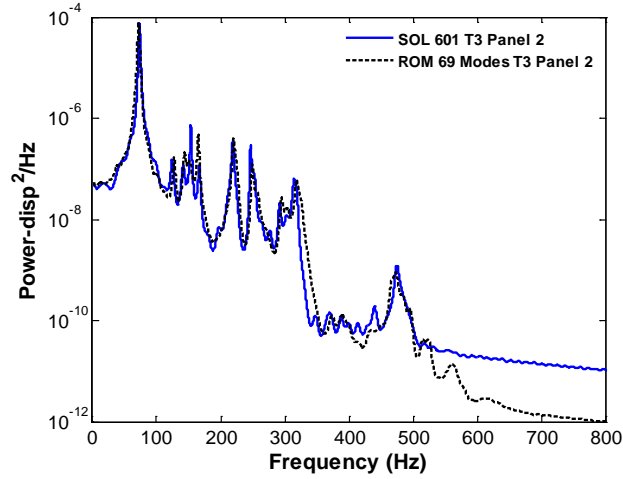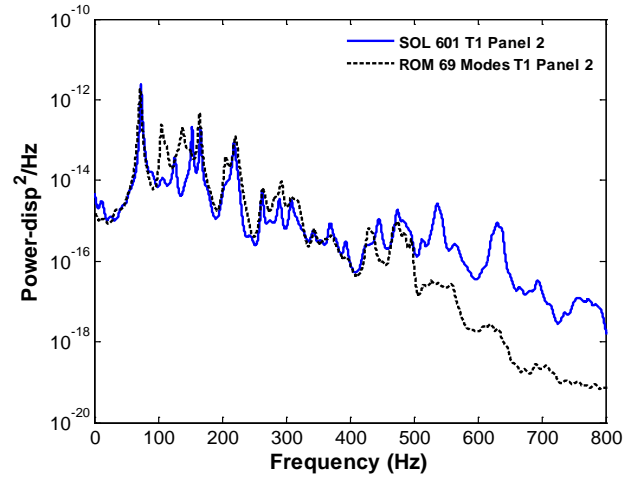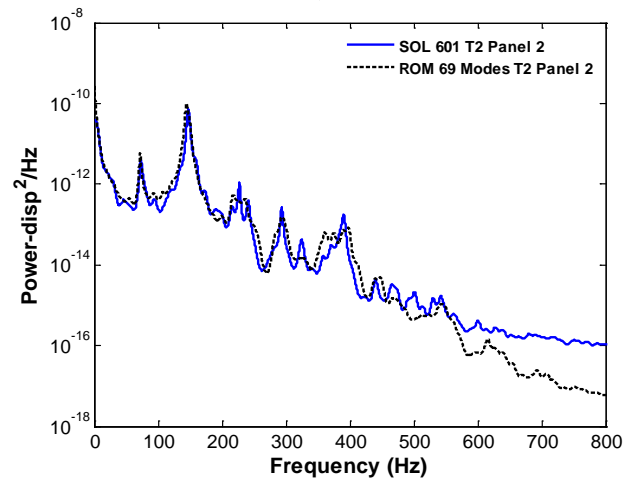Figure 4.30. Power spectral density of the transverse (T3) and in-plane (T1 and T2) deflections at the middle point of bay 1. Reduced order model and finite element ("SOL 601"), *SPL* =136dB.
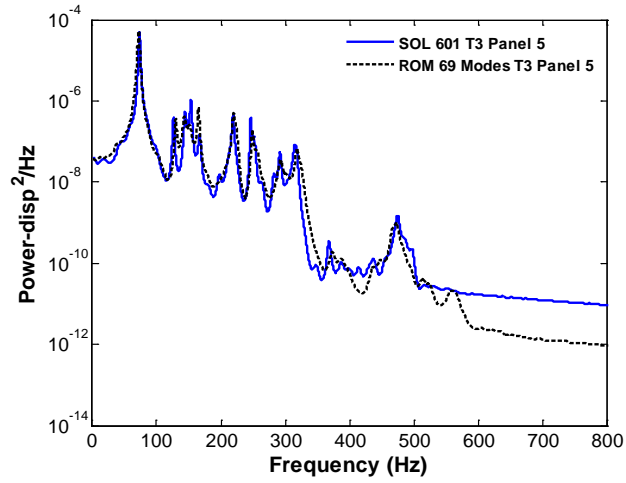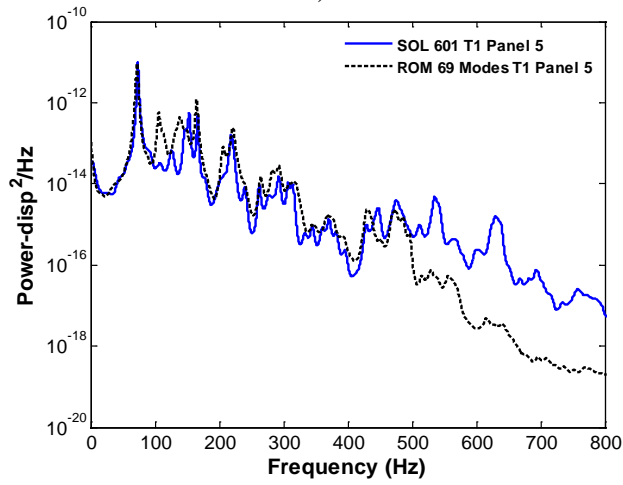
Figure 4.31. Power spectral density of the transverse (T3) and in-plane (T1 and T2) deflections at the middle point of bay 2. Reduced order model and finite element ("SOL 601"), *SPL* =136dB.
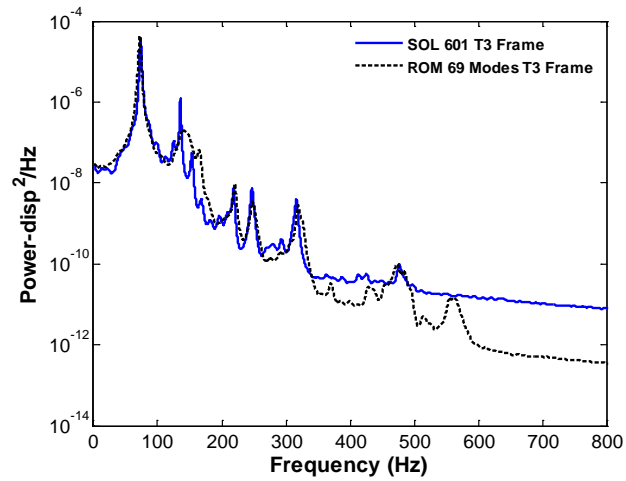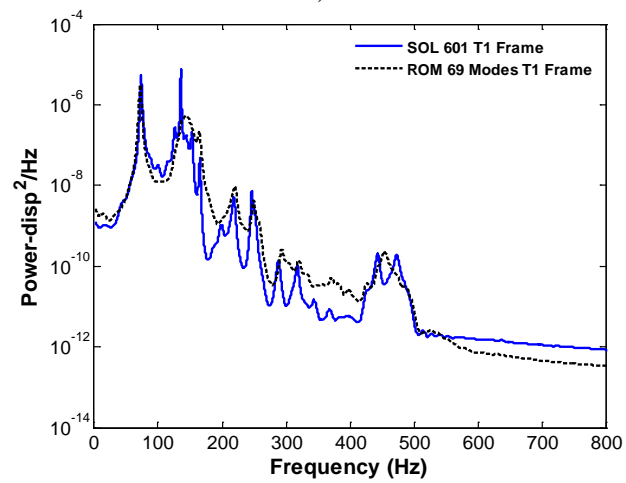
Figure 4.32. Power spectral density of the transverse (T3) and in-plane (T1) deflections at the middle point of bay 5. Reduced order model and finite element ("SOL 601"), *SPL* =136dB.
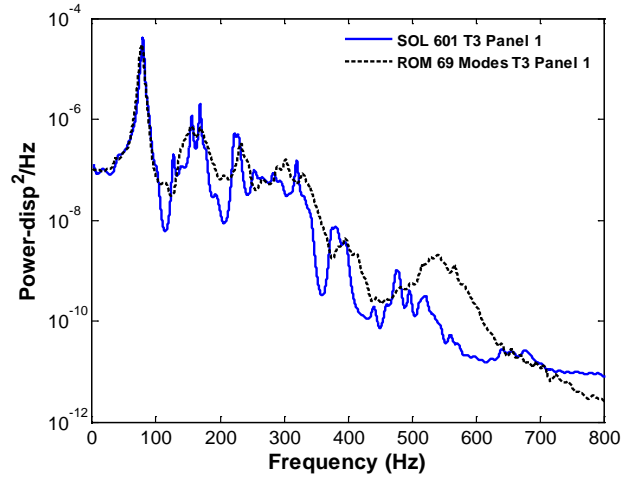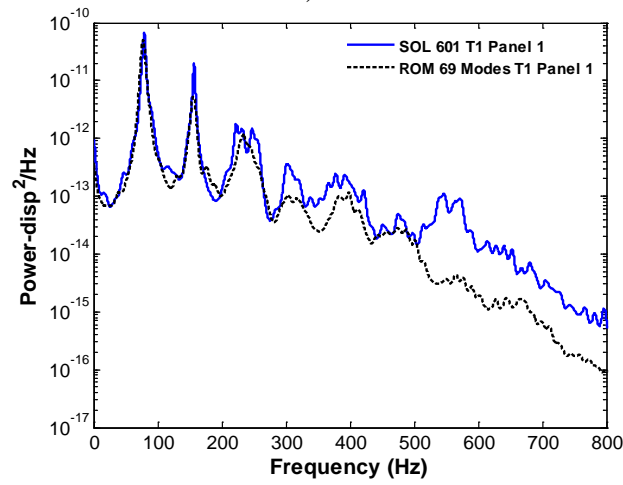
Figure 4.33. Power spectral density of the transverse (T3) and in-plane (T1) deflections at point A of the frame. Reduced order model and finite element ("SOL 601"), *SPL* =136dB.

Figure 4.34. Power spectral density of the transverse (T3) and in-plane (T1 and T2) deflections at the middle point of bay 1. Reduced order model and finite element ("SOL 601"), *SPL* =144dB.

Figure 4.35. Power spectral density of the transverse (T3) and in-plane (T1 and T2) deflections at the middle point of bay 2. Reduced order model and finite element ("SOL 601"), *SPL* =144dB.

a)

b)

Figure 4.36. Power spectral density of the transverse (T3) and in-plane (T1) deflections at the middle point of bay 5. Reduced order model and finite element ("SOL 601"), *SPL* =144dB.

a)

b)
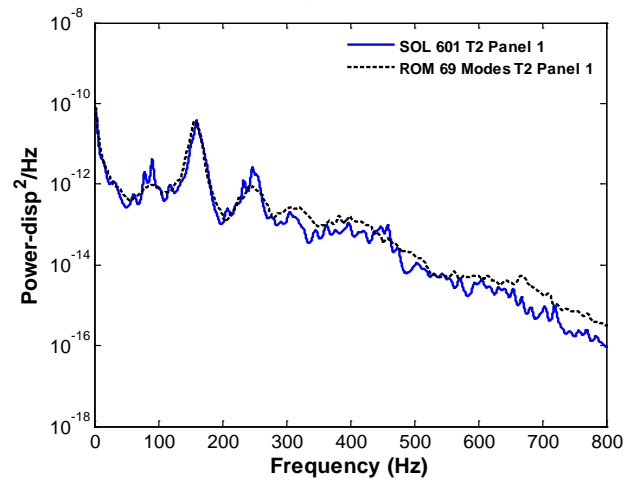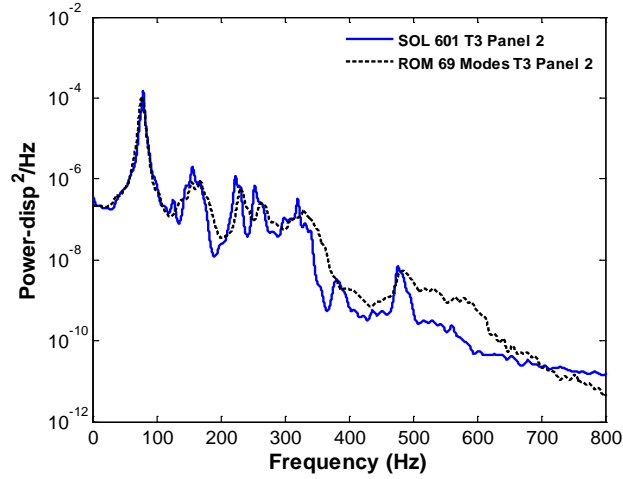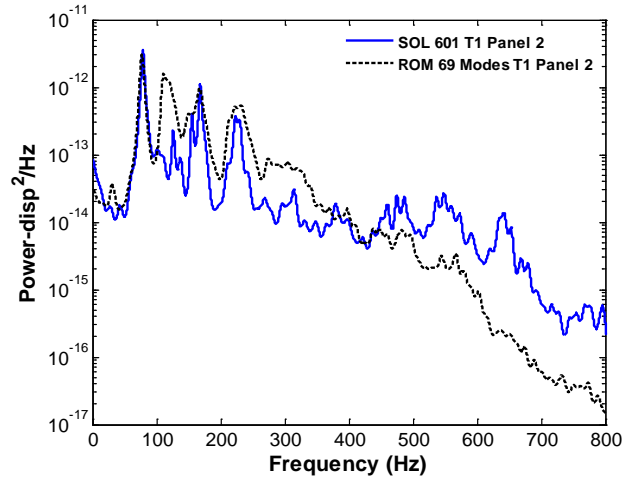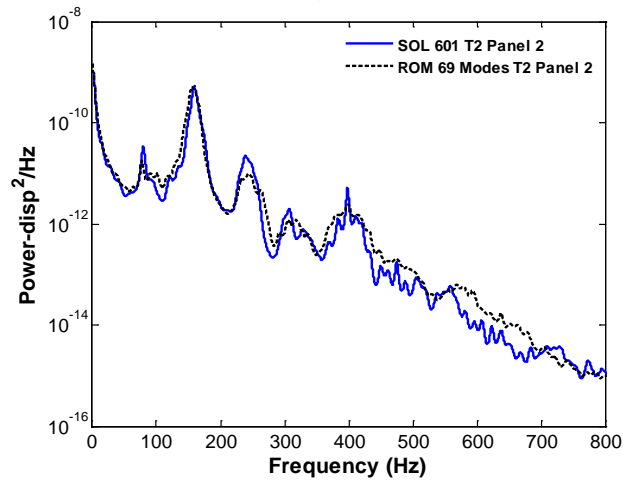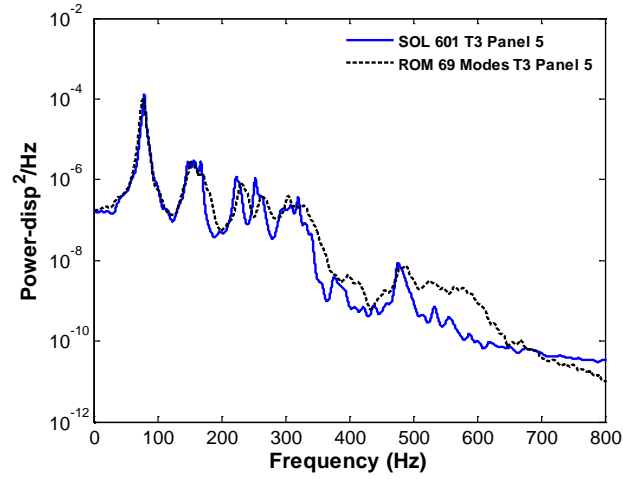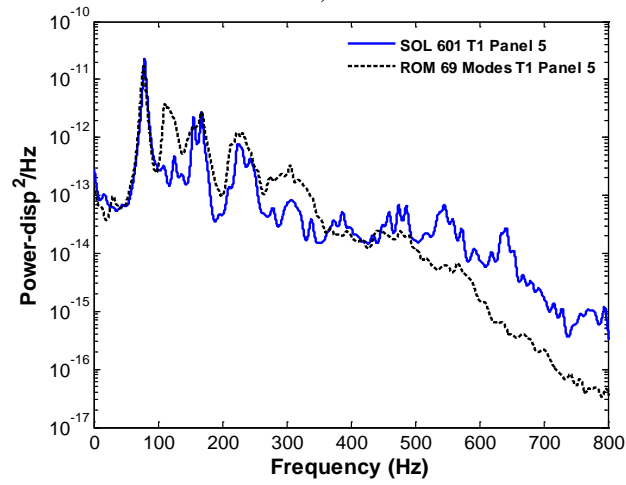
Figure 4.37. Power spectral density of the transverse (T3) and in-plane (T1) deflections at the frame. Reduced order model and finite element ("SOL 601"), *SPL* =144dB.

A first assessment of the 69-mode ROM prediction with its MSC/Nastran SOL 400 counterpart was done for the 144dB excitation level. Four shorter time histories (100,000 time steps vs. 250,000) were analyzed, the power spectral densities computed, and their mean compared with the SOL 601 and the 69-mode ROM results. The amount of scratch space generated during the analysis of 100,000 time steps was within our computational resources. Shown in Figs. 4.37-4.38 are power spectral density plots of the transverse and in-plane displacements at some of the most important locations. As noted in the linear case, there are differences between the SOL 601 and SOL 400 predictions,

63

although they are less significant in the nonlinear case. The 69-mode model still does a good qualitative job, although a better matching of the third and fourth peaks of the T3 components would be desired.

a)

b)
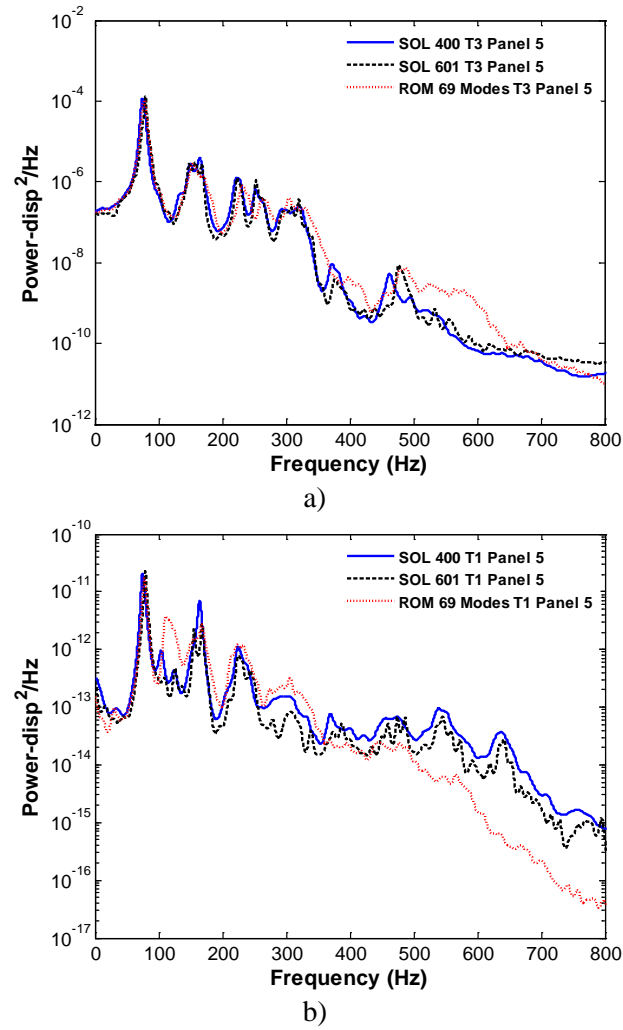
Figure 4.38. Power spectral density of the transverse (T3) and in-plane (T1) deflections at the middle point of bay 5. Reduced order model and finite element ("SOL 400" and "SOL 601"), *SPL* =144dB.
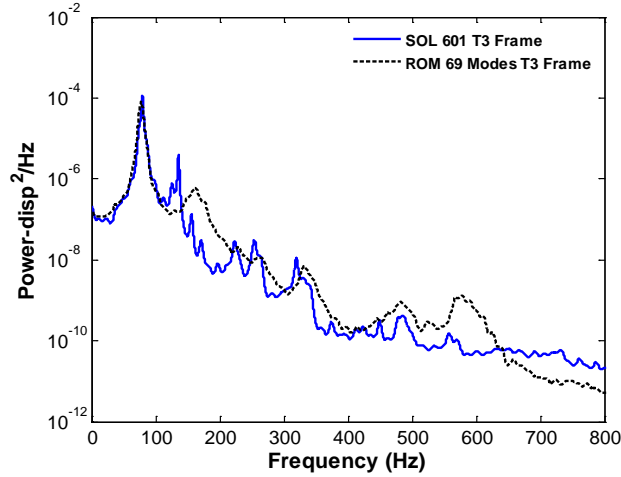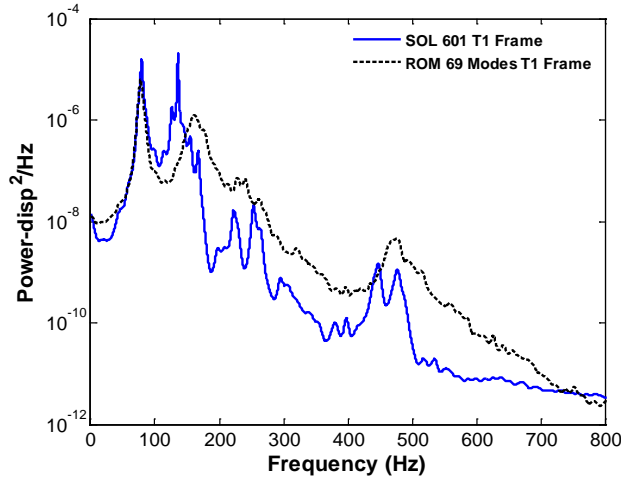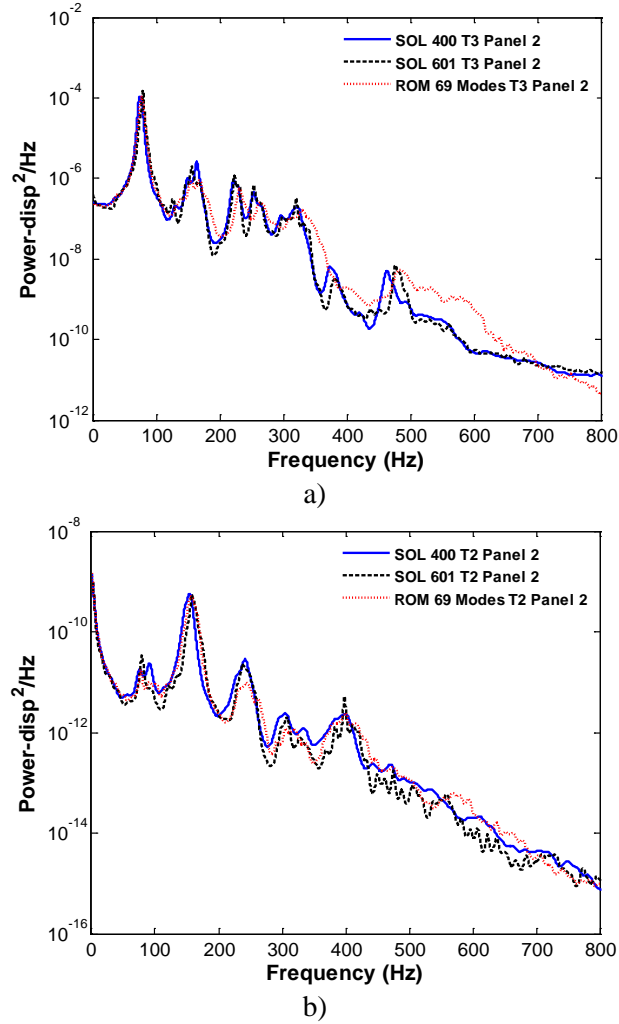
Figure 4.39. Power spectral density of the transverse (T3) and in-plane (T2) deflections at the middle point of bay 2. Reduced order model and finite element ("SOL 400" and "SOL 601"), *SPL* =144dB.

The dynamic excitation in the previous validation cases consisted of a white noise band-limited process used to simulate an acoustic excitation. Next, it was desired to assess the ROM methodology by assuming the 9-bay panel to be excited by a uniform deterministic pressure acting on the skin panel. The energy was assumed to be flat in the range [-500,500] Hz, see Fig. 4.40 for time history and Fig. 4.41 for its frequency content. A more detailed description of this type of excitation can be found in [34]. Shown in Fig. 4.42 is the time history of the transverse displacement of the middle point of the middle panel. In addition, shown in Fig. 4.43 is the Fourier transform of the SOL

65

400 and SOL 601 responses. The first peak of the SOL 601 response has a lower magnitude and it's located at a higher frequency than the first peak of the SOL 400 response. This indicates that the response from SOL 601 is stiffer. This, in fact, can be observed with the other peaks as well.

A comparison between SOL 400 and the 69-mode ROM is shown in Figs. 4.44-4.46. Clearly, the most dominant features of the response are well captured by the 69-mode model. The matching of the T2 component is very good for all frequencies; the correlation of the T1 and T3 components is good for frequencies within the frequency band of excitation.

The results presented for the static and dynamic validations show that the ROM methodology can be used for the approximation of the response of complex structures.
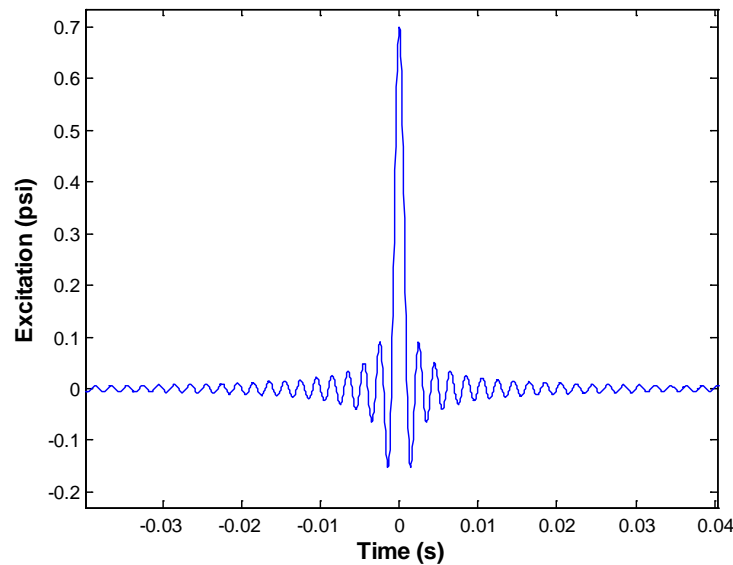
Figure 4.40. Time history of the loading.
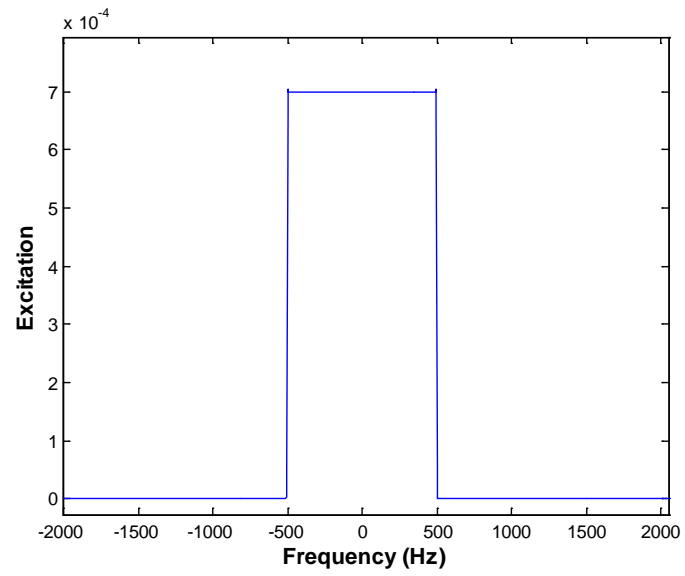
Figure 4.41. Frequency content of the loading.
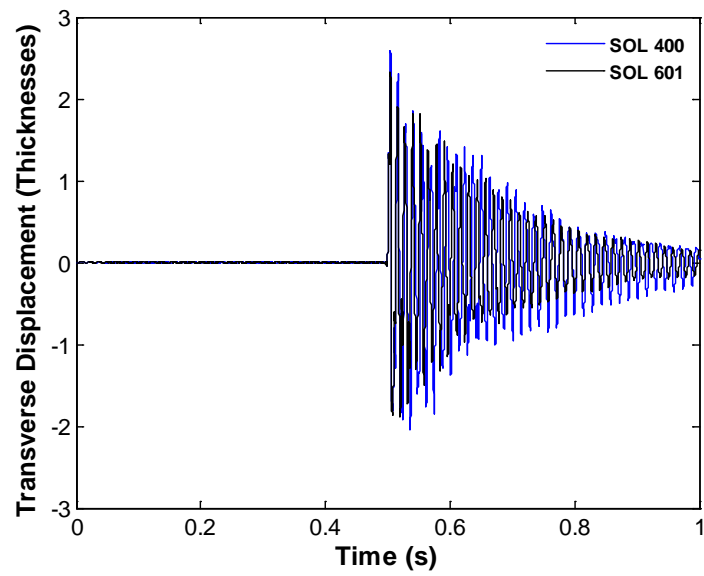
Figure 4.42. Transverse displacement of the middle point of the middle panel (full FEA results) as a function of time.
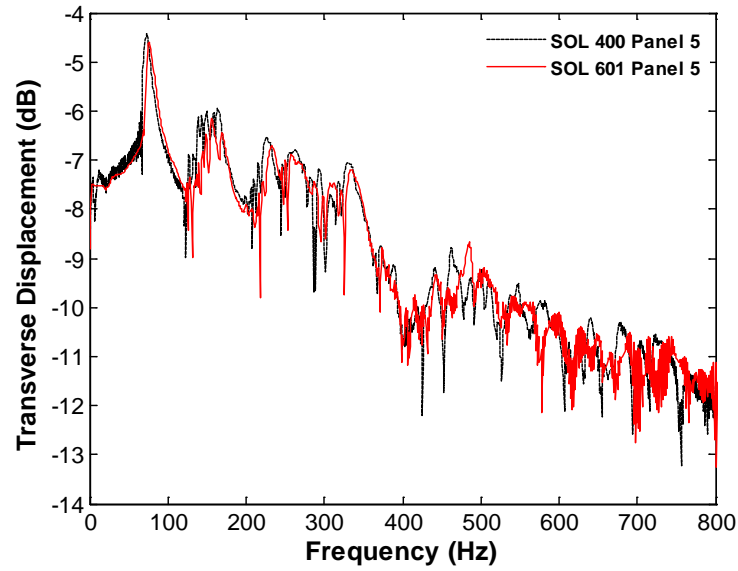
Figure 4.43. Transverse displacement of the middle point of bay 5 as a function of frequency, MSC/Nastran SOL 400 and NX/Nastran SOL601.

Figure 4.44. Transverse displacement of the middle point of bay 5 as a function of frequency, MSC/Nastran SOL 400 and ROM 69-mode model.
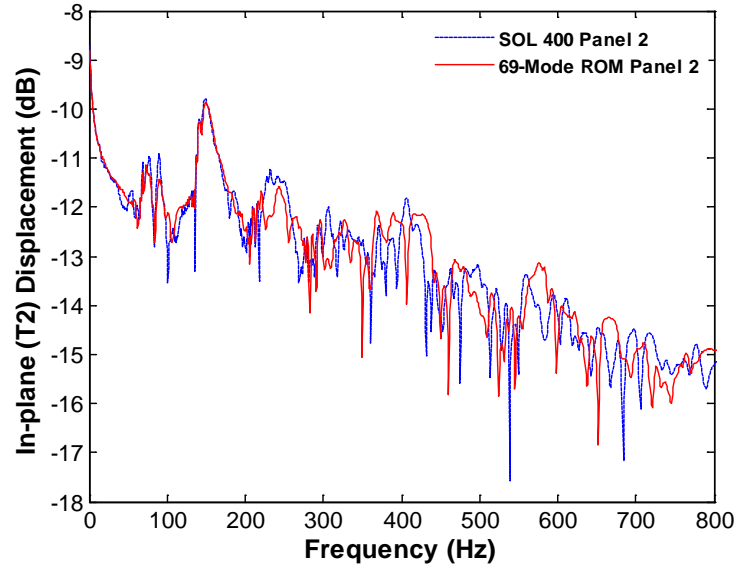
Figure 4.45. In-plane (T2) displacement of the middle point of bay 2 as a function of frequency, MSC/Nastran SOL 400 and ROM 69-mode model.
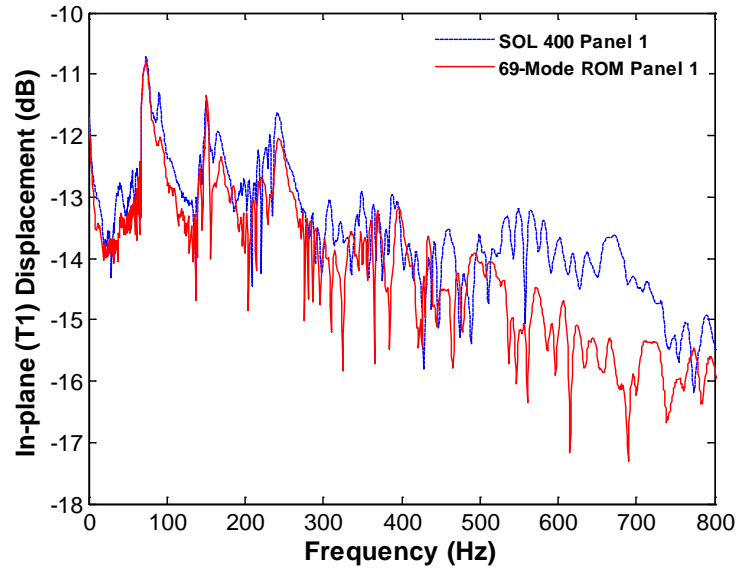
Figure 4.46. In-plane (T1) displacement of the middle point of bay 1 as a function of frequency, MSC/Nastran SOL 400 and ROM 69-mode model.

4.5. Multi-Scale Approach

The validation effort from previous sections showed that a monolithic ROM, i.e. one constructed from the entire structure, is capable of predicting the dominant features of the response of a complex multi-bay panel with a much smaller number of degrees-of-

freedom. Nonetheless, the 9-bay panel used in this validation effort is made of different substructures, which makes a multi-scale approach an attractive alternative to the monolithic ROM. In this case, the full model corresponds to the "macro-scale" and the response of a single bay lies in the "meso-scale".

In this light, a reduced order model could be built for each substructure at a time in a *Bottom-Up* approach, and then these reduced order models assembled in order to predict the response of the entire structure (see left half of Fig. 4.47). Or, the global response of the entire model could be approximated and the interface information of a particular substructure used to compute the response of that substructure in a *Top-Down* approach (see right half of Fig. 4.47).
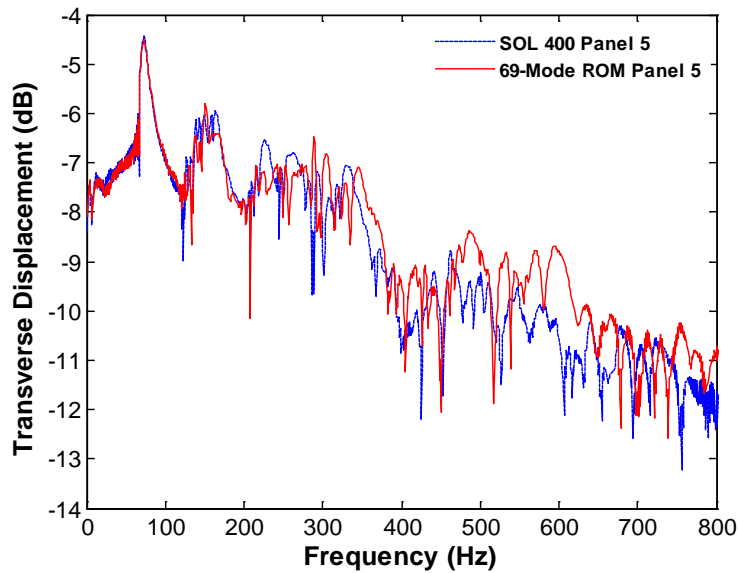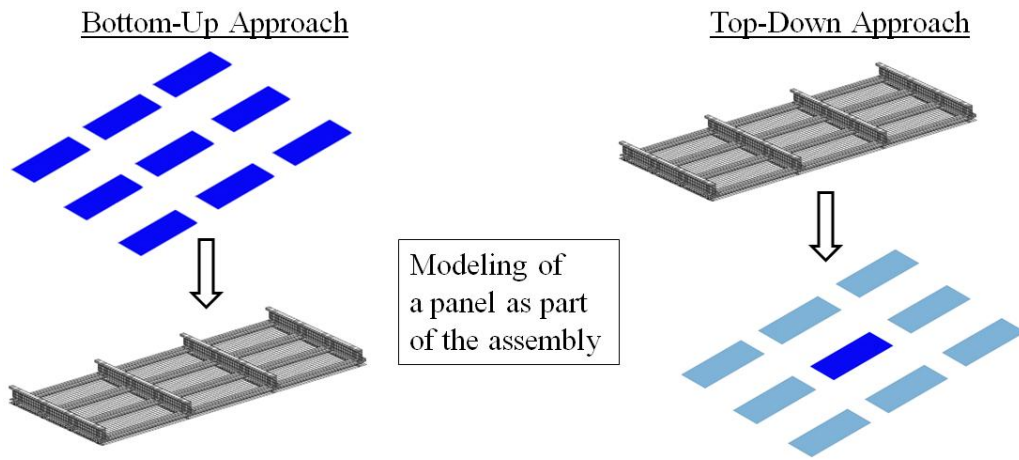

Figure 4.47. In-plane (T1) displacement of the middle point of bay 1 as a function of frequency, MSC/Nastran SOL 400 and ROM 69-mode model.

The modeling of a panel as part of the assembly is a key aspect in both approaches, and the successful development of reduced order models for single beams and panels during the last decade or so makes the proposed multi-scale approach very appealing. Another advantage of this approach is in a possible reduction of the computational cost, which could be achieved by building the reduced order model of one substructure at a time. Furthermore, a multi-scale approach may help in gaining a better

70

understanding of the complexities of the response induced by the interaction between substructures.

In the present work, a first assessment of a *Bottom-Up* approach, based on the Criag-Bampton Method, will be presented.

4.3.1. Background on CMS

The objective of Component Mode Synthesis methods in the analysis of dynamic structures is to reduce the complexity associated with large finite element models that arise from complex structures. In essence, these methods involve the division of the structure into substructures, the development of reduced order models of the substructures, and the coupling of the component reduced order models to form one for the entire system [32]. In general, the accuracy of the reduced order model is improved by using an increasing quantity of modes in each substructure.

The equation of motion of an undamped substructure *s* may be written as follows,

$$\underline{\underline{M}}^{(s)}\underline{\ddot{u}}^{(s)} + \underline{\underline{K}}^{(s)}\underline{u}^{(s)} = \underline{F}^{(s)}. \tag{4.2}$$

where $\underline{\underline{M}}^{(s)}$, $\underline{\underline{K}}^{(s)}$, $\underline{u}^{(s)}$, and $\underline{F}^{(s)}$ are the mass matrix, stiffness matrix, displacement vector, and the force vector of the substructure, all expressed in physical coordinates. The mass and stiffness of substructure *s* can be expressed as follows,

$$\begin{bmatrix} \underline{\underline{M}}_{ii} & \underline{\underline{M}}_{iB} \\ \underline{\underline{M}}_{Bi} & \underline{\underline{M}}_{BB} \end{bmatrix}^{s} \tag{4.3}$$

$$\begin{bmatrix} \underline{\underline{K}}_{ii} & \underline{\underline{K}}_{iB} \\ \underline{\underline{K}}_{Bi} & \underline{\underline{K}}_{BB} \end{bmatrix}^{s} \tag{4.4}$$

where *i* corresponds to the interior degrees-of-freedom and *B* corresponds to the boundary degrees-of-freedom.

A reduced order model of the substructure, using the Craig-Bampton method, can be obtained by expressing the internal and boundary degrees-of-freedom as

$$\underline{u}^{(s)} = \underline{\underline{\Phi}}^{(s)} \underline{q}^{(s)} + \underline{\underline{\Xi}}^{(s)} \underline{Y}^{(s)}$$
$$\underline{u}_B^{(s)} = \underline{Y}^{(s)}$$

(4.5)

where $\underline{\underline{\Phi}}^{(s)}$ denotes a matrix of p selected fixed-interface modes, where one of its columns $\underline{\varphi}_j$ is obtained from

$$\underline{\underline{K}}_{ii}^{(s)} \underline{\varphi}_j^{(s)} = \lambda_j^{(s)} \underline{\underline{M}}_{ii}^{(s)} \underline{\varphi}_j^{(s)}.$$

(4.6)

Furthermore, Ξ is the matrix of constraint modes obtained as follows

$$\underline{\underline{\Xi}}^{(s)} = -\left(\underline{\underline{K}}_{ii}^{(s)}\right)^{-1} \underline{\underline{K}}_{iB}^{(s)}.$$

(4.7)

Finally, the vector $\underline{q}^{(s)}$ contains the generalized coordinates of the fixed-interface modes.

The transformation matrix where the fixed-interface modes and constraint modes are included is

$$\underline{\underline{T}}_1^{(s)} = \begin{bmatrix} \underline{\underline{\Phi}}^{(s)} & \underline{\underline{\Xi}} \\ 0 & \underline{\underline{I}} \end{bmatrix}$$

(4.8)

where $\underline{\underline{I}}$ denotes the identity matrix of appropriate dimensions.

The reduced Craig-Bampton mass and stiffness matrices can be obtained as follows

$$\underline{\underline{\overline{M}}}^{(s)} = \left(\underline{\underline{T}}_1^{(s)}\right)^T \underline{\underline{M}}^{(s)} \underline{\underline{T}}_1^{(s)} = \begin{bmatrix} \underline{\underline{\overline{M}}}_{qq} & \underline{\underline{\overline{M}}}_{qY} \\ \underline{\underline{\overline{M}}}_{Yq} & \underline{\underline{\overline{M}}}_{YY} \end{bmatrix}^s$$

(4.9)

and

$$\underline{\overline{\underline{K}}}^{(s)} = \left(\underline{\underline{T}}_1^{(s)}\right)^T \underline{\underline{K}}^{(s)} \underline{\underline{T}}_1^{(s)} = \left[\begin{array}{cc} \overline{\underline{\underline{K}}}_{qq} & \overline{\underline{\underline{K}}}_{qY} \\ \overline{\underline{\underline{K}}}_{Yq} & \overline{\underline{\underline{K}}}_{YY} \end{array}\right]^s. \tag{4.10}$$

Two observations from the stiffness matrix are in order. First, the top left partition is diagonal and it contains the eigenvalues of the fixed-interface problem. Second, the fixed-interface modal coordinates and the modal coordinates from the constraint modes are uncoupled. This means that the only coupling between these sets of coordinates appears in the dynamic case since the mass matrix is full.

The reduced order model that results from the Craig-Bampton method has two types of degrees-of-freedom: modal coordinates for the interior degrees-of-freedom and physical coordinates for the boundary degrees-of-freedom. A "full" reduced order model can be developed by expressing the physical boundary degrees-of-freedom of the entire system [33] as

$$\underline{Y} = \underline{\underline{\Psi}}\,\underline{z} \tag{4.11}$$

where $\underline{\underline{\Psi}} = \begin{bmatrix} \underline{\psi}_1 & \underline{\psi}_2 & \cdots & \underline{\psi}_r \end{bmatrix}$ is a matrix whose columns are the eigenvectors corresponding to

$$\underline{\underline{K}}_{BB}\underline{\psi}_j = \lambda_j \underline{\underline{M}}_{BB}\underline{\psi}_j. \tag{4.12}$$

This second reduction of degrees-of-freedom is achieved by the following transformation matrix

$$\underline{\underline{T}}_2 = \left[\begin{array}{cc} \underline{\underline{I}} & 0 \\ 0 & \underline{\underline{\Psi}} \end{array}\right]. \tag{4.13}$$

Using this transformation, the mass and stiffness matrices are reduced as follows

$$\underline{\hat{\underline{M}}}^{(s)} = \left(\underline{\underline{T}}_2^{(s)}\right)^T \overline{\underline{\underline{M}}}^{(s)} \underline{\underline{T}}_2^{(s)} = \left[\begin{array}{cc} \hat{\underline{\underline{M}}}_{qq} & \hat{\underline{\underline{M}}}_{qu} \\ \hat{\underline{\underline{M}}}_{uq} & \hat{\underline{\underline{M}}}_{uu} \end{array}\right]^s \tag{4.14}$$

and

$$\underline{\hat{K}}^{(s)} = \left(\underline{T}_2^{(s)}\right)^T \underline{\overline{K}}^{(s)} \underline{T}_2^{(s)} = \begin{bmatrix} \underline{\hat{K}}_{qq} & \underline{\hat{K}}_{qu} \\ \underline{\hat{K}}_{uq} & \underline{\hat{K}}_{uu} \end{bmatrix}^s .$$ (4.15)

4.3.2. Modeling Assumptions

The 9-bay panel was divided into 11 substructures as shown in Fig. 4.48; the skin panel was divided into 9 bays of equal size (substructures 1 to 9); the part of the skin panel surrounding the bays (substructure 10); and the frames and longerons (substructure 11). For most of the bay boundaries the skin panel is riveted to the frame-longeron substructure. However, as shown in Fig. 4.49 there are some nodes on the skin panel, between the frames and the longerons, which are not attached to the frame-longeron substructure; these are the nodes next to the red dots shown in Fig. 4.49. This has a local effect in the linear response, but also in the in-plane displacement induced by the nonlinear response.

It was seen that the fixed-interface modes of substructure 10 did not have a visible contribution in the synthesis of the global modes; therefore, only the constraint modes for this substructure were kept.
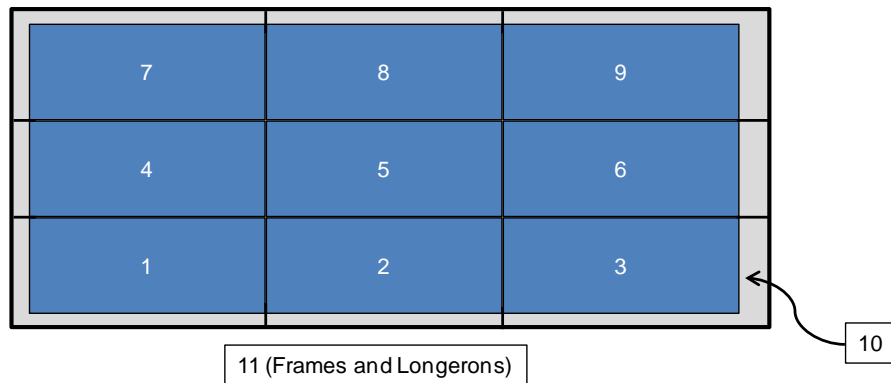

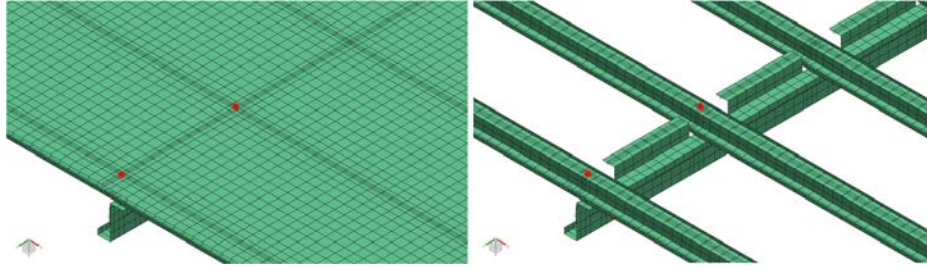Figure 4.48. 9-bay panel divided into 11 substructures.

Figure 4.49. Zoomed-in view of skin-frame connection.

It is of interest to use the Craig-Bampton Method to create a basis for the 9-bay panel following a *Bottom-Up* approach. Based on the previous discussion, there are two families of modes that need to be obtained: i) fixed-interface modes and ii) constraint modes. Shown in Fig. 4.50 is a contour plot of the transverse component of the first fixed-interface mode of one of the bays of the 9-bay panel. Shown in Fig. 4.51 is a constraint mode, obtained from the linear static response due to a unit displacement in the transverse direction of an interface node of one of the bays. The constraint modes computed by imposing a unit in-plane displacement along the T1 or T2 direction also resulted in a localized transverse response. However, the transverse response due to a unit rotation with respect to a vector along the T1 or T2 direction (R1 and R2, respectively) was not localized.
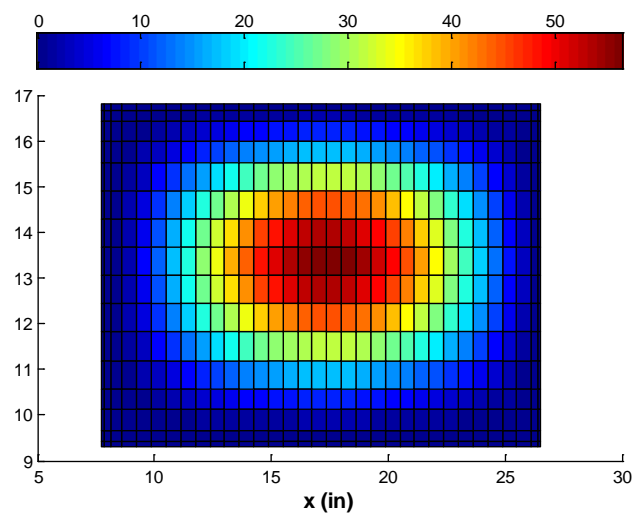

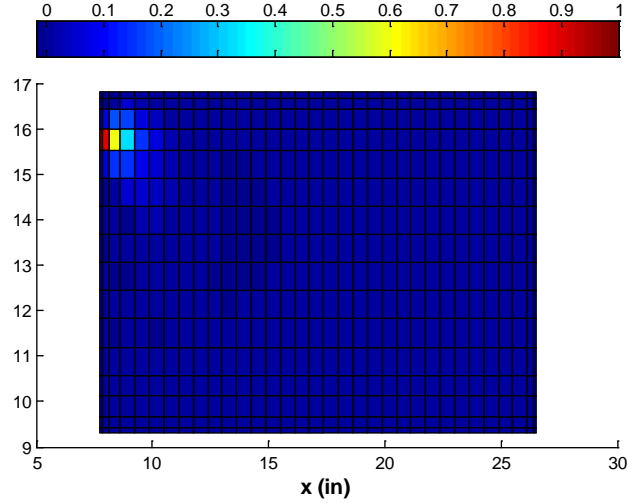Figure 4.50. Transverse component of a bay first fixed-interface mode.

Figure 4.51. Transverse component of the linear static response due to a unit displacement in the transverse direction of an interface node of one of the bays.

The number of boundary and interior nodes, for each substructure, is shown in Table 4.5. Since the interface degrees-of-freedom are expressed in terms of physical coordinates, the number of constraint modes matches the number of interface degrees-of-freedom. The 9-bay panel has a total of 3,771 free interface degrees-of-freedom, so a total of 3,771 constraint modes were be created.

Table 4.5. Node and degree-of-freedom (Dof) number for each substructure.

Substructure ID	Boundary Node #	Interior Node #	Total Dof
1 – 9	98×9	480×9	$3,468 \times 9$
10	350	1,094	8,664
11	532	9,976	63,048

4.3.3. Linear Problem

While the "exact" response predicted by the full FEA model of the 9-bay panel would be recovered if all the fixed-interface modes and constraint modes were included, a compact reduced order model was sought. To this end, a reduced order model of the entire model was assembled using different combinations of fixed-interface modes for each substructure while keeping the entire set of constraint modes. The final model selected led to a good matching of the modes and natural frequencies of the entire system

and the synthesized ones, which in turn ensures a good matching of the linear dynamic response. The difference between the synthesized and original modes was assessed in terms of the norm of the difference of these modes divided by the norm of the original mode.

Only the 46 modes of the entire system within the [0,500]Hz frequency band that had a significant contribution to the linear dynamic response were included. Shown in Fig. 4.52 are the relative errors of the transverse component (i.e., dominant component) of the skin panel nodes for different numbers of bay and frame fixed-interface modes. Shown in Fig. 4.53 are the relative errors of the natural frequencies. Clearly, even the smallest model yielded a good prediction of the natural frequencies. However, this was not the case with the mode shapes, where a more clear effect can be seen from using different numbers of bay and frame fixed-interface modes. For example, the "10 Bay, 100 Frame" model led to good agreement for a majority of the original modes. Increasing the number of bay or frame fixed-interface modes led to improvements in the other cases, but at a higher cost in the number of modes.

With this in mind, it was desired to further assess the "10 Bay, 100 Frame" model by comparing its linear dynamic response with the one corresponding to the original modes of the full structure. To this end, the 9-bay panel was subjected to a uniform pressure on its top surface varying randomly in time as a white noise band-limited process in the frequency range [0,500Hz] used to simulate an acoustic loading. The acoustic excitation consisted of an overall sound pressure level (*OASPL*) of 106dB. As in the dynamic validation of the monolithic ROM (see the previous section), a simple Rayleigh damping model was adopted with α=7.55/s and β=5.6E-6s. This selection led to damping ratios between 0.65% and 1% for all transverse modes in the excitation band. The power spectral density of the transverse displacement of the middle point of the

middle panel, for the original modes and the synthesized modes, is shown in Fig. 4.54. The matching of the dominant features of the dynamic response is excellent, which indicates the suitability of the "10 Bay, 100 Frame" model.
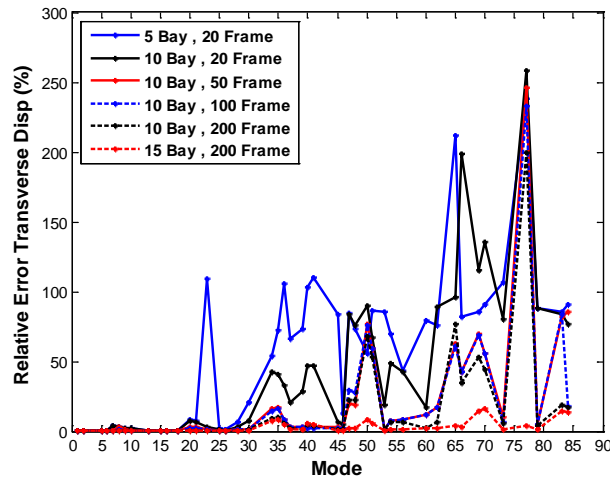

Figure 4.52. Relative errors of the transverse (normal) component of the skin degrees-of-freedom for different combinations of bay-frame fixed-interface mode numbers.
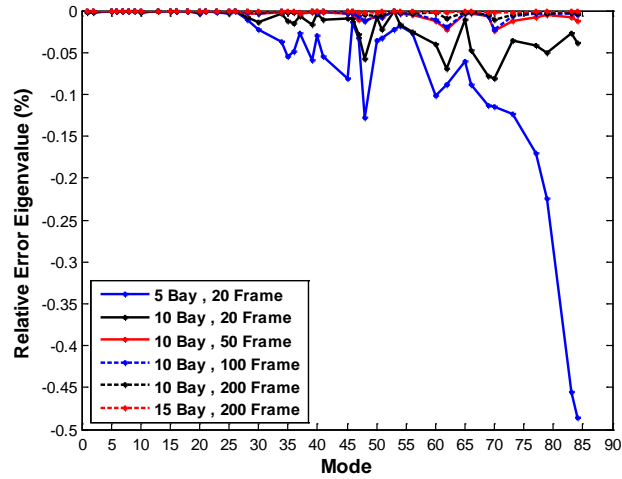

Figure 4.53. Relative errors of the natural frequencies for different combinations of bay-frame fixed-interface mode numbers.
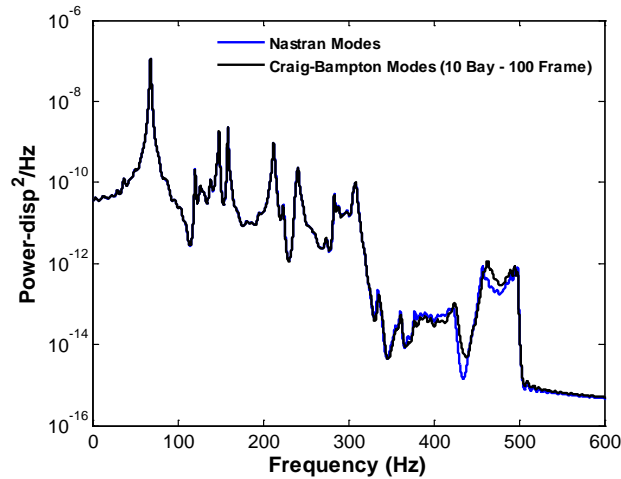
Figure 4.54. Power spectral density of the transverse (T3) deflection at the middle point of bay 5. Craig-Bampton model and finite element ("Nastran Modes"), *SPL* =106dB.

Notwithstanding the good prediction of the linear dynamics of the entire system by the "10 Bay, 100 Frame" model, the large number of fixed-interface frame modes and most importantly the large number of constraint modes deserve a closer examination. The use of a methodology to reduce the number of fixed-interface frame modes and constraint modes was explored next.

In order to reduce the large number of fixed-interface frame modes two alternatives were explored. The first one consisted of assessing the effect of the mass of the frame-longeron substructure (substructure 11) on the natural frequencies of the original mode shapes of the entire structure. To this end, the mass of the frame in the Craig-Bampton computations was divided by different factors and the resulting natural frequencies in the band [0,500]Hz were compared. A small effect would suggest the possibility of statically condensing the fixed-interface frame modes. However, as seen in Fig. 4.55 the effect was not negligible.
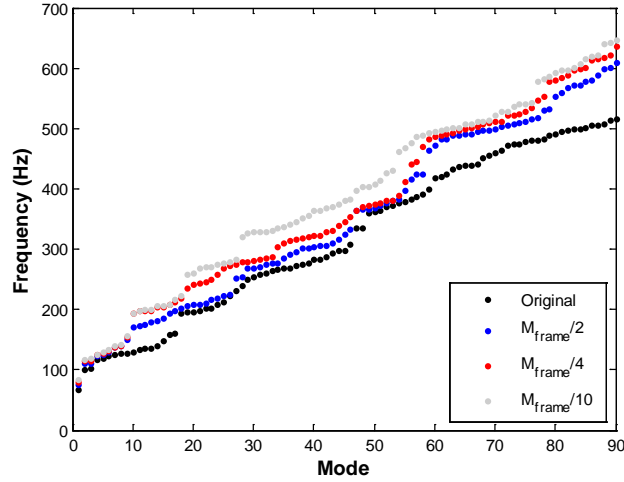
Figure 4.55. First 90 natural frequencies for different scaling factors of the frame-longeron mass matrix: 1, 0.5, 0.25, and 0.10.

The frame-longeron substructure is formed by 4 equal longerons and frames. Therefore, one would expect to have families of modes with natural frequencies that are close to each other (e.g., one mode with motions localized to longeron 1 and another localized to longeron 2, and so on). This can be seen in Fig. 4.56, which is a plot of the first 200 natural frequencies of the fixed-interface modes of the frame-longeron substructure. The first 12 modes have frequencies in the [0,500]Hz band of excitation, so these modes were kept as they would be directly excited. Then, the frame deflections from the first 89 system modes (i.e., those with natural frequencies within the [0,500]Hz band) were obtained, the first 12 fixed-interface modes were extracted, and a POD analysis of the residual was performed. Shown in Figs. 4.57-4.58 are the relative errors of the transverse component of the skin degrees-of-freedom and of the natural frequencies for different numbers of POD modes. The difference between including 40 and 50 POD modes was found to be very small; therefore, the number of fixed-interface modes was reduced from 100 to 52 (40 POD modes plus the 12 in-band normal modes).
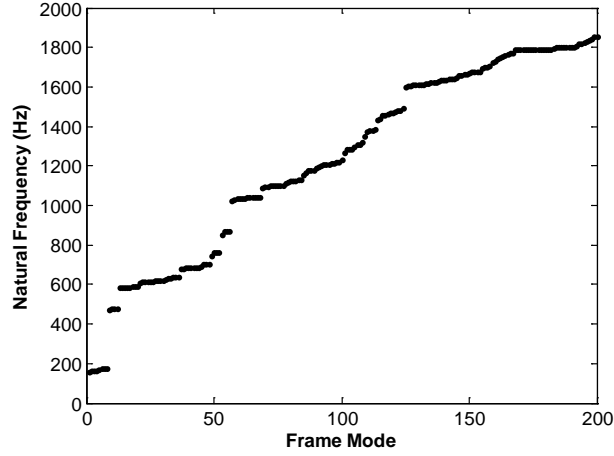
Figure 4.56. First 200 natural frequencies of the fixed-interface frame modes.
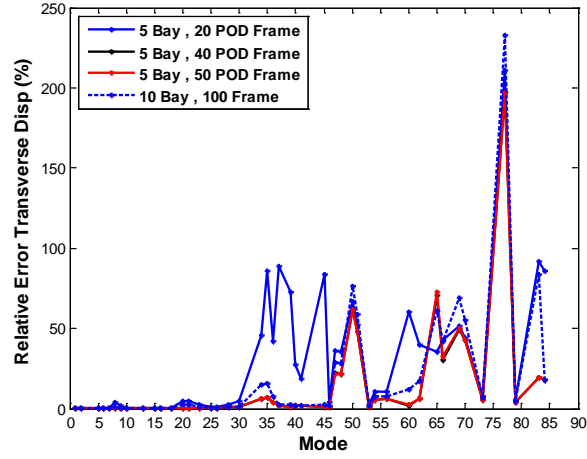

Figure 4.57. Relative errors of the transverse (normal) component of the skin degrees-of-freedom for different number of fixed-interface frame mode numbers.
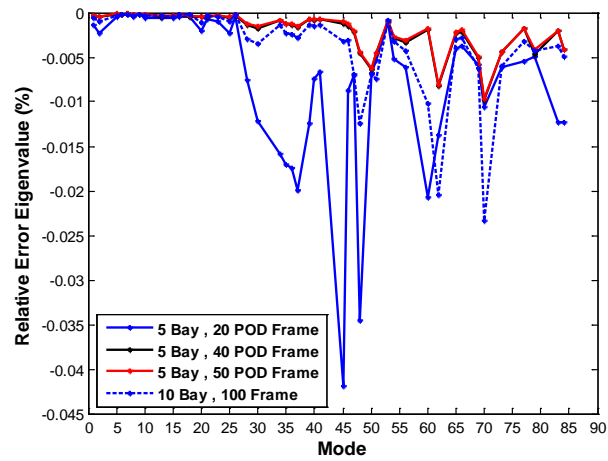

Figure 4.58. Relative errors of the natural frequencies for different number of fixed-interface frame mode numbers.

Next, it was desired to use the full model reduction from Eqs. (4.11)-(4.15) to express the response of the interface in terms of a reduced order model. By expressing the response of the interface in terms of a reduced order model, a substantial reduction in the number of interface degrees-of-freedom was expected. Furthermore, in terms of physical coordinates, the constraint modes are sensitive to the level of mesh refinement; in addition, mesh refinement would also affect the number of interface degrees-of-freedom and consequently the number of constraint modes. On the other hand, the modes of a reduced order model are associated to a natural frequency, which for the low frequency modes is not very sensitive to mesh refinement assuming that the original mesh size is appropriate.

Shown in Fig. 4.59 are the first 80 natural frequencies of the constraint modes computed from Eq. (4.12). There are 36 constraint modes in the frequency band [0,500]Hz that must be included since they could be directly excited by the dynamic loading. Shown in Figs. 4.60-4.61 are the relative errors of the transverse component of the skin panel degrees-of-freedom and of the natural frequencies for different numbers of constraint modes. Approximately 150 constraint modes were needed to match the results obtained with the full set of constraint modes and there were 114 constraint modes outside of the [0,500]Hz frequency band. Therefore, the POD approach used to reduce the number of fixed-interface constraint modes was used. In a similar way, the 36 in-band constraint modes were extracted from the displacement of the boundary degrees-of-freedom of the first 89 global modes. Then, a POD analysis of the residual was performed. Shown in Figs. 4.62-4.63 are the relative errors of the transverse component of the skin degrees-of-freedom and of the natural frequencies for different numbers of POD modes. In order to recover the results obtained with the full set of constraint modes, 54 POD modes were required; a total of 90 constraint modes were selected.
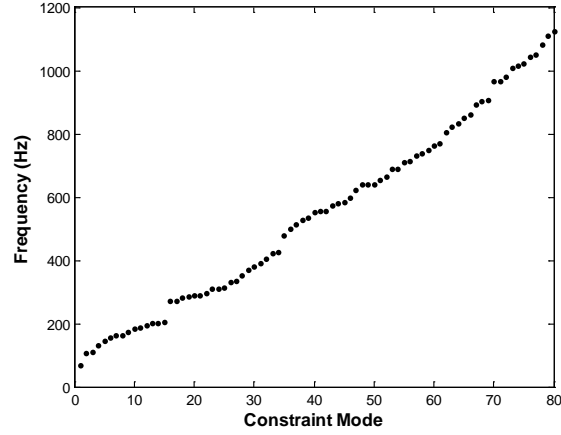
82

Figure 4.59. First 80 natural frequencies of the constraint modes from Eq. (4.12).
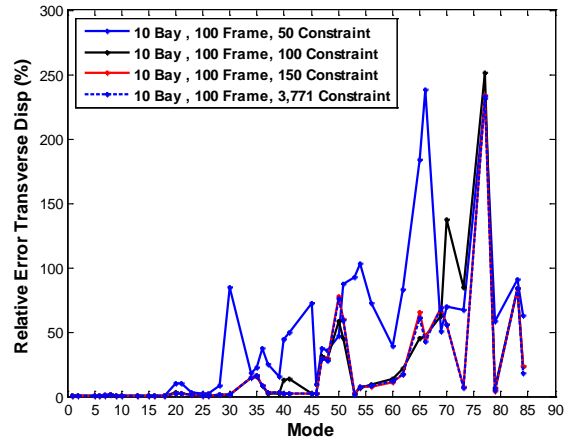

Figure 4.60. Relative errors of the transverse (normal) component of the skin degrees-of-freedom for different number of constraint modes.
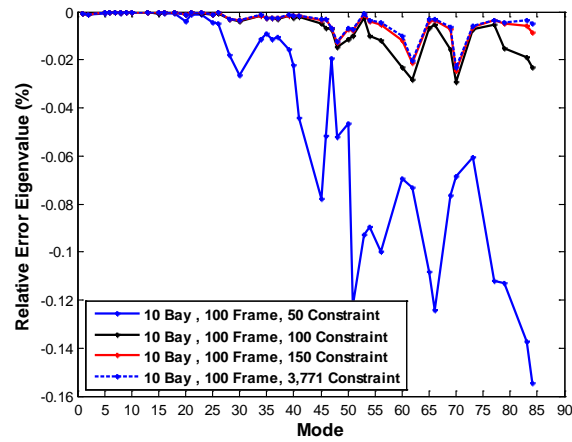

Figure 4.61. Relative errors of the natural frequencies for different number of constraint modes.
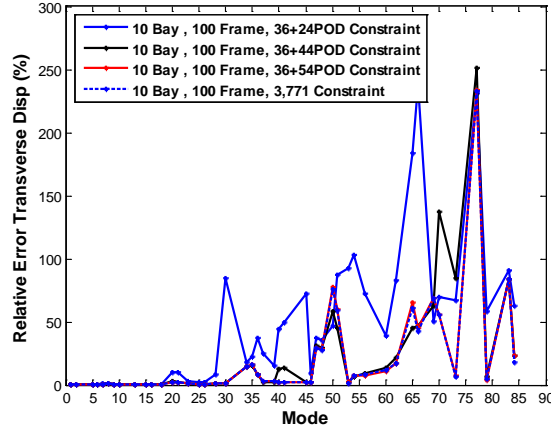
83

Figure 4.62. Relative errors of the transverse (normal) component of the skin degrees-of-freedom for different number of POD constraint modes.
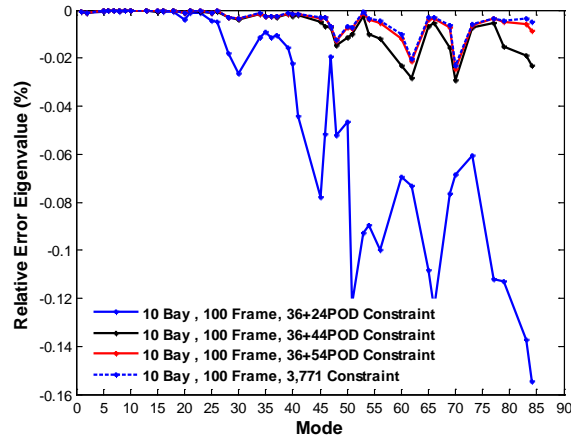
Figure 4.63. Relative errors of the natural frequencies for different number of POD constraint modes.

Therefore, the final reduced model consisted of 10 fixed-interface modes per bay, 52 fixed-interface frame modes (40 POD modes plus 12 in-band normal modes), and 90 constraint modes (54 POD modes plus 36 in-band normal modes). Shown in Fig. 4.64 is the power spectral density of the transverse displacement of the middle point of the middle panel, for the original 89 modes in the frequency band [0,500]Hz and the modes from the Craig-Bampton model. The matching of the dominant features of the response is excellent. However, the total size of the model (232 modes) is much larger than the 89 system modes that are within the frequency band [0,500]Hz. This is an important

84

challenge in the use of a *Bottom-Up Approach* which arises from the global aspects of the response of the 9-bay panel.

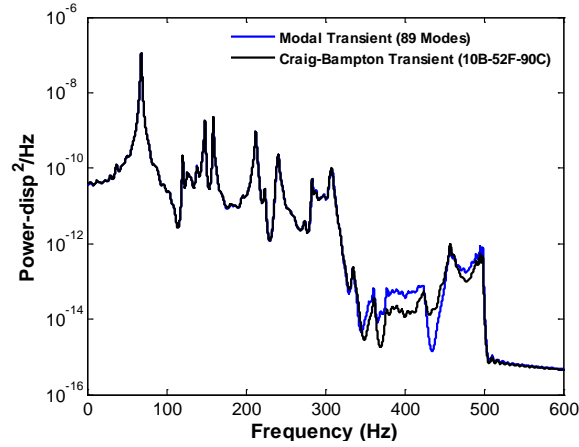Figure 4.64. Power spectral density of the transverse (T3) deflection at the middle point of bay 5. Modal transient response (89 linear modes of the entire 9-bay panel) and Craig-Bampton model, *SPL* =106dB.

4.3.4. Nonlinear Problem

Shown in Figs. 4.65-4.69 are plots of the first five reduced constraint modes, computed from Eq. (4.12) and mapped back to physical coordinates by the transformation matrix T_1 (see Eq. 4.8). Also shown, are the first five modes of the entire 9-bay panel. Interestingly, the first four reduced constraint modes are very similar to their counterparts of the entire structure. Clearly, the motion of the interface nodes drives the motion of the bays and of the frame-longeron substructure. This global motion illustrates the strong coupling that exists between the bays. This in turn is a positive aspect, since it means that it will be difficult for the motion to get localized in a particular bay, which could be a concern from a fatigue failure perspective. On the other hand, from the nonlinear reduced order model perspective, the strong coupling between the bays implies that the nonlinear stiffness coefficients of the constraint modes will have an effect on the response.

85

<p style="text-align:center">(a)   (b)</p>
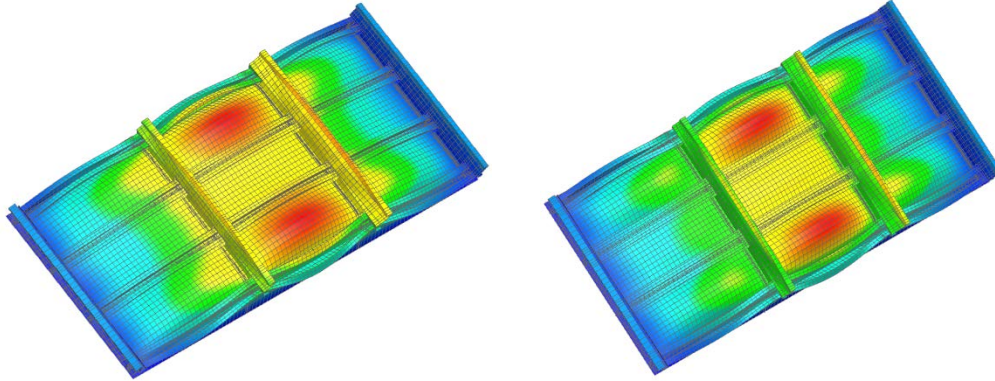
Figure 4.65. (a) First reduced constraint mode (f = 69.7Hz) and (b) first mode of the entire 9-bay panel (f = 68.2Hz).

<p style="text-align:center">(a)   (b)</p>

Figure 4.66. (a) Second reduced constraint mode (f = 106.4Hz) and (b) second mode of the entire 9-bay panel (f = 99.7Hz).

<p style="text-align:center">(a)   (b)</p>

Figure 4.67. (a) Third reduced constraint mode (f = 111.1Hz) and (b) third mode of the entire 9-bay panel (f = 103.3Hz).

<p style="text-align:center">86</p>

<center>(a)   (b)</center>
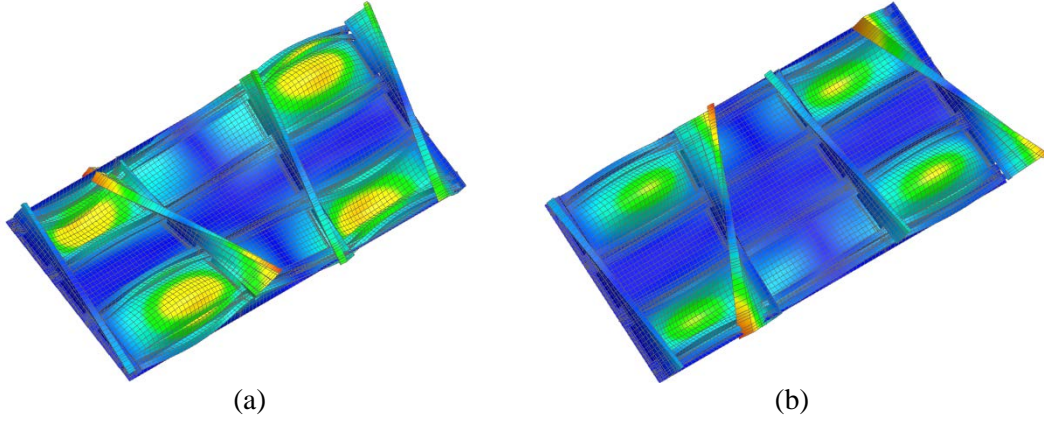
Figure 4.68. (a) Fourth reduced constraint mode (f = 131.9Hz) and (b) fourth mode of the entire 9-bay panel (f = 116.5Hz).

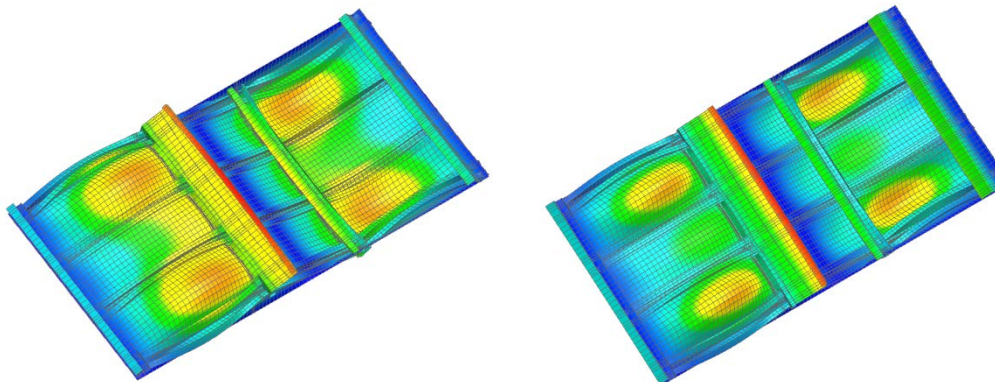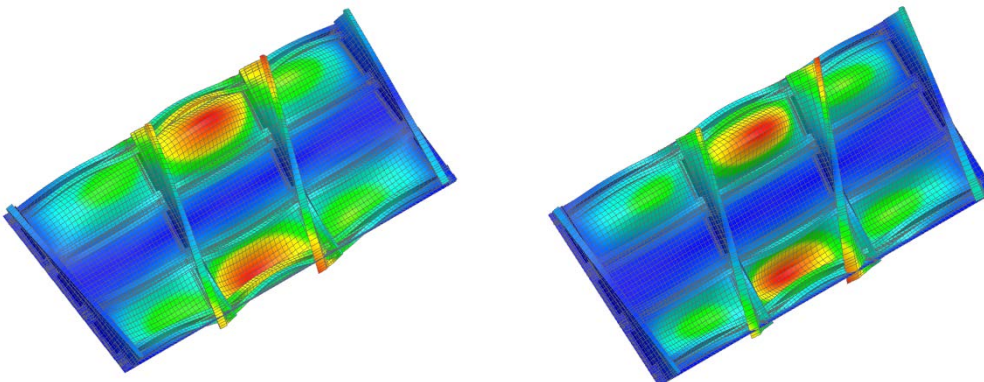<center>(a)   (b)</center>
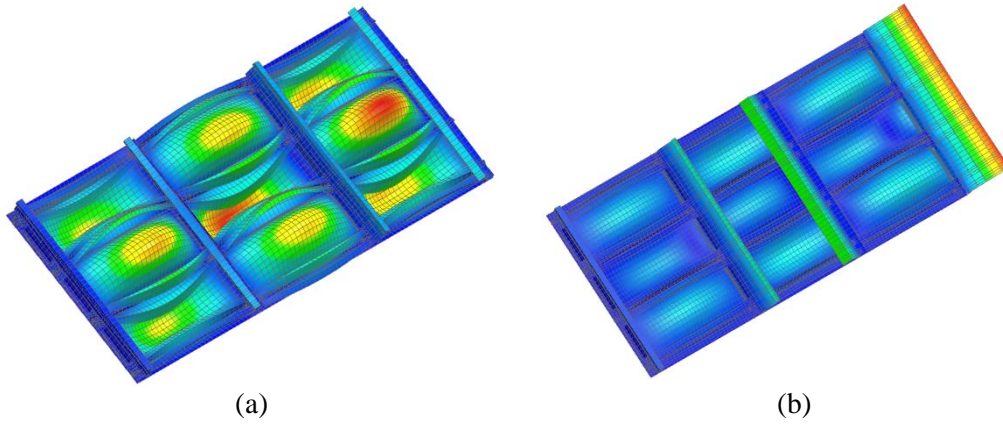
Figure 4.69. (a) Fifth reduced constraint mode (f = 146.7Hz) and (b) fifth mode of the entire 9-bay panel (f = 120Hz).

Another challenge in the implementation of a *Bottom-Up* approach is in the nonlinear interaction between substructures, which needs to be built in the basis. Shown in Fig. 4.70 are the translational displacement magnitude of the entire model and the T2 component of the middle bay obtained from the nonlinear static analysis due to a uniform pressure loading of 0.6psi. Clearly, the middle bay is loaded by the top and bottom bays (bays 8 and 2, respectively).

<center>87</center>
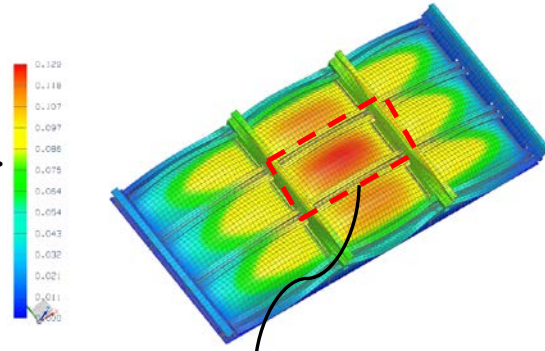
Figure 4.70. Contour plots showing the translational displacement magnitude of the entire 9-bay panel and the in-plane (T2) displacement at bay 5. Nonlinear static displacement due to a uniform pressure of 0.6psi.

The preloading of a substructure by its neighbors can be seen even if the transverse response is mostly localized to one substructure. An example of this can be seen in the localized response shown in Fig. 4.71, which corresponds to a "snapshot" obtained from the nonlinear dynamic response of the 144dB excitation level described earlier in this chapter. This is an interesting case because the response is mostly localized to bay 5; however, the in-plane loading of bays 2 and 8 in the T2 direction can be seen clearly.
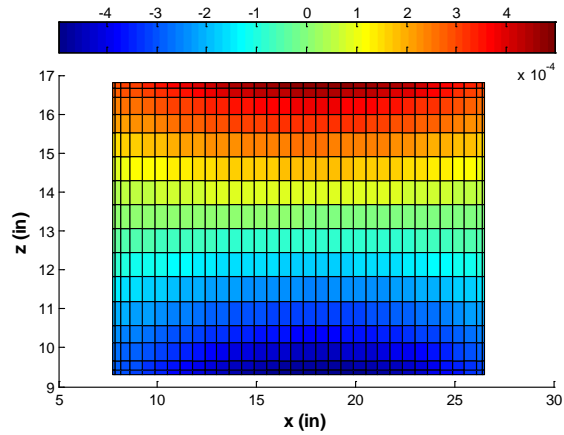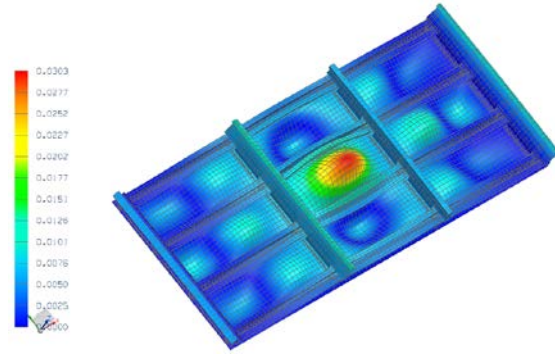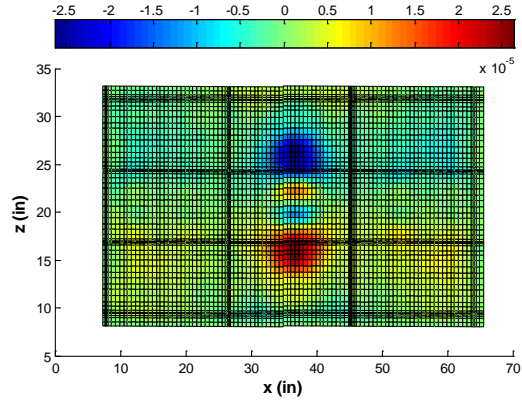
Figure 4.71. Contour plots showing the translational displacement magnitude of the entire 9-bay panel and the in-plane (T2) displacement of the skin panel. "Snapshot" from the nonlinear dynamic response at the 144dB excitation level.

As shown in Fig. 4.72, the preloading of a bay induced by the nonlinear interaction between bays not only leads to significant differences with respect to the original dual construction, but also with respect to duals from different bays. The preloaded duals shown in Fig. 4.72 were obtained by imposing boundary displacements in all directions, in addition to loading of the interior degrees-of-freedom with forces proportional to the first mode of the clamped-clamped bay. The boundary displacement was chosen as the nonlinear static response obtained from a load proportional to the first linear mode of the entire system (i.e., the loading used for the computation of the 1-1 dual of the monolithic ROM). Furthermore, 6 different loading factors $\alpha_i^{(m)}$ were used, half positive and half negative, and leading to peak deflections ranging from 0.9 to approximately 1.5 skin panel thicknesses. The loading of the interior degrees-of-freedom

89

,with forces proportional to the first modes of the clamped-clamped bay, consisted of 12 different loading factors $\alpha_i^{(m)}$, half positive and half negative, which led to overall peak transverse deflections ranging from 1.5 to approximately 2.2 skin panel thicknesses. Finally, the contribution from the reduced constraint modes in the representation of the interface displacement was subtracted, and the residuals of the 12×3 deflections per bay, after projection on the 10 linear fixed-interface modes identified above, were analyzed by POD.
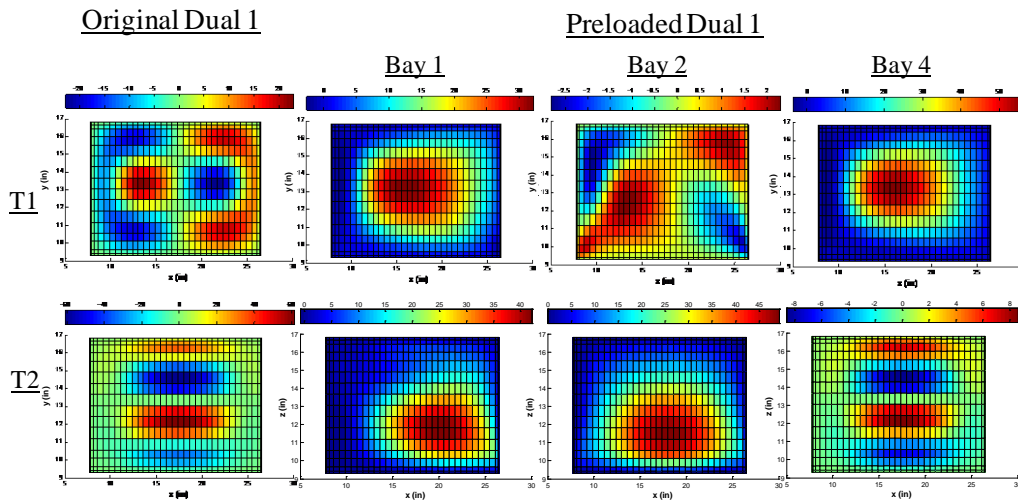
Figure 4.72. In-plane components of the 1-1 dual computed with and without preloading of the interface.

The previous discussion highlights the importance of extending the dual modes concept to include preloading of a substructure by its neighbors. The global features of the response of the 9-bay panel are dominant over the localized characteristics, which was seen in that the modes from the monolithic ROM were a more compact basis than the substructure modes from the previous section. Similarly, the introduction of the preloaded duals by themselves did not lead to a satisfactory reduction of the representation error as compared to the monolithic ROM.

The physical challenges observed here indicate that the representation of the global response from a *Bottom-Up* perspective is not more efficient than using the monolithic ROM. These findings also indicate that a key aspect for the multi-scale modeling of the 9-bay panel is in the representation of its global response. In this light, future work should explore the possibility of following a *Top-Down* multi-scale approach. In this case, the global response would be approximated (macro-scale) and then, this information would be used to compute the response of a particular bay (meso-scale).

CHAPTER 5

REDUCED ORDER MODELING FOR THE NONLINEAR GEOMETRIC

RESPONSE OF PANELS WITH GEOMETRIC DISCONTINUITIES

5.1. Introduction

The purpose of this chapter is to assess the ROM capabilities for problems in the micro-scale. As mentioned in Chapter 1.3, problems in the micro-scale lead to localizations of the stress field. The source of these localizations may arise from cracks, debondings, fasteners, shock impingement points, etc. The main question to be addressed here is: Can a displacement-based ROM capture a localized stress distribution? In addition, the following phenomenological will be the focus of this chapter:

1) Is the displacement field affected by the local defect?

2) Does the defect need to be accounted for in the displacement?

3) Can a local enrichment of the stress be developed?

5.2. Models for Validation: Notched and Virgin Panel Models

A beam-like panel was considered here with and without a stress "hot spot", with the properties of the beam provided in Table 5.1. The panel was assumed to exhibit clamped-clamped boundary conditions and to be subjected to a uniform pressure of varying magnitude.

A rounded notch of length equal to one-fourth of the beam thickness was placed at 30% of the length of the beam (henceforth referred to as the notched beam) and along its entire width as shown in Figs. 5.1 and 5.2. Clearly, plane stress conditions cannot be assumed to exist on the *x-z* plane since it is not a thin membrane. On the other hand, plane strain conditions do not exist since this is not a long body problem. Therefore, the structure was discretized throughout its entire domain with 8-node brick elements (CHEXA in NX/Nastran), and 14 such elements were used along the width of

the beam. Along the length, the notched beam was divided in different parts, as shown in Fig. 5.1, to capture the local effects of the notch without excessive meshing away from that zone. Away from the notch (parts (a) and (c) in Fig 5.1), 4 elements were used through the thickness of the beam and a uniform division along the length was performed with 20 elements for part (a) and 47 elements for part (c). The finer meshing around the notch (part (b) in Fig 5.1) is shown in Fig. 5.2(a). Note further from this figure that the notch is rounded to avoid any plasticity in its vicinity, which is not considered in this first effort. The purpose of this work was to validate the reduced order modeling strategy, therefore, a very fine mesh was not used in order to accelerate the finite element computations.

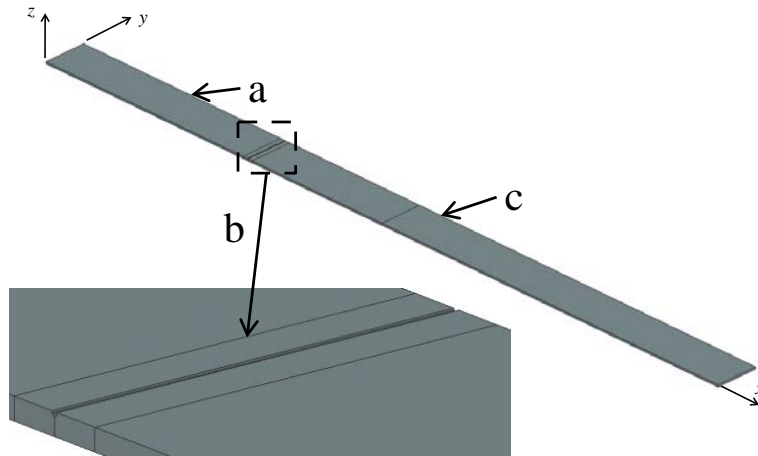Figure 5.1. Notched beam model: Part (b) shows the zone near the notch with a finer mesh than parts (a) and (c) which are away from the notch.

A virgin beam model was also considered and, for ease of comparison, its meshing was selected to be identical to the one of the notched beam but with the notch filled with CHEXA elements, see Fig. 5.2(b), and with the same material properties, see Table 5.1.

Table 5.1. Clamped-Clamped Beam Properties

Beam Length	0.2286 m
Cross-section Width	0.0127 m
Cross-section Thickness	7.88 10^{-4} m
Density	2700 kg/m^3
Young's Modulus	73,000 MPa
Shear Modulus	27,730 MPa
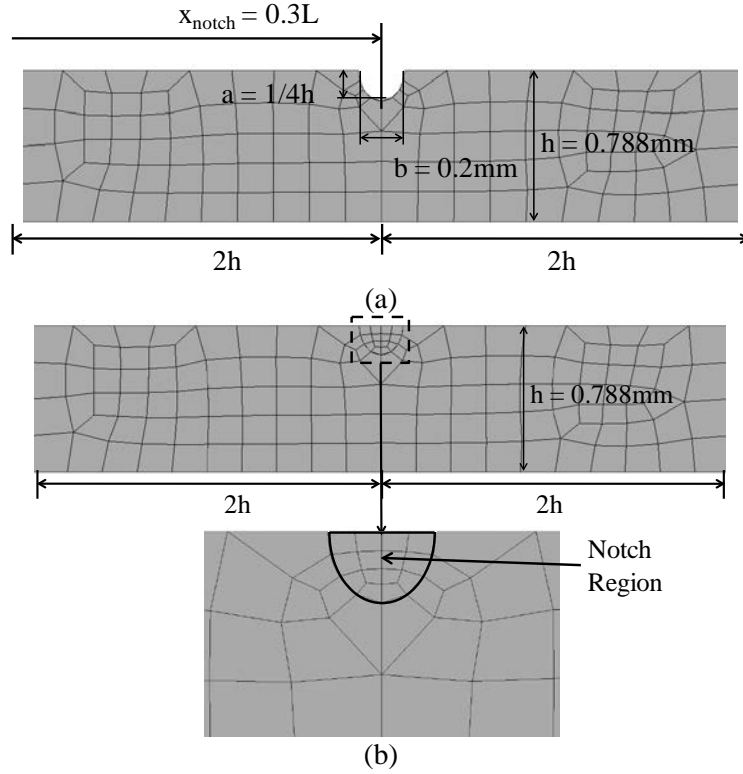
Figure 5.2. Geometry and finite element mesh near the notch region: (a) notched beam and (b) virgin beam. Where L=0.2286m and h=7.88x10^{-4}m.

5.3. Reduced Order Basis: Notched and Virgin Panels

It was first of interest to compare the basis functions of the reduced order models, i.e., the transverse and duals modes, of the virgin and notched beams to assess the effects, local and/or global, of the notch.

The transverse linear modes were first investigated and were obtained, for the two beams, from a normal modes solution in NX/Nastran (SOL 103). The natural

frequencies of the first 4 symmetric modes of the two beams are shown in Table 5.2. As expected, given the small size of the notch, its effect on the first few natural frequencies is very small.

Table 5.2. Natural frequencies along with relative error between notched and virgin beams.

Mode No.	Virgin Beam (Hz)	Notched Beam (Hz)	Relative Difference (%)
1	81.561	81.551	0.010
3	442.075	441.900	0.040
6	1098.527	1097.261	0.110
10	2061.725	2061.693	0.001

The transverse and in-plane (along the length of the beam) components of the first mode shape along one of the top edges of the beams ($y=0$, $z=h$) are shown in Figs. 5.3-5.4. The first observation to be drawn is that the notch does not affect noticeably the transverse displacements, but appears to induce a sharp peak in its in-plane counterpart. However, this peak is an artifact of the geometry, i.e., the notched beam data presented includes the displacement at the nodes along the flat edge of the beam but also those along the faces of the notch. Since these points are much closer to the neutral axis of the beam, their in-plane displacements are expected to be smaller as seen in Fig. 5.5. Plotting the same nodal displacements for the virgin beam, see Figs. 5.6-5.7, confirms this explanation of the peak.

The linear modes of the structure only represent one part of the basis, modeling primarily the transverse displacements, while the dual modes (see [9,12,14]) capture the nonlinearly induced in-plane motions. In this light, it was also desired to assess the effects of the notch on these dual modes. Thus, the 4 dual modes corresponding to the 4 linear modes were created, for both notched and virgin beams.

Shown in Figs. 5.8-5.9 are the transverse and in-plane components of the first (dominant) dual. Note that the notch is most present in the *transverse* component, see

95

Fig. 5.8, of the dual mode which is quite different for the notched and virgin beams. In particular, note for the former the presence of a large, broad (as measured by the width of the notch) peak at the location of the notch. On the contrary, the in-plane components of this dual mode are almost unaffected by the notch, see Fig. 5.9. The most noticeable difference in the in-plane displacement is a jump occurring at the location of the notch, as seen in Fig. 5.10. Similar observations were drawn for the other 3 dual modes.
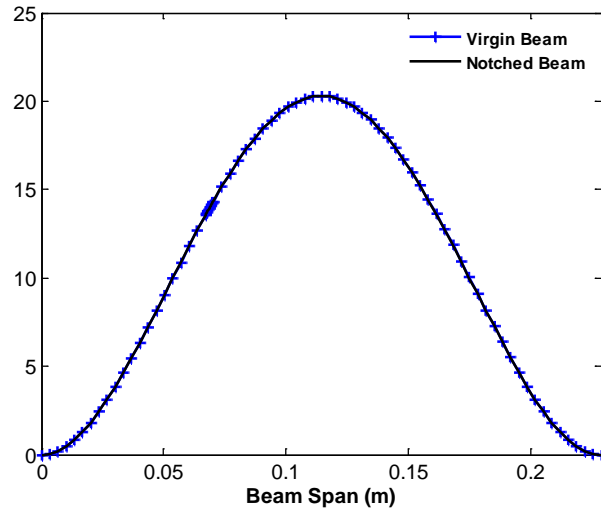

Figure 5.3. Transverse component of the first linear mode along one of the top edges of the beam.
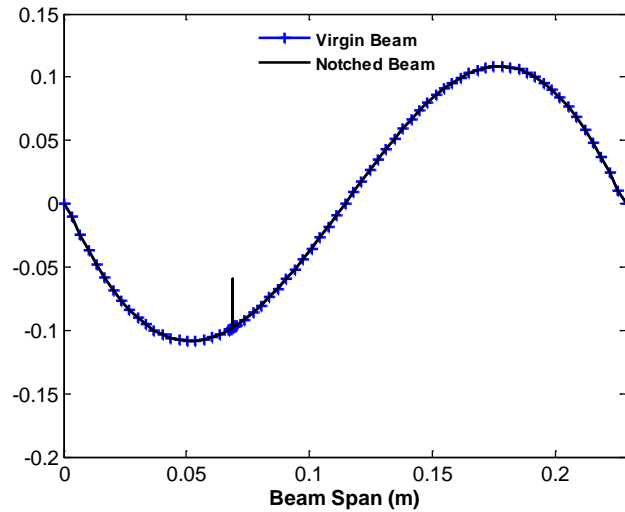

Figure 5.4. In-plane component of the first linear mode along one of the top edges of the beam.

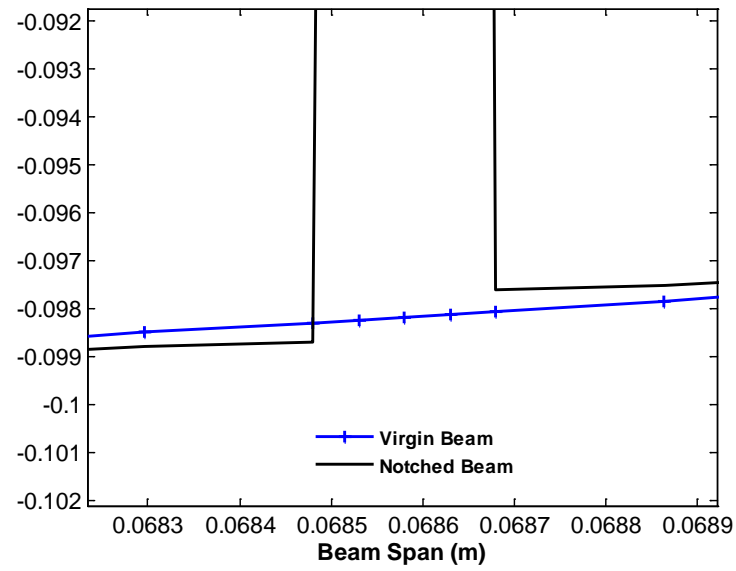Figure 5.5. Zoomed-in view of the in-plane displacements near the location of the notch.

Figure 5.6. In-plane component of the first linear mode, curves correspond to displacements at the same nodes.
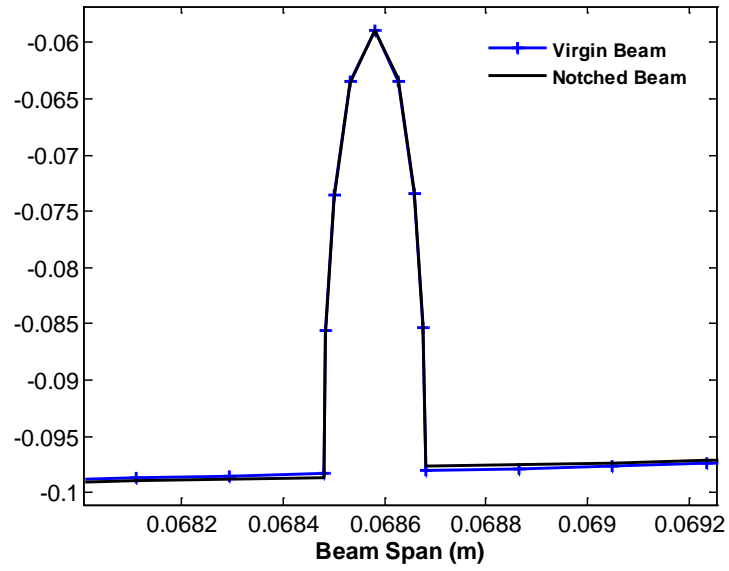
Figure 5.7. Zoomed-in view of the in-plane component, curves correspond to displacements at the same nodes.
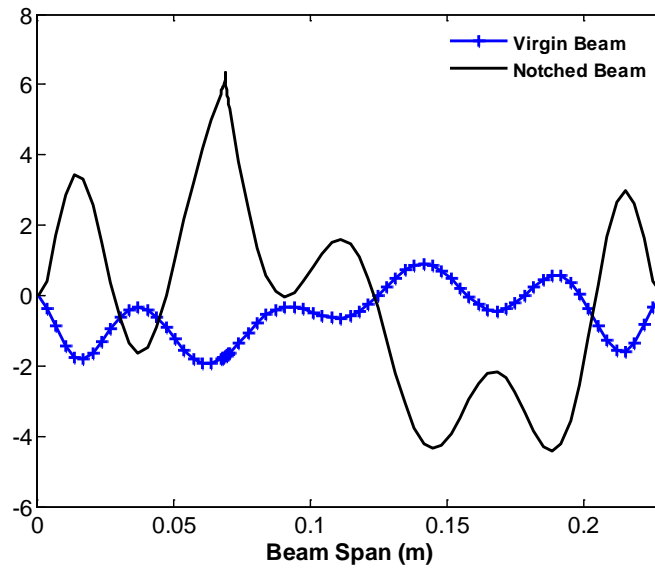
Figure 5.8. Transverse component of the first dual mode along one of the top edges of the beam.
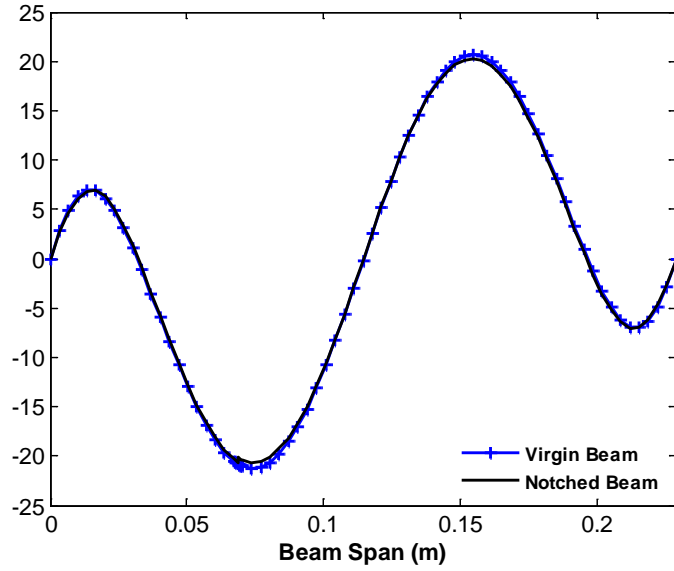
Figure 5.9. In-plane component of the first dual mode along one of the top edges of the beam.

Figure 5.10. Zoomed-in view of the in-plane displacements near the location of the notch.
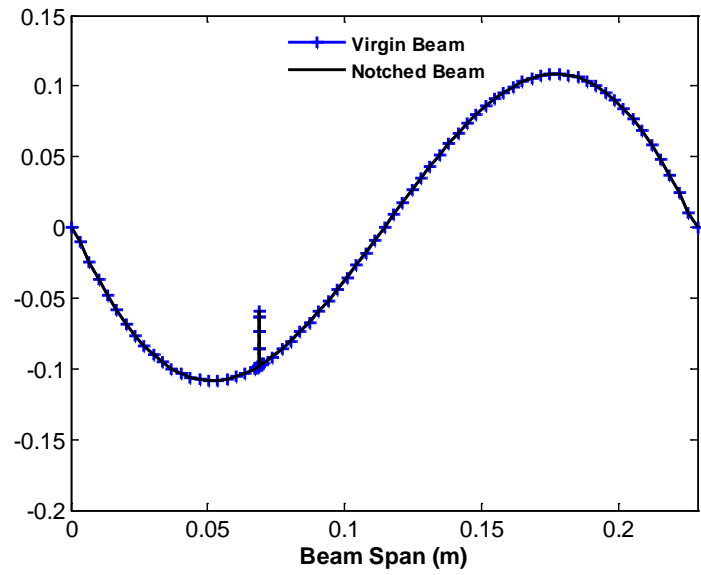
Using the 4 linear and 4 dual modes analyzed above, reduced order models were built for both notched and virgin beams with the coefficients estimated from the stiffness evaluation procedure of [28] as modified in [10-12].

5.4. Static Validation: Displacement and Stress Fields

To assess the adequacy of the reduced order models obtained and assess the effects of the notch, the beams were loaded with a uniform pressure acting on the bottom surface. Two different press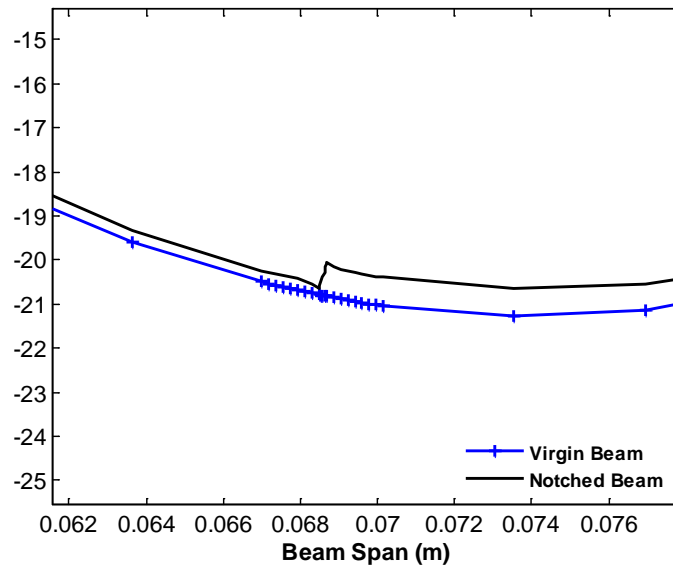ures were chosen, 2.6kPa and 17kPa, which led to peak transverse displacements of approximately 2 and 4 beam thicknesses, well within the nonlinear range. The static responses were computed with the reduced order model as well as by a nonlinear NX/Nastran analysis (SOL 106). Shown in Figs. 5.11-5.14 is a comparison of the predicted transverse and in-plane displacements at the beam's upper and lower edges. Clearly, the matching is excellent for both transverse and in-plane displacements, even in the direct vicinity of the notch (see Fig. 5.15). In Figs. 5.15-5.16, the response of the virgin beam was plotted at the same node locations as the response of the notched beam. Interestingly, the reduced order model of the virgin beam does an excellent job in capturing the in-plane displacement field in the notch region.

Figures 5.17-5.20 show the static response of the beam to pressures equal to -2.6kPa and -17kPa, applied on the bottom surface of the beam, and leading to peak transverse displacements of -2 and -4 beam thicknesses. Clearly, the matching is excellent for both cases, and once more the reduced order model of the virgin beam does an excellent job in capturing the in-plane displacement field in the notch region.

Figure 5.11. Transverse displacements at the top ($y=0$, $z=h$) edge of the beam induced by a uniform pressure of 2.6kPa on its bottom surface. Reduced order models ("ROM 4T4D"), nonlinear static FEA ("NX/Nastran NL").

Figure 5.12. Transverse displacements at the top ($y=0$, $z=h$) edge of the beam induced by a uniform pressure of 17kPa on its bottom surface. Reduced order models ("ROM 4T4D"), nonlinear static FEA ("NX/Nastran NL").

101

Figure 5.13. In-plane disp. at the top ($y=0$, $z=h$) and bottom ($y=0$, $z=0$) edges of the beam induced by a uniform pressure of 2.6kPa on its bottom surface. Reduced order models ("ROM 4T4D"), nonlinear static FEA ("NX/Nastran NL").

Figure 5.14. In-plane disp. at the top ($y=0$, $z=h$) and bottom ($y=0$, $z=0$) edges of the beam induced by a uniform pressure of 17kPa on its bottom surface. Reduced order models ("ROM 4T4D"), nonlinear static FEA ("NX/Nastran NL").

Figure 5.15. Close-up view of the in-plane disp. (T1) at the beam top edge ($y=0$, $z=h$) due to a uniform pressure of 2.6kPa. Reduced order models ("ROM 4T4D"), nonlinear static FEA ("NX/Nastran NL").
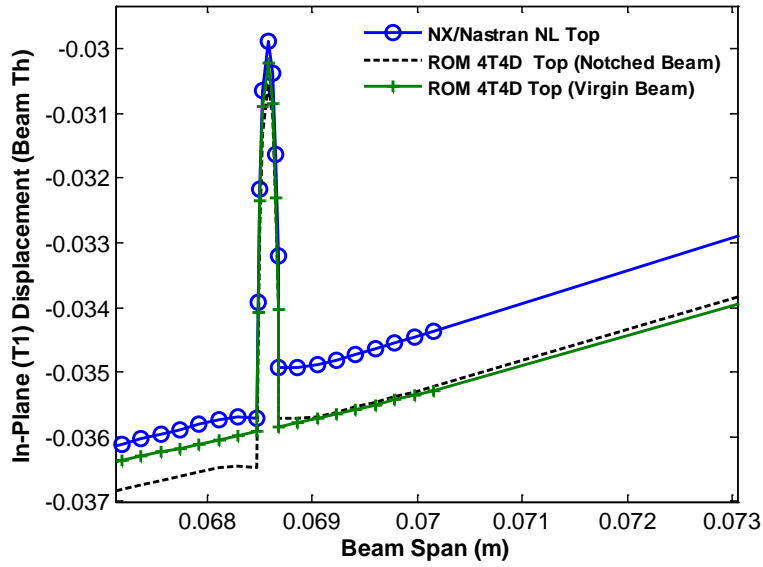
Figure 5.16. Close-up view of the in-plane disp. (T1) at the beam top edge ($y=0$, $z=h$) due to a uniform pressure of 17kPa. Reduced order models ("ROM 4T4D"), nonlinear static FEA ("NX/Nastran NL").
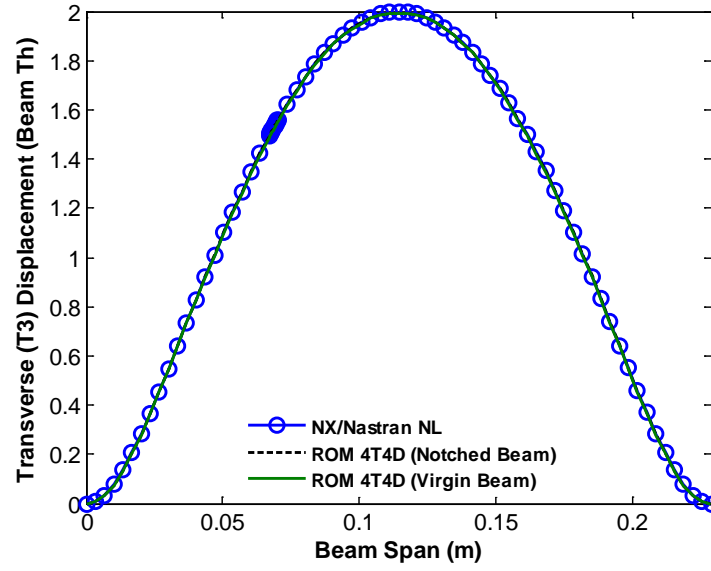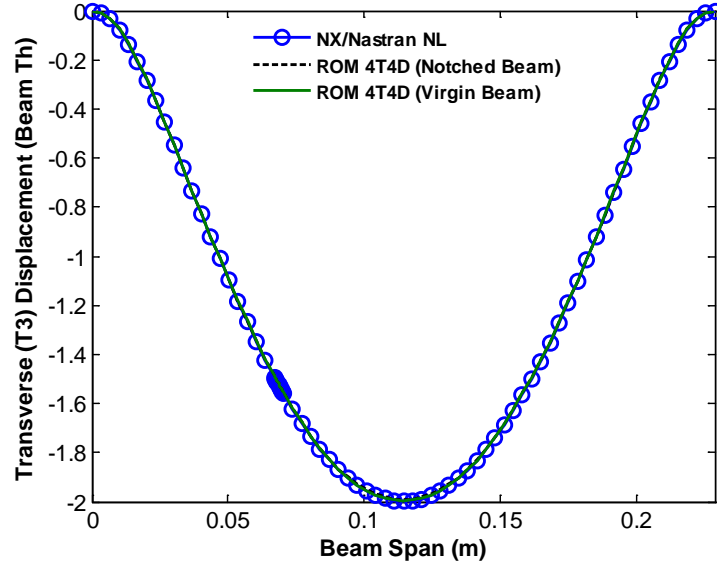
Figure 5.17. Transverse disp. at the top (*y=0*, *z=h*) edge of the beam induced by a uniform pressure of -2.6kPa on its bottom surface. Reduced order models ("ROM 4T4D"), nonlinear static FEA ("NX/Nastran NL").
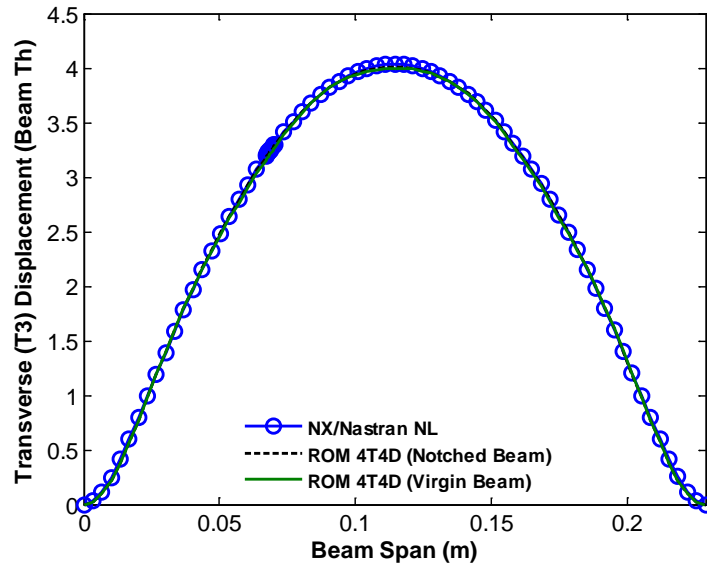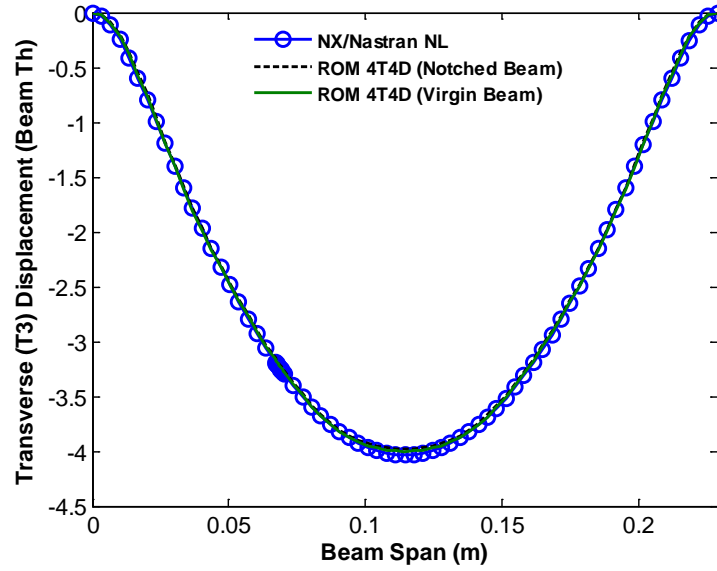

Figure 5.18. Transverse disp. at the top (*y=0*, *z=h*) edge of the beam induced by a uniform pressure of -17kPa on its bottom surface. Reduced order models ("ROM 4T4D"), nonlinear static FEA ("NX/Nastran NL").
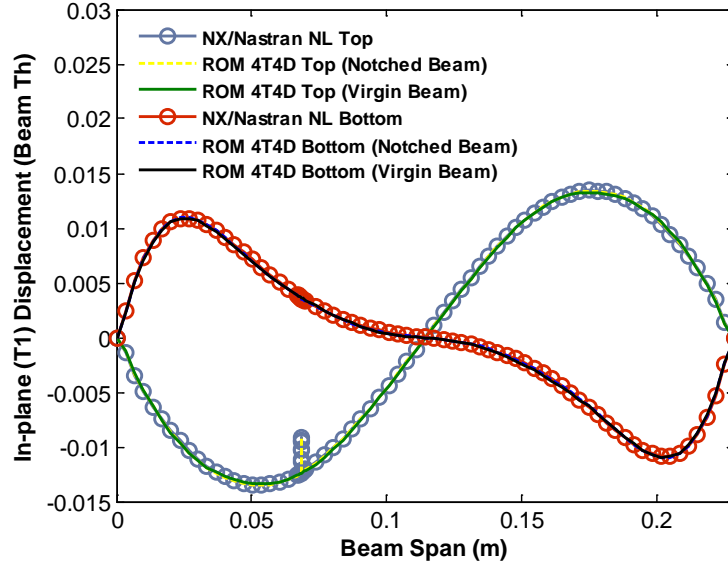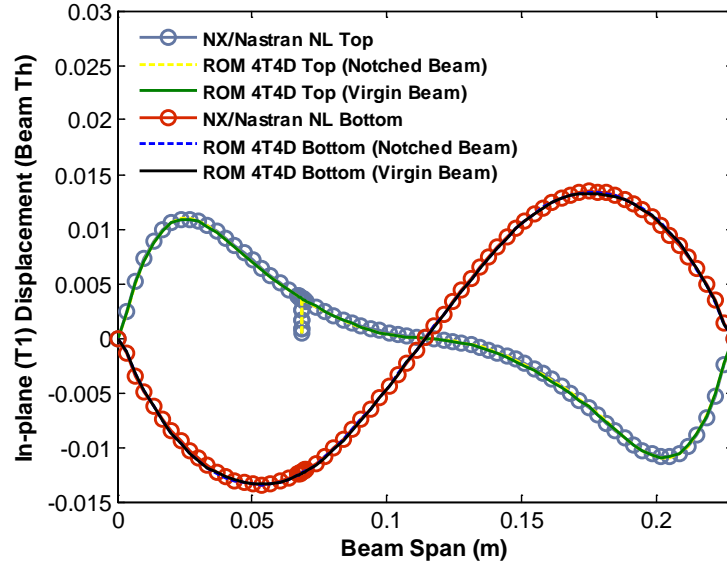
Figure 5.19. In-plane disp. at the top ($y=0$, $z=h$) and bottom ($y=0$, $z=0$) edges of the beam induced by a uniform pressure of -2.6kPa on its bottom surface. Reduced order models ("ROM 4T4D"), nonlinear static FEA ("NX/Nastran NL").
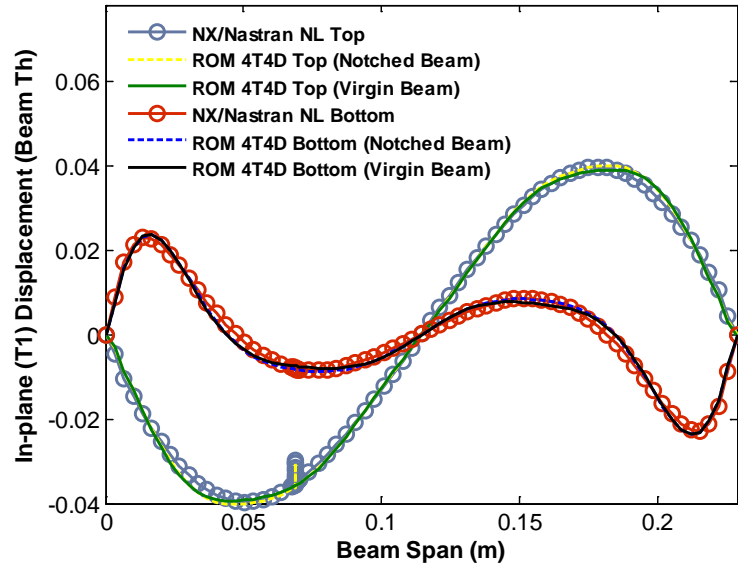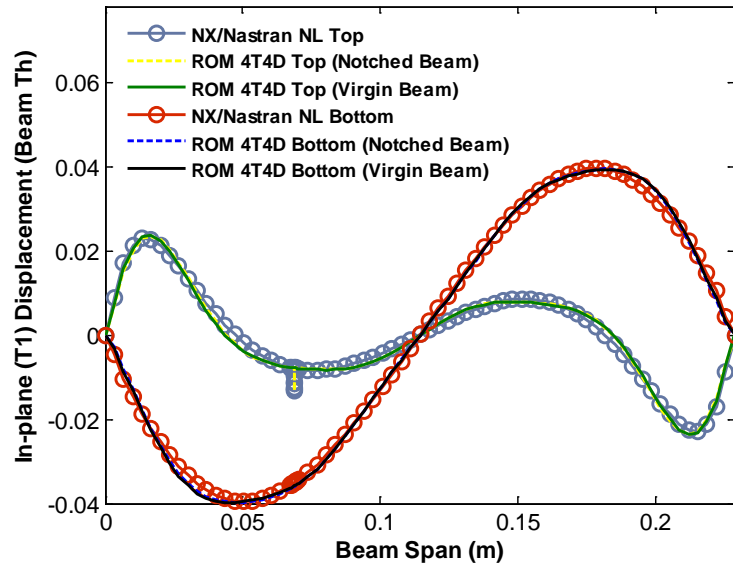

Figure 5.20. In-plane disp. at the top ($y=0$, $z=h$) and bottom ($y=0$, $z=0$) edges of the beam induced by a uniform pressure of -17kPa on its bottom surface. Reduced order models ("ROM 4T4D"), nonlinear static FEA ("NX/Nastran NL").
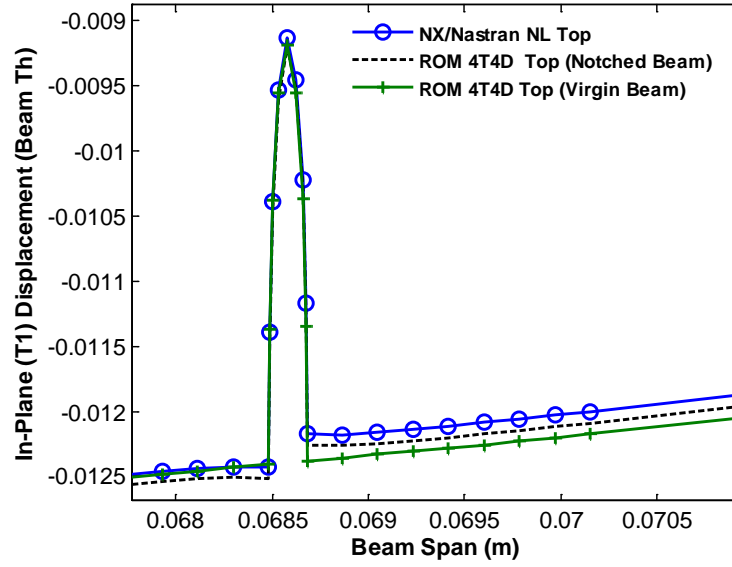
Figure 5.21. Close-up view of the in-plane disp. (T1) at the beam top edge (*y=0*, *z=h*) due to a uniform pressure of (a) -2.6kPa and (b) -17kPa. Reduced order models ("ROM 4T4D"), nonlinear static FEA ("NX/Nastran NL").

Figure 5.22. Close-up view of the in-plane disp. (T1) at the beam top edge (*y=0*, *z=h*) due to a uniform pressure of (a) -2.6kPa and (b) -17kPa. Reduced order models ("ROM 4T4D"), nonlinear static FEA ("NX/Nastran NL").

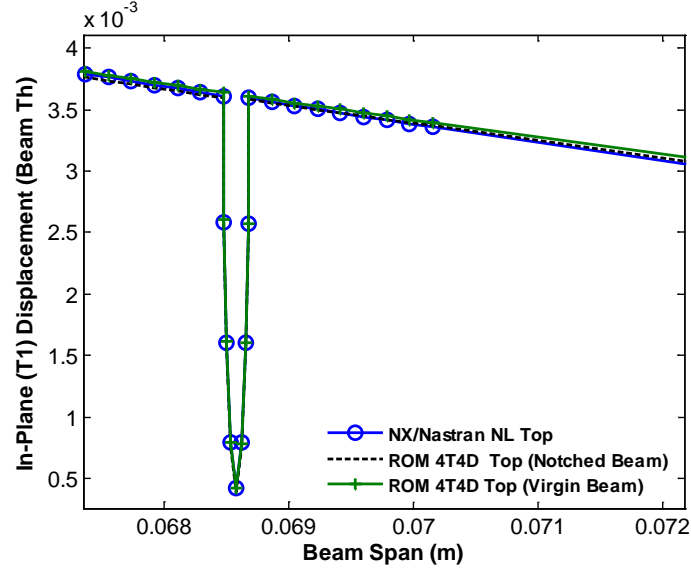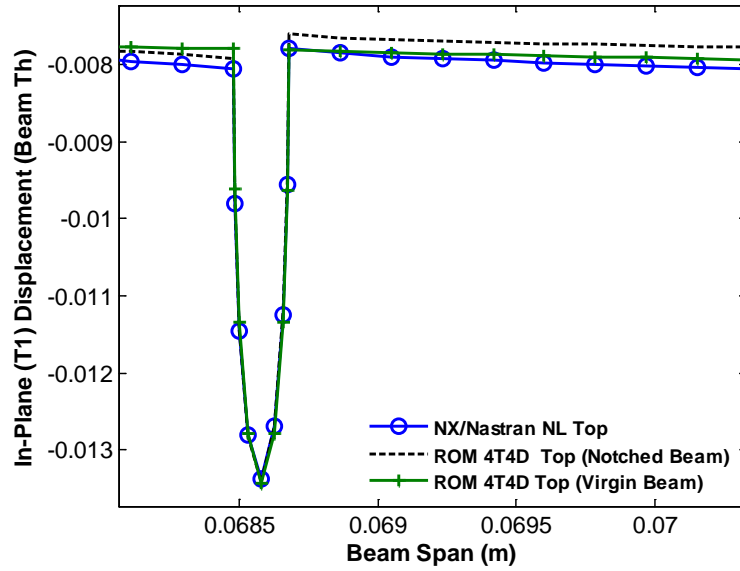Table 5.3. Summary of prediction errors, notched beam and virgin beam ROMs.

Peak T3 Disp (Beam Thicknesses)	Prediction Error Transverse (T3) Component (%)		Prediction Error Transverse (T1) Component (%)		Prediction Error Transverse (T2) Component (%)	
	Notched Beam	Virgin Beam	Notched Beam	Virgin Beam	Notched Beam	Virgin Beam
2	0.2	0.4	1	1.4	2.4	3.4
4	0.5	0.9	3.9	3.7	5.9	7.4
-2	0.3	0.3	1.4	1.4	3.4	3
-4	1	0.6	3.8	3.9	7.4	7.1

Shown in Table 5.3 is a summary of the prediction errors for the three displacement components. The prediction errors were computed from Eq. 4.1. Results are shown for the ROMs of the notched and virgin beam. Clearly, the linear modes chosen to represent the transverse displacements, along with the modeling of the in-plane displacements by the duals, result in a very good matching of the transverse component with respect to NX/Nastran.

The previous results have demonstrated that the reduced order model of the notched beam is able to capture accurately the displacement field of this beam, thereby extending the existing validation cases of [9, 12 and 21-24]. Furthermore, it has been observed, not too unexpectedly, that the displacement fields of the notched and virgin beams are indeed very close to each other, suggesting that the latter could be used for the prediction of the response of the former. Before any such connection can be established, however, it is necessary to assess the capability of the notched beam reduced order model to capture the *stress* distribution of this beam.

To this end, shown in Figs 5.23-5.26 are the dominant stresses S_{xx} along the top edge of the beam ($y=0$, $z=h$), as computed by the reduced order model of the notched beam, see Eq. (2.35), and by NX/Nastran nonlinear for all loading cases analyzed above. Clearly, the agreement is very good to excellent, even in the notch near field, as seen from the results in Tables 5.3-5.4. It is thus concluded from these validation cases that the

nonlinear geometric reduced order modeling technique developed is also applicable to notched panels for the prediction of both their displacement and stress fields.
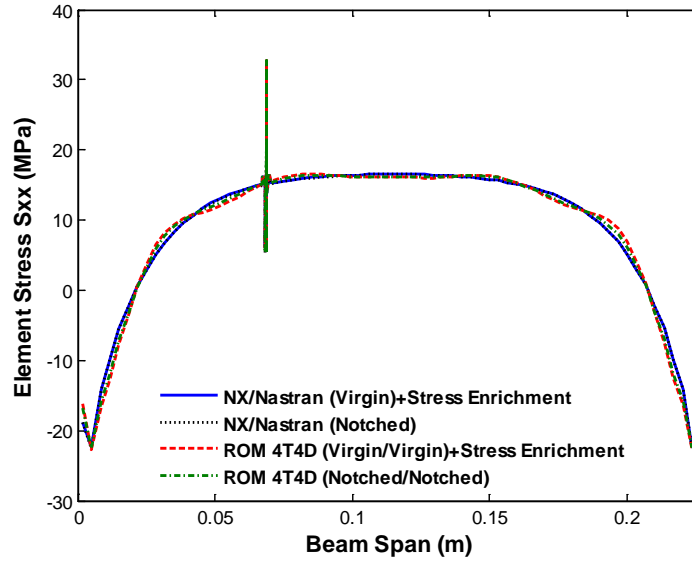
Figure 5.23. Element stress S_{xx} near the beam edge at $y=0$, $z=h$, induced by a uniform pressure of 2.6kPa. Reduced order model with stress enrichment ("ROM 4T4D+Stress Enrichment)", nonlinear static FEA ("NX/Nastran").
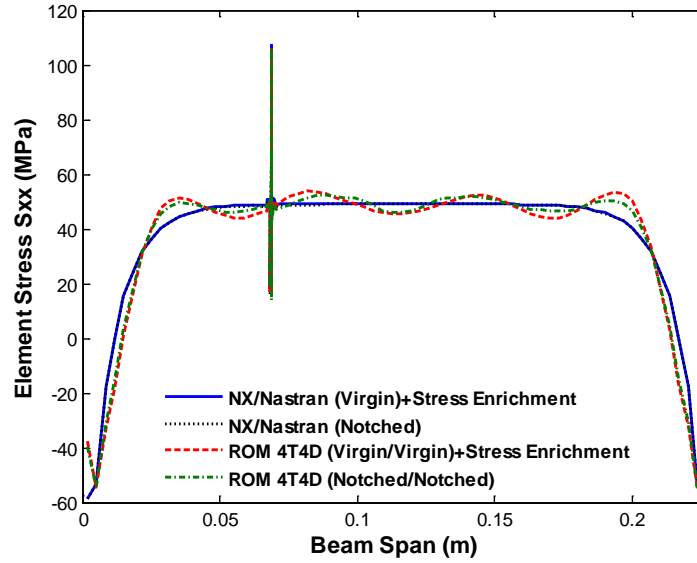
Figure 5.24. Element stress S_{xx} near the beam edge at $y=0$, $z=h$, induced by a uniform pressure of 17kPa. Reduced order model with stress enrichment ("ROM 4T4D+Stress Enrichment)", nonlinear static FEA ("NX/Nastran").

Figure 5.25. Element stress S_{xx} near the beam edge at $y=0$, $z=h$, induced by a uniform pressure of -2.6kPa. Reduced order model with stress enrichment ("ROM 4T4D+Stress Enrichment)", nonlinear static FEA ("NX/Nastran").
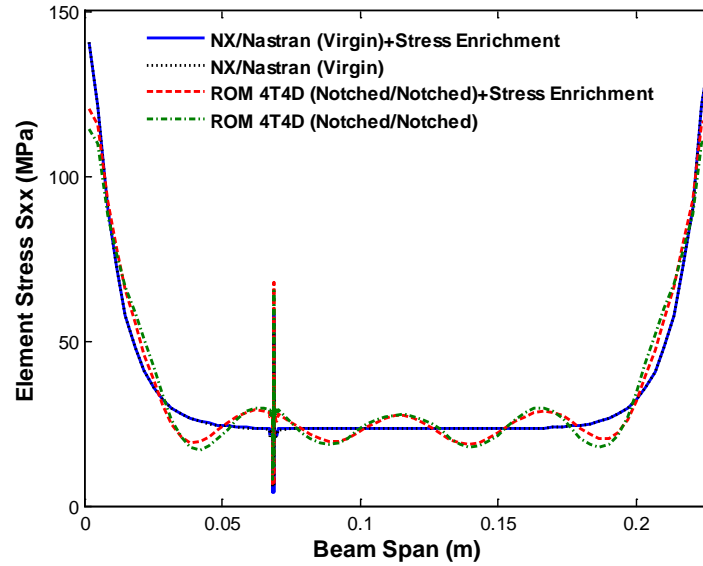
Figure 5.26. Element stress S_{xx} near the beam edge at $y=0$, $z=h$, induced by a uniform pressure of -17kPa. Reduced order model with stress enrichment ("ROM 4T4D+Stress Enrichment)", nonlinear static FEA ("NX/Nastran").
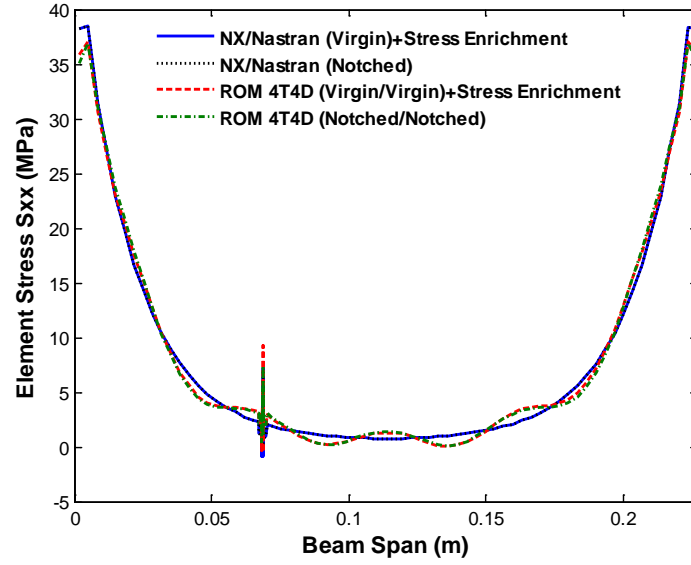
5.5. Dynamic Displacement and Stress Fields

Lastly, a dynamic transverse loading was added and the response computed in

NX/Nastran. The beam was subjected to a uniform pressure on its bottom surface varying

109

randomly in time as a white noise band-limited process in the frequency range [0,1042Hz] to simulate an acoustic loading. The acoustic excitation consisted of an overall sound pressure level (*OASPL*) of 147dB. Furthermore, to permit a close comparison between the NX/Nastran and ROM results, a simple Rayleigh damping model was adopted, i.e. for which the damping matrix is $D = \alpha M + \beta K$ with α=12.838/s and β=2.061E-6s. This selection led to damping ratios between 0.5% and 1.3% for all four transverse modes in the excitation band.

The power spectra of the transverse displacement at the middle of the beam and of the in-plane displacement at the beam quarter point, both at the upper edge (i.e., *y=0, z=h*) are shown in Figs. 5.27-5.29. Clearly, based on the matching of the power spectral density of the NX/Nastran results, the ROM of the notched beam and of the virgin beam match very well the dynamics of the beam. Interestingly, the matching of the power spectrum of the in-plane displacement along the T1 direction at the notch tip is very good as well, even for the ROM of the virgin beam.

The power spectral density of the dominant S_{xx} element stresses, at different locations along the beam are shown in Figs. 5.30-5.32. Away from the notch, the power spectrum of both ROMs match NX/Nastran. Figure 5.32 shows clearly the amplification of the stress field at the notch. The power spectrum corresponding to the ROM of the notched beam matches its NX/Nastran counterpart very well.
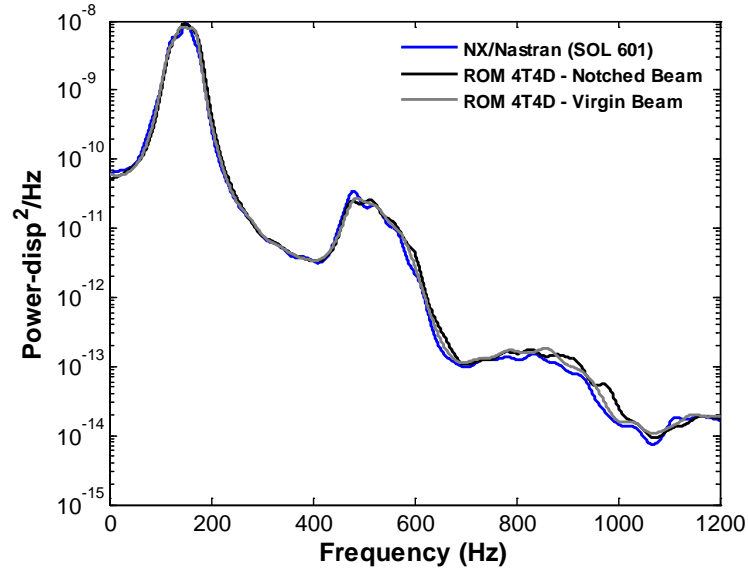
Figure 5.27. Power spectral density of the transverse displacement at the beam middle point, $x=1/2L$, $y=0$, $z=h$ (*OASPL* = 147dB). Reduced order model ("ROM(4T4D)") and FEA ("NX/Nastran").
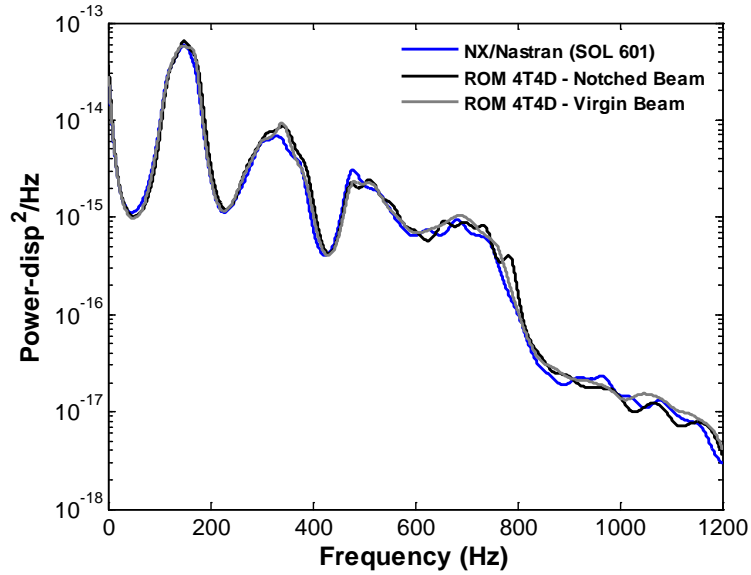
Figure 5.28. Power spectral density of the in-plane displacement at the notch tip (*OASPL* = 147dB). Reduced order model ("ROM(4T4D)") and FEA ("NX/Nastran").
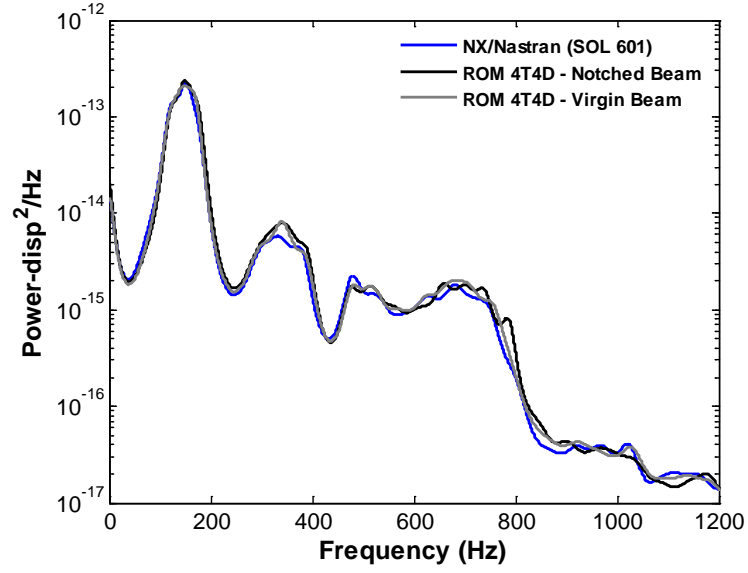
Figure 5.29. Power spectral density of the in-plane displacement at the beam quarter point, $x=1/4L$, $y=0$, $z=h$ (*OASPL* = 147dB). Reduced order model ("ROM(4T4D)") and FEA ("NX/Nastran").
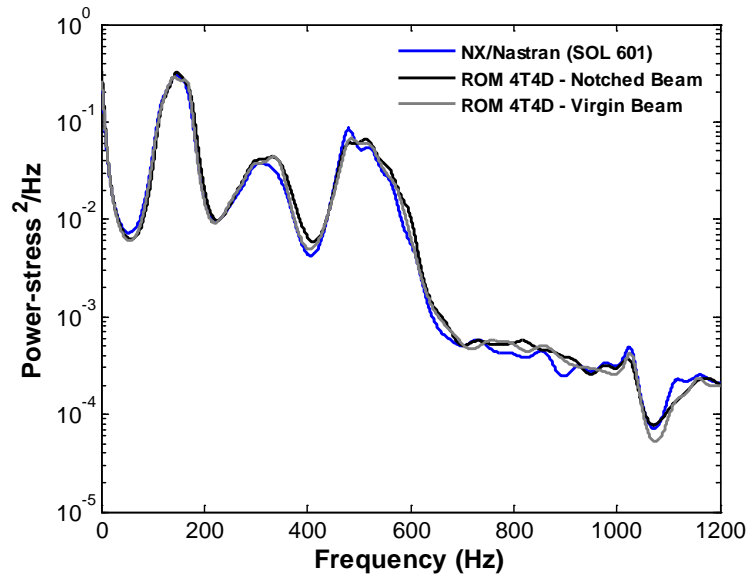
Figure 5.30. Power spectral density of the S_{xx} element stress near the middle of the beam at $y=0$, $z=h$ (*OASPL* = 147dB). Reduced order model ("ROM(4T4D)") and FEA ("NX/Nastran").
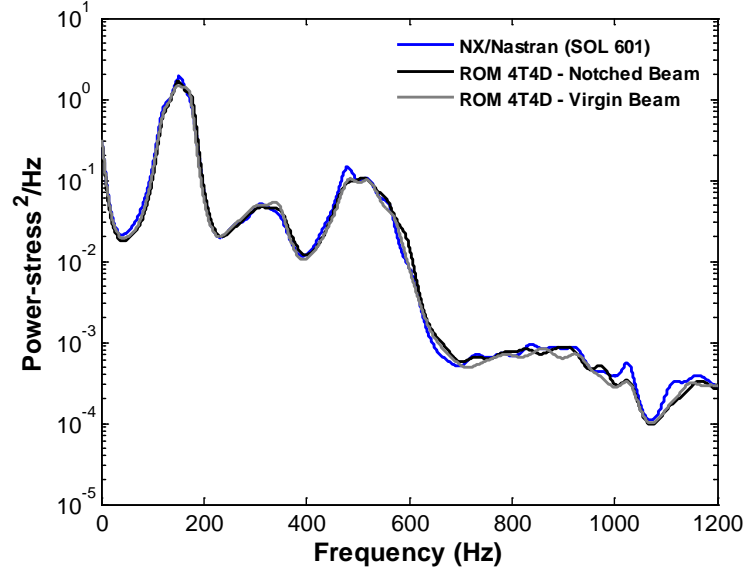
Figure 5.31. Power spectral density of the S_{xx} element stress near the support of the beam at $y=0$, $z=h$ ($OASPL$ = 147dB). Reduced order model ("ROM(4T4D)") and FEA ("NX/Nastran").
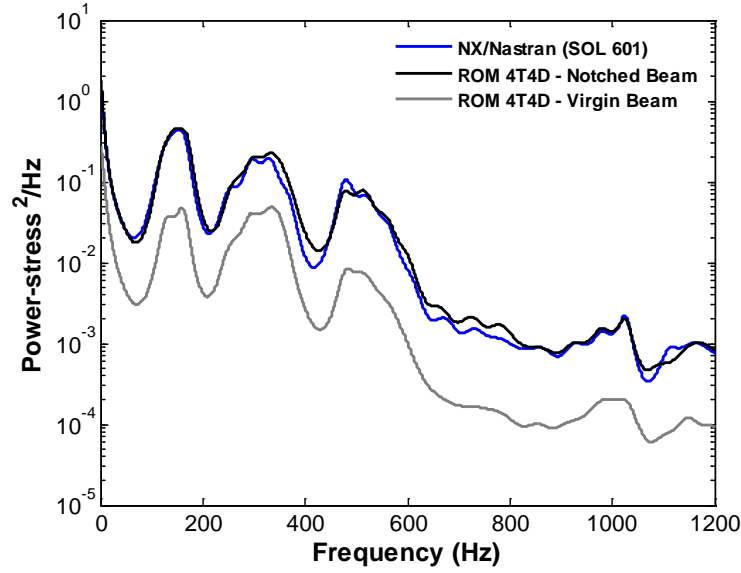
Figure 5.32. Power spectral density of the S_{xx} element stress near the notch at $y=0$, $z=h$ ($OASPL$ = 147dB). Reduced order model ("ROM(4T4D)") and FEA ("NX/Nastran").

5.6. Stress Field Local Enrichment

While the findings from the previous section provide a framework to carry out dynamic simulations at a much reduced computational cost, its applicability to study the propagation of a crack seems limited as the model, i.e., basis functions and coefficients,

113

would need to be updated as the crack propagates. For such analyses, it would be highly desirable to rely on a reference geometry, most simply the virgin beam, and enrich the solution by an extra component accounting for the existence and geometry of the crack.

The loading considered in the present validation cases, and representative of the applied loads on panels, leads primarily to bending and stretching (from the nonlinear effects) and thus a mode I fracture mode is dominant. Accordingly, it is proposed here to add to the virgin beam stress distribution, induced by the pressure loading, a term that accounts for the presence of the crack. Following a stress intensity factor perspective, it is suggested that this term, referred to as an enrichment, be computed as the increment of stress induced by the crack, for a loading corresponding to the in-plane stress distribution of the virgin beam in the vicinity of the crack. Further, this enrichment term will be computed in a linear static analysis. Effectively, this approach replaces the stress distribution of the virgin beam in the vicinity of the crack by a stress distribution of the cracked beam that smoothly connects to the virgin far-field behavior.

Two separate versions of this strategy were considered and assessed on the notched beam from previous sections. In the first one, the loading applied to the notched beam is uniform through the thickness with magnitude equal to the stress estimated from the virgin reduced order model on the top of the beam at 2 thicknesses away from the notch. Note that the stress distribution on the notched beam was computed from the finite element model. However, only one such computation is necessary, i.e., for a unit in-plane load, and then is scaled according to the stress predicted on the virgin beam. This enrichment is equivalent to having a constant stress intensity factor, equal to $S_{xx}^{(\max)}\big/S_{xx}^{(\mathrm{nominal})}$, where $S_{xx}^{(\mathrm{nominal})}$ is equal to the virgin beam stress.

The large deformations considered here lead to a coupling between bending and membrane stretching that modifies the configuration of the stresses for different

114

loading levels. Therefore, the stress intensity factor is also expected to change as the loading level is modified. In this light, the second stress enrichment considered was computed by applying a pressure varying through the thickness and equal to the S_{xx} stress distribution at a location 2 beam thicknesses from the center of the notch. This pressure distribution was applied in a linear static analysis to one of the ends of the beam, while keeping the other end fixed. As with the previous enrichment, this analysis was performed on both notched and virgin beams. Then, the resulting stress from the notched beam was subtracted by the stress field from the virgin beam to obtain the localized stress at the location of the notch. The disadvantage of this method is that a linear static analysis has to be performed every time the loading changes.

5.7. Validation of Stress Enrichment: Static Loading

Shown in Table 5.4 are the peak stresses at the notch, as computed by the reduced order model of the virgin beam with the two enrichments previously described. Clearly, the agreement is very good for the largest stresses (Case 1 and Case 2). Note that the stresses of the NX/Nastran analysis for the virgin beam were enriched as well to assess the accuracy of the enrichment procedure independently of the reduced order model. The enriched NX/Nastran stress results agree very well with the corresponding predictions on the notched beam.

Table 5.4. Peak in-plane element stresses in the notch region for the four loading cases studied: 2.6kPa (Case 1), 17kPa (Case 2), -2.6kPa (Case 3), -17kPa (Case 4). Relative errors are with respect to the Nastran results of the notched beam.

Computation	Case 1		Case 2		Case 3		Case 4	
	MPa	Erel (%)	MPa	Erel (%)	MPa	Erel (%)	MPa	Erel (%)
Nastran Notched Beam	32.3		105.7		6.4		55.4	
Nastran Virgin Beam + Enrichment #1	32.2	0.3	107	1.2	7.2	12.5	58.2	5
Nastran Virgin Beam + Enrichment #2	32.3	0	107.2	1.4	7.1	11	58	4.6
ROM Notched Beam	32.7	1.2	105.8	0.1	7.3	14	65.2	17
ROM Virgin + Enrichment #1	32.7	1.2	105.6	0.1	9.3	45	67.7	22
ROM Virgin + Enrichment #2	32.8	1.5	105.9	0.2	9.2	44	67.7	22

5.8. Validation of Stress Enrichment: Dynamic Loading

For completeness it was desired to assess the effect of the enrichments in a dynamic analysis. The dynamic loading described in section 5.5 was used. The power spectral density of the S_{xx} element stresses, at different locations along the beam are shown in Figs. 5.33-5.36. Interestingly, both enrichments lead to almost identical stress results. As seen in Fig. 5.33, the addition of the two enrichment schemes (described in section 5.5) to the ROM of the virgin beam, resulted in a good matching of NX/Nastran near the notch. This clearly is very pleasing, especially after looking at the results shown in Fig. 5.32.

Figure 5.33. Power spectral density of the S_{xx} element stress near the notch tip at $y=0$, $z=h$ (*OASPL* = 147dB). Reduced order model ("ROM(4T4D)") and FEA ("NX/Nastran").

Figure 5.34. Power spectral density of the S_{xx} element stress near the middle of the beam at $y=0$, $z=h$ (*OASPL* = 147dB). Reduced order model ("ROM(4T4D)") and FEA ("NX/Nastran").

117

Figure 5.35. Power spectral density of the S_{xx} element stress at 2 beam thicknesses from the notch tip and $y=0$, $z=h$ (*OASPL* = 147dB). Reduced order model ("ROM(4T4D)") and FEA ("NX/Nastran").
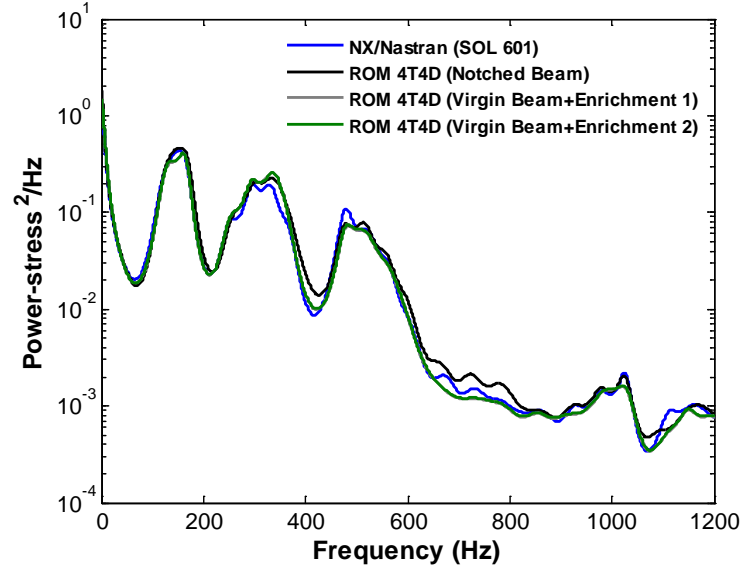

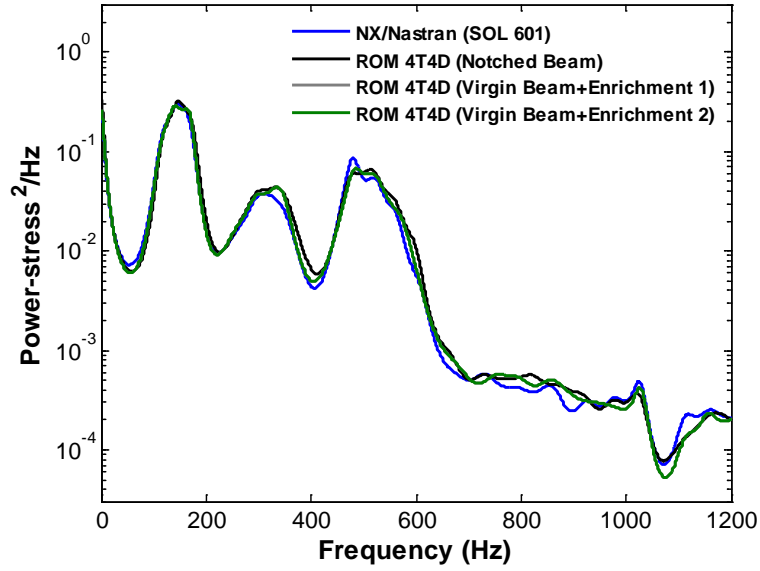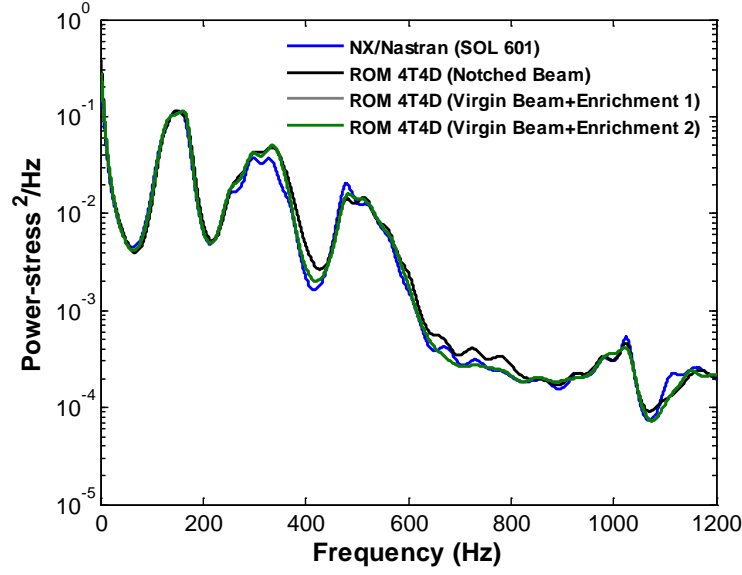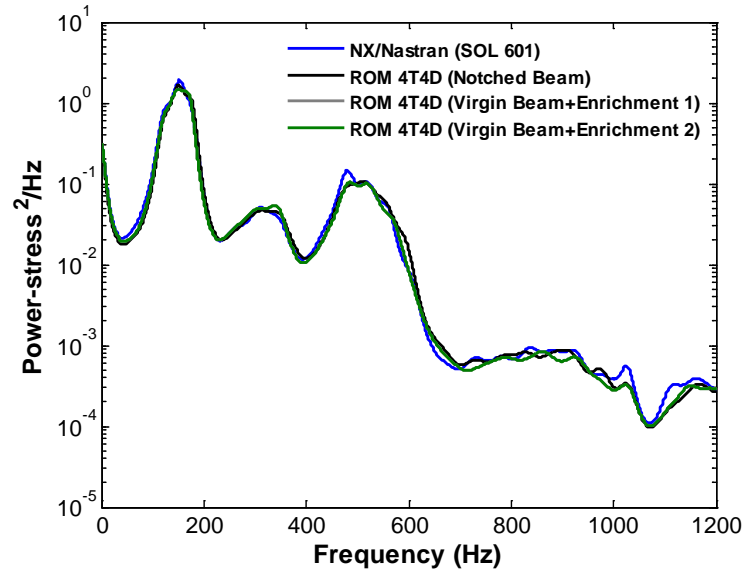Figure 5.36. Power spectral density of the S_{xx} element stress near the support of the beam at $y=0$, $z=h$ (*OASPL* = 147dB). Reduced order model ("ROM(4T4D)") and FEA ("NX/Nastran").

CHAPTER 6

ALGORITHMIC IMPROVEMENTS

6.1. Introduction

As discussed previously, due the large number of modes that may be needed to capture the response of a complex structure computational challenges may arise, not only in the construction process but also in the solution of the ROM equations. Challenges in the construction were addressed in Chapter 3, more specifically in the identification of the nonlinear stiffness coefficients. With respect to the solution of the ROM equations, two approaches will be presented in the present chapter to reduce the computational effort associated with their solution.

6.2. Benefits of "Cleaning" the Model in CPU Time

One of the major computational challenges associated with the solution of the ROM equations is the evaluation of the nonlinear restoring force

$$\left(\underline{\overline{K}}_{NL}\right)_i = \sum_{j=1}^{m}\sum_{l=j}^{m}\overline{K}_{ijl}^{(2)}q_j q_l + \sum_{j=1}^{m}\sum_{l=j}^{m}\sum_{p=1}^{m}\overline{K}_{ijlp}^{(3)}q_j q_l q_p \ . \tag{6.1}$$

As mentioned in Chapter 2, the number of nonlinear stiffness coefficients for a ROM with M modes is approximately equal to $M^4/6$. Therefore, a basis with 60 modes would lead to approximately 2 million coefficients. Clearly, the computational effort involved in computing the expression in Eq. (6.1) can be very large if one considers that this has to be performed for every iteration in the nonlinear solution and every time step to be analyzed.

The reduced order modeling procedure relies on a finite element model of the structure. In the present situation of "large" deflections, the von Karman strain definition is generally adopted.

$$\varepsilon_x = \frac{\partial u_1}{\partial x} + \frac{1}{2}\left(\frac{\partial u_3}{\partial x}\right)^2 \qquad \varepsilon_y = \frac{\partial u_2}{\partial y} + \frac{1}{2}\left(\frac{\partial u_3}{\partial y}\right)^2 \qquad \varepsilon_z = \frac{\partial w}{\partial z} = 0$$

$$\gamma_{xy} = \frac{1}{2}\left[\frac{\partial u_1}{\partial y} + \frac{\partial u_2}{\partial x} + \left(\frac{\partial u_3}{\partial x}\right)\left(\frac{\partial u_3}{\partial y}\right)\right] \qquad \gamma_{xz} = \frac{1}{2}\left[\frac{\partial u_1}{\partial z} + \frac{\partial u_3}{\partial x}\right] \qquad (6.2)$$

$$\gamma_{yz} = \frac{1}{2}\left[\frac{\partial u_2}{\partial z} + \frac{\partial u_3}{\partial y}\right].$$

The basic assumption of the von Karman strain definition is that the force induced transverse motions in the weak bending direction are much larger than the in-plane displacement induced by the nonlinear coupling with the transverse displacement. While the low-frequency linear modes included in the reduced order model have in general dominant transverse components (i.e., in the direction normal to the panel), the dual modes have dominant in-plane features.

In this light, since the nonlinear stiffness coefficients are computed from the finite element model of the structure, the coefficients related to the product of two or three dual modes are expected to have a negligible effect in the solution of the generalized coordinates from the ROM equations of motion. This is expected to be the case as long as the strain-displacement relations from Eq. (6.2) are used in the finite element package used to compute the stiffness coefficients. With this in mind, the following stiffness coefficients could be ignored in the evaluation of Eq. (6.1): $K^{(2)}_{tii}$, $K^{(2)}_{iti}$, $K^{(2)}_{iii}$, $K^{(3)}_{ttii}$, $K^{(3)}_{tiii}$, $K^{(3)}_{itti}$, $K^{(3)}_{itii}$, and $K^{(3)}_{iiii}$, where, the index t corresponds to a linear mode, the index i corresponds to a dual mode. Furthermore, due to the symmetry of the coefficients, $K^{(2)}_{tii}$ and $K^{(2)}_{tii}$ have to be eliminated because K_{tii} and K_{ttii} were removed. In order to ensure convergence of the solution, the cubic coefficients $K^{(3)}_{ttti}$ and $K^{(3)}_{ittt}$ were ignored in the evaluation of Eq. (6.1).

This approach was validated on the nonlinear static and dynamic solutions from Chapter 4. First, the 82-mode model from the nonlinear static validation was investigated. Shown in Table 6.1 are the prediction errors for the full and the "cleaned" models along with the computation times needed for the solution of the problem.

Table 6.1. Comparison of relative errors and CPU time between "Full Model" and "Cleaned Model".

	T3	In-plane Mag.	T2	T1	CPU Time
Full Model	1.2%	4.3%	3.3%	36%	9 minutes
Cleaned Model	1.4%	4.5%	3.4%	37.7%	1 minute

The correlation of the cleaned solution with the full one is very good and the reduction in the CPU time is noticeable.

The validation on the dynamic problem with an acoustic excitation of 144dB yielded excellent results as well. Shown in Figs. 6.1-6.6 is a comparison of the transverse and in-plane response at bays 1, 2, and 5 of the 9-bay panel from Chapter 4. Clearly, the correlation between the "full" and "cleaned" solutions is excellent. In addition, the CPU time for the "cleaned" solutions was 6.5 times lower than the one for the "full" solution.

Figure 6.1. Power spectral density of the transverse (T3) displacement at the middle point of bay 5. Reduced order models "Full" and "Cleaned", *SPL* =144dB.

Figure 6.2. Power spectral density of the in-plane (T1) displacement at the middle point of bay 5. Reduced order models "Full" and "Cleaned", *SPL* =144dB.
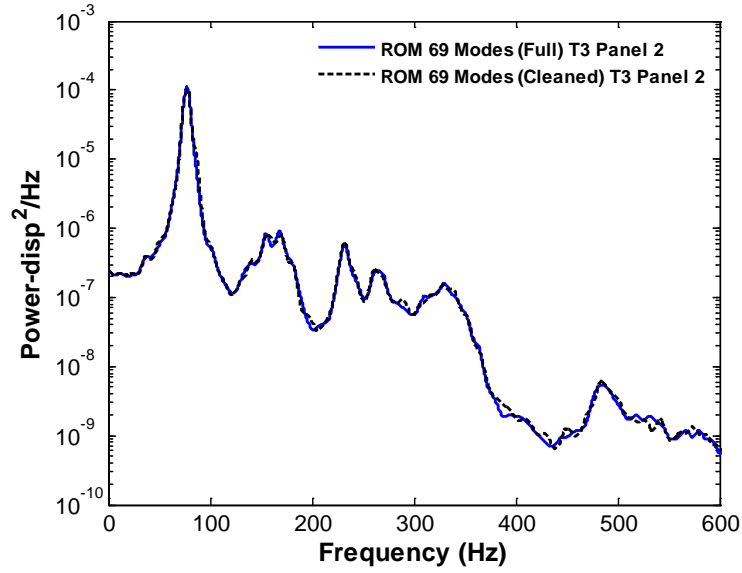
Figure 6.3. Power spectral density of the transverse (T3) displacement at the middle point of bay 2. Reduced order models "Full" and "Cleaned", *SPL* =144dB.

Figure 6.4. Power spectral density of the in-plane (T2) displacement at the middle point of bay 2. Reduced order models "Full" and "Cleaned", *SPL* =144dB.
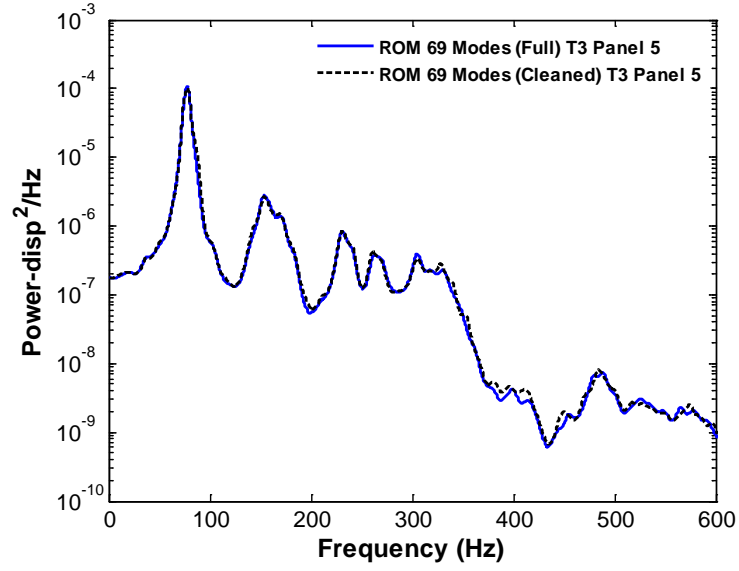
Figure 6.5. Power spectral density of the transverse (T3) displacement at the middle point of bay 1. Reduced order models "Full" and "Cleaned", *SPL* =144dB.
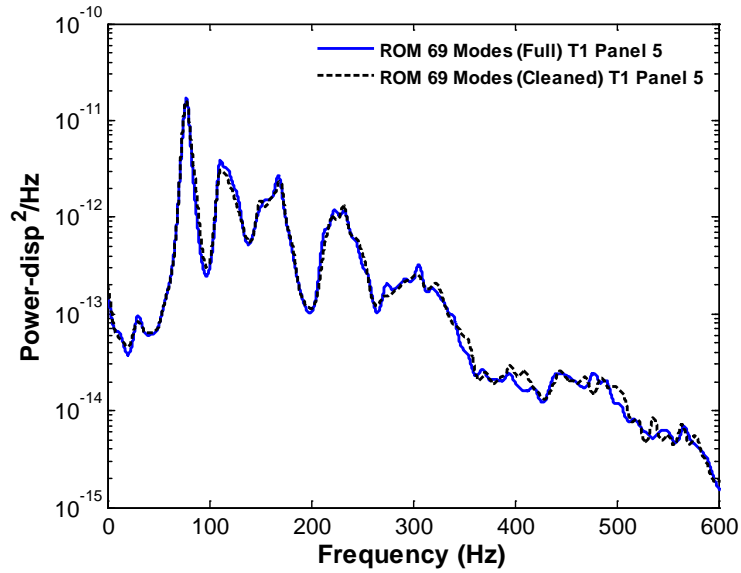

Figure 6.6. Power spectral density of the in-plane (T1) displacement at the middle point of bay 1. Reduced order models "Full" and "Cleaned", *SPL* =144dB.

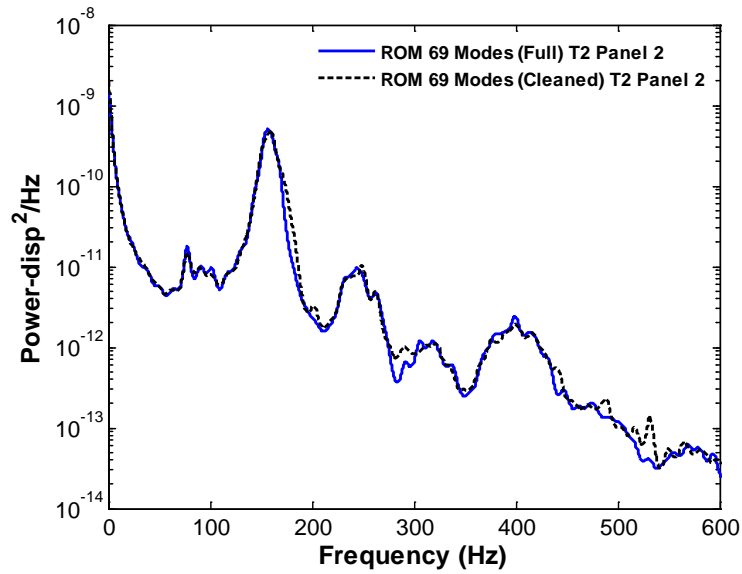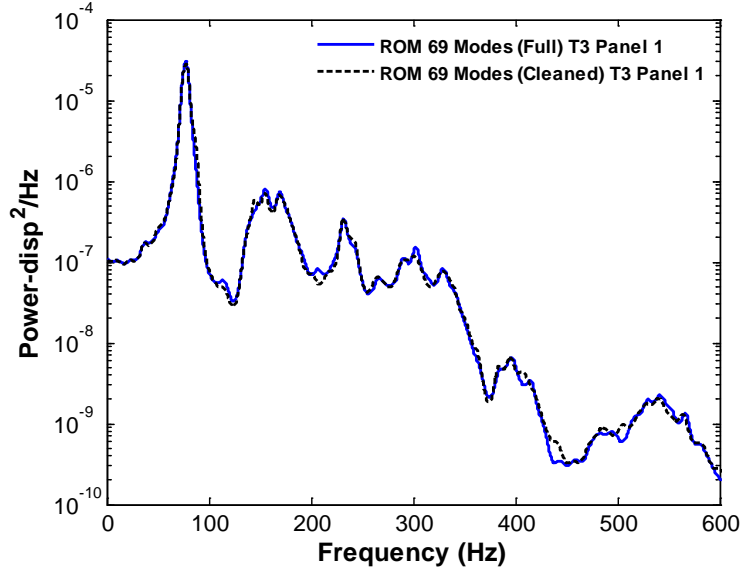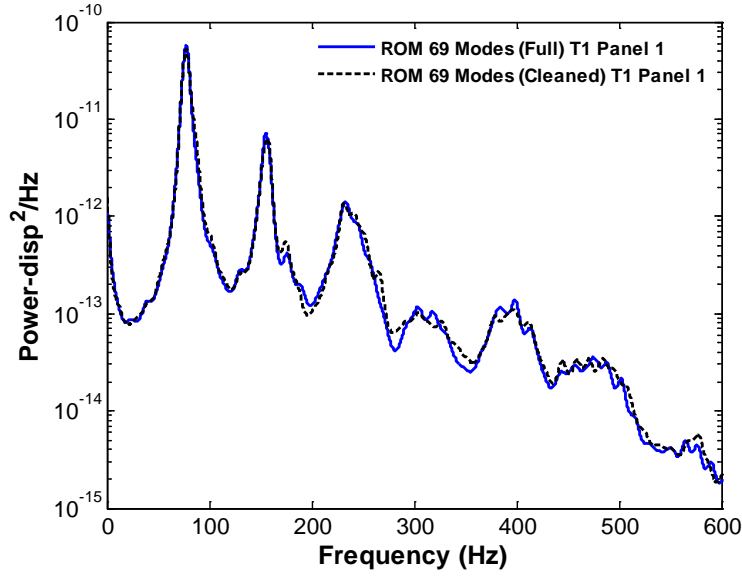### 6.3. Static Condensation of the Dual Modes

As discussed in previous chapters, the purpose of the dual modes is to capture the

in-plane displacement induced by large loading conditions through the nonlinear coupling

with the transverse deflection. For simple structures, such as a clamped-clamped beam under pure transverse loading conditions, they are not directly excited by the loading, but respond quasi-statically [4, 14-15]. With this in mind, the inertia of the duals could be neglected and the generalized coordinates of the dual modes solved for explicitly and substituted into the equations of the linear modes. This in turn would lead to a reduction of the number of equations to be solved and possibly of the nonlinear iterations needed for the solution to converge at every time step.

In this light, the ROM equations can be split into the equations of the linear modes and those of the dual modes. Assuming that the model consists of one linear mode and one dual, using the "cleaning" scheme from the previous section, and assuming the dual modes to act quasi-statically, the resulting equations are as follows

$$
\begin{aligned}
M_{tt}\ddot{q}_t + C_{tt}\dot{q}_t + K_{tt}q_t + K_{ttt}q_t^2 + K_{tti}q_tq_i + K_{tttt}q_t^3 &= F_t \\
K_{ii}q_i + K_{itt}q_t^2 &= F_i
\end{aligned}
\tag{6.3}
$$

where, the index t corresponds to a linear mode, the index i corresponds to a dual mode, and the forces F_t and F_i are time dependent. Then, solving for the generalized coordinate of the dual mode, q_i, from the second equation, and substituting it into the equation of the linear mode yields

$$
M_{tt}\ddot{q}_t + C_{tt}\dot{q}_t + K_{tt}q_t + K_{ttt}q_t^2 + K_{tti}q_t K_{ii}^{-1}\left(F_i - K_{itt}q_t^2\right) + K_{tttt}q_t^3 = F_t .
\tag{6.4}
$$

Finally, rearranging terms the following expression is obtained

$$
M_{tt}\ddot{q}_t + C_{tt}\dot{q}_t + \left(K_{tt} + K_{tti}K_{ii}^{-1}F_i\right)q_t + K_{ttt}q_t^2 + \\
+ \left(K_{tttt} - K_{tti}K_{ii}^{-1}K_{itt}\right)q_t^3 = F_t .
\tag{6.5}
$$

For the 9-bay panel F_i is not equal to zero, so it leads to a parametric type excitation. In this case, the computational effort is increased since the inverse of

125

$K_{tt} + K_{tti} K_{ii}^{-1} F_i$ would have to be computed for every time step. Accordingly, this

approach was not adopted.

CHAPTER 7

SUMMARY

The focus of this investigation has been on the expansion of the current reduced order modeling techniques of geometrically nonlinear problems to problems in the micro-scale and macro-scale.

First, a background on the derivation of the ROM equations of motion was given. In addition, the identification of the ROM parameters and the selection of the basis needed to represent the displacement field of the structure were discussed.

Then, two challenges associated with the analysis of complex structural models were identified: the identification of the ROM stiffness coefficients and the selection of the basis. Two key modifications of the existing approaches were described:

(1) A novel identification strategy of the reduced order model parameters was derived which is based on the use of the tangent stiffness matrix and necessitates a computational effort only proportional to M^2, where M is the number of basis functions, as opposed to M^3 in the current formulations.

(2) The linear and dual mode basis selection strategy was extended to include eigenvectors of the tangent stiffness matrix at key static deformations.

The above novel developments were successfully validated on the nonlinear static and dynamic responses of a 9-bay panel structure modeled with 96,156 degrees of freedom within Nastran. In addition to the conventional ROM approach, a multi-scale analysis was explored. This approach was useful in gaining more understanding of the physics of the 9-bay panel considered in this section.

Furthermore, a first assessment of the predictive capabilities of nonlinear reduced order models for notched panels was carried out. An aluminum clamped-clamped beam with a notch placed at 30% of its length and of depth equal to a quarter of the thickness

was considered as a typical panel. As expected, the notch was found to have a negligible effect on the first few natural frequencies of the beam, as compared to the virgin beam, but also on the corresponding mode shapes. In addition, only small notch-related effects could be detected on the in-plane component of the dual modes, which are basis functions constructed to capture the nonlinear transverse in-plane coupling occurring in large deformations. However, a large, rather broad peak was observed in the smaller transverse component of the dual modes of the notched beam which is absent on the corresponding plot for the virgin beam.

A displacement field induced by a uniform pressure on the beam, large enough to induce nonlinearity, i.e. peak transverse displacements of the order of 2 and 4 thicknesses, was also found to be very weakly dependent on the notch. Furthermore, this displacement field was shown to be well predicted by the reduced order models of both notched and virgin beams. Also, a dynamic validation was carried out and the matching of the power spectrum of the displacement at selected points was excellent.

In regards to the prediction of the stress field, it was found that the notched beam reduced order model was indeed able to capture accurately the stress distribution induced by the pressure loading in both static and dynamic loading cases.

Nevertheless, it was questioned whether a prediction based on the virgin beam reduced order model could also be used if appropriately "enriched" with the notched beam stress field in a superposition-like manner. Two enrichment options were assessed that rely on this stress field as obtained, in a *linear* finite element static analysis, from a notched beam subjected to the stress state induced on the virgin beam near the notch location. This methodology led to good to excellent predictions of the stress field near the notch for both static and dynamic loading cases.

The last chapter of this work dealt with the assessment of a series of algorithmic improvements aimed at further reducing the CPU time of the solution of the ROM equations of motion. First, it was seen that by taking advantage of the von Karman strain assumption used for the beam and shell elements in NX/Nastran, the computational effort in the evaluation of the nonlinear restoring force could be reduced. This in turn led to substantial reductions in the computational time, with execution times which were up to 9 times faster than before. Also, given that the dual modes are excited quasi-statically, a static condensation of the duals modes was proposed. It was found that the force in the in-plane direction appeared in the coefficient of the linear equations leading to a type of parametric excitation. This in turn increased the computational effort in problems where the in-plane force is not equal to zero.

REFERENCES

[1] Blevins, R.D., Holehouse, I., and Wentz, K.R. "Thermoacoustic Loads and Fatigue of Hypersonic Vehicle Skin Panels." *Journal of Aircraft*, no. 30 (1993): 971-978.

[2] Rao, S.S. *Mechanical Vibrations.* Upper Saddle River, New Jersey: Pearson/Prentice Hall, 2004.

[3] Mignolet, M.P. *Encyclopedia of Aerospace Engineering* by R. Blockley and W. Shyy (joint editors). 1st ed., 3 vols. "Dynamic Response Computations." Wiley & Sons, 2010.

[4] Mignolet, M.P., Przekop, A., Rizzi, S.A., and Spottswood, S.M., "A Review of Indirect/Non-Intrusive Reduced Order Modeling of Nonlinear Geometric Structures," *Journal of Sound and Vibration*, To appear, 2012.

[5] McEwan, M.I., Wright, J.R., Cooper, J.E., and Leung, A.Y.T. "A combined Modal/Finite Element Analysis Technique for the Dynamic Response of a Nonlinear Beam to Harmonic Excitation." *Journal of Sound and Vibration* 243 (2001): 601-624.

[6] Hollkamp, J.J., Gordon, R.W., and Spottswood, S.M. "Nonlinear Modal Models for Sonic Fatigue Response Prediction: A Comparison of Methods." *Journal of Sound and Vibration* 284 (2005): 1145-1163.

[7] Hollkamp, J.J., and Gordon, R.W., 2008, "Reduced-Order Models for Nonlinear Response Prediction: Implicit Condensation and Expansion," *Journal of Sound and Vibration*, Vol. 318, pp. 1139–1153.

[8] Przekop, A., and Rizzi, S.A., "A Reduced Order Method for Predicting High Cycle Fatigue of Nonlinear Structures," *Computers and Structures*, Vol. 84, No. 24-25, pp. 1606-1618, 2006.

[9] Kim, K., Khanna, V., Wang, X.Q., and Mignolet, M.P., "Nonlinear Reduced Order Modeling of Flat Cantilevered Structures," *Proceedings of the 50th Structures, Structural Dynamics, and Materials Conference*, Palm Springs, California, May 4-7, 2009. AIAA Paper AIAA-2009-2492.

[10] Mignolet, M.P., Radu, A.G., and Gao, X. "Validation of Reduced Order Modeling for the Prediction of the Response and Fatigue Life of Panels Subjected to Therm-Acoustic Effects." *Proceedings of the 8th International Conference on Recent Advances in Structural Dynamics.* Southampton, United Kingdom, 2003.

[11] Radu, A., Yang, B., Kim, K., and Mignolet, M.P. "Prediction of the Dynamic Response and Fatigue Life of Panels Subjected to Thermo-Acoustic Loading." *Proceedings of the 45th Structures, Structural Dynamics, and Materials Conference.* Palm Springs, California, 2004. AIAA Paper AIAA-2004-1557.

[12] Kim, K., Wang, X.Q., and Mignolet, M.P., "Nonlinear Reduced Order Modeling of Functionally Graded Plates," *Proceedings of the 49th Structures, Structural Dynamics, and Materials Conference*, Schaumburg, Illinois, Apr. 7-10, 2008. AIAA Paper AIAA-2008-1873.

[13] Przekop A., and Rizzi S.A., "Nonlinear Reduced Order Random Response Analysis of Structures with Shallow Curvature," AIAA Journal Vol. 44 (8), pp. 1767-1778, 2006.

[14] Gordon R.W., and Hollkamp, J.J., "Reduced-Order Modeling of the Random Response of Curved Beams using Implicit Condensation," AIAA-2006-1926, 2006.

[15] Spottswood, S.M., Hollkamp, J.J., and Eason, T.G., "On the Use of Reduced-Order Models for a Shallow Curved Beam Under Combined Loading," *Proceedings of the 49th Structures, Structural Dynamics, and Materials Conference*, Schaumburg, Illinois, Apr. 7-10, 2008. AIAA Paper AIAA-2008-1873.

[16] Przekop, A., and Rizzi, S.A., "Dynamic Snap-Through of Thin-Walled Structures by a Reduced-Order Method," *AIAA Journal*, Vol. 45, No. 10, pp. 2510–2519, 2007.

[17] Spottswood, S.M., Eason, T.G., Wang, X.Q., and Mignolet, M.P., "Nonlinear Reduced Order Modeling of Curved Beams: A Comparison of Methods," *Proceedings of the 50th Structures, Structural Dynamics, and Materials Conference*, Palm Springs, California, May 4-7, 2009. AIAA Paper AIAA-2009-2433.

[18] Kim, K., Kim, Y.C., Mignolet, M.P., Liu, D.D., Chen, P.C., Lee, D.H., "Random Aeroelastic Response Due to Strong Hypersonic Unsteady-Wave/Shock Interaction with Acoustic Loads," *Proceedings of the 48th Structures, Structural Dynamics, and Materials Conference*, Honolulu, Hawaii, Apr. 23-26, 2007. AIAA Paper AIAA-2007-2014.

[19] Liu, D.D., Chen, P.C., Zhang, Z., Wang, Z., Yang, S., Lee, D.H., Mignolet, M.P., Kim, K., Liu, F., Lindsley, N., and Beran, P., "Continuous Dynamic Simulation of Nonlinear Aerodynamic/Nonlinear Structure Interaction (NANSI) for Morphing Wing Aeroelasticity," *Proceedings of the 50th Structures, Structural Dynamics, and Materials Conference*, Palm Springs, California, May 4-7, 2009. AIAA Paper AIAA-2009-2572.

[20] Liu, D.D., Wang, Z., Yang, S., Cai, C., Wang, X.Q., and Mignolet, M.P., "Nonlinear Aeroelastic Methodology for A Membrane-on-Ballute Model with Hypersonic Bow Shock," *Proceedings of the 50th Structures, Structural Dynamics, and Materials Conference*, Palm Springs, California, May 4-7, 2009. AIAA Paper AIAA-2009-2363.

[21] Perez, R., Wang, X.Q., and Mignolet, M.P., "Nonlinear Reduced Order Models for Thermoelastodynamic Response of Isotropic and FGM Panels," *AIAA Journal*, Vol. 49, pp. 630-641, 2011.

[22] Perez, R., Wang, X.Q., and Mignolet, M.P., "Steady and Unsteady Nonlinear Thermoelastodynamic Response of Panels by Reduced Order Models," *Proceedings of the 51th Structures, Structural Dynamics, and Materials Conference*, Orlando, Florida, April 12-15, 2010. AIAA Paper AIAA-2010-2724.

[23] Matney, Perez, R., and Mignolet, M.P., "Nonlinear Unsteady Thermoelastodynamic Response of a Panel Subjected to an Oscillating Flux by Reduced Order Models," *Proceedings of the 52th Structures, Structural Dynamics, and Materials Conference*, Denver, Colorado, April 4-7, 2011. AIAA Paper AIAA-2011-2016.

[24] Matney, A., Perez, R., Spottswood, S.M., Wang, X.Q., and Mignolet, M.P., "Nonlinear Structural Reduced Order Modeling Methods for Hypersonic Structures", *Proceedings of the 53rd Structures, Structural Dynamics, and Materials Conference*, Honolulu, Hawaii, April 23-26, 2012. AIAA Paper AIAA-2012-1972.

[25] Perez, R., Wang, X.Q., and Mignolet, M.P., "Reduced Order Modeling for the Nonlinear Geometric Response of Cracked Panels," *Proceedings of the 52th Structures, Structural Dynamics, and Materials Conference*, Denver, Colorado, April 4-7, 2011. AIAA Paper AIAA-2011-2018.

[26] Bonet, J., and Wood, R.D., *Nonlinear Continuum Mechanics for Finite Element Analysis*, Cambridge: Cambridge University Press, 1997.

[27] Fung, Y.C., and Tong, P. *Classical and Computational Solid Mechanics* . River Edge, New Jersey: World Scientific, 2001.

[28] Muravyov, A.A., and Rizzi, S.A., "Determination of Nonlinear Stiffness with Application to Random Vibration of Geometrically Nonlinear Structures," Computers and Structures, Vol. 81, pp. 1513-1523, 2003

[29] Przekop, A., Rizzi, S.A., and Groen, D.S., "Nonlinear Acoustic Response of an Aircraft Fuselage Sidewall Structure by a Reduced-Order Analysis," *Proceedings of the 9th International Conference on Recent Advances in Structural Dynamics*, Southampton, United Kingdom, Jul. 17-19, 2006.

[30] P. Tiso, E. Jansen, M. Abdalla, "Reduction Method for Finite Element Nonlinear Dynamic Analysis of Shells," *AIAA Journal*, Vol. 49 pp. 2295-2304, 2011.

[31] Buehrle, R.D. Fleming, G.A., Pappa, R.S., and Grosveld, F.W., "Finite Element Model Development For Aircraft Fuselage Structures," *Proceedings of the 18th Modal Analysis Conference*, San Antonio, Texas, Feb., 2000.

[32] Craig Jr., R.R. and Kurdilla, A.J. *Fundamentals of Structural Dynamics.* Hoboken, New Jersey: John Wiley & Sons, 2006.

[33] Mignolet M.P. Soize, C., "Nonparametric Stochastic Modeling of Structures with Uncertain Boundary Conditions and Uncertain Coupling Between Substructures," *Proceedings of the 49th Structures, Structural Dynamics, and Materials Conference*, Schaumburg, Illinois, Apr. 7-10, 2008.

[34] Mignolet, M.P. and Soize, C., "Stochastic reduced order models for uncertain geometrically nonlinear dynamic systems," *Comput. Methods Appl. Mech. Engrg.,* Vol. 197, pp. 3951-3963, 2008.

ATTACHMENT D

Chang, Y.W., "Reduced Order Modeling for the Nonlinear Geometric Response of a Curved Beam," M.S., August 2011.

Reduced Order Modeling For The Nonlinear Geometric Response Of A

Curved Beam

by

Yao-Wen Chang

A Thesis Presented in Partial Fulfillment
of the Requirements for the Degree
Master of Science

Approved June 2011 by the
Graduate Supervisory Committee:

Marc Mignolet, Chair
Joseph Davidson
Stephen Spottswood

ARIZONA STATE UNIVERSITY

July 2011

ABSTRACT

The focus of this investigation is on the renewed assessment of nonlinear reduced order models (ROM) for the accurate prediction of the geometrically nonlinear response of a curved beam. In light of difficulties encountered in an earlier modeling effort, the various steps involved in the construction of the reduced order model are carefully reassessed. The selection of the basis functions is first addressed by comparison with the results of proper orthogonal decomposition (POD) analysis. The normal basis functions suggested earlier, i.e. the transverse linear modes of the corresponding flat beam, are shown in fact to be very close to the POD eigenvectors of the normal displacements and thus retained in the present effort. A strong connection is similarly established between the POD eigenvectors of the tangential displacements and the dual modes which are accordingly selected to complement the normal basis functions.

The identification of the parameters of the reduced order model is revisited next and it is observed that the standard approach for their identification does not capture well the occurrence of snap-throughs. On this basis, a revised approach is proposed which is assessed first on the static, symmetric response of the beam to a uniform load. A very good to excellent matching between full finite element and ROM predicted responses validates the new identification procedure and motivates its application to the dynamic response of the beam which exhibits both symmetric and antisymmetric motions. While not quite as accurate as in the static case, the reduced order model predictions match well their full Nastran counterparts and support the reduced order model development strategy.

DEDICATION

To my parents, my twin brother, and my sister.

ACKNOWLEDGMENTS

TABLE OF CONTENTS

LIST OF TABLES

LIST OF FIGURES

Chapter 1

INTRODUCTION

Modal models have long been recognized as the computationally efficient analysis method of complex linear structural dynamic systems, yielding a large reduction in computational cost but also allowing a convenient coupling with other physics code, e.g. with aerodynamics/CFD codes for aeroelastic analyses. Further, these modal models are easily derived from a finite element model of the structure considered and thus can be obtained even for complex geometries and boundary conditions. However, a growing number of applications require the consideration of geometric nonlinearity owing to the large structural displacements. For example, panels of supersonic/hypersonic vehicles have often in the past been treated in this manner because of the large acoustic loading they are subjected to as well as possible thermal effects. Novel, very flexible air vehicles have provided another, more recent class of situations in which geometric nonlinearity must be included.

For such problems, it would be very desirable to have the equivalent of the modal methods exhibiting: (i) high computational efficiency, (ii) an ease of coupling to other physics codes, and (iii) generality with respect to the structure considered and its boundary conditions. To this end, nonlinear reduced order modeling techniques have been proposed and validated in the last decade [1-13]. Although several variants exist, their construction share the same aspects. First, they involve a *parametric* form of the model, i.e. one in which the nonlinearity is only on the "stiffness" and includes linear, quadratic, and cubic terms of the

1

displacement field generalized coordinates (see chapter below). Second, they rely on an identification strategy of the parameters of the model, i.e. the linear, quadratic, and cubic stiffness coefficients, from a finite element model of the structure for a particular set of "modes" or basis functions. Differences between the existing methods center in particular on the way the linear and nonlinear stiffness coefficients are estimated from a finite element model and on the extent and specificity of the basis functions, i.e. modeling of only the displacements transverse to the structure or all of them.

As may be expected, the first validations of these reduced order models focused on flat structures, beams and plates, and an excellent match between responses predicted by the reduced order models and their full finite element counterparts have been demonstrated. Curved structures, curved beam most notably, have also been investigated in the last few years and a very good match of reduced order model and full finite element results was obtained. Yet, the construction of the reduced order model was not as straightforward in this case as it had been in flat structures, instabilities of the model were sometime obtained.

The issue of constructing stable and accurate nonlinear reduced order models for curved structures is revisited here and an extension of the displacement-based (STEP) identification procedure [14, 8] is first proposed. Then, its application to a curved beam model is demonstrated, and shown to lead to an excellent matching between reduced order model and full finite element predictions.

2

Chapter 2

PARAMETRIC FORMS OF NONLINEAR REDUCED ORDER MODELS

The reduced order models considered here are representations of the response of elastic geometrically nonlinear structures in the form

$$u_i(\underline{X},t) = \sum_{n=1}^{M} q_n(t)\, \psi_i^{(n)}(\underline{X}) \,, i = 1, 2, 3 \tag{2.1}$$

where $u_i(\underline{X},t)$ denotes the displacement components at a point $\underline{X}$ of the structure and at time t. Further, $\psi_i^{(n)}(\underline{X})$ are specified, constant basis functions and $q_n(t)$ are the time dependent generalized coordinates.

A general derivation of linear modal models is classically carried out from linear (infinitesimal) elasticity and it is thus desired here to proceed similarly but with finite deformation elasticity to include the full nonlinear geometric effects. Then, the first issue to be addressed is in what configuration, deformed or undeformed, the governing equations ought to be written. In this regard, note that the basis functions $\psi_i^{(n)}(\underline{X})$ are expected to (a) be independent of time and (b) satisfy the boundary conditions (at least the geometric or Dirichlet ones). These two conditions are not compatible if the basis functions are expressed in the deformed configuration as the locations at which the boundaries are will vary with the level of deformations or implicitly with time. However, these conditions are compatible if one proceeds in the undeformed configuration and thus $\underline{X}$ in Eq. (2.1), will denote the coordinates of a point in the undeformed configuration.

Accordingly, the equations of motion of an infinitesimal element can be expressed as (e.g. see [15, 16], summation over repeated indices assumed)

$$\frac{\partial}{\partial X_k}\left(F_{ij}\, S_{jk}\right) + \rho_0\, b_i^0 = \rho_0\, \ddot{u}_i \ \text{ for } \underline{X} \in \Omega_0 \qquad (2.2)$$

where S denotes the second Piola-Kirchhoff stress tensor, ρ_0 is the density in the reference configuration, and $\underline{b}^0$ is the vector of body forces, all of which are assumed to depend on the coordinates X_i. Further, in Eq. (2.2), the deformation gradient tensor F is defined by its components F_{ij} as

$$F_{ij} = \frac{\partial x_i}{\partial X_j} = \delta_{ij} + \frac{\partial u_i}{\partial X_j} \qquad (2.3)$$

where δ_{ij} denotes the Kronecker symbol and the displacement vector is $\underline{u} = \underline{x} - \underline{X}$, $\underline{x}$ being the position vector in the deformed configuration. Finally, Ω_0 denotes the domain occupied by the structure in the undeformed configuration. It has a boundary $\partial\Omega_0$ composed of two parts: $\partial\Omega_0^t$ on which the tractions $\underline{t}^0$ are given and $\partial\Omega_0^u$ on which the displacements are specified (assumed zero here). Thus, the boundary conditions associated to Eq. (2.2) are

$$F_{ij}\, S_{jk}\, n_k^0 = t_i^0 \ \text{ for } \underline{X} \in \partial\Omega_0^t \qquad (2.4)$$

$$\underline{u} = \underline{0} \ \text{ for } \underline{X} \in \partial\Omega_0^u \qquad (2.5)$$

Note in Eqs (2.2) and (2.4) that the vectors $\underline{b}^0$ and $\underline{t}^0$ correspond to the transport ("pull back") of the body forces and tractions applied on the deformed configuration, i.e. $\underline{b}$ and $\underline{t}$, back to the reference configuration (see [15, 16]).

To complete the formulation of the elastodynamic problem, it remains to specify the constitutive behavior of the material. In this regard, it will be assumed here that the second Piola-Kirchhoff stress tensors S is linearly related to the Green strain tensor E defined as

$$E_{ij} = \frac{1}{2}\left(F_{ki}\,F_{kj} - \delta_{ij}\right)$$ (2.6)

That is,

$$S_{ij} = C_{ijkl}\,E_{kl}$$ (2.7)

where C_{ijkl} denotes the fourth order elasticity tensor.

Introducing the assumed displacement field of Eq. (2.1) in Eqs (2.2)-(2.7) and proceeding with a Galerkin approach leads, after some manipulations, to the desired governing equations, i.e.

$$M_{ij}\ddot{q}_j + D_{ij}\dot{q}_j + K_{ij}^{(1)}\,q_j + K_{ijl}^{(2)}q_jq_l + K_{ijlp}^{(3)}q_jq_lq_p = F_i$$ (2.8)

in which M_{ij} are mass components, $K_{ij}^{(1)}$, $K_{ijl}^{(2)}$, and $K_{ijlp}^{(3)}$ are the linear, quadratic, and cubic stiffness coefficients, and F_i are the modal forces. Note that the damping term $D_{ij}\dot{q}_j$ has been added in Eq. (2.8) to collectively represent various dissipation mechanisms. Further, the symmetrical role of j and l in the quadratic terms and j, l, and p in the cubic ones indicates that the summations over those indices can be restricted to $p \geq l \geq j$.

Once the generalized coordinates $q_j(t)$ have been determined from Eq. (2.8), the stress field can also be evaluated from Eqs. (2.3), (2.6), and (2.7). Specifically, it is found that every component of the second Piola-Kirchhoff stress tensor can be expressed as

$$S_{ij} = \bar{S}_{ij} + \sum_m \hat{S}_{ij}^{(m)} q_m + \sum_{m,n} \tilde{S}_{ij}^{(m,n)} q_m q_n \qquad (2.9)$$

where the coefficients $\bar{S}_{ij}$, $\hat{S}_{ij}^{(m)}$, and $\tilde{S}_{ij}^{(m,n)}$ depend only on the point $\underline{X}$ considered.

Chapter 3

INDENTIFICATION OF THE REDUCED ORDER MODEL PARAMETERS

One of the key component of the present as well as related nonlinear reduced order modeling approaches (see introduction) is the identification of the parameters of Eqs (8) and (9) from a finite element model of the structure considered in a standard (e.g. Nastran, Abaqus, Ansys) software. The reliance on such commercial codes gives access to a broad database of elements, boundary conditions, numerical algorithms, etc. but is a challenge from the standpoint of the determination of the parameters of Eqs (2.8) and (2.9) as one has only limited access to the detailed element information and matrices.

In a finite element format, the displacement field of components $u_i(\underline{X}, t)$ is replaced by its discretized counterpart, the vector $\underline{u}(t)$, represented as

$$\underline{u}(t) = \sum_{n=1}^{M} q_n(t) \, \underline{\psi}^{(n)} \tag{3.1}$$

where $\underline{\psi}^{(n)}$ are the discretized basis functions. The estimation of the mass components M_{ij} and modal forces F_i is achieved as in linear modal models, i.e.

$$M_{ij} = \underline{\psi}^{(i)T} \, M_{FE} \, \underline{\psi}^{(j)} \tag{3.2}$$

$$F_i = \underline{\psi}^{(i)T} \, \underline{F}(t) \tag{3.3}$$

where M_{FE} is the finite element mass matrix and $\underline{F}(t)$ is the excitation vector on the structure.

7

Next is the determination of the stiffness coefficients $K_{ij}^{(1)}$, $K_{ijl}^{(2)}$, and $K_{ijlp}^{(3)}$. In this regard, note first that the linear coefficients $K_{ij}^{(1)}$ could be determined as in linear modal models, i.e.

$$K_{ij}^{(1)} = \underline{\psi}^{(i)T}\, K_{FE}^{(1)}\, \underline{\psi}^{(j)} \tag{3.4}$$

where $K_{FE}^{(1)}$ is the finite element linear stiffness matrix. Another approach must be adopted however for $K_{ijl}^{(2)}$ and $K_{ijlp}^{(3)}$ as nonlinear stiffness matrices are typically not available. Two approaches have been proposed to identify these parameters (and potentially the linear ones as well) from a series of static finite element solutions. The first one relies on prescribing a series of load cases and projecting the induced responses on the basis functions $\underline{\psi}^{(n)}$ to obtain the corresponding generalized coordinates values $q_j^{(p)}$, p being the index of the load cases. Then, introducing these values into Eq. (2.8) for each load case yields

$$K_{ij}^{(1)}\, q_j^{(p)} + K_{ijl}^{(2)} q_j^{(p)} q_l^{(p)} + K_{ijlr}^{(3)}\, q_j^{(p)} q_l^{(p)} q_r^{(p)} = F_i^{(p)}$$

$$i = 1, ..., M \tag{3.5}$$

Proceeding similarly for P load cases yields a set of linear algebraic equations for the coefficients $K_{ijl}^{(2)}$ and $K_{ijlp}^{(3)}$, and possibly the linear stiffness coefficients $K_{ij}^{(1)}$ as well, which can be solved in a least squares format to complete the identification of the stiffness parameters.

8

An alternate strategy has also been proposed (e.g. see [14]) in which the *displacements* are prescribed and the required force distributions are obtained from the finite element code. The corresponding modal forces are then evaluated from Eq. (3.3) and a set of equations of the form of Eq. (3.5) is again obtained. Appropriately selecting the displacement fields to be imposed can lead to a particularly convenient identification of the stiffness coefficients. Specifically, the imposition of displacements proportional to the basis function $\underline{\psi}^{(n)}$ only, i.e.

$$\underline{u} = q_n \, \underline{\psi}^{(n)}$$

$$\underline{\hat{u}} = \hat{q}_n \, \underline{\psi}^{(n)} \tag{3.6}$$

$$\underline{\tilde{u}} = \tilde{q}_n \, \underline{\psi}^{(n)}$$

leads to the 3 sets of equations

$$K_{in}^{(1)} \, q_n + K_{inn}^{(2)} q_n^2 + K_{innn}^{(3)} \, q_n^3 = F_i$$

$$K_{in}^{(1)} \, \hat{q}_n + K_{inn}^{(2)} \hat{q}_n^2 + K_{innn}^{(3)} \, \hat{q}_n^3 = \hat{F}_i$$

$$K_{in}^{(1)} \, \tilde{q}_n + K_{inn}^{(2)} \tilde{q}_n^2 + K_{innn}^{(3)} \, \tilde{q}_n^3 = \tilde{F}_i \tag{3.7}$$

(no sum on *n*)

for $i = 1, ..., M$. In fact, these 3 sets of equations permit the direct evaluation of the coefficients $K_{in}^{(1)}$, $K_{inn}^{(2)}$, and $K_{innn}^{(3)}$ for all *i*. Repeating this effort for $n = 1, ..., M$ thus yields a first set of stiffness coefficients.

Proceeding similarly but with combinations of two basis functions, i.e.

9

$$u = q_n \, \underline{\psi}^{(n)} + q_m \, \underline{\psi}^{(m)} \quad m \geq n \tag{3.8}$$

and relying on the availability of the coefficients $K_{in}^{(1)}$, $K_{inn}^{(2)}$, $K_{innn}^{(3)}$ and $K_{im}^{(1)}$, $K_{imm}^{(2)}$, $K_{immm}^{(3)}$ determined above, leads to equations involving the three coefficients $K_{inm}^{(2)}$, $K_{innm}^{(3)}$, and $K_{inmm}^{(3)}$. Thus, imposing three sets of displacements of the form of Eq. (3.8) provides the equations needed to also identify $K_{inm}^{(2)}$, $K_{innm}^{(3)}$, and $K_{inmm}^{(3)}$.

Finally, imposing displacement fields linear combination of three modes, i.e.

$$u = q_n \, \underline{\psi}^{(n)} + q_m \, \underline{\psi}^{(m)} + q_r \, \underline{\psi}^{(r)} \quad r \geq m \geq n \tag{3.9}$$

permits the identification of the last coefficients, i.e. $K_{inmr}^{(3)}$.

The above approach, referred to as the STEP (STiffness Evaluation Procedure), has often been used and has generally led to the reliable identification of the reduced order model parameters, especially in connection with flat structures, with values of the generalized coordinates q_s of the order of, or smaller than, the thickness. However, in some curved structures, e.g. the curved beam of [11], several of the models identified by the STEP process were found to be unstable, i.e. a finite valued static solution could not be obtained with a time marching algorithm, when the applied load magnitude exceeded a certain threshold. This problem occurred most notably for loads inducing a snap-through of the curved beam.

10

In studying this problem, it was observed that the magnitude of some of the terms $K_{ij}^{(1)} q_j$, $K_{ijl}^{(2)} q_j q_l$, and/or $K_{ijlr}^{(3)} q_j q_l q_r$ computed at a large amplitude (of the order of 10 thicknesses say) snap-through solution were much larger (2 orders of magnitude was routinely observed) than the driving $F_i^{(p)}$. Accordingly, the balance of the terms on the left-hand-side of Eq. (2.8) must be accomplished quite accurately or, equivalently, a very good accuracy is required on the stiffness coefficients, to have a good match of the full finite element solution in such cases. A sensitivity analysis of the stiffness coefficients identified by the above approach in the curved beam case (see description below) suggested that the accuracy requirements were right at the limit of what could be expected and thus another identification procedure was sought.

The perceived weakness of the procedure based on Eqs (3.6)-(3.9) is that the identification is conducted near the undeformed configuration for which the linear terms are much larger than the quadratic ones, themselves much larger than the cubic terms. That is, in conditions in which the critical balance of the terms on the left-hand-side does not take place. In this light, it was proposed to shift the baseline point around which the identification is achieved from the undeformed state to one in or near the expected difficult conditions, e.g. in a snap-through configuration for the curved beam. This baseline solution admits the representation

$$\underline{u}_0 = \sum_{n=1}^{M} q_{n,0}\ \underline{\psi}^{(n)} \tag{3.10}$$

11

Then, the test displacement fields imposed for identification are

$$\underline{u} = \underline{u}_0 + q_n \ \underline{\psi}^{(n)} \tag{3.11}$$

$$\underline{u} = \underline{u}_0 + q_n \ \underline{\psi}^{(n)} + q_m \ \underline{\psi}^{(m)} \quad m \geq n \tag{3.12}$$

$$\underline{u} = \underline{u}_0 + q_n \ \underline{\psi}^{(n)} + q_m \ \underline{\psi}^{(m)} + q_r \ \underline{\psi}^{(r)} \quad r \geq m \geq n \tag{3.13}$$

More specifically, for each value of $n = 1, ..., M$, three cases of the form of Eq. (3.11) were considered with $q_n = +q, -q$, and $q/2$ as before with q typically smaller than the thickness. The four cases corresponding to positive and negative values of q_n and q_m in Eq. (3.12) were also included for each n and $m \geq n$. Finally, all eight cases associated with positive and negative values of q_n, q_m, and q_r for $r \geq m \geq n$ and all n were used.

The displacement fields of Eqs (3.11)-(3.13) include generalized coordinates along all basis functions and thus no simplification of Eq. (3.5) takes place as in Eq. (3.7). Accordingly, the stiffness coefficients were obtained by a least squares solution of Eq. (3.5) with the complete set of displacement fields imposed by Eq. (3.11)-(3.13). Note that the linear, quadratic, and cubic stiffness coefficients are often of very different magnitudes and thus an appropriate scaling of the terms is recommended to keep low the condition number of the least squares matrix. It was also found beneficial to include the equations corresponding to two different baseline displacement fields $\underline{u}_0$.

12

Chapter 4

BASIS SELECTION

4.1 Introduction

The two previous chapters have focused on the derivation of the parametric form of the reduced order model governing equations, Eqs (2.8) and (3.5), and on the estimation of the parameters from a set of well chosen finite element solutions. The last key aspect of the construction of reduced order models is the selection of the basis functions $\underline{\psi}^{(n)}$. In this regard, the expected features of the reduced order model are that (i) it leads to an accurate representation of the full finite element results and (ii) it includes a "reasonably" small number of basis functions.

The selection of such a basis is not as straightforward a task as in linear systems. Consider for example a flat homogenous structure subjected to transverse loads. In the linear response range, only transverse deflections result from the loading. However, these deflections induce a stretching in the in-plane direction and thus give rise to in-plane motions as well which are a second order effect and thus not captured by linear analyses. Nevertheless, such motions must be captured when constructing the nonlinear reduced order model.

As another example of complexity introduced by nonlinear effects, note the existence of "symmetry breaking bifurcations". The response of the symmetric curved beam shown in Fig. 4.1 to a uniform dynamic loading is known (see [4]) to be symmetric, as in the linear case, for small loading levels. However, when the response becomes large enough, antisymmetry arises through a

nonlinear coupling of antisymmetric and symmetric modes. In such cases, it is thus necessary to also include antisymmetric modes in the basis to accurately capture the beam response.

In light of the above observations, this chapter is focused on the clarification of the steps followed for the selection of the basis used in connection with the curved beam of Fig. 4.1.
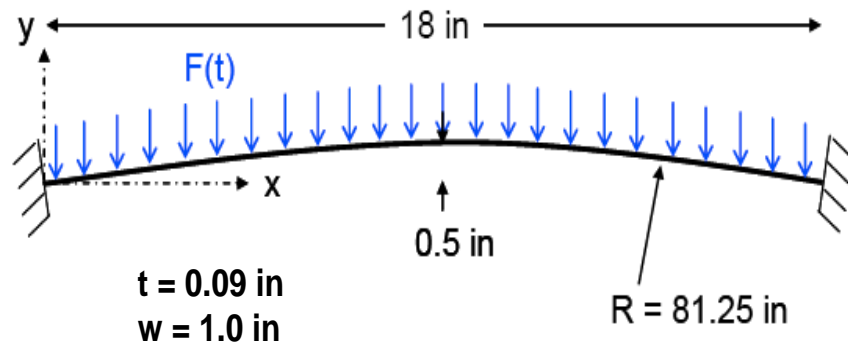

Figure 4.1. Curved beam geometry.

4.2 Representation Error

Since the selection of the basis is not a straightforward task, it is necessary to quantify the appropriateness of a particular choice of modes for the representation of the response. It is proposed here to introduce the representation error

$$E_{rep} = \frac{\left\| \text{EMBED Equation. 3 } - \text{EMBED Equation. 3 }_{proj} \right\|}{\left\| \text{EMBED Equation. 3 } \right\|} \tag{4.1}$$

where $\underline{u}$ is a particular response of the finite element model (referred to as a test case) and $\text{EMBED Equation. 3 }_{proj}$ is its projection on the basis selected, i.e.

14

$$\underline{u}_{proj} = \sum_{n=1}^{M} q_{n,proj} \, \underline{\psi}^{(n)} \qquad (4.2)$$

where

$$q_{n,proj} = \underline{\psi}^{(n)T} M_{FE} \underline{u} \qquad (4.3)$$

assuming that the basis functions $\underline{\psi}^{(n)}$ are orthonormalized with respect to the

finite element mass matrix M_{FE}.

A basis will be considered to be acceptable for the modeling of the

structural response when the representation error for a series of test cases,

including both static and dynamic ones, is below a certain threshold. Visual

correlations of the responses $\underline{u}$ and their projections suggest that this threshold

should be taken of the order of 0.01.

Note that even a zero representation error does not guarantee that the

reduced order model constructed with the basis will lead to a good match of the

ROM and finite element predicted displacement fields as the generalized

coordinates $q_n(t)$ will not be obtained from Eq. (4.3) but rather through the

governing equations, Eqs (2.8) and (3.5). So, the representation error should be

considered as only an *indicator*, not an absolute measure of the appropriateness of

the basis. Further, the worth of the representation error is dependent on the test

cases selected which must span the space of loading and responses of interest. For

example, including only symmetric basis functions and considering test cases in

which this symmetry also holds may suggest that the basis is appropriate while in

fact it may not if symmetry breaking does take place for some loadings of interest.

4.3 Dual Modes

The discussion of section 4.1 highlights that the basis appropriate for a nonlinear geometric ROM must include other modes than those considered for a linear modal model but provides no guidance on how to select them. This issue has been investigated recently, see [8], and it has been suggested that the "linear basis", i.e. the modes necessary in linear cases, be complemented by "dual modes" which capture the nonlinear interactions in the structure.

While the construction of the dual modes is applicable to any structural modeling, it is most easily described in the context of an isotropic flat structure, e.g. beam or plate, subjected to a transverse loading. Selecting an appropriate basis for the transverse displacements follows the same steps as in a linear analysis in which no further modeling is necessary. When the response level is large enough for nonlinear geometric effects to be significant, small in-plane displacements appear in the full solution which are associated with the "membrane stretching" effect. While small, these in-plane motions induce a significant softening of the stiffening nonlinearity associated with pure transverse motions.

One approach to construct a full basis, i.e. modeling both transverse and in-plane displacements, appropriate for the modeling of the nonlinear response is to focus specifically on capturing the membrane stretching effects. The key idea in this approach is thus to subject the structure to a series of "representative" static loadings, determine the corresponding *nonlinear* displacement fields, and extract

from them additional basis functions, referred to as the "dual modes" that will be appended to the linear basis, i.e. the modes that would be used in the linear case.

In this regard, note that the membrane stretching effect is induced by the nonlinear interaction of the transverse and in-plane displacements, not by an external loading. Thus, the dual modes can be viewed as associated (the adjective "companion" would have been a better description than "dual") with the transverse displacements described by the linear basis. The representative static loadings should then be selected to excite primarily the linear basis functions and, in fact, in the absence of geometric nonlinearity (i.e. for a linear analysis) should only excite these "modes". This situation occurs when the applied load vectors on the structural finite element model are of the form

$$\underline{F}^{(m)} = \sum_i \alpha_i^{(m)} \, K_{FE}^{(1)} \, \underline{\psi}^{(i)} \tag{4.4}$$

where $\alpha_i^{(m)}$ are coefficients to be chosen with m denoting the load case number. A detailed discussion of the linear combinations to be used is presented in [8] but, in all validations carried out, it has been sufficient to consider the cases

$$\underline{F}_i^{(m)} = \alpha_i^{(m)} \, K_{FE}^{(1)} \, \underline{\psi}^{(i)} \quad i = \text{dominant mode} \tag{4.5}$$

$$\underline{F}_{ij}^{(m)} = \frac{\alpha_i^{(m)}}{2} \left[K_{FE}^{(1)} \, \underline{\psi}^{(i)} \, K_{FE}^{(1)} \, \underline{\psi}^{(j)} \right] \tag{4.6}$$

$$i = \text{dominant mode}, \; j \neq i$$

where a "dominant" mode is loosely defined as one providing a large component of the response. The ensemble of loading cases considered is formed by selecting

17

several values of $\alpha_i^{(m)}$ for each dominant mode in Eq. (4.2) and also for each mode $j \neq i$ in Eq. (4.3). Note further that both positive and negative values of $\alpha_i^{(m)}$ are suggested and that their magnitudes should be such that the corresponding displacement fields $\underline{u}_i^{(m)}$ and $\underline{u}_{ij}^{(m)}$ range from near linear cases to some exhibiting a strong nonlinearity.

The next step of the basis construction is the extraction of the nonlinear effects in the obtained displacement fields which is achieved by removing from the displacements fields their projections on the linear basis, i.e. by forming the vectors

$$\underline{v}_i^{(m)} = \underline{u}_i^{(m)} - \sum_s \left\lfloor \underline{\psi}_s^T \, M_{FE} \, \underline{u}_i^{(m)} \right\rfloor \underline{\psi}_s \qquad (4.7)$$

$$\underline{v}_{ij}^{(m)} = \underline{u}_{ij}^{(m)} - \sum_s \left\lfloor \underline{\psi}_s^T \, M_{FE} \, \underline{u}_{ij}^{(m)} \right\rfloor \underline{\psi}_s \qquad (4.8)$$

assuming that the finite element mass matrix serves for the orthonormalization of the basis functions $\underline{\psi}^{(n)}$ (including the linear basis functions and any dual mode already selected).

A proper orthogonal decomposition (POD) of each set of "nonlinear responses" $\underline{v}_i^{(m)}$ and $\underline{v}_{ij}^{(m)}$ is then sequentially carried out to extract the dominant features of these responses which are then selected as dual modes. The POD eigenvectors $\underline{\phi}_r$ selected as dual modes should not only be associated with a large eigenvalue but should also induce a large strain energy, as measured by

18

$\underline{\phi}_r^T \, K_{FE}^{(1)} \, \underline{\phi}_r$, since the membrane stretching that the dual modes are expected to model is a stiff deformation mode.

To exemplify the above process, a flat aluminum beam (see [17] for details), cantilevered on both ends was considered and the duals corresponding to the first four symmetric transverse modes are shown in Fig. 4.2. Note that these duals are all antisymmetric as expected from the symmetry of the transverse motions assumed. To obtain a better sense of the appropriateness of these functions, a POD analysis of an ensemble of nonlinear responses was carried out and also shown on Fig. 4.2 are the mass normalized POD eigenvectors found for the in-plane displacements. In fact, two such analyses were conducted, one using a series of static responses and the other using snapshots obtained during a dynamic run. It is seen from these results that the dual modes proposed in [8] are in fact very close to the POD eigenvectors obtained from both static and dynamic snapshots. Note that both POD eigenvectors and dual modes are dependent on the responses, e.g. their magnitude, from which they are derived. The results of Fig. 4.2 were obtained with responses ranging typically from 0.08 to 0.8 beam thickness. In fact, in this range of displacements, the POD analysis of the static responses yielded only two eigenvectors with significant eigenvalue and thus no POD-static curve is present in Figs 4.2(c) and 4.2(d).

(a)

(b)

20
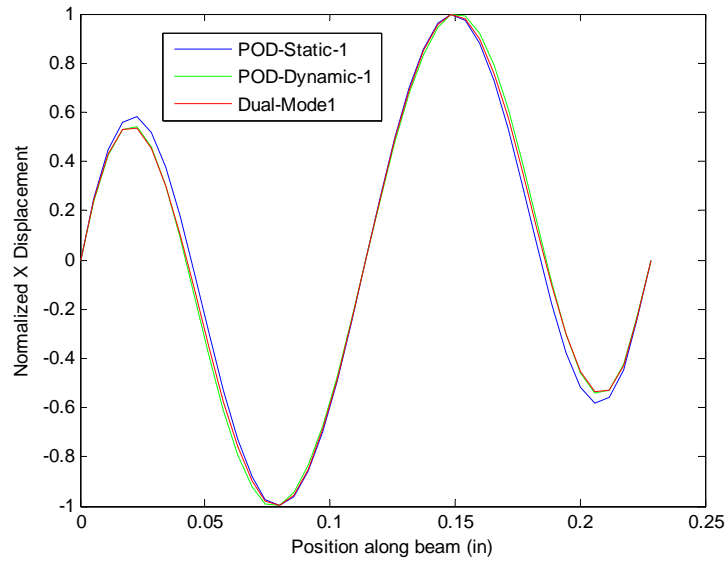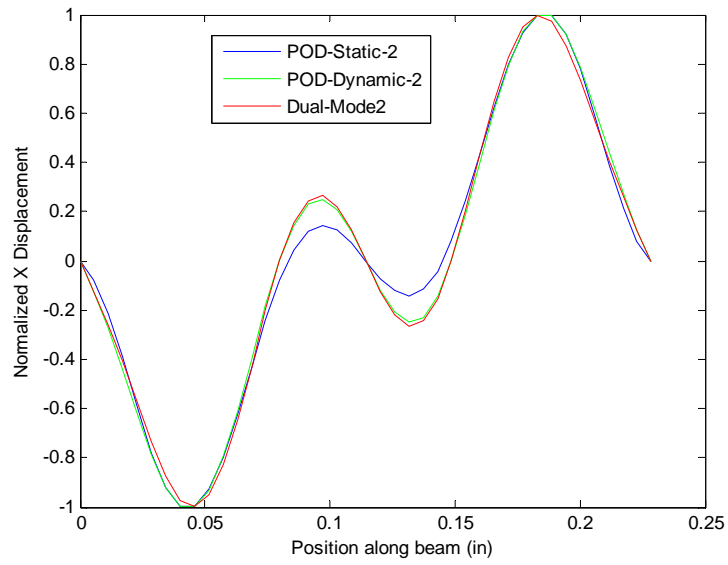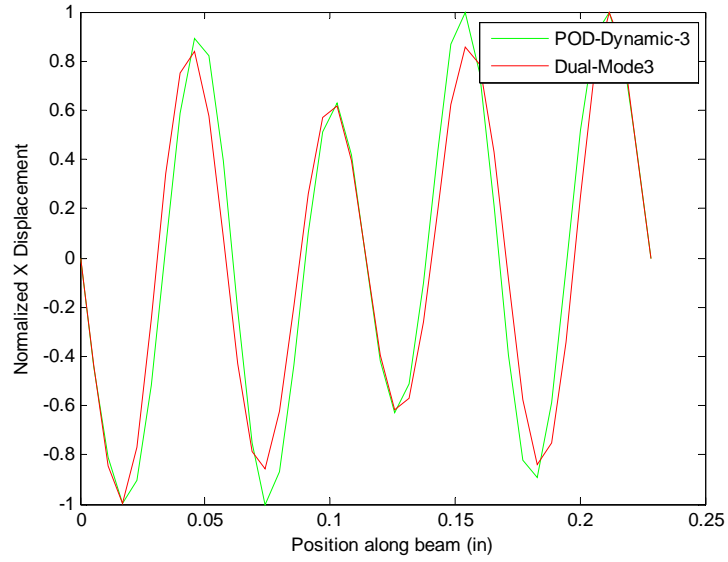
(c)
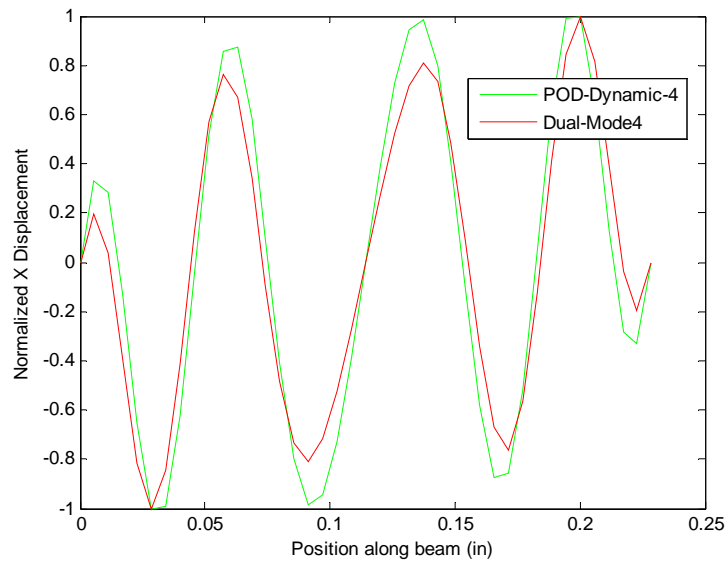
(d)

Figure 4.2. Comparison of dual modes and POD eigenvectors of static and

dynamic responses, clamped-clamped flat beam.

4.4 Curved Beam - Observations

The first step in the selection of the basis for the curved beam of Fig. 4.1 was the determination of its linear mode shapes and of a series of static and dynamic nonlinear test cases to be used in the evaluation of the representation error, Eq. (4.1). Shown in Fig. 4.3 are the first 6 modes with dominant components in the plane of the beam. Modes 5 and 6 were found to be out-of-plane modes and thus were not included in the reduced order model as no such motion was observed in the validation cases considered. Displayed in Fig. 4.3 are modal displacements along the locally normal and tangential directions, not along the global X and Y coordinates.

Shown similarly in Fig. 4.4 are static responses of the curved beam induced by a uniform pressure P acting along the negative Y axis, see Fig. 4.1. For ease of presentation, the responses were scaled by their respective peak values which are given in Table 4.1. Note that the cases $P = 1$ and 1.5 lb/in lead to nonlinear deflections but no snap-through while the load of $P = 2$ lbs/in does induce such an event. Further, the normal components are all symmetric while the tangential ones are antisymmetric, consistent with the symmetry of the beam and its excitation.

Table 4.1. Maximum absolute normal and tangential displacements of some uniform negative pressure loads on the curved beam (in thickness)

	P=1	P=1.5	P=2
Max Normal Disp.	0.158	0.262	9.7

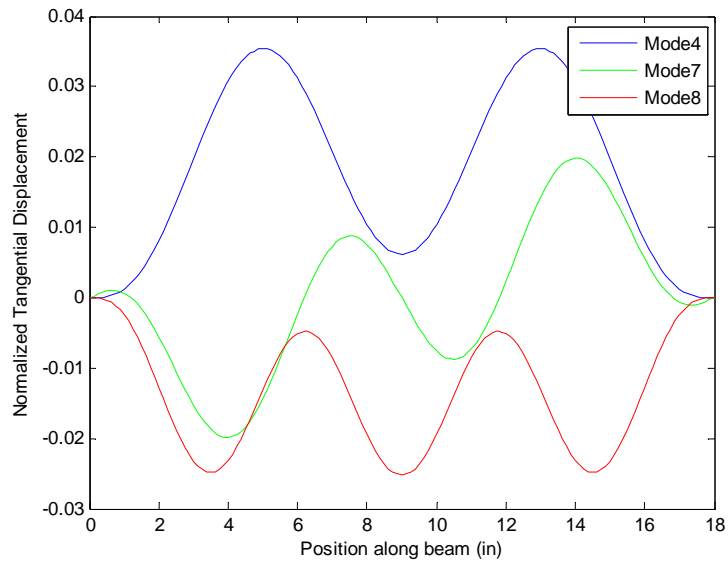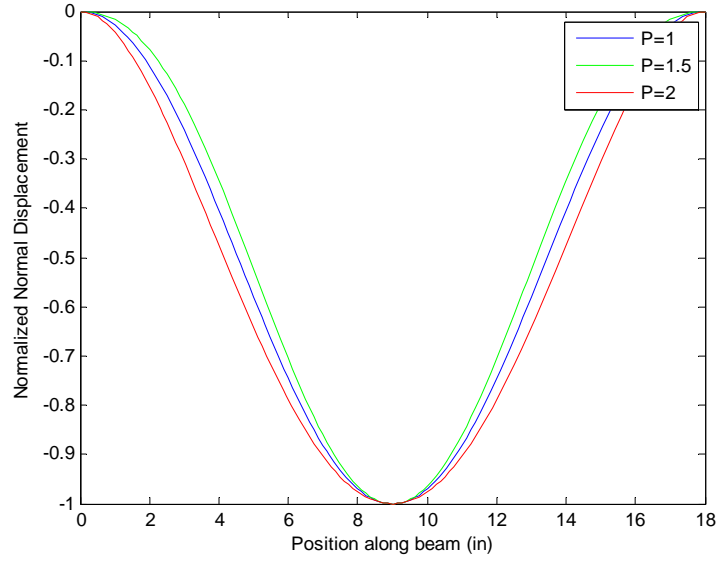| Max Tangential Disp.	0.0028	0.0046	0.2551

(a)

(b)

23
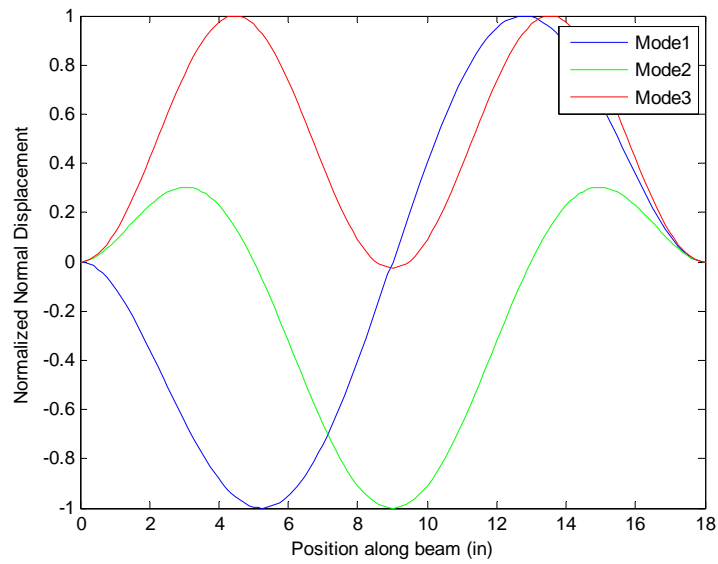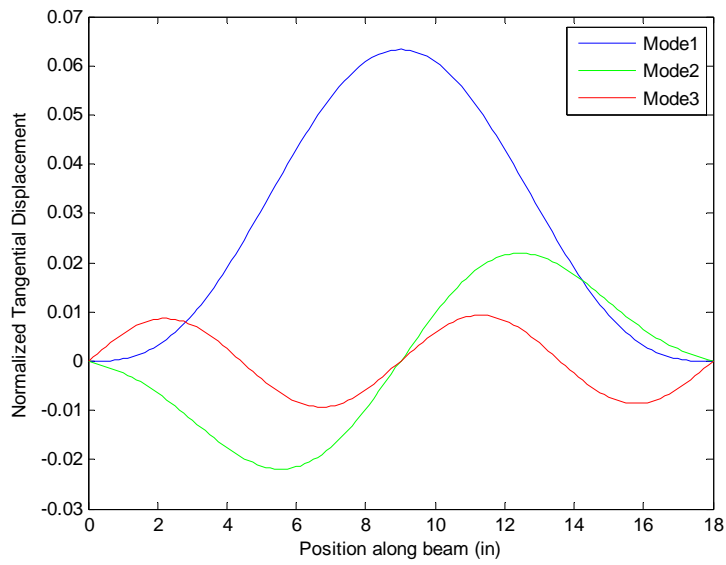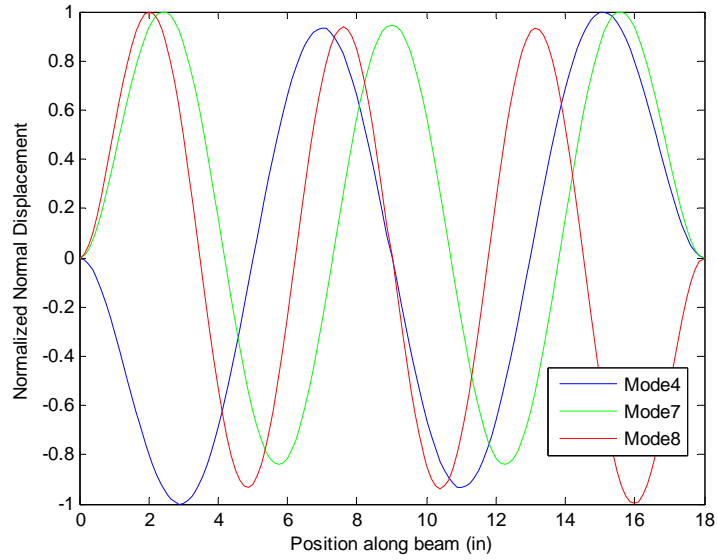
(c)

(d)

Figure 4.3. Linear mode shapes 1, 2, 3, 4, 7, and 8 of the curved beam.

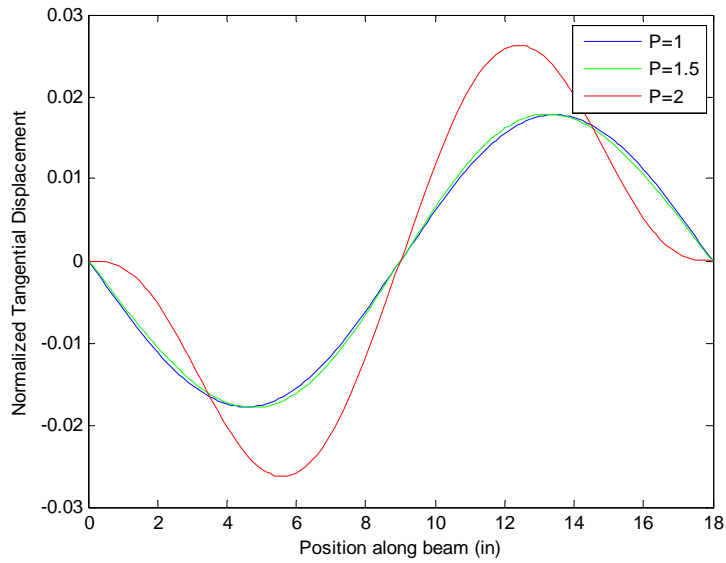(a) Modes 1, 2 and 3 – Normalized normal displacement.

(b) Modes 1, 2 and 3 – Tangential displacement.

(c) Modes 4, 7, and 8 – Normalized normal displacement.

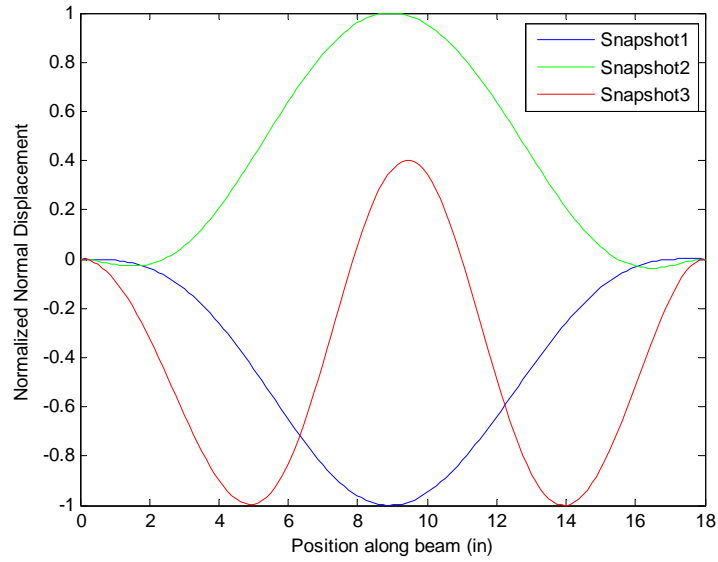(d) Modes 4, 7, and 8 – Tangential displacement.

(a)

(b)

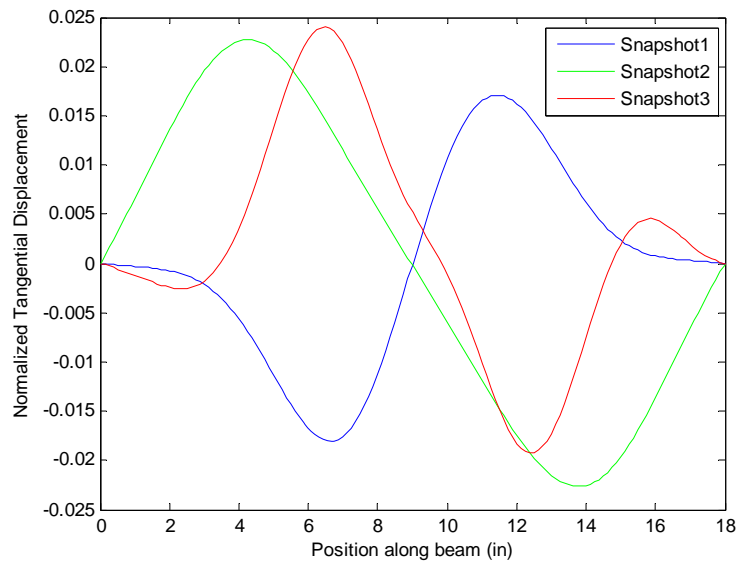Figure 4.4. Normalized static responses of the curved beam to uniform loads *P*.

(a) Normalized normal displacement.

(b) Normalized tangential displacement.

Snap-shots of the dynamic response of the beam are shown in Figs 4.5 and 4.6. On the former figure, the responses are strongly symmetric in the normal direction and antisymmetric in the tangential, although not exactly as in the static cases, see Fig. 4.4. However, in the latter figure 4.6, no symmetry of the responses is observed, either exactly or even approximately. These observations confirm the observations of [4,11] that a symmetry breaking bifurcation takes place dynamically and thus the lack of symmetry will need to be reflected in the basis.

(a)

(b)

Figure 4.5. Snap-shots of the dynamic response of the curved beam - I.

27

(a) Normalized normal displacement.

(b) Normalized tangential displacement.
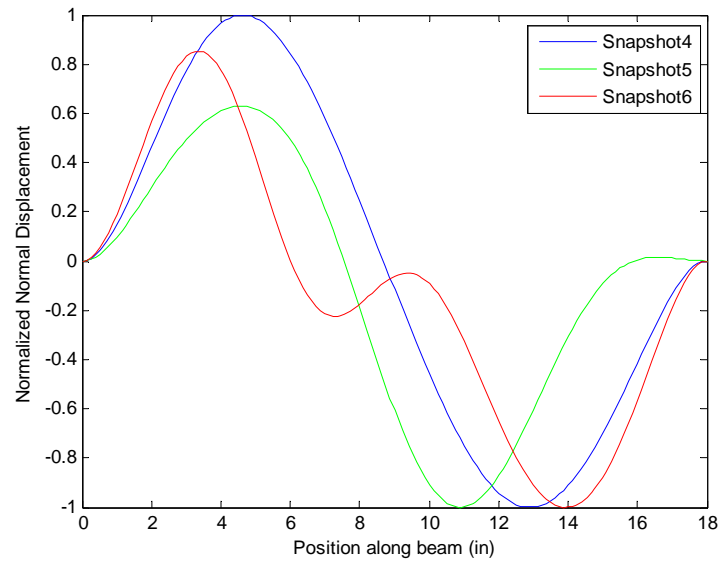
(a)
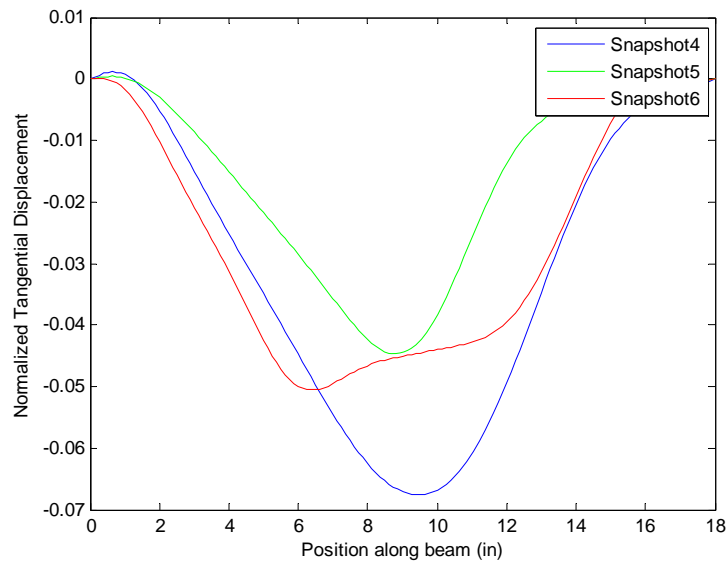
(b)

Figure 4.6. Snap-shots of the dynamic response of the curved beam - II.

(a) Normalized normal displacement.

(b) Normalized tangential displacement.
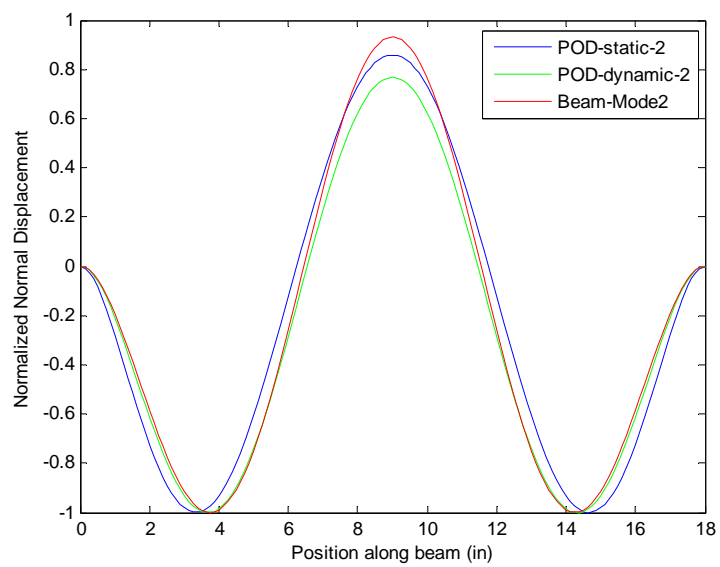
4.5 Curved Beam - Normal Basis Functions

Consistently with linear modal models, the appropriateness of the linear mode shapes to represent the nonlinear responses was first investigated. From Fig. 4.3, it is seen that all mode shapes exhibit at least one zero of the normal displacements which thus alternate (except mode 3) between positive and negative values. However, all static responses and most large dynamic ones do not, their normal displacements are all one sided and no zero at the middle (as the linear mode 3). To get an overall perspective on that issue, the ensembles of static and dynamic responses were analyzed separately in a POD format to extract the dominant features of the beam response. The corresponding POD eigenvectors of the normal components (treated separately of the tangential ones), shown in Fig 4.7, do indeed confirm the above impression: the first normal POD eigenvector of both static and dynamic responses does indeed exhibit a one-sided normal displacement reaching its maximum value at the middle, at the contrary of the linear mode shapes. However, the second normal POD eigenvector is somewhat similar to the second (lowest symmetric) mode shape. While the mode shapes are known to form a complete basis for all deflections, linear or nonlinear, of the curved beam, the above observations suggest that the convergence with the number of modes used may be slow.

On this basis, it was decided here not to use the linear mode shapes but rather a set of basis functions that is consistent with the POD eigenvectors of Fig.

4.7. Certainly, the POD eigenvectors themselves could have been selected but it was desired to select basis functions originating from a natural family of modes. In this regard, a strong similarity was observed between the normal POD eigenvectors and the mode shapes of a flat beam spanning the same distance, see Figs 4.7. Accordingly, it was decided to use these mode shapes as basis functions for the normal direction. Note that the value of the modal displacement of the flat beam in the transverse direction was directly used for the curved beam basis functions as a normal component with zero tangential counterpart.
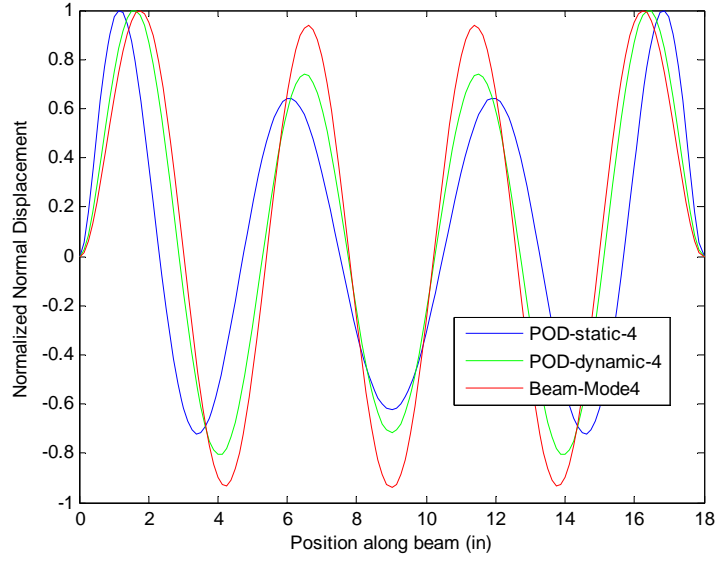

(a)

(b)

(c)

31
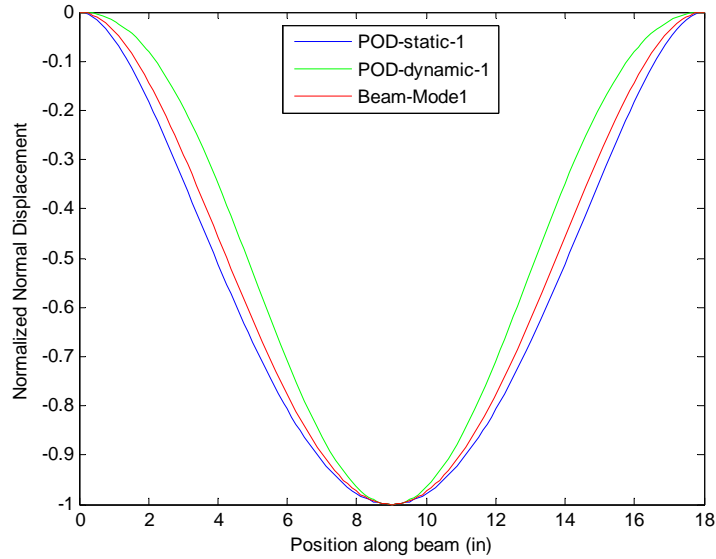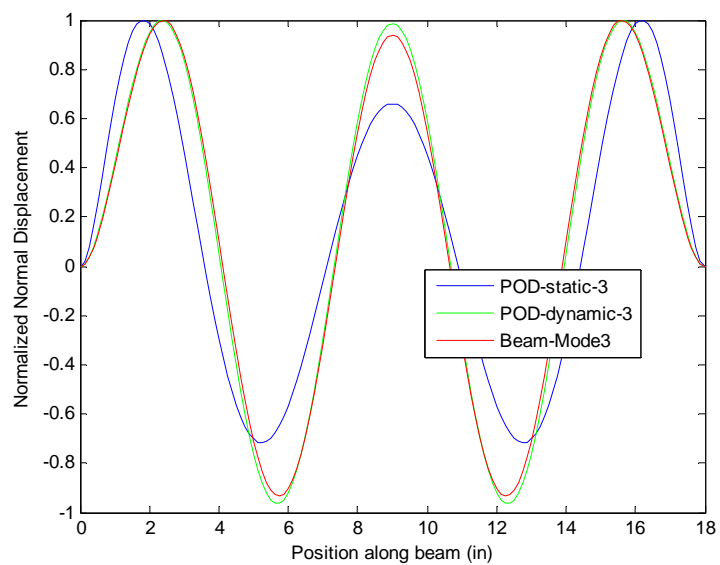
(d)

Figure 4.7. Comparison of the POD eigenvectors of static and dynamic responses

in normal direction of the curved beam and the corresponding flat beam

transverse modes.

4.6 Curved Beam - Tangential Basis Functions

The basis functions introduced in the previous sections do not have any

tangential component and thus cannot provide a complete representation of the

beam response. This situation closely parallels the flat beam where the modes first

selected were purely transverse. For that structure, the "dual modes" of section

4.3 were successfully used to complement the transverse modes suggesting a

similar choice for the curved beam using the normal basis functions as linear

basis. In fact, the dual modes and POD eigenvectors were found to be very similar

for the flat beam, see Fig. 4.2 and it was desired to first assess whether a similar

property would hold for the curved beam.

32

Since the normal basis functions do not have any tangential component, it was decided that the dual modes that would be used should exhibit purely tangential displacements and the procedure of section 4.3 was modified accordingly by zeroing the normal components of the "nonlinear responses" $\underline{v}_i^{(m)}$ and $\underline{v}_{ij}^{(m)}$ before performing the POD analysis. The resulting dual modes corresponding to the symmetric normal basis functions are compared in Fig. 4.8 to the POD eigenvectors obtained from the ensemble of static and dynamic tangential responses. A good qualitative agreement is observed although the quantitative match is not as close as seen for the flat beam, see Fig. 4.2. On the basis of this successful comparison, the dual modes were selected to complement the normal basis functions for the representation of the curved beam response.
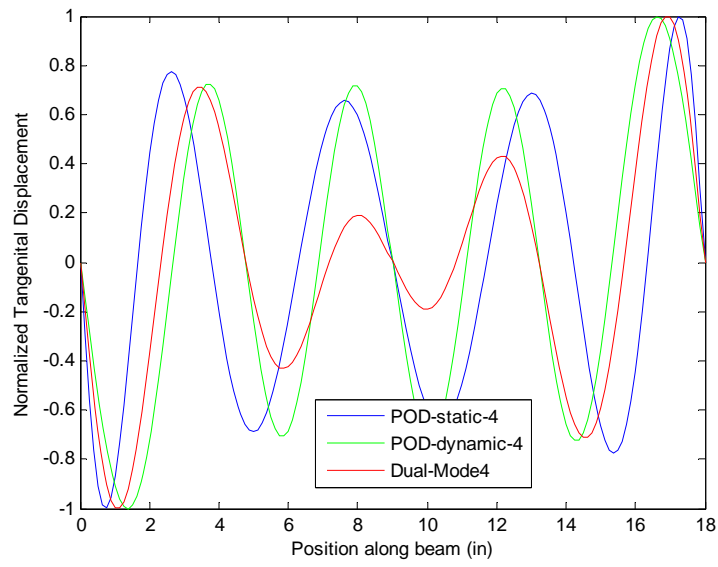

(a)

33

(b)

(c)

34
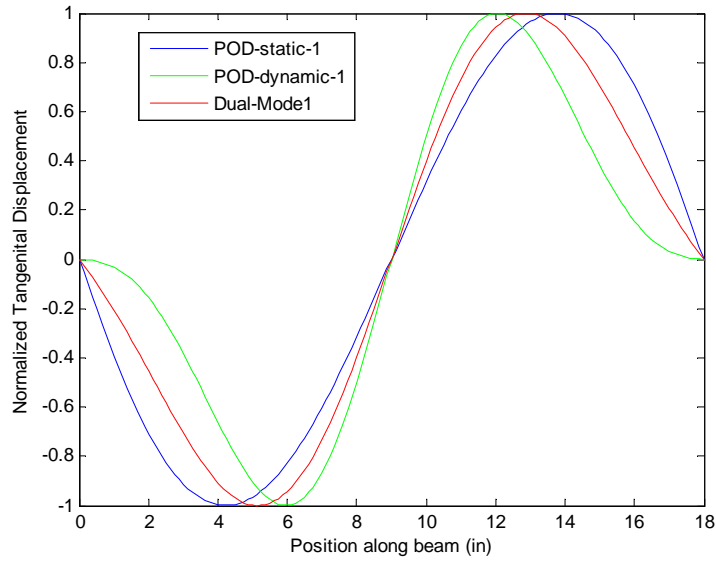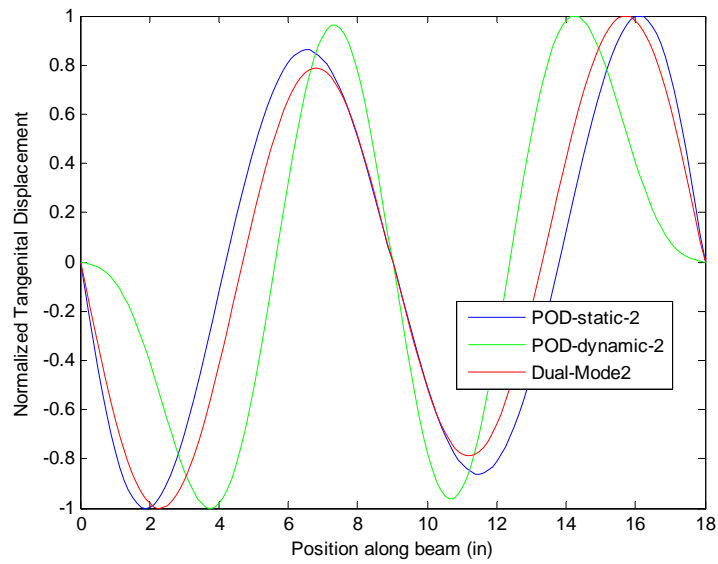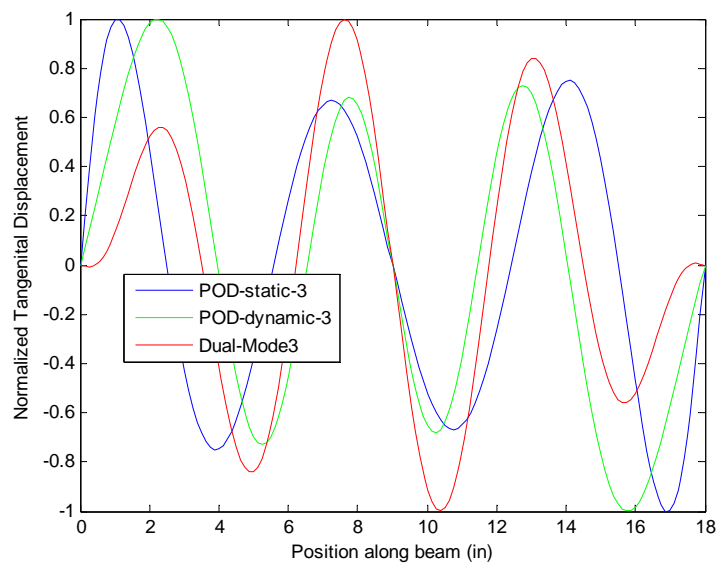
(d)

Figure 4.8. Comparison of the POD eigenvectors of static and dynamic responses

in tangential direction and the dual modes, curved beam.

Chapter 5

CURVED BEAM STATIC RESPONSE VALIDATION

This chapter presents static response validation for the identification strategy based on Eqs (3.10)-(3.13) using the clamped-clamped curved beam of [4, 5, 11], see Fig. 4.1. The beam has an elastic modulus of 10.6×10^6 psi, shear modulus of 4.0×10^6 psi, and density of 2.588×10^{-4} lbf-sec^2/in^4. A Nastran finite element model with 144 CBEAM elements was developed to first construct the reduced order model and then assess its predictive capabilities. The reduced order model development aimed at the dynamic response to a pressure uniform in space but varying in time. This chapter focuses solely on the static response to such a loading, i.e. $F(t) = P$ constant, and shown in Fig. 5.1 is the vertical displacement induced at the middle of the beam as a function of P. Note that the beam exhibits a snap-through at $P = 1.89$ lb/in and that the magnitude of the snap-through deformation is quite large, of the order of 10 thicknesses. If the beam is unloaded from this point, it will not go back to the neighborhood of the undeformed position, i.e. on the left branch, until the loads reduces to approximately 0.45 lb/in, which represents the snap-back condition.
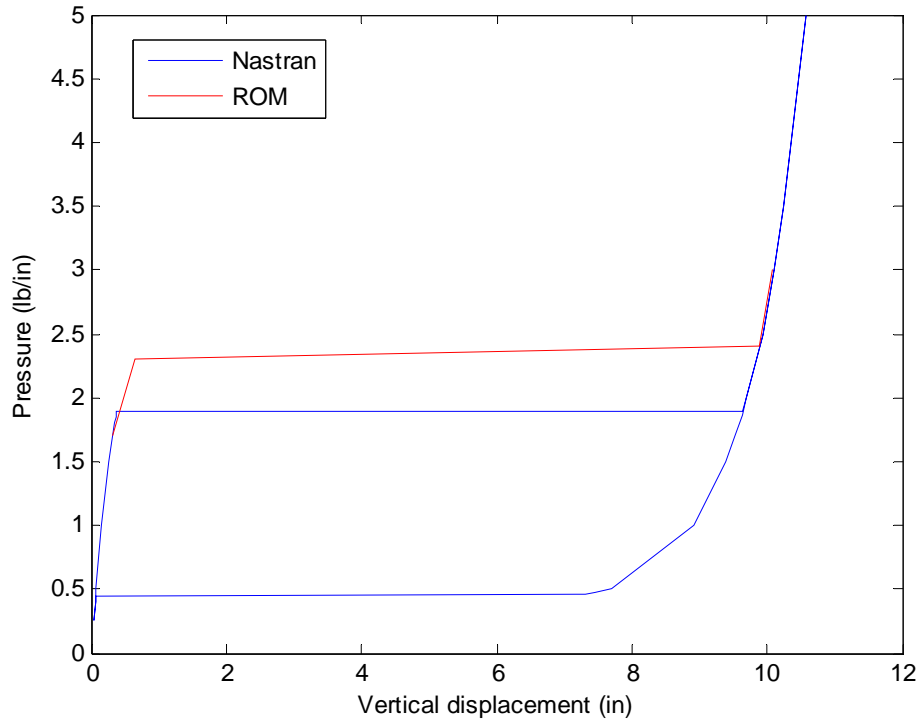
Figure 5.1. Relation between applied static pressure and vertical displacement of

the beam middle, curved beam, predicted by Nastran and ROM.

The basis used for the reduced order model included the first 6 normal

basis functions and the corresponding 6 dual modes next step of the reduced order

model construction focused on the modeling of the locally tangent displacements

which was achieved using the dual modes of chapter 4 with the first basis function

(first mode of the flat beam) dominant. Since the first 6 basis functions included

only normal components, the 6 dual modes were made purely tangential by

stripping their normal components. This process led for the present static

computations to a 12 mode model similar to the one considered in [11], see [17]

for additional models and results. To get an idea of how well this 12-modes basis

could capture the uniform pressure static responses, representation error was computed at some load cases, see Table 5.1. Since the errors are reasonably small, this basis was considered to be acceptable.

Table 5.1. Representation error in percentage of the basis at some negative uniform pressure static loadings.

	P=1 lb/in	P=1.7 lb/in	P=2 lb/in	P=3 lb/in
Normal	1.095e-002	1.159e-002	1.478e-002	1.848e-002
Tangential	2.152e-002	1.637e-002	2.418e-002	4.749e-002

The construction of the reduced order model according to the STEP procedure of Eqs (3.6)-(3.9) led to the same difficulties as those encountered in [11] and described in chapter 3, i.e. difficulty in obtaining a static solution by a time marching integration of the reduced order equations of Eq. (2.8). Even when a solution could be found, it led to a poor matching of the finite element results. This issue was resolved in [11] by a detailed study of coefficients and a zeroing out of those that drove the instability; a model matching well the full finite element results was then obtained.

The present effort relied instead on the revised identification procedure, i.e. Eqs (3.10)-(3.13). Specifically, two baseline solutions were considered that correspond to the projection of the full finite element results at $P = 1.7$lb/in on the left branch, i.e. below the snap-through limit, and at $P = 2$lb/in, i.e. above the snap-through transition. No instability of the model was found in any of the computations carried out thereby suggesting that this phenomenon was indeed

related to the near cancelation of terms and demonstrating the benefit of the revised identification of Eqs (3.10)-(3.13).

The assessment of the reduced model in matching the full finite element results was carried out in two phases corresponding to the two branches, left and right, of the response curve of Fig. 5.2. Shown in Fig. 5.3 are the normal and tangential displacements obtained at the load of $P = 1.7$lb/in which are typical of the left branch. An excellent match between Nastran and reduced order model results is obtained. A similar analysis was conducted with loading conditions on the right branch and shown in Fig. 5.4 are the normal and tangential displacements obtained for $P = 3$ lb/in. Both Nastran and reduced order models were then unloaded to $P = 1$ lb/in, see Fig. 5.5. Finally, a load of $P = 10$ lb/in was also considered and the responses are shown in Fig. 5.6. In all of these cases, an excellent match is obtained between the full finite element model results and the reduced order model predictions. Additional comparisons, in particular with other good reduced order models, are presented in [17]. Clearly, the identification algorithm based on Eqs (3.10)-(3.13) has led to very reliable reduced order models.
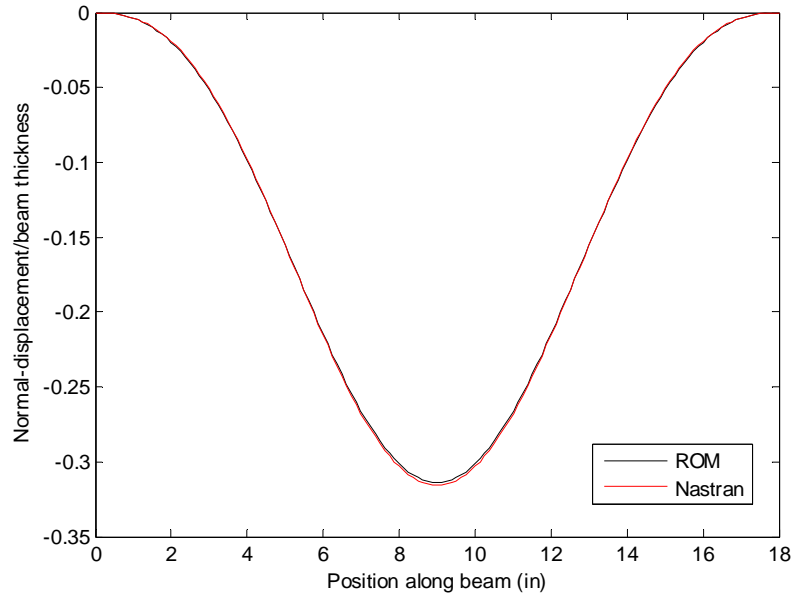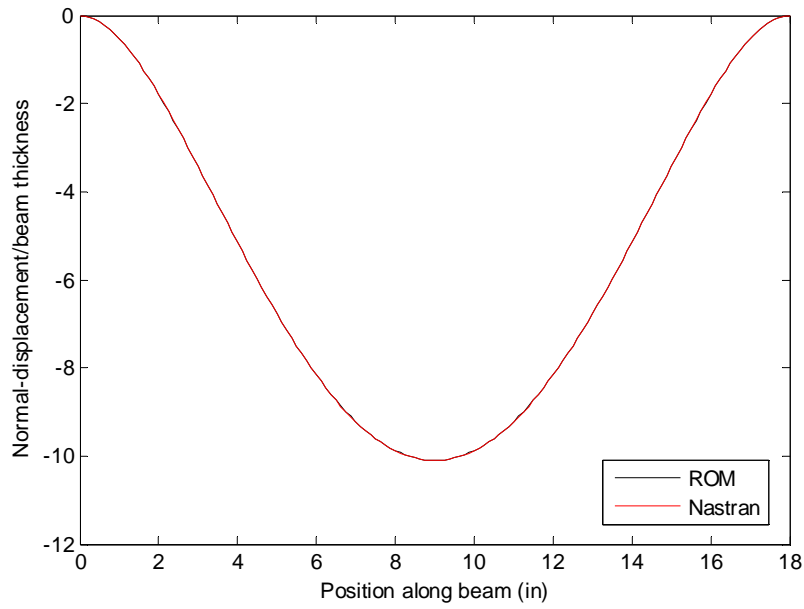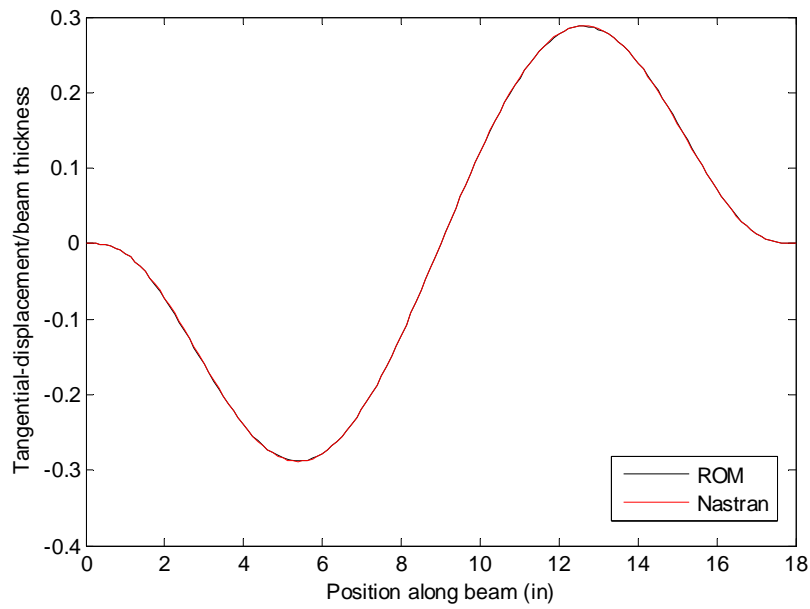
(a)
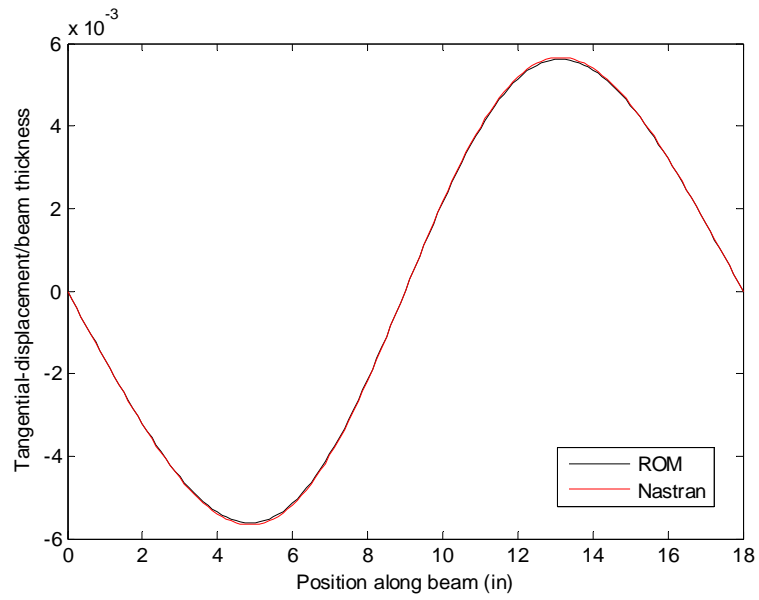
(b)

Figure 5.2. Comparison of static responses predicted by Nastran and by the

reduced order model, curved beam, $P = 1.7$ lb/in.

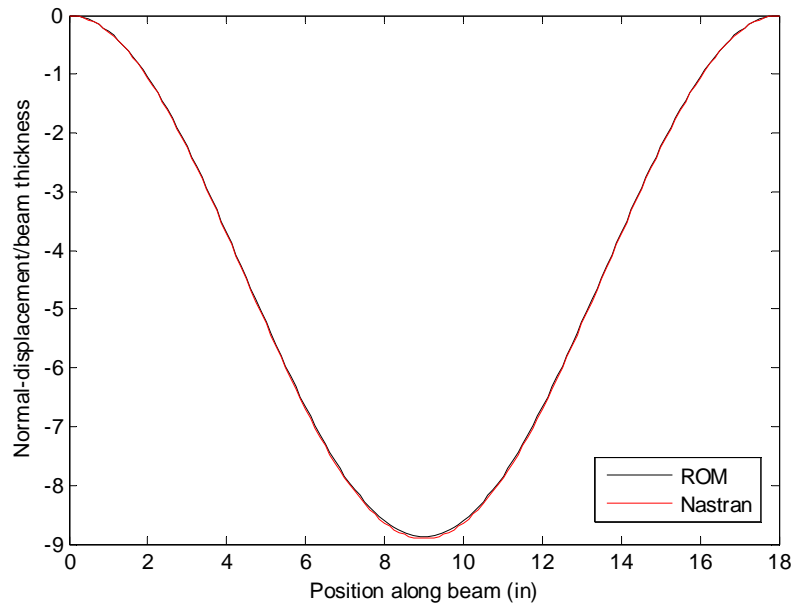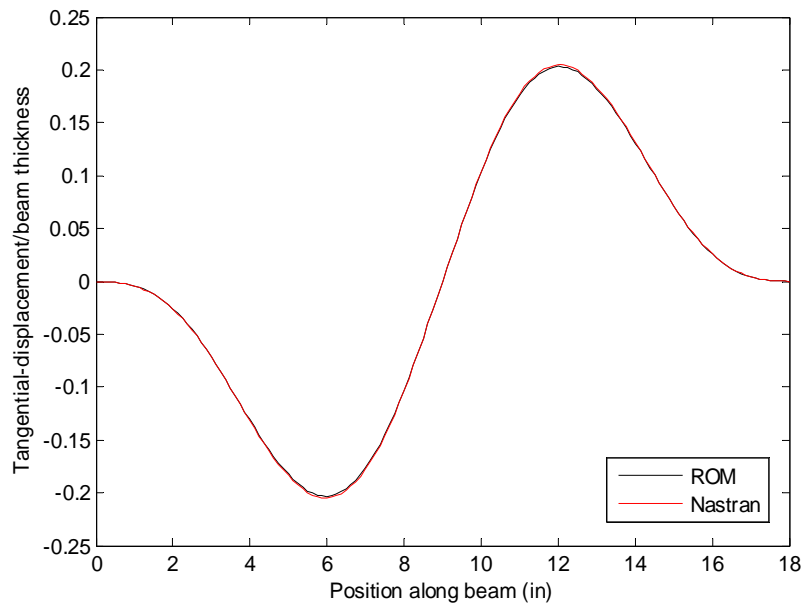(a) Normal and (b) tangential displacements.

(a)

(b)

Figure 5.3. Comparison of static responses predicted by Nastran and by the

reduced order model, curved beam, $P = 3$ lb/in.
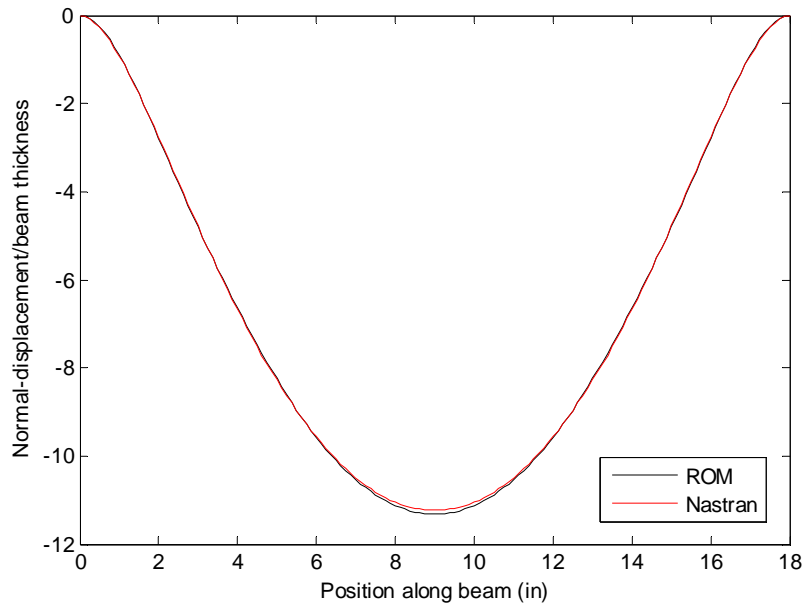
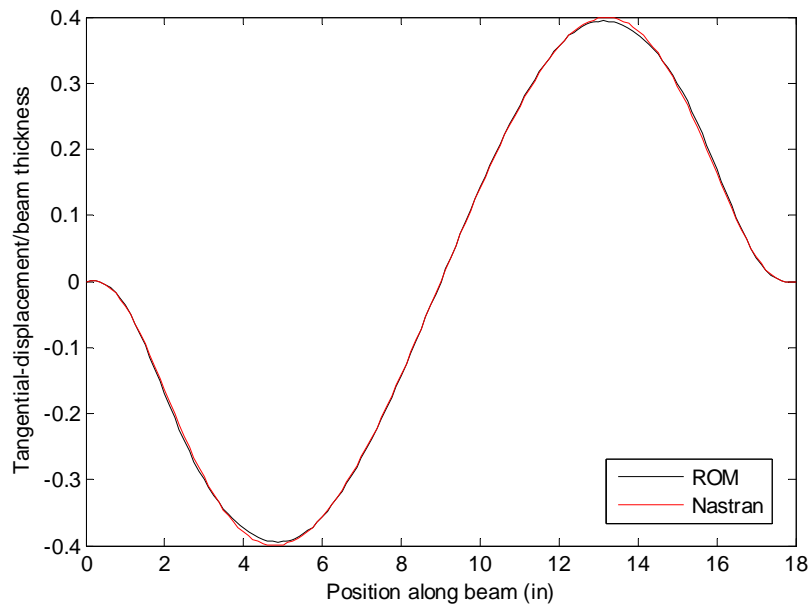(a) Normal and (b) tangential displacements.

(a)

(b)

Figure 5.4. Comparison of static responses predicted by Nastran and by the

reduced order model, curved beam, $P = 1$ lb/in (right branch).

(a) Normal and (b) tangential displacements.

(a)

(b)

Figure 5.5. Comparison of static responses predicted by Nastran and by the

reduced order model, curved beam, $P = 10$ lb/in.

(a) Normal and (b) tangential displacements.

Chapter 6

CURVED BEAM DYNAMIC RESPONSE VALIDATION

This chapter proceeds to present dynamic response validation for the identification strategy based on Eqs (3.10)-(3.13) using the same beam and Nastran finite element model of previous chapter. In order to capture the anti-symmetric motion of the snap-through behavior of the curved beam in dynamic response, the inclusions of anti-symmetric modes are thus necessary.

With the same strategy as chapter 5, three anti-symmetric and four symmetric linear modes of the corresponding straight beam were considered and assumed to define the displacement in the locally normal direction to the beam. Same antisymmetric dual modes of chapter 5 were included here, and, by using Eq. (4.4) with each anti-symmetric linear mode and Eq. (4.5) with each anti-symmetric linear mode and first symmetric mode, five "*symmetric*" dual modes were created and added to the bases. These dual modes were also made purely tangential by stripping their normal components. These processes led to a totally 18 modes model. To make sure this 18-modes basis could capture the complexity of the dynamic response, representation error was computed on a series of snap-shots from the dynamic response. Note that here the snapshots were made with purely-symmetric normal components or with purely-antisymmetric tangential components or with purely-antisymmetric normal components or with purely symmetric tangential components for the purpose of judging the 4 symmetric modes; 6 antisymmetric duals; 3 antisymmetric modes; and 5 symmetric duals of the 18-modes basis separately.

Table 6.1. Representation error in percentage of the basis on the snapshots with symmetric normal components.

|	Snap-shot1	Snap-shot2	Snap-shot3	Snap-shot4
Normal	2.46E-01	1.13E-02	4.69E-02	1.69E-01

Table 6.2. Representation error in percentage of the basis on the snapshots with antisymmetric tangential components.

	Snap-shot1	Snap-shot2	Snap-shot3	Snap-shot4
Tangential	2.49E-02	1.68E-02	1.38E-02	1.73E-01

Table 6.3. Representation error in percentage of the basis on the snapshots with antisymmetric normal components.

	Snap-shot1	Snap-shot2	Snap-shot3	Snap-shot4
Normal	1.82E-01	1.31E-01	1.37E-01	2.23E-01

Table 6.4. Representation error in percentage of the basis on the snapshots with symmetric tangential components.

|	Snap-shot1	Snap-shot2	Snap-shot3	Snap-shot4
Tangential	1.63E-01	1.48E-01	3.39E-02	2.97E-01

As for the identification of the ROM parameters, two baseline solutions were considered that correspond to the projection of the full finite element results at P=0.98-1.82 lb/in, P=1.4-2.6 lb/in. The baseline solution P=1.4-2.6 lb/in has a

45

mean value of 2 lb/in and it is actually very close to symmetric. However, the baseline solution P=0.98-1.82 lb/in does not snap and it contains lots of antisymmetric motion, which allows the model capturing well the anti-motion of the curved beam.

The validation was achieved by considering a white noise random loading exhibiting a flat spectrum in the range of [0, 4000Hz]. Three excitations levels were considered yielding RMS forces of 0.5, 1, and 2 lb/in, see [11]. The higher levels 1 and 2 lb/in displayed intermittent and nearly continuous snap-through excursions. The power spectrum of the responses for both X and Y displacements of quarter and center points at each load level comparing to Nastran results are presented. Note the good agreement between the reduced order modeling displacement predictions with the Nastran full finite element results.
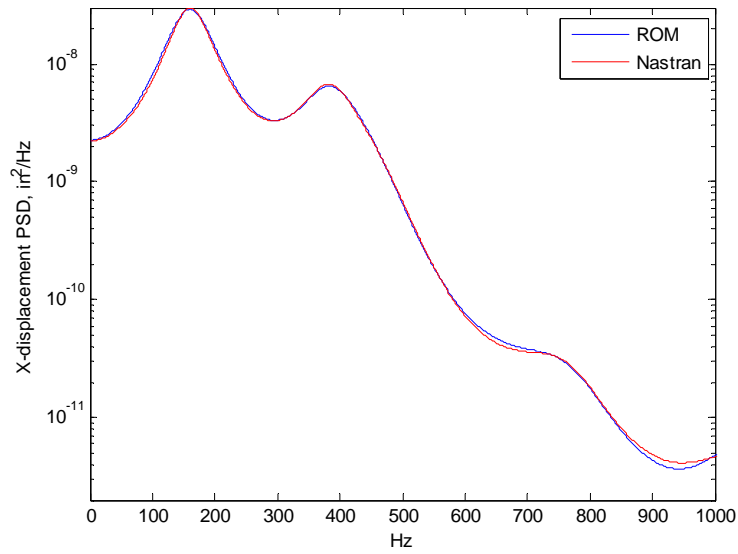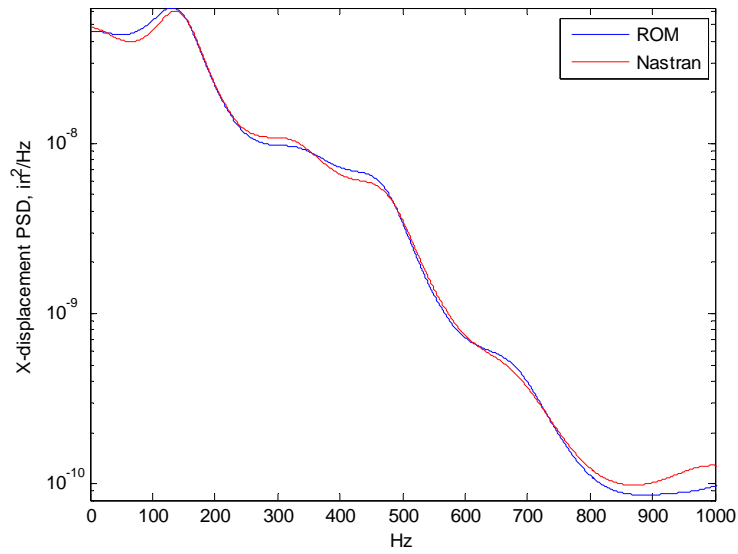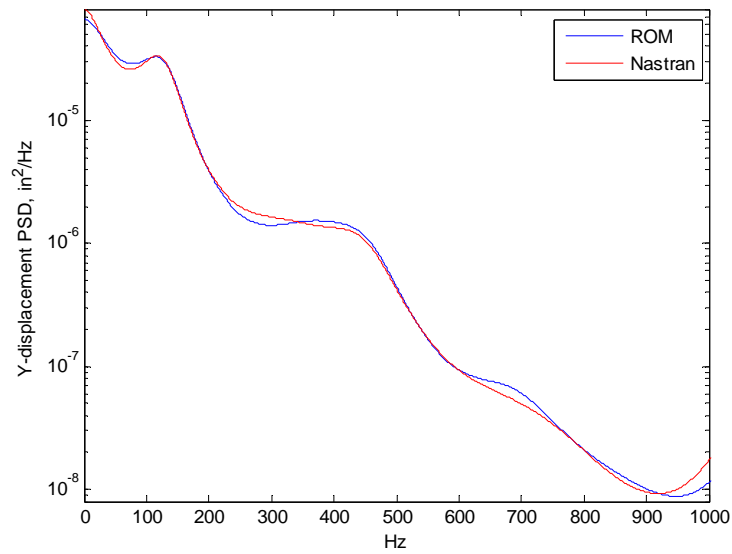
(a)
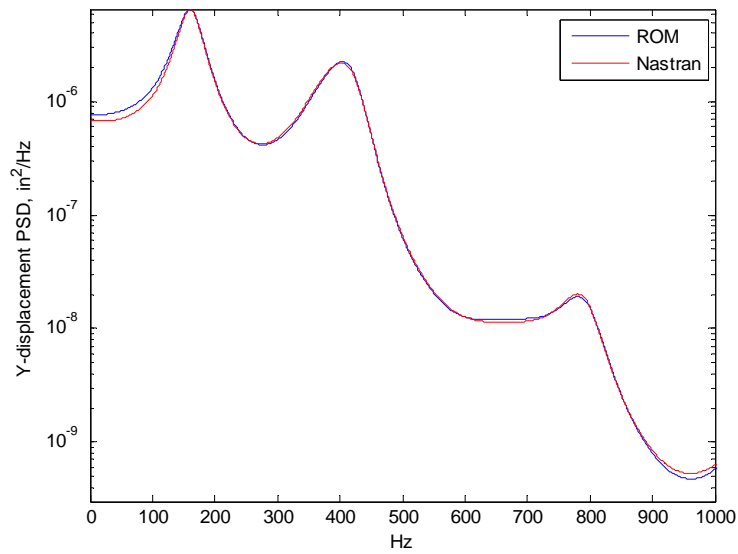
(b)

Figure 6.1. Curved beam quarter-point power spectrum density for random

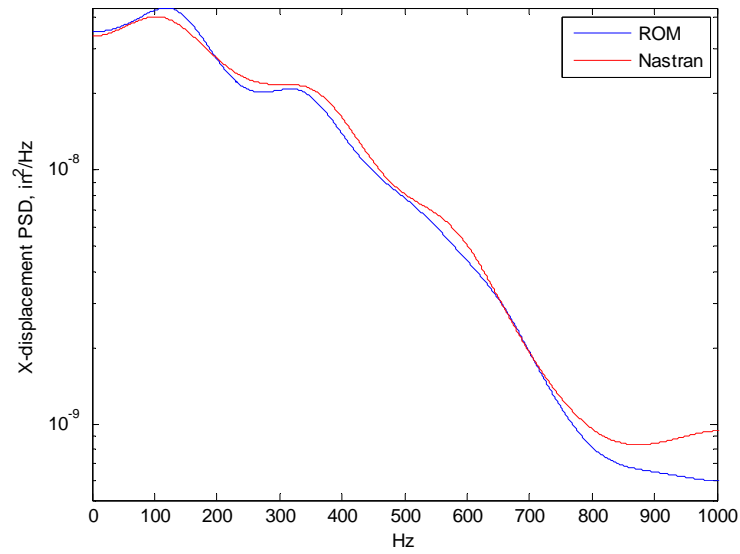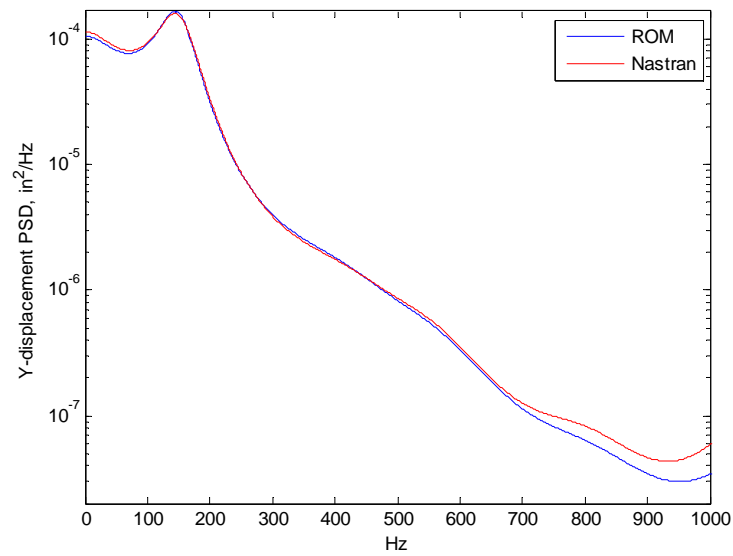loading = 0.5 lb/in, [0, 4000Hz]. (a) X and (b) Y displacements.

47

(a)

(b)

Figure 6.2. Curved beam quarter-point power spectrum density for random

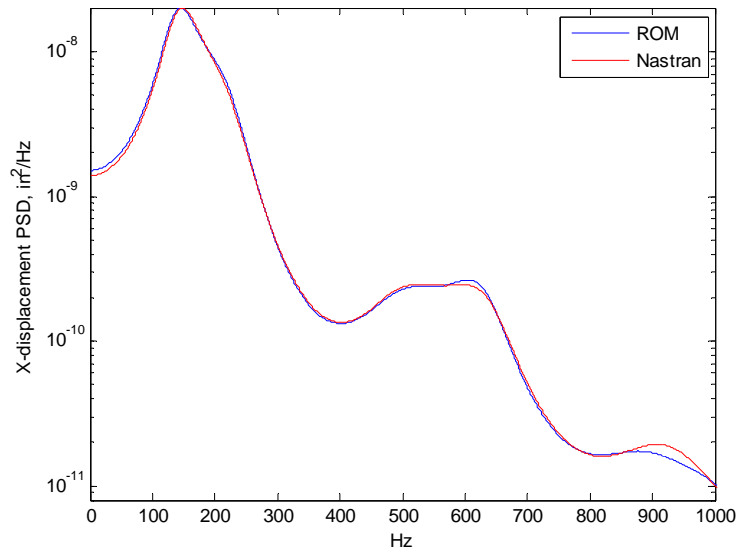loading = 1 lb/in, [0, 4000Hz]. (a) X and (b) Y displacements.

48

(a)

(b)

Figure 6.3. Curved beam quarter-point power spectrum density for random

loading = 2 lb/in, [0, 4000Hz]. (a) X and (b) Y displacements.

49

(a)

(b)

Figure 6.4. Curved beam center-point power spectrum density for random loading

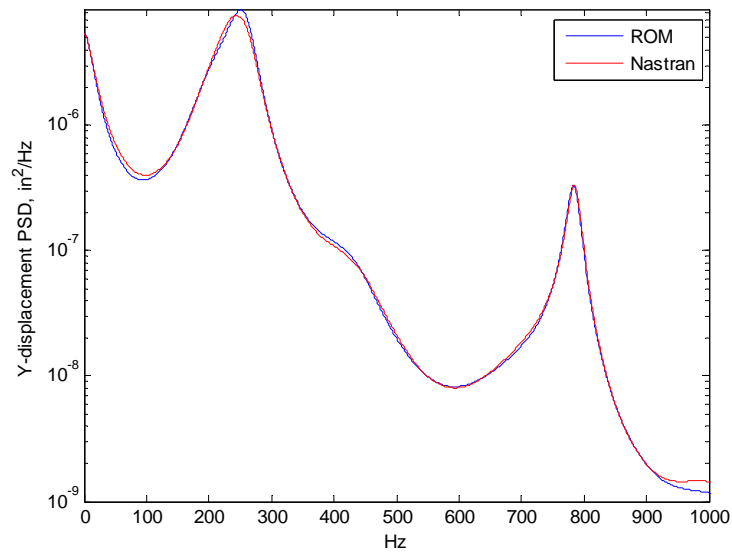= 0.5 lb/in, [0, 4000Hz]. (a) X and (b) Y displacements.

50

(a)

(b)

Figure 6.5. Curved beam center-point power spectrum density for random loading

= 1 lb/in, [0, 4000Hz]. (a) X and (b) Y displacements.

(a)

(b)

Figure 6.6. Curved beam center-point power spectrum density for random loading
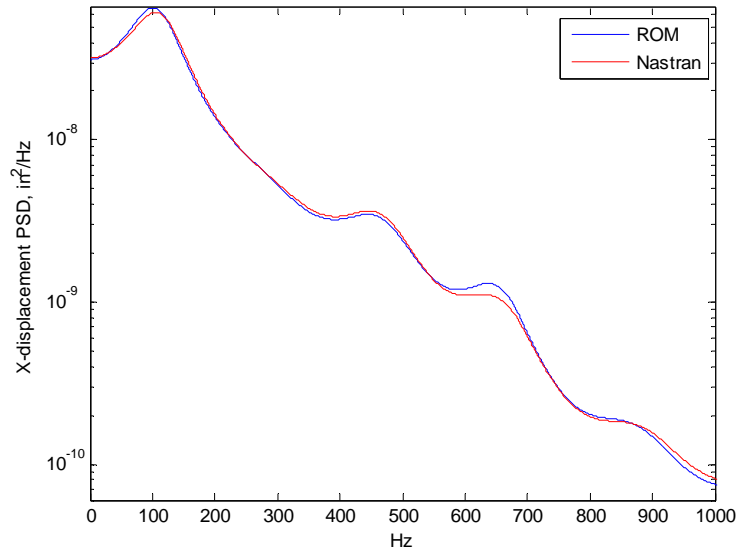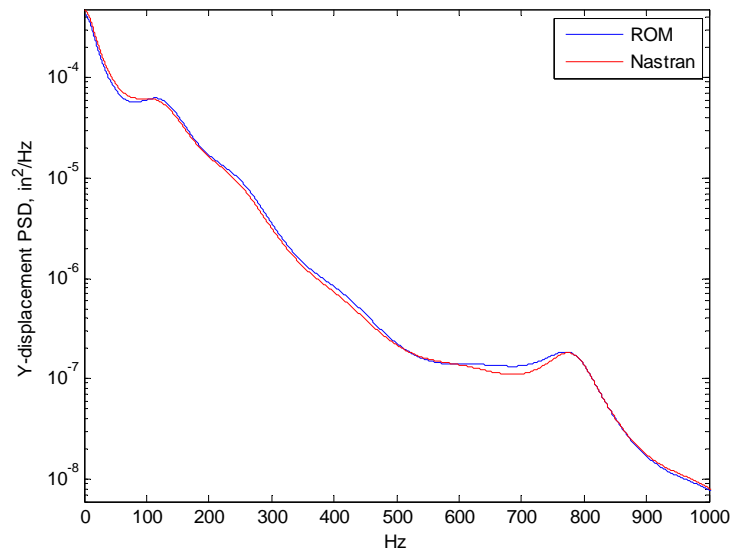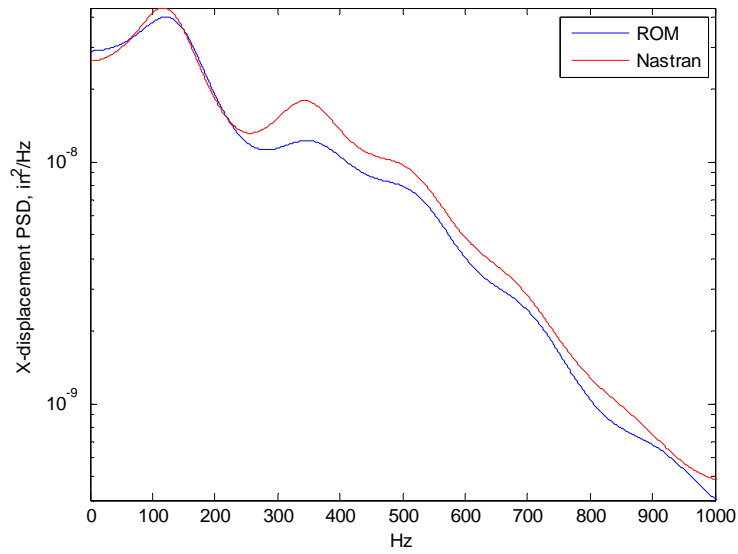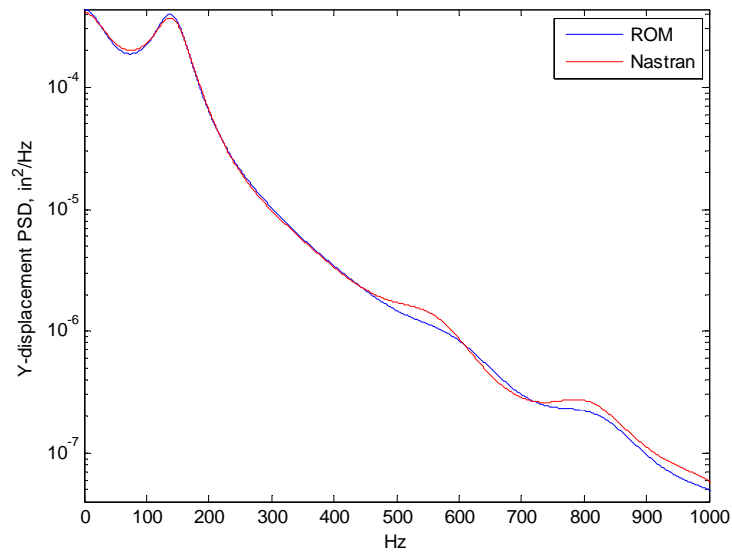
= 2 lb/in, [0, 4000Hz]. (a) X and (b) Y displacements.

Chapter 7

SUMMARY

The present investigation focused on a revisit and extension of existing approaches for the reduced order modeling of the geometrically nonlinear response of a curved beam. Difficulties, i.e. instability of the reduced order model, encountered in the past were first analyzed. This effort then served as the basis for the formulation of a revised identification procedure of the parameters of the reduced order model, see Eqs (3.10)-(3.13). The application of this procedure to the previous curved beam model removed the instability issue and led to an excellent matching of reduced order model and finite element predictions for a broad range of external loading. The present results extend previous validation studies in demonstrating the worth of reduced order modeling of nonlinear geometric structures.

REFERENCES

[1] McEwan, M.I., Wright, J.R., Cooper, J.E., and Leung, A.Y.T, "A combined Modal/Finite Element Analysis Technique for the Dynamic Response of a Nonlinear Beam to Harmonic Excitation", *Journal of Sound and Vibration* 243 (2001): 601-624.

[2] Hollkamp, J.J., Gordon, R.W., and Spottswood, S.M, "Nonlinear Modal Models for Sonic Fatigue Response Prediction: A Comparison of Methods", *Journal of Sound and Vibration* 284 (2005): 1145-1163.

[3] Radu, A., Yang, B., Kim, K., and Mignolet, M.P, "Prediction of the Dynamic Response and Fatigue Life of Panels Subjected to Thermo-Acoustic Loading", *Proceedings of the 45th Structures, Structural Dynamics, and Materials Conference.* Palm Springs, California, 2004. AIAA Paper AIAA-2004-1557.

[4] Przekop, A. and Rizzi, S.A, "Nonlinear Reduced Order Finite Element Analysis of Structures With Shallow Curvature", *AIAA Journal* 44, no. 8 (2006): 1767-1778.

[5] Gordon, R.W. and Hollkamp, J.J, "Reduced-Order Modeling of the Random Response of Curved Beams using Implicit Condensation", *AIAA Journal* (2006).

[6] Spottswood, S.M., Hollkamp, J.J., and Eason, T.G, "On the Use of Reduced-Order Models for a Shallow Curved Beam Under Combined Loading", *Proceedings of the 49th Structures, Structural Dynamics, and Materials Conference.* Schaumburg, Illinois, 2008. AIAA Paper AIAA-2008-1873

[7] Kim, K., Khanna, V., Wang, X.Q., Mignolet, M.P, "Nonlinear Reduced Order Modeling of Flat Cantilevered Structures", *Proceeding of the 50th Structures, Structural Dynamics, and Materials Conference.* Palm Springs, 2009. AIAA Paper AIAA-2009-2492.

[8] Kim, K., Wang, X.Q., and Mignolet, M.P, "Nonlinear Reduced Order Modeling of Functionally Graded Plates", *Proceedings of the 49th Structures, Structural Dynamics, and Materials Conference.* Schaumburg, Illinois, Apr. 7-10, 2008. AIAA Paper AIAA-2007-2014

[9] Perez, R., Wang, X.Q., Mignolet, M.P, "Nonlinear reduced order models for thermoelastodynamic response of isotropic and FGM panels", *AIAA Journal* 49 (2011): 630-641.

[10] Perez, R., Wang, X.Q., Mignolet, M.P, "Reduced order modeling for the nonlinear geometric response of cracked panels", *Proceeding of the 52th*

Structures, Structural Dynamics and Materials Conference. Denver, 2011. AIAA Paper AIAA-2011-2018.

[11] Spootswood, S.M., Eason, T.G., Wang, X.Q., Mignolet, M.P, "Nonlinear reduced order modeling of curved beams: a comparison of methods", *Proceeding of the 50th Structures, Structural Dynamics, and Materials Conference*. Palm Springs, 2009. AIAA Paper AIAA-2009-2433.

[12] Rizzi, S.A. Przekop, A, "System identification-guided basis selection for reduced-order nonlinear response analysis", *Journal of Sound and Vibration* 315 (2008): 467-485.

[13] Przekop, A. Rizzi, S.A, "Nonlinear reduced-order analysis with time-varying spatial loading distributions", *Journal of Aircraft* 46 (2009): 1395-1402.

[14] Muravyov, A.A. and Rizzi, S.A, "Determination of Nonlinear Stiffness with Application to Random Vibration of Geometrically Nonlinear Structures", *Computers and Structures* 81 (2003): 1513-1523.

[15] Fung, Y.C., and Tong, P, *Classical and Computational Solid Mechanics*. River Edge, New Jersey: World Scientific, 2001.

[16] Bonet, J., and Wood, R.D., *Nonlinear Continuum Mechanics for Finite Element Analysis*, Cambridge: Cambridge University Press, 1997.

[17] Kerschen, G., Golinval, J.-C., Vakakis, A.F., Bergman, L.A., "The method of proper orthogonal decomposition for dynamical characterization and order reduction of mechanical systems: an overview", *Nonlinear Dynamics* 41 (2005): 147-169.